U.S. Department of Energy
FreedomCAR and Vehicle Technologies, EE-2G
1000 Independence Avenue, S.W.
Washington, D.C. 20585-0121

FY 2004

Oak Ridge National Laboratory
Annual Progress Report for the Power Electronics and Electric Machinery Program

Prepared by:

Oak Ridge National Laboratory

Laura D. Marlino, Program Manager

Submitted to:

Energy Efficiency and Renewable Energy
FreedomCAR and Vehicle Technologies
Vehicle Systems Team

Susan A. Rogers, Technology Development Manager

January 2005

CONTENTS

FIGURES

2. Thermal Management System for Motor and Inverter

FIGURES (cont.)

3. Electric Machinery R&D

A. Radial Gap Permanent Magnet Motors

Figure

B. Studies of Competitive Products

C. Electric Machine R&D

FIGURES (cont.)

D. Study of HEV Traction Motors

Figure

4. Power Electronics Research and Technology Development

A. Wide Bandgap Semiconductors

B. Integrated dc-dc Converter for Multi-Voltage Bus Systems in HEVs and Fuel Cell Vehicles

FIGURES (cont.)

Figure

C. Integrated Inverter for HEVs and Fuel Cell Powered Vehicles

FIGURES (cont.)

FIGURES (cont.)

6. Power Electronics Crosscut Activities for EERE and OETD

Figure

7. Technology Assessments

TABLES

ACRONYMS

ac	alternating current
AEMD	automotive electric motor drive
AGPM	axial-gap permanent magnet
AIEC	Automotive Integrated Electronics Corporations
AIPM	automotive integrated power module
ANL	Argonne National Laboratory
APRF	Advanced Powertrain Research Facility
BDCM	brushless dc motor
BLDC	brushless dc
BLPM	brushless permanent magnet
CHO	Chinese hamster ovary cells
COP	coefficient of performance
CPA	conventional phase advance
CPSR	constant power speed ratio
CRADA	cooperative research and development agreement
dc	direct current
DOE	Department of Energy
DMIC	dual-mode inverter control
DSP	digital signal processor
EERE	Energy Efficiency and Renewable Energy
EETT	Electrical and Electronics Technical Team
emf	electromotive force
EMI	electromagnetic interference
ESR	equivalent series resistance
FEA	finite-element analysis
HEV	hybrid electric vehicle
HF	high frequency
H.V.	high-voltage
HSU	high-strength undiffused
HSUB	high-strength undiffused brushless
HSUI	hybrid-secondary-uncluttered induction
HSUPM	hybrid-secondary-uncluttered permanent magnet
HVAC	heating, ventilating, and air-conditioning
IGBT	insulated gate bipolar transistor
IEEE	Institute of Electrical and Electronics Engineers, Inc.
I/O	input/output
IM	induction motor
IMPM	interior mounted permanent magnet
IPM	interior permanent magnet
ISR	Isothermal Systems Research
JFET	junction field-effect transistor
MOSFET	metal oxide semiconductor field-effect transistor
MSU	Michigan State University
NdFeB	Neodinium Iron Boron
NRE	non-recurring engineering
OEM	original equipment manufacturer
OETD	Office of Electric Transmission and Distribution
ORNL	Oak Ridge National Laboratory
PC	personal computer
PEEMRC	Power Electronics and Electric Machinery Research Center
PM	permanent magnet
PMDC	permanent magnet direct current
PMSM	permanent magnet synchronous motor
PNGV	Partnership for a New Generation of Vehicles
PWM	pulse-width modulation
R&D	research and development
RSI	resonant snubber inverter
Si	silicon
SiC	silicon carbide
SCR	silicon-controlled rectifier
SDP	switch device power
SHV	series hybrid vehicle
SMC	soft magnetic composite
SMPM	surface mounted permanent magnet
SoC	System on a Chip
SRM	switched reluctance motor
THS	Toyota hybrid system (2003)
THS II	Toyota hybrid system (2004)
VJFET	vertical junction field-effect transistor
VSI	voltage source inverter
WBG	wide bandgap
ZSC	zero-sequence circuit
ZVS	zero-voltage-switching

1. INTRODUCTION

The U.S. Department of Energy (DOE) and the U.S. Council for Automotive Research (composed of automakers Ford, General Motors, and DaimlerChrysler) announced in January 2002 a new cooperative research effort. Known as FreedomCAR ("CAR" stands for "Cooperative Automotive Research"), it represents DOE's commitment to developing public/private partnerships to fund high-risk, high-payoff research into advanced automotive technologies. Efficient fuel cell technology, which uses hydrogen to power automobiles without air pollution, is a very promising pathway to achieve the ultimate vision. The new partnership replaces and builds upon the Partnership for a New Generation of Vehicles (PNGV) initiative that ran from 1993 through 2001.

The Vehicle Systems subprogram within the FreedomCAR and Vehicle Technologies Program provides support and guidance for many cutting-edge automotive and heavy truck technologies now under development.

Research is focused on understanding and improving the way the various new components of tomorrow's automobiles and heavy trucks will function as unified systems to improve fuel efficiency. This work also supports the development of advanced automotive accessories and the reduction of parasitic losses (e.g., aerodynamic drag, thermal management, friction and wear, and rolling resistance).

In supporting the development of hybrid propulsion systems, the Vehicle Systems subprogram has enabled the development of technologies that will significantly improve fuel economy, comply with projected emissions and safety regulations, and use fuels produced domestically.

The Vehicle Systems subprogram supports the efforts of the FreedomCAR and Fuel and the 21st Century Truck Partnerships through a three-phase approach intended to

- Identify overall propulsion and vehicle-related needs by analyzing programmatic goals and reviewing industry's recommendations and requirements and then develop the appropriate technical targets for systems, subsystems, and component research and development (R&D) activities;
- Develop and validate individual subsystems and components, including electric motors, emission control devices, battery systems, power electronics, accessories, and devices to reduce parasitic losses; and
- Determine how well the components and subsystems work together in a vehicle environment or as a complete propulsion system and whether the efficiency and performance targets at the vehicle level have been achieved.

The research performed under the Vehicle Systems subprogram will help remove technical and cost barriers to enable technology for use in such advanced vehicles as hybrid and fuel-cell-powered vehicles that meet the goals of the FreedomCAR Program.

A key element in making hybrid electric vehicles (HEVs) practical is the development of a low-cost automotive integrated power module (AIPM) capable of handling up to approximately 100 kW of power for vehicle operation. The AIPM is one of a new class of power electronic building block technologies integrating a complex system of power electronics into a single, lightweight propulsion unit.

The control system in a conventional vehicle controls the performance characteristics of the combustion engine and other performance aspects of the vehicle. An HEV control system serves the same function, but the AIPM would also control

- The transmission of power into and out of the electric drive motors,
- The power output of the engine, and
- The energy storage interface.

Integral to the AIPM's function is the use of advanced power semiconductors to control the flow of electric power by shaping the supplied voltages.

Recent advances in packaging have eliminated the need for wire bonding, or the use of fine wires to connect a power semiconductor device to the leads on its package. Work is also continuing to improve the performance and cost of induction, switched reluctance, and permanent magnet (PM) motors. The use of a virtual-reality-based computer model — ADVISOR (developed by the National Renewable Energy Laboratory) — is an important part of this effort.

Other supporting research includes

- Improving thermal management,
- Developing advanced sensors for precise current measurement,
- Evaluating HEV traction drive systems,
- Performing HEV motor inverter modeling, and
- Exploring advanced propulsion concepts and control.

The Oak Ridge National Laboratory's (ORNL's) Power Electronics and Electric Machinery Research Center (PEEMRC) conducts fundamental research, evaluates hardware, and assists in the technical direction of the DOE Office of FreedomCAR and Vehicle Technologies Program, Power Electronics and Electric Machinery Program. In this role, ORNL serves on the FreedomCAR Electrical and Electronics Technical Team (EETT), evaluates proposals for DOE, and lends its technological expertise to the direction of projects and evaluation of developing technologies.

ORNL also executes specific projects for DOE. The following report discusses those projects executed in FY 2004 and conveys highlights of their accomplishments. Numerous project reviews, technical reports, and papers have been published for these projects, if the reader is interested in pursuing details of the work.

2. Thermal Management System for Motor and Inverter

John S. Hsu
Oak Ridge National Laboratory
National Transportation Research Center
2360 Cherahala Boulevard
Knoxville, Tennessee 37932-6472
Voice: (865) 946-1325; Fax: (865) 946-1262; E-mail: hsujs@ornl.gov

DOE Technology Development Manager: Susan A. Rogers
Voice: (202) 586-2314; Fax (202) 586-1600; E-mail: Susan.Rogers@hq.doe.gov

ORNL Program Manager: Laura D. Marlino
Voice: (865) 946-1245; Fax: (865) 946-1262; E-mail: marlinold@ornl.gov

---

Objectives

- Reduce cost, weight, and volume of electric machinery, drives, and the thermal management system.
- Improve performance.
- Simplify the system.
- Increase reliability.

Approach

- Assess various leading two-phase cooling technologies developed by external companies and a university.
- Investigate stand-alone floating loop cooling system for cooling motors and silicon (Si) dies.
- Complete initial design work on incorporating a floating loop cooling system to the vehicle air-conditioning system for cooling motors and inverters.
- Study floating loop components.
- Prepare for floating loop system integration.

Accomplishments

- Derived the ORNL floating loop concept that can be used as a stand-alone system or can be incorporated into the vehicle air-conditioning system to cool the motors and inverter/converter.
- Determined the major challenges of the floating loop components.

Future Direction

- Conduct a continuous technology assessment effort with leading external companies/university and integrate the motor and inverter into the ORNL floating loop.
- Conduct further work on floating loop components such as the sealed terminal, capacitor cooling, and cascade die mountings.

Publications

1. I. Sauers, D. R. James, A. R. Ellis, C. E. Easterly, and J. S. Hsu, *Preliminary Measurements of Dielectric And Toxic Properties Of Potential Refrigerants For Two-Phase Cooling Of Power Electronics And Motors*, ORNL/TM-2004/210, Oak Ridge National Laboratory, UT-Battelle, LLC, September 2004.

Patents

1. Provisional patent application filed for the floating loop.
2. Utility patent application filed for using the zero-sequence component for a single inverter to drive both the traction motor and the air-conditioning motor.

Technical Discussion

The thermal management status of the motor and power electronic inverter versus their targets is clearly shown in Fig 1. The cooling and lifetime are lagging. The cost needs to be further reduced.

In the effort to meet the FreedomCAR objectives of high power density, low cost, and a 15-year life expectancy, the thermal management of the inverter/converter and motor/generator plays an important role. It is known that two-phase (i.e., liquid to vapor) cooling is an order of magnitude better than single-phase cooling. ORNL's role is to assess various leading two-phase cooling technologies developed by external companies and a university for an inverter. These two-phase cooling technologies being assessed are as follows:

- VIBE/VIDA cooling from the bottom developed by Georgia Tech University and Innovative-Fluidics Company with 105°C ethylene-glycol water. This technology uses piezoelectric vibrators for bubble ejections.
- Jet impingement from the bottom the developed by Rockwell Scientific Company with 105°C ethylene-glycol water.
- Spray cooling from the top of dies developed by Isothermal Systems Research (ISR) with 80°C ethylene-glycol water that cools a low-pressure secondary coolant.

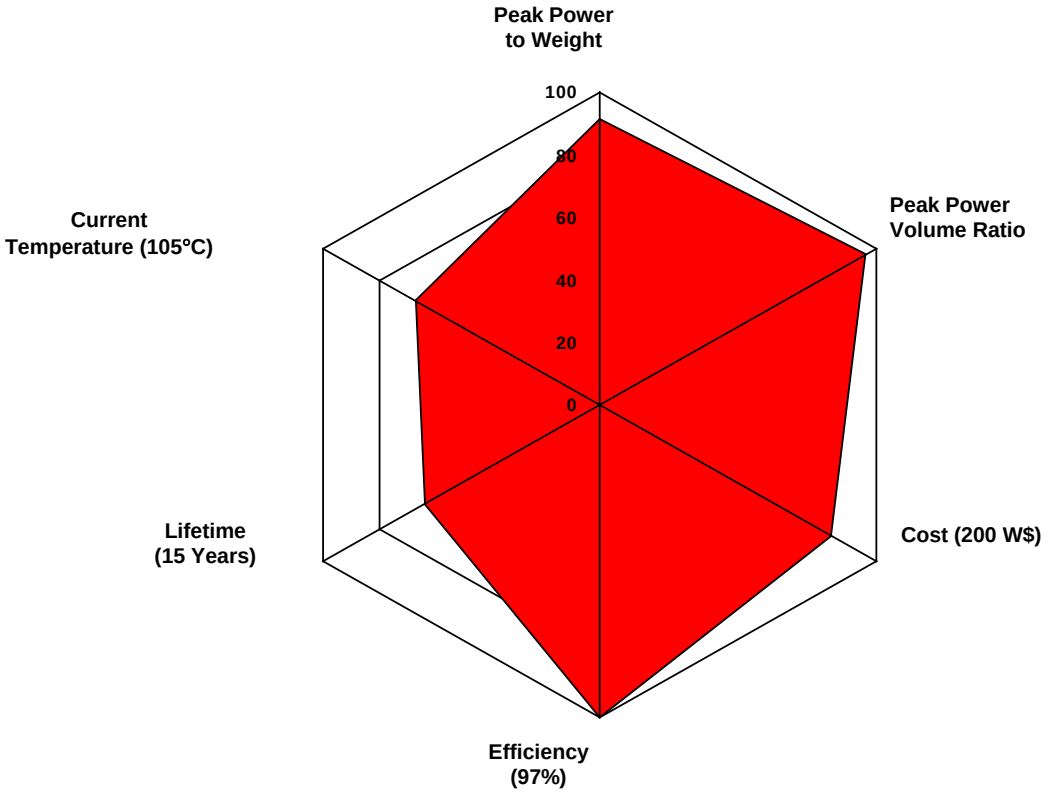

Inverter

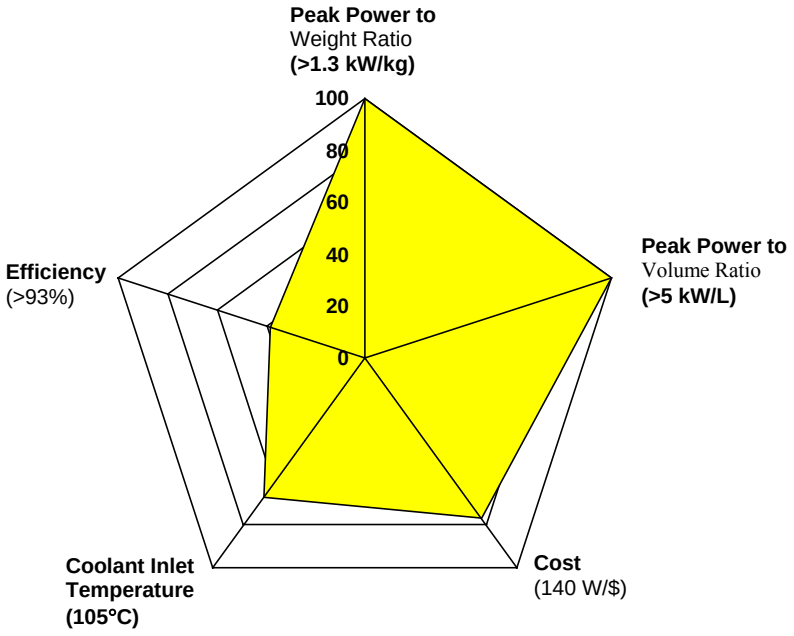

Motor

Fig. 1. Thermal management status of motor and inverter vs. their targets.

Source: Vijay Garg, Ford – Co Chair, Susan Rogers, DOE – Co Chair, "Electrical and Electronics Tech Team NAS Review," November 18, 2004.

The first is a direct current (dc) test with currents flowing through the insulated gate bipolar transistors (IGBTs). The second is an alternating current (ac) switching test with currents flowing through both the IGBTs and the diodes. The preliminary tests indicate that when the ethylene-glycol water is used directly for two-phase cooling, the two-phase heat transfer is less significant because of the ethylene-glycol water higher boiling temperature of 106+°C and is limited by the thermal resistance from the junction to the cold plate and the low permissible junction temperature of 125°C.

ISR spray cooling uses not 105°C but 80°C ethylene-glycol water that cools a low-pressure secondary coolant. A relatively significant two-phase cooling is expected.

Another ORNL role for thermal management is to develop a floating loop cooling system that may be either incorporated into the vehicle air-conditioning system or operated independently without being attached to the air-conditioning system. Very little additional energy is required for the cooling of the motor and inverter/converter. The reason is explained through the refrigeration cycle shown in Fig. 2.

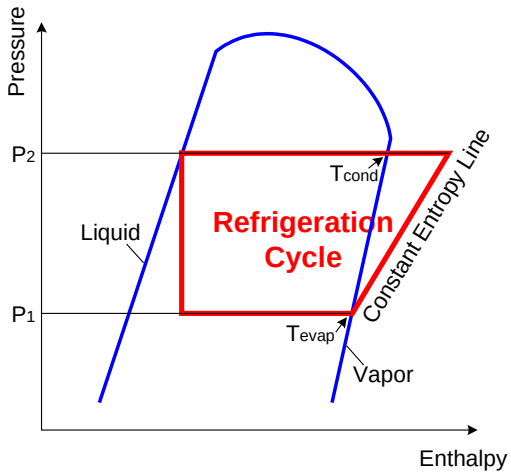

Enthalpy is the measurement of heat and energy of the system:
Enthalpy = Internal energy + Pressure * Volume

Entropy is the instantaneous measurement of the activity of the system:
Entropy = Integration of [(delta)Heat / Temperature K]

Fig. 2. A typical refrigeration cycle.

In a conventional air-conditioning system, the evaporator temperature needs to be very low to produce cool air. In order to have a very low temperature, the pressure, P_1, at the evaporator must be very low. The hot liquid refrigerant coming out from the condenser would squeeze through an expansion valve or a capillary tube for dropping the pressure from P_2 to P_1. The relative large pressure difference, $P_2 - P_1$, is proportional to the power required by the compressor to compress the low-pressure vapor back to a high pressure. This is the reason for the high cost of air-conditioning a household. The floating loop system derived at ORNL avoids this

pressure drop. Consequently, it dramatically reduces the power required for the floating loop cooling system.

Figure 3 shows a sample floating loop system built on top of the existing vehicle air conditioning system.

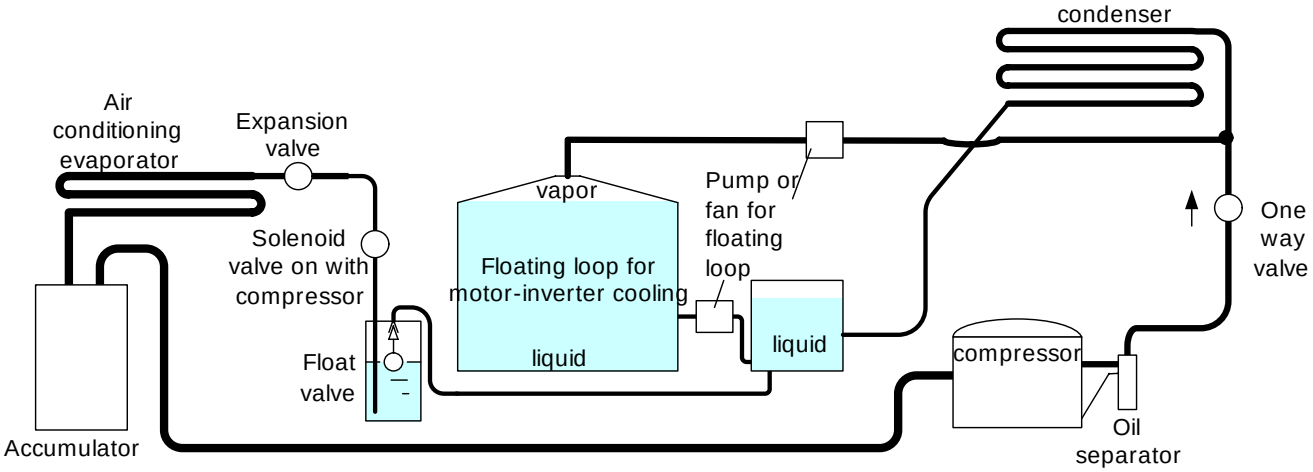

Fig. 3. A sample floating-loop system incorporated into the air-conditioning system.

The motor and inverter do not require that the liquid refrigerant inlet temperature be very low. They can use hot liquid refrigerant. As the hot refrigerant evaporates, the significant latent heat of the liquid refrigerant can take away the losses of the motor and inverter. The pressure difference between the inlet and outlet of the refrigerant is small without going through an expansion valve or a capillary tube in the floating loop. Therefore, very little power is required for cooling the motor and inverter through the ORNL floating loop system. The condenser should be selected to dissipate the heat generated by both the passengers and the motor/inverter. During the winter, the compressor is idle and only the small refrigerant pump in the floating loop is working. The condenser is used by the floating loop only.

When the compressor is not running, the solenoid valve shuts the refrigerant path to the air-conditioning evaporator. The refrigerant is circulated around the floating loop and the condenser by a small pump or fan for heat dissipation. The floating loop system does not require many additional components for incorporation into the vehicle air-conditioning system. This will help to cut down the cost and the required space.

Later on in this report, examples of using the stand-alone floating loop to cool the motor and dies will be shown.

In FY 2004, initial investigations were conducted on the motor and electronics components to see the cooling effects and the problems, such as the terminal sealing associated with the refrigerant liquid. These investigations help to identify the research tasks on the floating loop systems.

Temperature Rise Tests for Motor with Cooling Jacket

The first of the initial floating loop component investigations was conducted on a traction motor built with a supposed water jacket, as shown in Fig. 4. Without going through either a compressor or an expansion valve, liquid refrigerant will pass through the supposed water jacket for the cooling test. However, in order to examine the safety of the frame under the pressure of the conventional R134a refrigerant for cars, the liquid pressure versus the frame deformation is tested. From the frame deformation, the housing circumferential (hoop) stress can be assessed from strain measurements obtained. The frame material stress versus the liquid stress can be derived and plotted in Fig. 5. This can be used to estimate the safe liquid-pressure limit for the test.

Because this motor is a surplus traction motor with a supposed water jacket, the flow path in the frame was unknown. The only flow paths known to the testers were the inlet and outlet, as shown in Fig. 6.

Figure 7 shows that the coolant flow path in the motor frame was detected non-invasively through an infrared camera. The path is drawn on the frame after the detection.

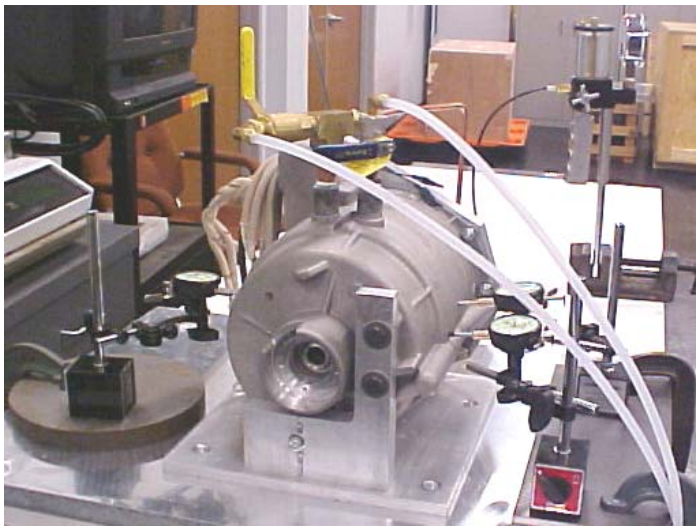

Fig. 4. A traction motor built with a supposed water jacket.

Aluminum Motor Housing Hoop Stress due to Coolant Pressure Test, 10-03-03

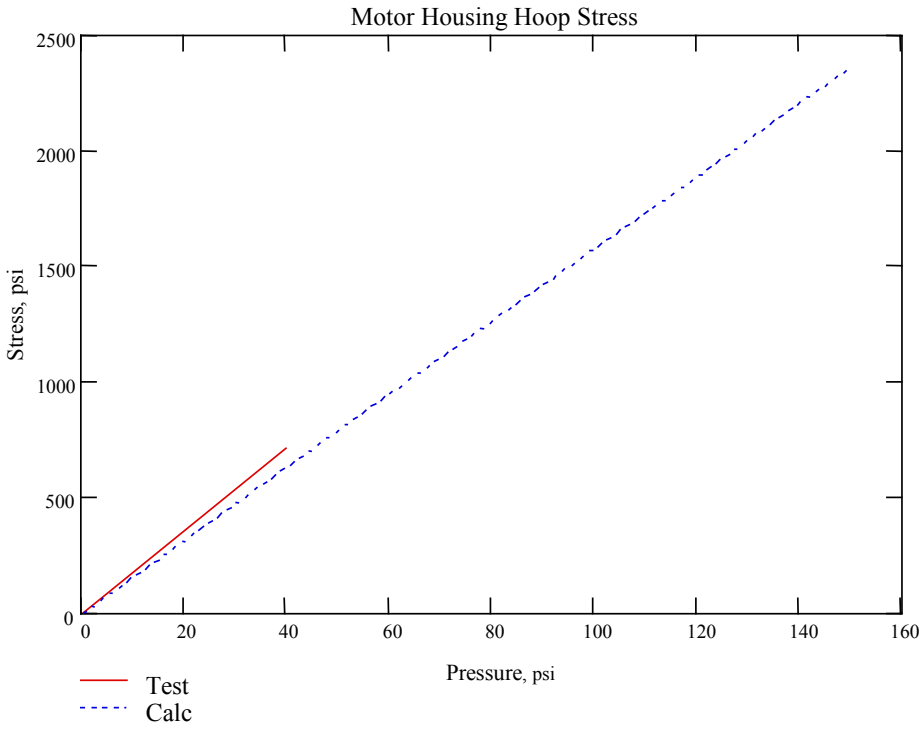

Fig. 5. Motor frame material stress vs. liquid pressure.

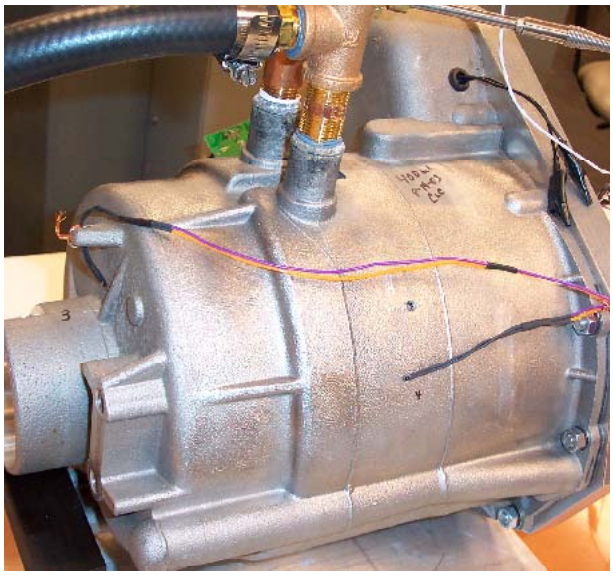

Fig. 6. Coolant inlet and outlet of the motor.

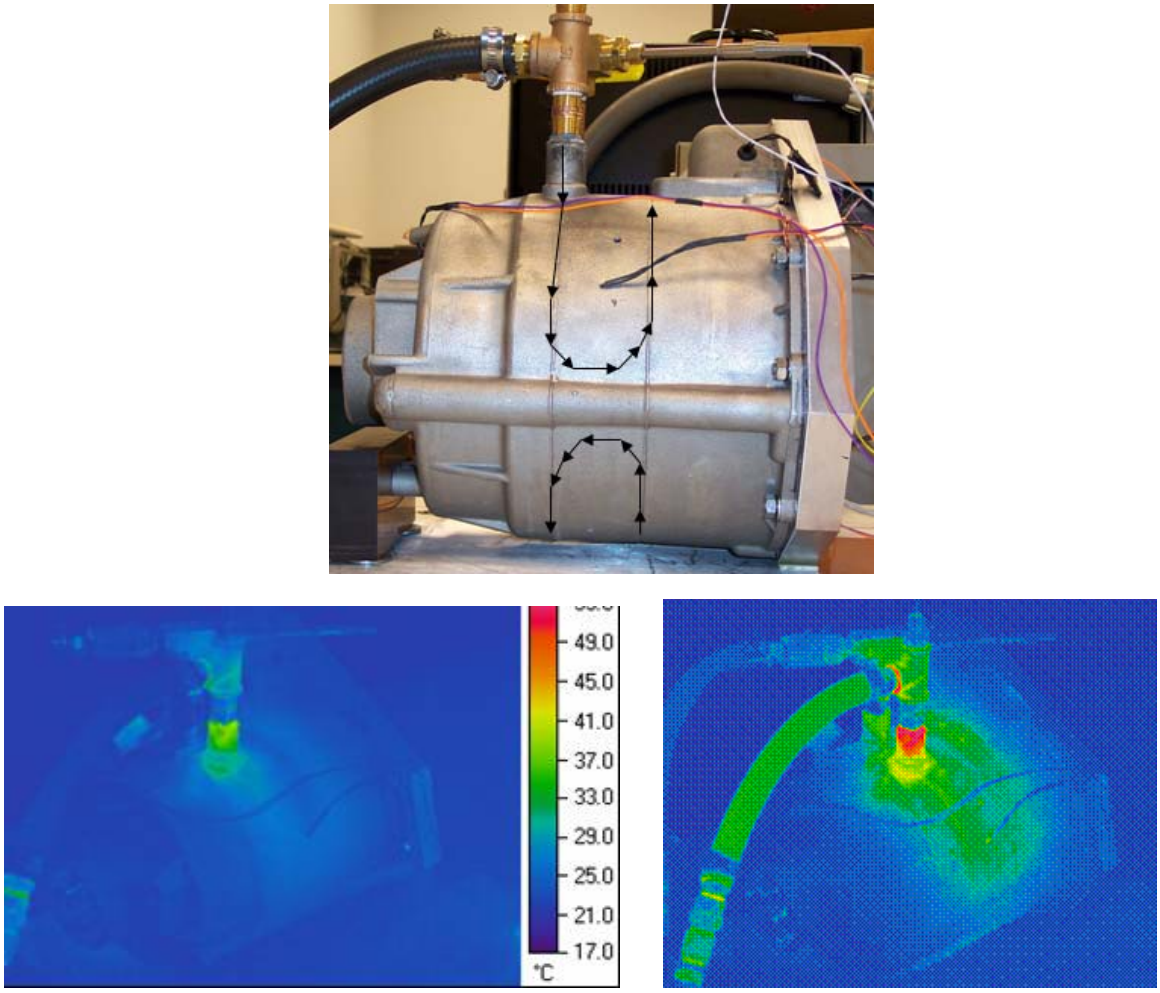

Fig. 7. Non-invasive detection of coolant flow path in the motor frame.

Figure 8 shows the test of the motor cooling in a stand-alone floating loop. The motor shown in the right of the picture is a traction motor with a supposed water-cooled jacket. A fuel pump shown in the middle of the picture is housed in a high-pressure tube, which is used to circulate the refrigerant in the floating loop. No capillary tube, expansion valve, or compressor is used in the floating loop. A fan-cooled condenser is shown in the left of the picture.

The tested temperature versus time for the setup shown in Fig. 8 is given in Fig. 9. The fuel pump takes 48 W to cool the motor, with a loss as high as 2150 W. The motor rating can be as high as 30 kW, depending on the motor efficiency.

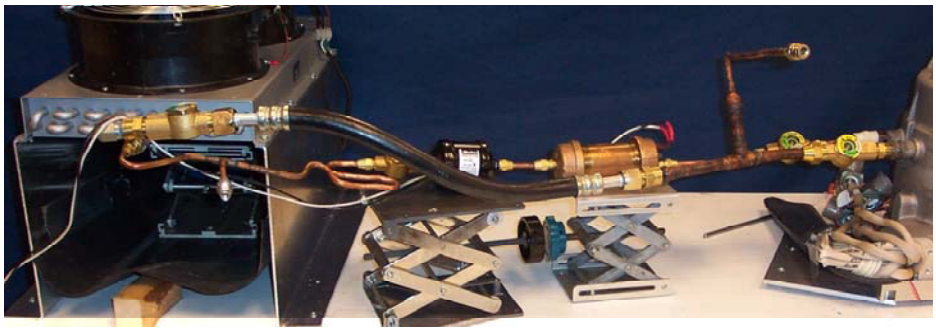

Fig. 8. Test of a motor cooling in a floating loop with a fuel pump.

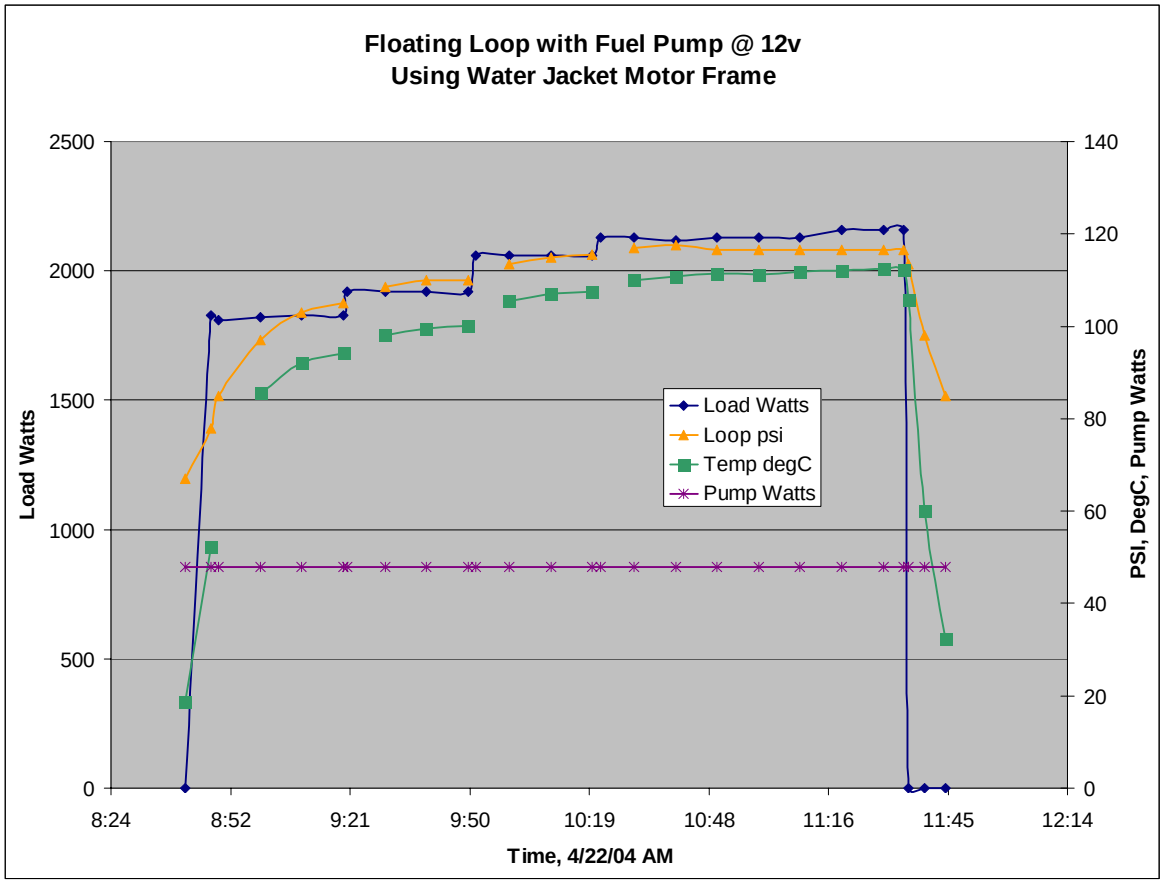

Fig. 9. Tested temperature, pump power in watts, loop pressure, and loss watts vs. time for a motor cooled in a floating loop driven by a fuel pump.

Figure 10 shows another option: using a fan housed in a high-pressure container (shown in the middle of the picture) to circulate the refrigerant vapor in the floating loop instead of using a fuel pump (Fig. 9) to circulate the refrigerant liquid. It works, but the fan is larger than the fuel pump. Therefore, a fan probably will not be used in the floating-loop system to circulate the refrigerant vapor because of its size.

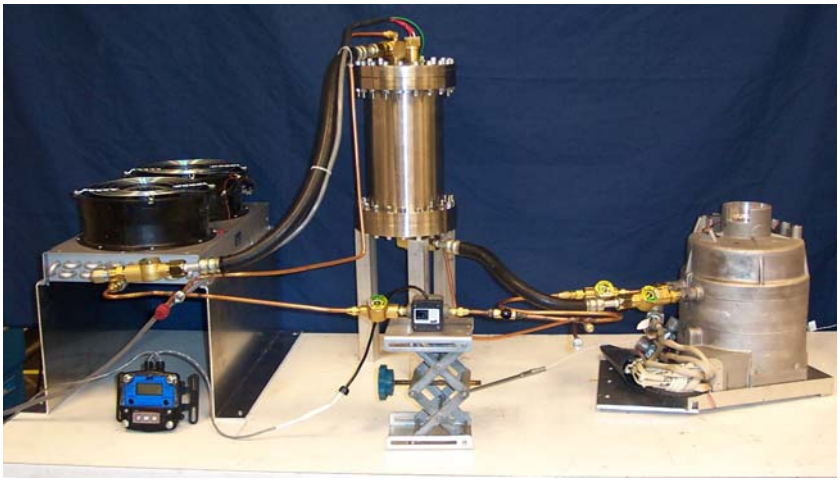

Fig. 10. Using a fan to circulate the refrigerant vapor in the floating loop for motor cooling.

Table 1 shows a comparison of cooling methods without oil droplets versus the motor loss. The comparison is based on the end-turn temperature stabilized at 150°C. For a 30-kW motor with 94% efficiency, the loss is around 1800 W. This gives some idea of the possible rating of a motor that can be cooled with the floating loop.

Table 1. Comparison of floating loop options for a motor

Floating loop options	Capability for motor loss dissipation at motor end-turn of 150°C
Air cooled (no fan, ambient 23°C), no loop	577 W (loss at stator only)
	494 W (loss split to stator + rotor)
Water cooled (inlet water 90°C), no loop	1536 W (stator only)
	1394 W (stator + rotor)
R134A floating loop (0 W no loop power)	1000 W (stator only)
R134A floating loop (110 W, compressor loop power)	2270 W (stator only)
R134A floating loop (210 W, fan loop power)	2200 W (stator only, end-turn at 112°C)
R134A floating loop (48 W, fuel-pump loop power)	2150 W (stator only, end-turn at 120°C)

Oil droplets can be introduced inside the motor frame to help the motor cooling further. Examples can be seen from the Chattanooga Bus Company's traction motor shown in Figs. 11 and 12.

Fig. 11. Chattanooga bus traction motor.

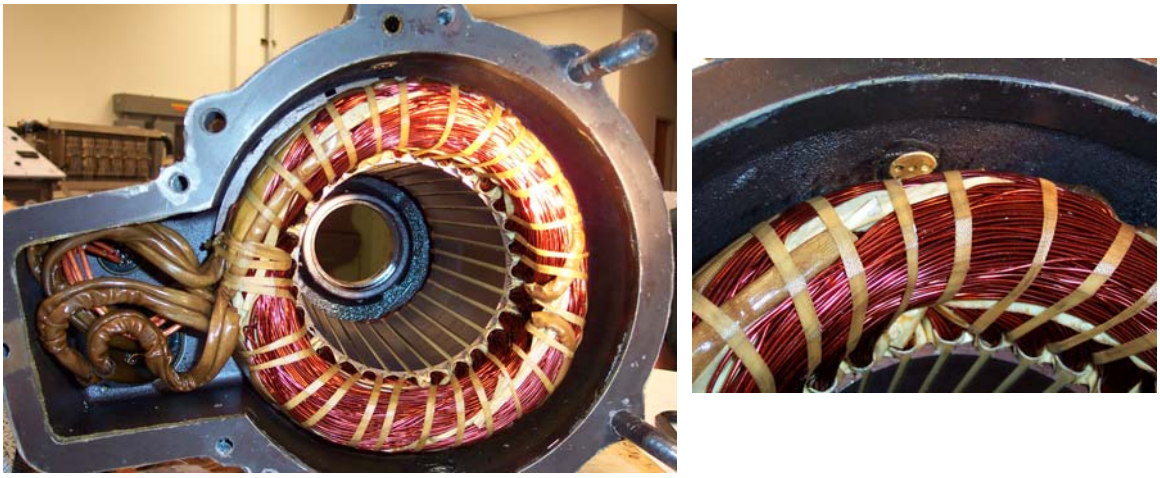

Fig. 12. Showerhead of oil-droplet-cooled Chattanooga bus motor.

Another example of an oil-droplet-cooled motor is the Toyota/Prius motor shown in Fig. 13.

It is possible that the motor and inverter can be integrated and cooled through a floating loop as shown in Fig. 14.

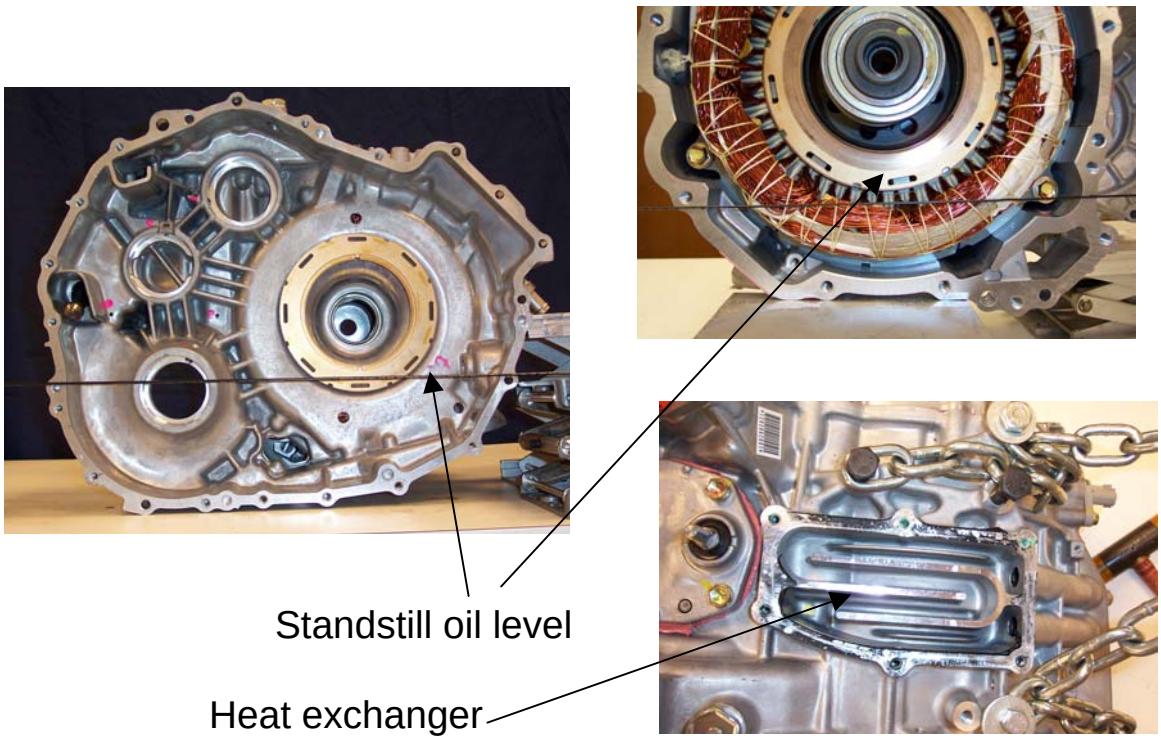

Fig. 13. Toyota/Prius motor with interior oil droplets for cooling assistance.

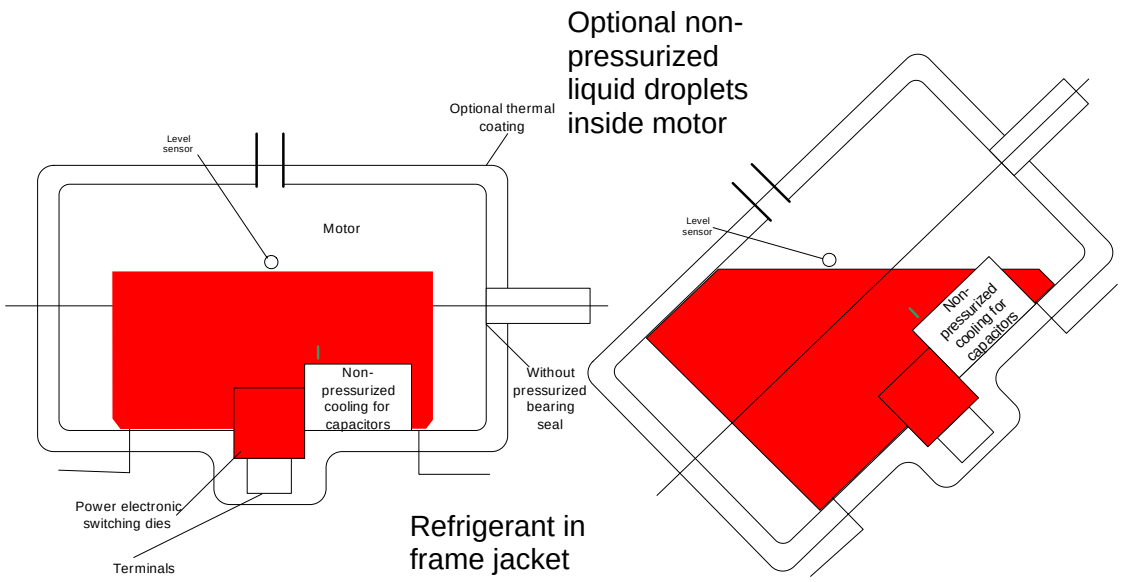

Fig. 14. Possible integration of motor and inverter cooled in a floating loop.

Figure 15 shows another possible cooling structure of an interior-mounted PM reluctance motor with brushless excitation. Liquid refrigerant for cooling the frame and the interior oil droplets is used in this floating loop cooling system. The oil slingers are attached to the rotor to create oil droplets.

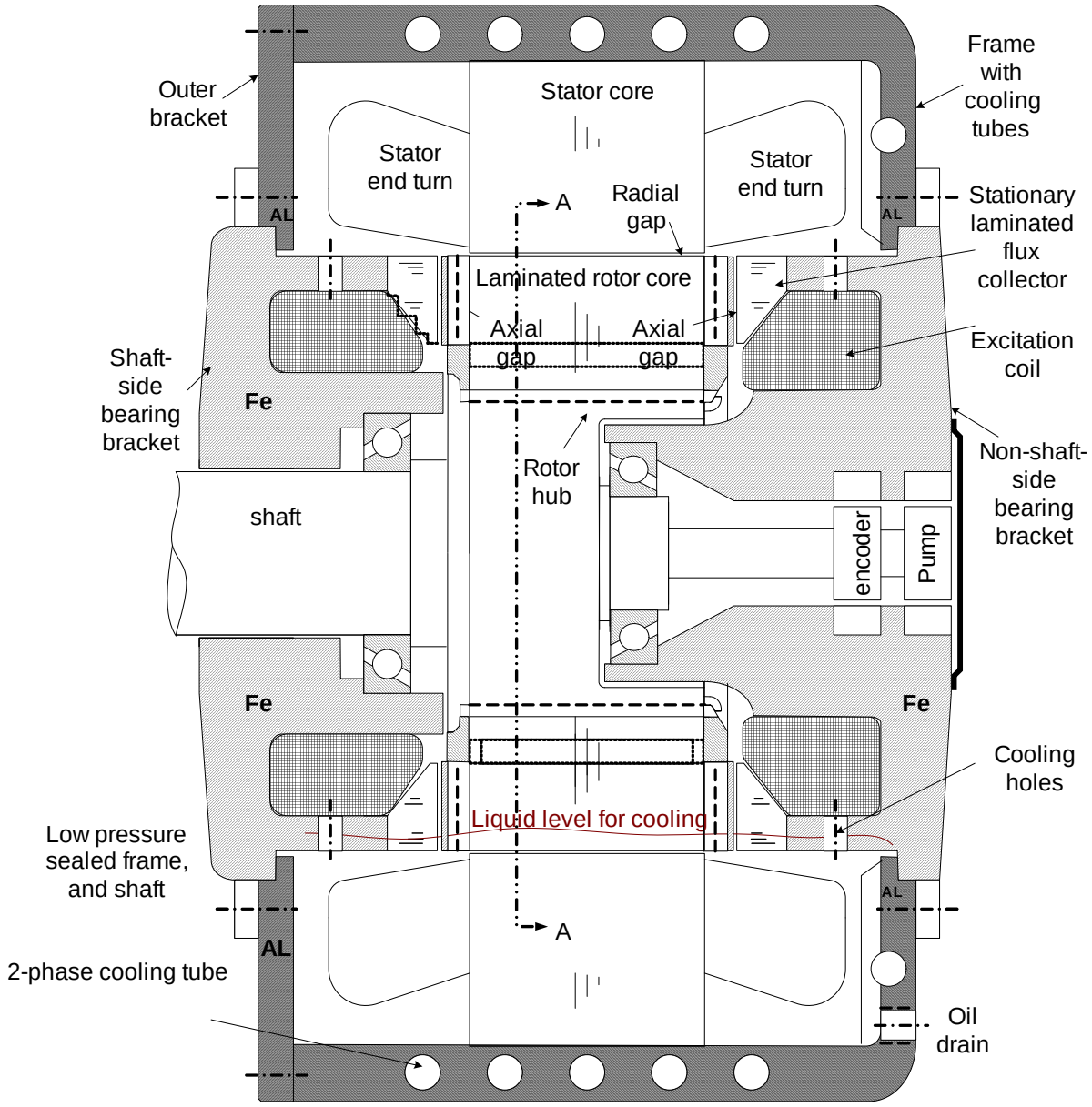

Fig. 15. Example of a motor cooled by liquid refrigerant and oil droplets.

Figure 16 shows an oil slinger driven by a hand drill to produce oil droplets.

Fig. 16. An oil slinger driven by a hand drill to produce oil droplets.

For the inverter cooling in a floating loop, the following tasks were initiated:

- Cascade die mounting
- Submerged die cooling
- Terminal technology
- Refrigerant investigation
- Capacitor investigation

Cascade Die Mounting

The concept of cascade die mounting is shown in Fig. 17. The goal is to cool the dies in a floating loop. The silicon dies of each leg are mounted in a cascade pattern. The assembly is submerged in the liquid refrigerant inside the floating loop for two-phase cooling.

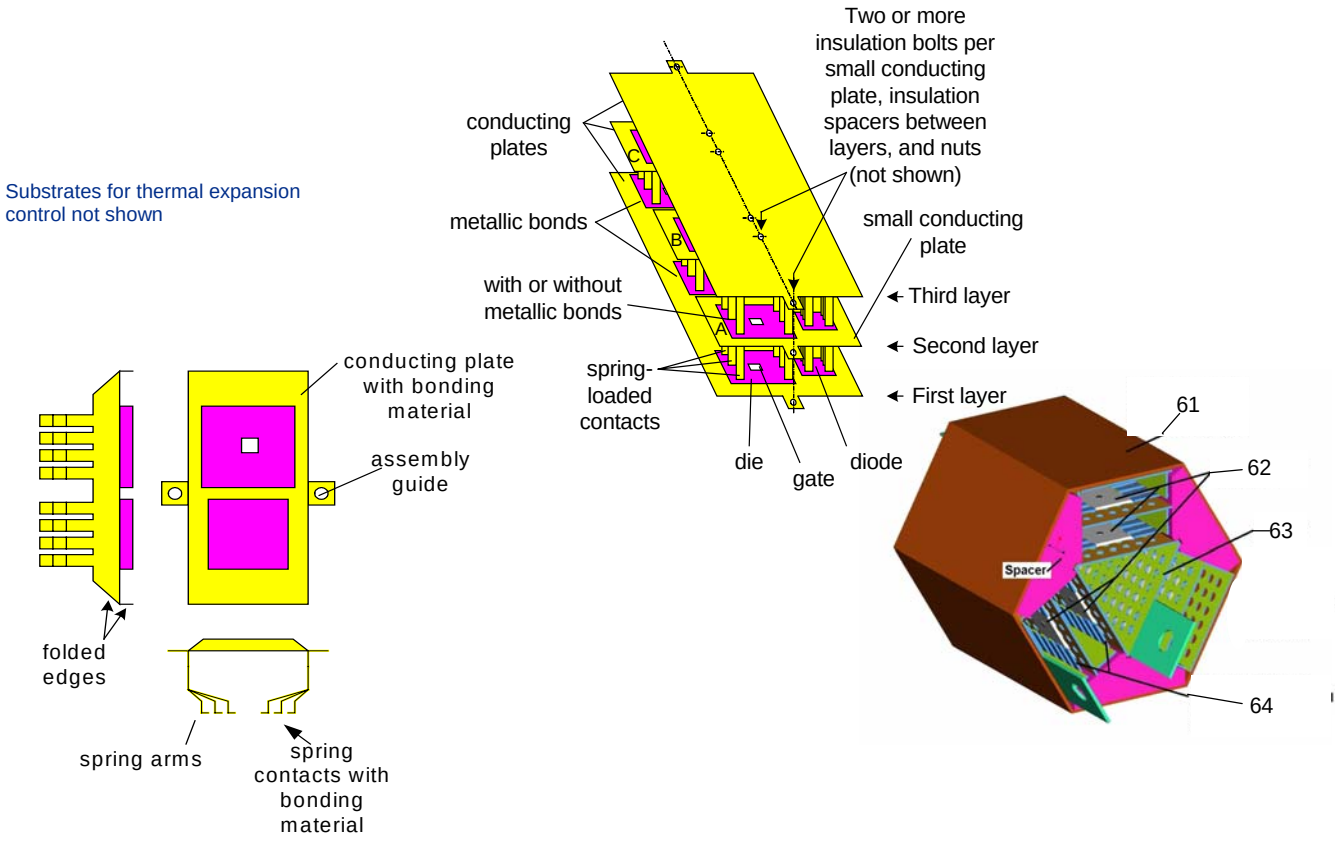

Fig. 17. Concept of cascade die mounting.

Submerged Die Cooling in a Stand-alone Floating Loop

Figure 18 shows the test results for submerged cooling with the refrigerant liquid supply pointing at the hot object. A 214 W/cm^2 cooling capability was obtained.

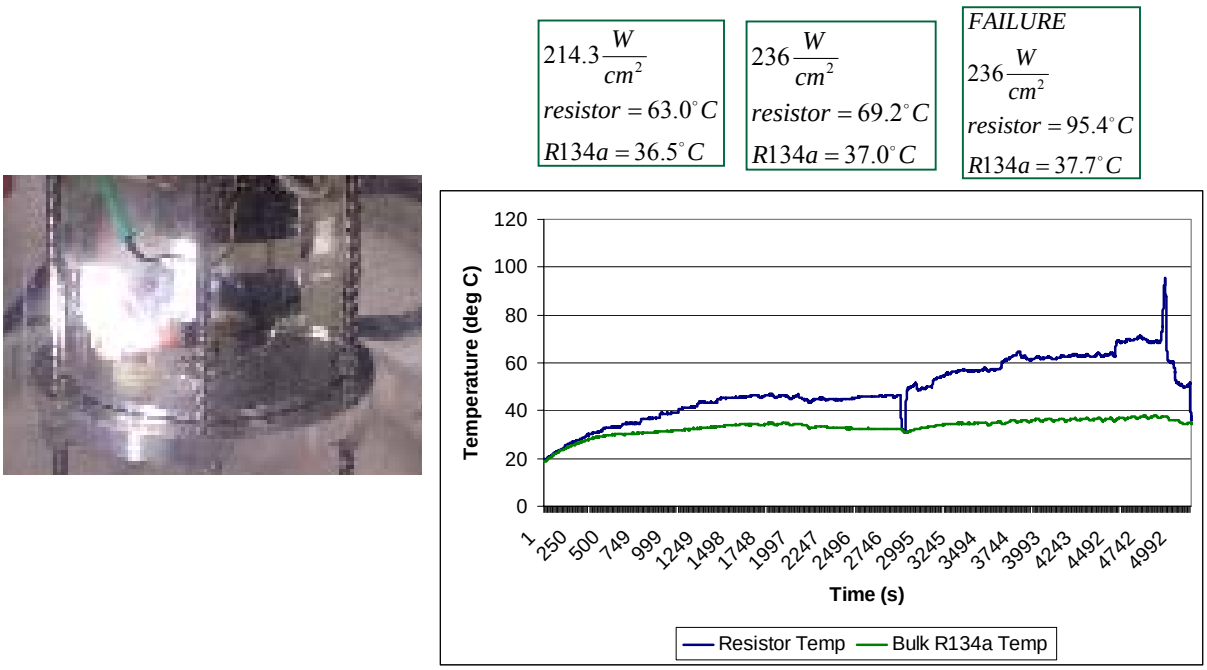

Fig. 18. Submerged cooling with refrigerant-liquid tube pointing at the hot object.

Terminal Technology for Floating Loops

Figure 19 shows an example of a terminal arrangement.

The terminal is very important for the success of the floating loop technology. The under-hood temperature range of –40 to +140 poses a very challenging requirement for the terminal because the materials inside a terminal do not have the same thermal expansion coefficients; different expansion levels between materials will cause leaking. The present status is that we can handle a stable room temperature for the seal of the terminal but not a wide temperature range.

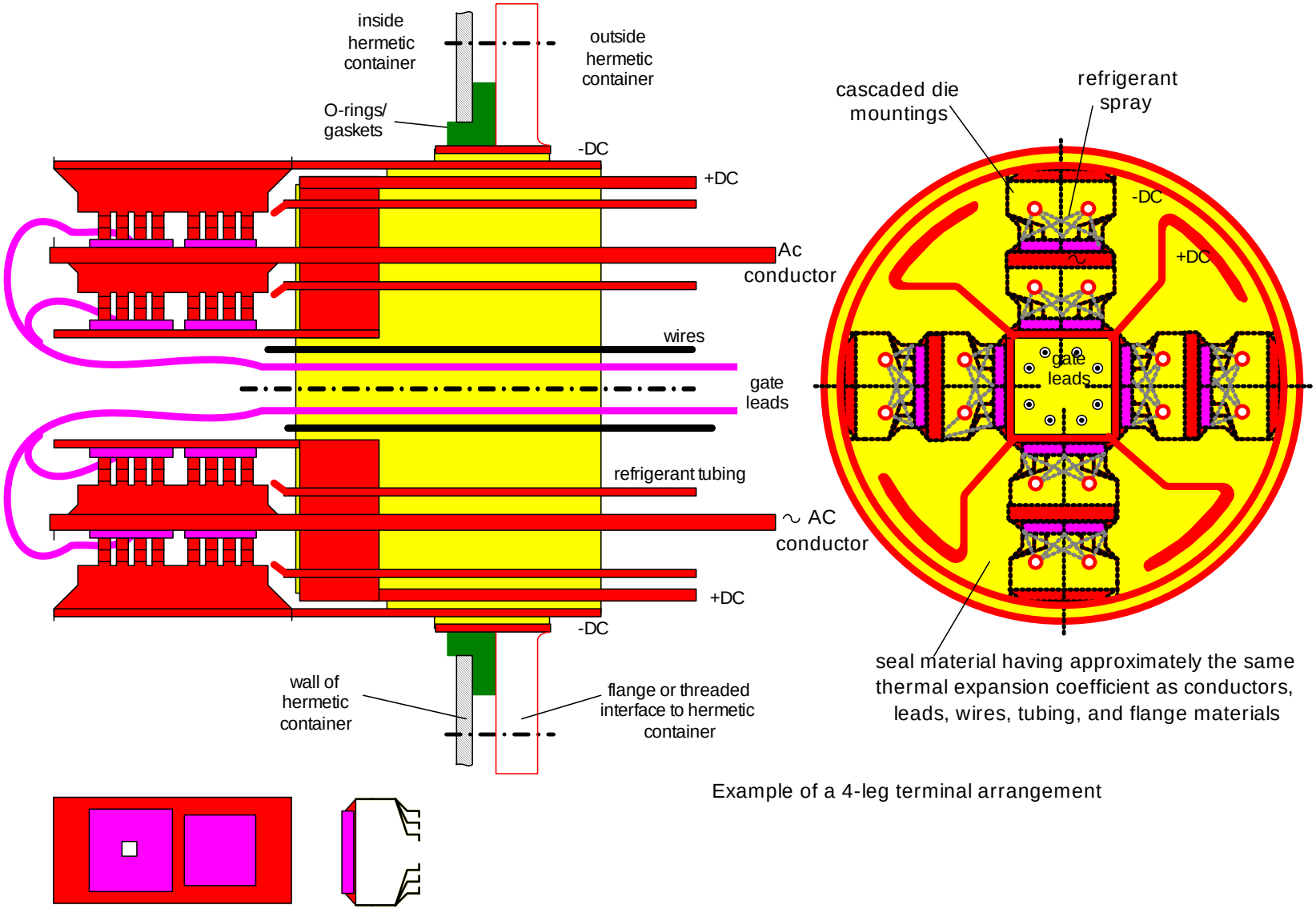

Fig. 19. Example of a terminal arrangement.

The terminal potting compounds shown in Table 2 have been tried. The experimental potting compound samples are illustrated in Fig. 20.

Table 2. Terminal potting compounds

Sample description	Mix ratio By wt	Viscosity	% growth/w 100°C delta	Adhesion	Sample ID
Cu rod	N/A	N/A	0.15%	N/A	
Epoxy & carbon fiber	2.5 to 1.0 (epoxy to fiber)	Does not pour	0.19%	Good	111303
Epoxy & carbon fiber	2.5 to 1.0 (epoxy to fiber)	Does not pour	0.13%	Good	111003
Epoxy & carbon fiber	2.0 to 1.0 (epoxy to fiber)	Does not pour	0.07%	N/A	111103
Epoxy & carbon fiber	10.0 to 1.0 (epoxy to fiber)	Barely pours	0.15%	N/A	12903
Epoxy & al. oxide	10.0 to 1.0 (epoxy/powder)	Pours	1.10%	Poor	16140
Epoxy & al. oxide	0.8 to 1.0 (epoxy/powder)	Barely pours	.59%	Poor	17040
Epoxy & al. oxide	0.75 to 1.0 (epoxy/powder)	Barely pours	.92%	Good	18040
Epoxy & al. oxide	0.71 to 1.0 (epoxy/powder)	Pours	0.78%	Poor	11504

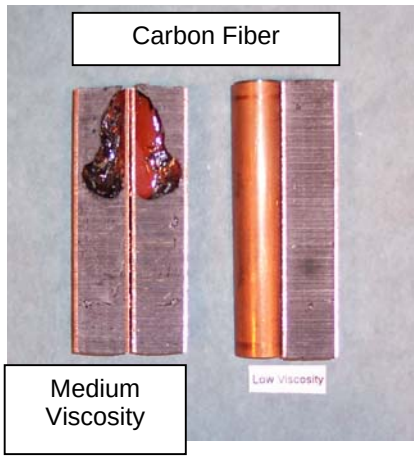

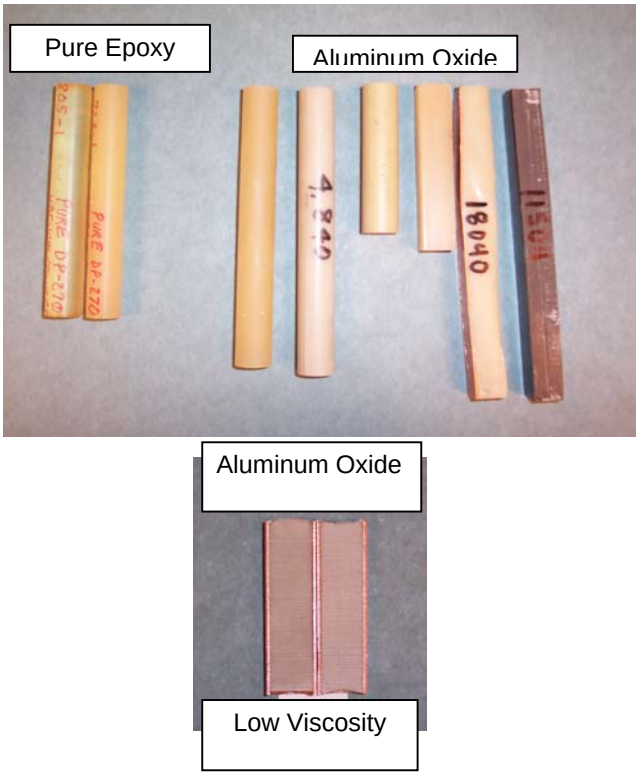

Fig. 20. Experimental potting compound samples.

Refrigerant Investigation

The refrigerant dielectric property and toxicity investigations are important for any direct cooling of power electronic switching components. The dies are exposed directly to the refrigerants in either a spray or submerged cooling. The toxicity investigation will show the potential danger to human health. Initial work on these investigations is outlined as follows. A detailed report was distributed.[1]

The apparatus for breakdown studies of refrigerant gases and liquids is shown in Fig. 21. It has a 50-kV dc power supply, 0–25 mm variable gap spacing (plane-plane electrode geometry) and 0–3 bar pressure. This same apparatus will be used to generate spark-decomposed gases for subsequent toxicity studies.

Fig. 21. Apparatus for breakdown studies of refrigerant gases and liquids.

The relative strength is relative to that of sulfur hexafluoride, which has a strength of 89 kV/cm-bar. The breakdown strengths vs. product of pressure and gap are illustrated in Fig. 22.

At a given temperature, the breakdown strength is a function of both pressure and the inter-electrode gap spacing

Figure 23 shows the dielectric strength test results for R134a.

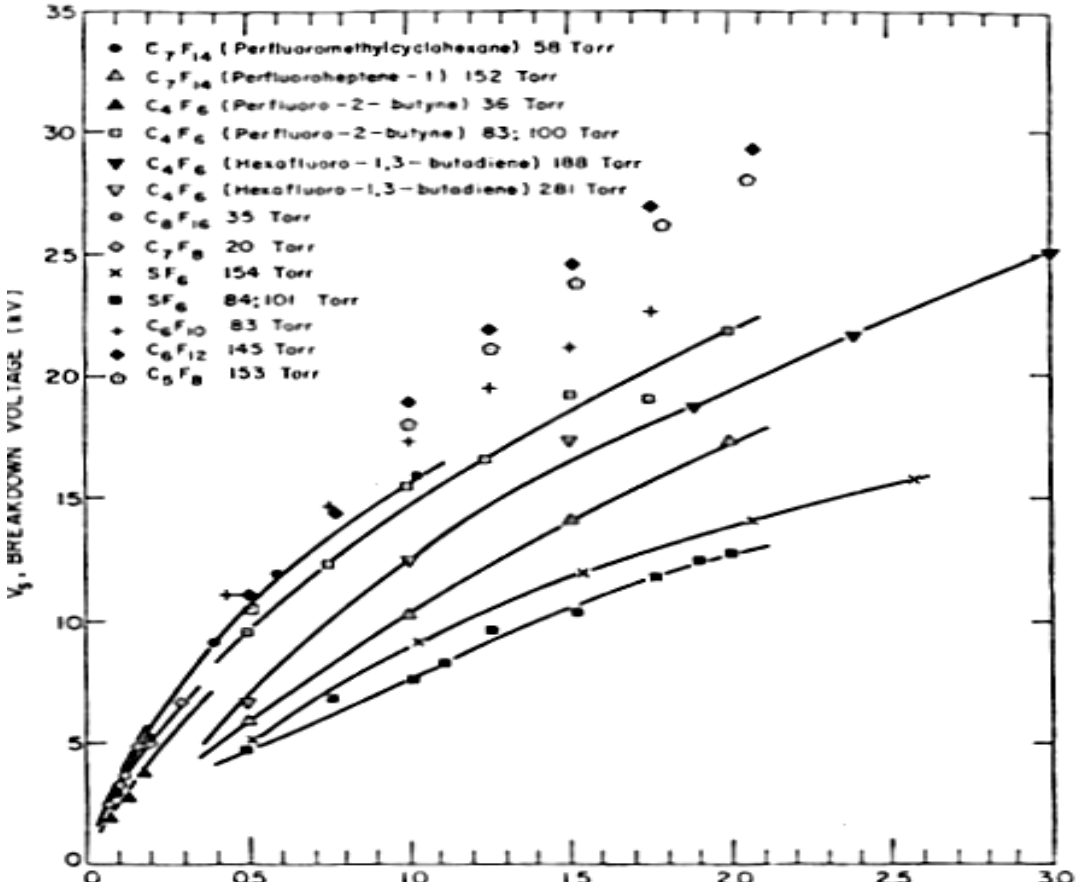

Fig. 22. Breakdown strengths vs. product of pressure and gap.

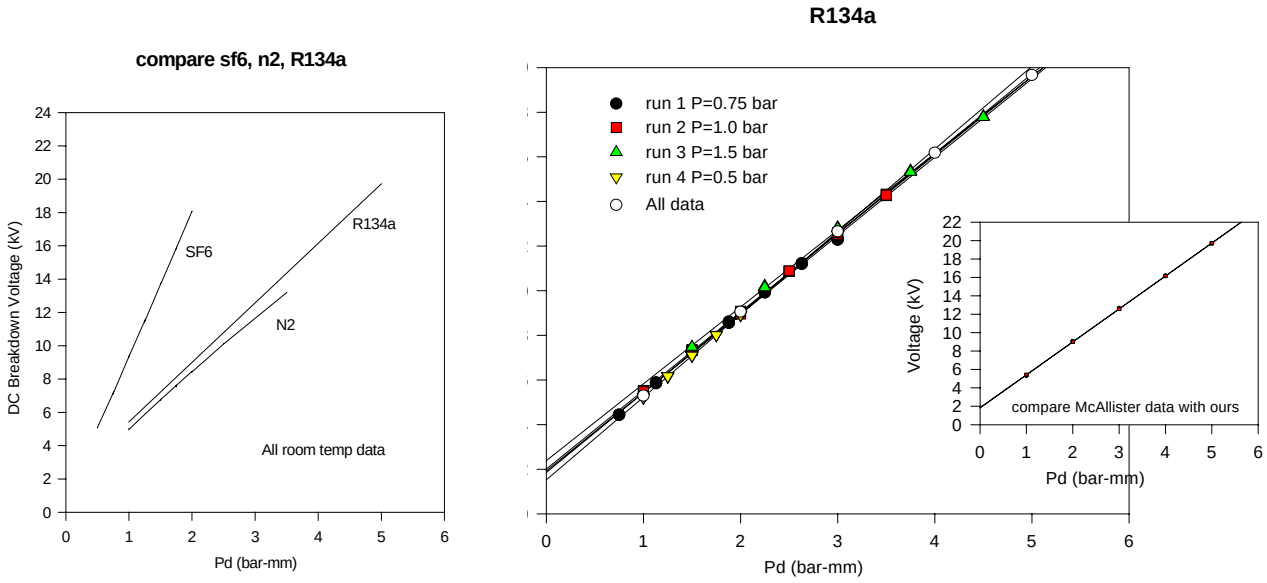

Fig. 23. Dielectric strength test results for R134a.

Figure 24 shows the coefficients of performance (COPs) of various refrigerants set to 0°C evaporating and 50°C condensing. The refrigeration cycle of the refrigerant with a higher normal boiling point, such as R11, may have a higher COP; but the pressure has to be lower than one bar for 0°C evaporating. The size may also be larger.

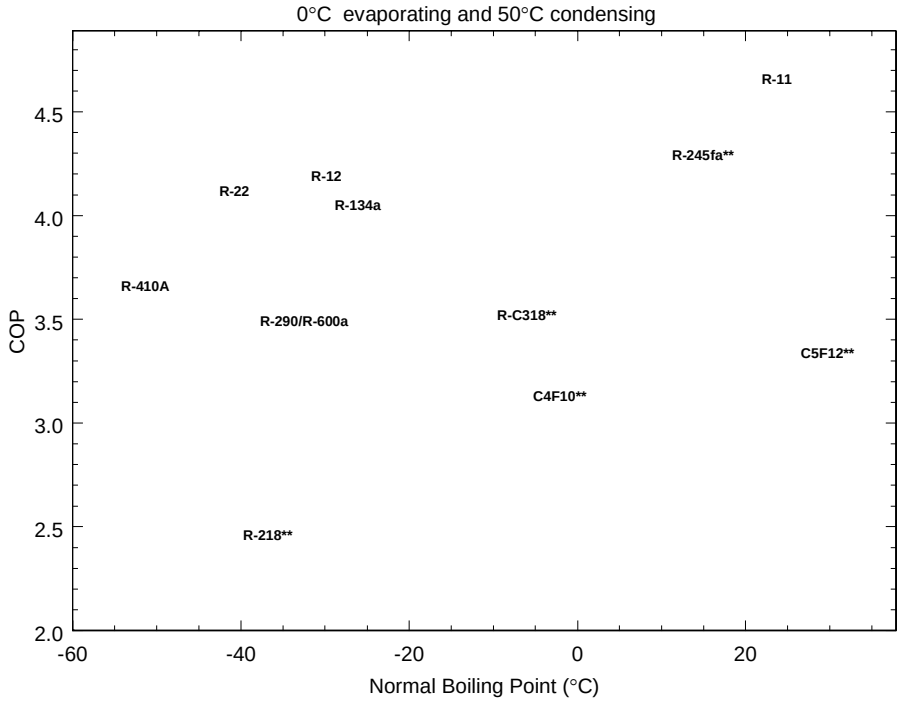

Fig. 24. Ideal refrigeration cycle performance.

The methodology of the toxicity studies is as follows.

Potential refrigerants are initially screened for toxicity, and generally only those with low toxicity are selected for use. This is the case with R134a, for example. But during the course of years of use in a vehicle, a material may undergo degradation to form small quantities of breakdown products. Degradation may occur by thermal or electrical mechanisms. ORNL has experience in measuring the toxicity of the insulating gases, such as sulfur hexafluoride, used in transformers and switches in electrical power distribution systems. Under certain conditions, electrical discharges in sulfur hexafluoride can result in the production of toxic byproducts. It is not known to what extent materials such as R134a, under conditions of prolonged use, might undergo degradation to produce toxic byproducts, or how toxic these byproducts might be. It is thus important to investigate these considerations early so that human health and the environment can be protected. If toxic products are found, they can be characterized and quantified as to their degree of toxicity. It may be possible to develop ways to minimize formation of these products or to identify maintenance procedures to minimize exposures. The first step is to evaluate the potential.

The approach initially adopted for evaluating the toxicity of potential refrigerants that have undergone electrical breakdown is to use a measure of cell survival with an in vitro assay. In

vitro assays use colonies of cells grown in dishes. A cell survival assay is considered to be a "screening" test for cytotoxic activity. Cytotoxicity is the term used to indicate damage to the cell. It does not include changes to cell DNA that would cause a mutation, a type of damage referred to as "genotoxic." If it is found that a particular stressed gas exhibits cytotoxicity, in vitro cell survival assays can be used to evaluate dose-response relationships. Other kinds of in vitro assays can be employed to evaluate different types of damage to develop a more complete picture of overall potential for harm. In addition, results for these assays of stressed gases can be compared with results for the same assays using well-known toxic materials. This procedure provides the data necessary to develop relative comparisons between the known toxic materials and the stressed refrigerant gases.

Ideally, the reference materials would have undergone significant studies in a large number of in vitro and in vivo experiments. In addition, a reference material might have been the subject of epidemiological studies of persons exposed. Results of these epidemiological studies often shed light on the risk of adverse effects upon exposure to the material, and they sometimes include dose-response information. By putting together data developed using in vitro assays with those from more widely studied materials, a reasonable perspective about the findings can be gained. This perspective can lead to future investigations.

The cells used in our initial studies are Chinese hamster ovary cells (CHO) that were originally isolated at ORNL by Dr. Abraham Hsie. Methods for maintaining these cells are well known and will not be presented in this report. While the concept behind the assay used is fairly straightforward, the execution is tedious. Briefly, the cells are grown to the point where about 10^6 cells can be transferred to evacuated 70-cc tubes known as vacutaners. (These tubes are used primarily for taking blood samples, since they contain a vacuum.) Transfer is accomplished by drawing the cells into a syringe and introducing them into the vacutaners by means of a needle through a rubber plenum that maintains the vacuum. These cells are allowed to attach to the container walls overnight in a rotating incubator. Once they are attached, the gas of interest is introduced into the vacutaner with another syringe. The vacutaner is incubated for a chosen "exposure" time. At the end of this time, cells are removed from the vacutaner exposure tube, and 200 are placed into 60-mm plates. These are incubated for 7 days. During the 7 days, viable cells of the initial 200 grow to form colonies of cells. At the end of this growth period, the cells are then "fixed" or killed, stained, and counted, using either manual counting or a cell colony counter. The number of control or unexposed colonies is compared with the number of exposed colonies to provide a relative survival rate. The process is depicted in Fig. 25.

The initial tests and results of the toxicity studies are presented as follows. Stressed gas was obtained from Curt Ayers of ORNL, who had been exposing R134a liquid to approximately 300 V across an inverter for several weeks. This gas was exposed to Group 1 CHO cells for 24 hours and Group 2 CHO cells for 5 days. Upon incubation of the resultant cells for 7 days, no difference was observed between the exposed and control cells for either group. Thus the gas sample had no toxicity that could be identified with the assay. It was also learned from this experiment that R134a has little if any toxicity in the cell survival assay, and that air exposure can be used as a control for future experiments.

Following this initial trial, R134a gas was exposed to spark breakdown in the chamber in the apparatus shown in Fig 25. Repeated discharges were used to deposit approximately 9 Joules/cm^3. The resulting gas was used to expose CHO cells for 1 and 4 hours. The controls were air exposures. The survival rate of exposed cells compared with controls was 2% for the 1-hour exposure and 0.5% for the 4-hour exposure. Essentially all exposed cells were killed.

Clearly, electrical sparks in R134a produce highly toxic byproducts. The question is what is an appropriate exposure condition for the R134a. It is believed that a more appropriate exposure condition would involve corona, not sparks. A modified experimental chamber will be developed in the future for expanded tests.

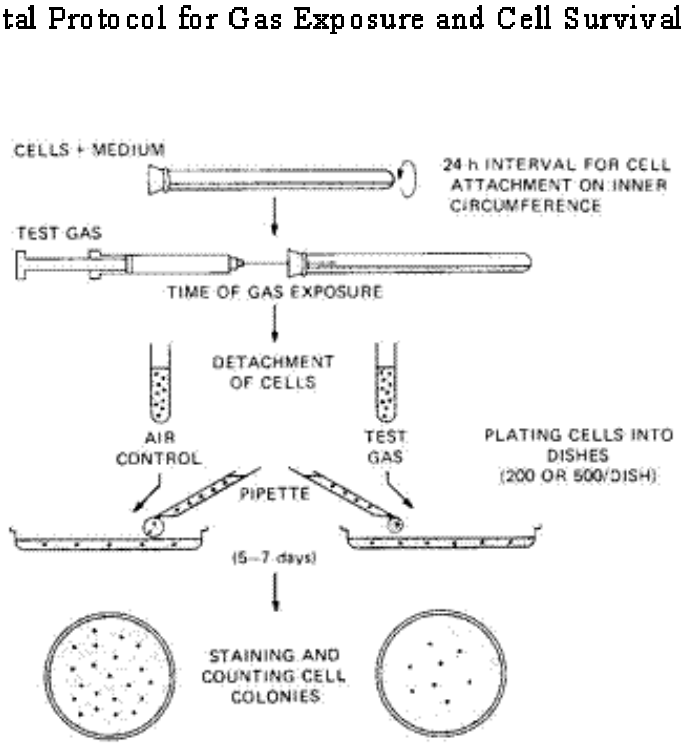

Fig. 25. Experimental protocol for toxicity study.

Capacitor Investigation

Thermal management for the capacitor is very important, because the cost for the capacitors and the inverter housing represent roughly half of the total inverter cost. The following report outlines thermal management issues for the electrolytic capacitors. Film and other types of capacitors will be investigated.

The operating temperature of the electrolytic capacitor is not the-lower-the-better, because at a very low temperature, the capacitance of a capacitor goes down. For a given harmonic current, the harmonic voltage goes up when the capacitance is lower. As long as the voltage permits, it is acceptable to operate at low temperature. The capacitor temperature will go up during operation

after the initial cold condition. If the capacitor temperature goes too high, the capacitor may fail at temperatures above the permissible temperature.

Figure 26 shows the equipment used for the capacitor investigation, including an amplifier rack that provides the ac ripple current for the thermal management electrolytic capacitor test, the environmental chamber that provides ambient temperature from subzero to 105°C, and the power supply that provides from zero to 450 V dc bias.

Fig. 26. Equipment used for the capacitor investigation.

The electrolytic capacitor failure mode is seen from Figs. 27 and 28. The capacitor failed at 185°C. It did not explode. A small amount of smoke was noticed, and the ripple current started dropping off until it was down in the single digits. The test was stopped at this point. Total time after the smoke was noted, and the failure mode realized was a couple of minutes

Based on several high-temperature test cycles for the electrolyte (150–168ºC), it appears that the electrolyte starts being baked out around 125 to 130°C. After several cycles at temperatures at that level or higher, the capacitor seems to heat up quicker in the core and will eventually fail.

Figure 27 shows that the top of the capacitor can pop off as a result of overheating of the capacitor. The can after the capacitor core is taken out is shown in Fig. 28. Some electrolyte remains at the bottom of the can.

It was noticed that low-voltage electronic printed circuit boards were being cooled in a low-pressure refrigerant spray chamber for certain products. Electrolytic capacitors are among other chips on the board. The question is how the electrolytic capacitors react to the environments with different coolants.

Fig. 27. A failed electrolytic capacitor.

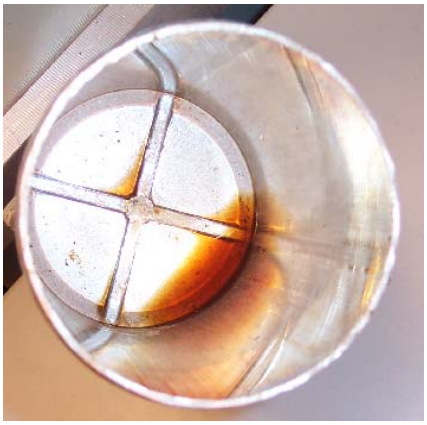

Fig. 28. The can of a failed electrolytic capacitor.

Figure 29 shows the 100-MFd, 35-V_{dc} electrolytic capacitors with and without cans for the environmental tests submerging them in various coolants.

(with can) (without can)

Fig. 29. Electrolytic capacitors with and without cans.

Figure 30 shows the setup of the electrolytic capacitor environmental tests. The capacitors with and without cans are submerged in different coolants. From left to right inside the protection box, the cups and pressure chamber contain flourinert, water, RTV, and R134a, respectively. The non-accelerated test (without dc bias) and the accelerated tests (with dc biased to 32 V and the maximum recommended ripple current of 240 mA applied to each capacitor) were planned. A pot and switch are added to allow each capacitor to be adjusted to 240 mA. The switch allows each capacitor to be checked for degradation without physically taking it from the circuit, and it also allows the current to be adjusted while the capacitor is still in the circuit.

Fig. 30. Setup of electrolytic capacitor environment tests.

The test results are shown in Figs. 31 through 34.

The electrolytic capacitor environmental suitability tests suggest that the electrolyte may be contaminated by the liquid coolant. Therefore, the high-voltage (H.V.) electrolytic capacitors are not suitable to be submerged in or sprayed by the liquid coolant.

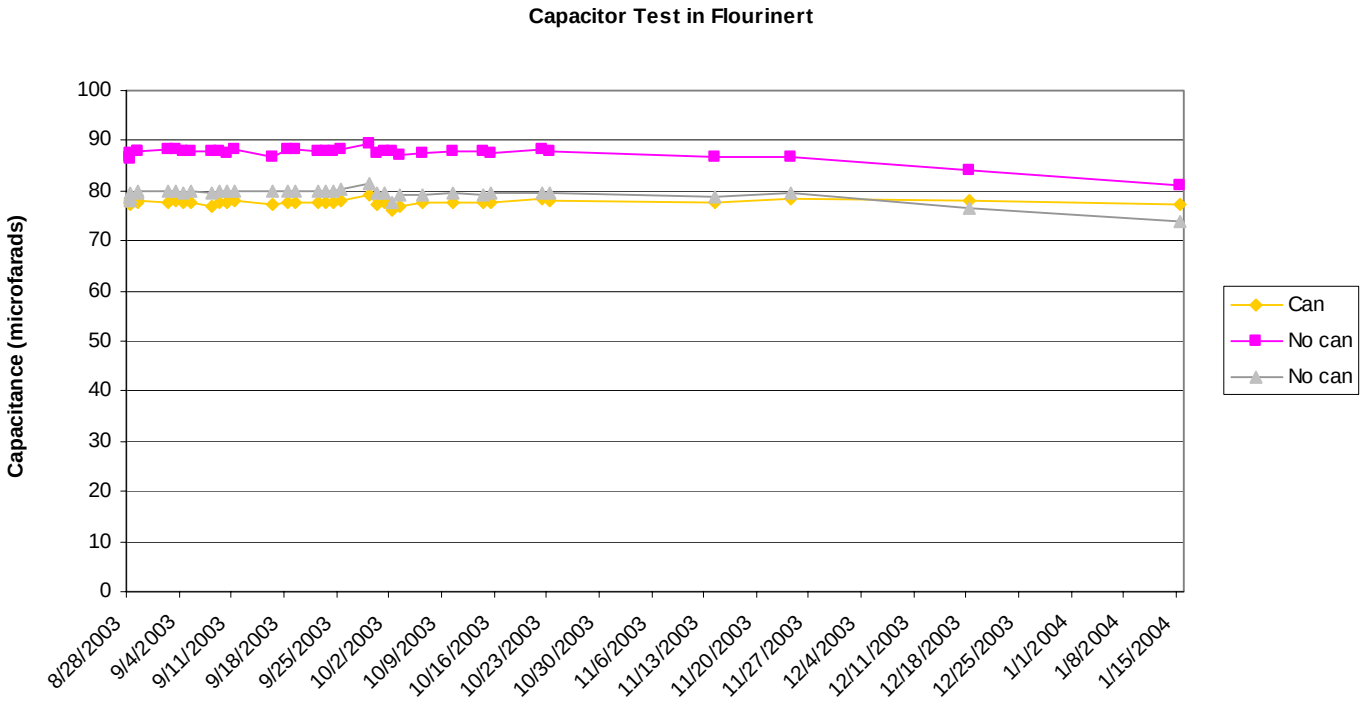

Fig. 31. Electrolytic capacitor environmental suitability test (in flourinert).

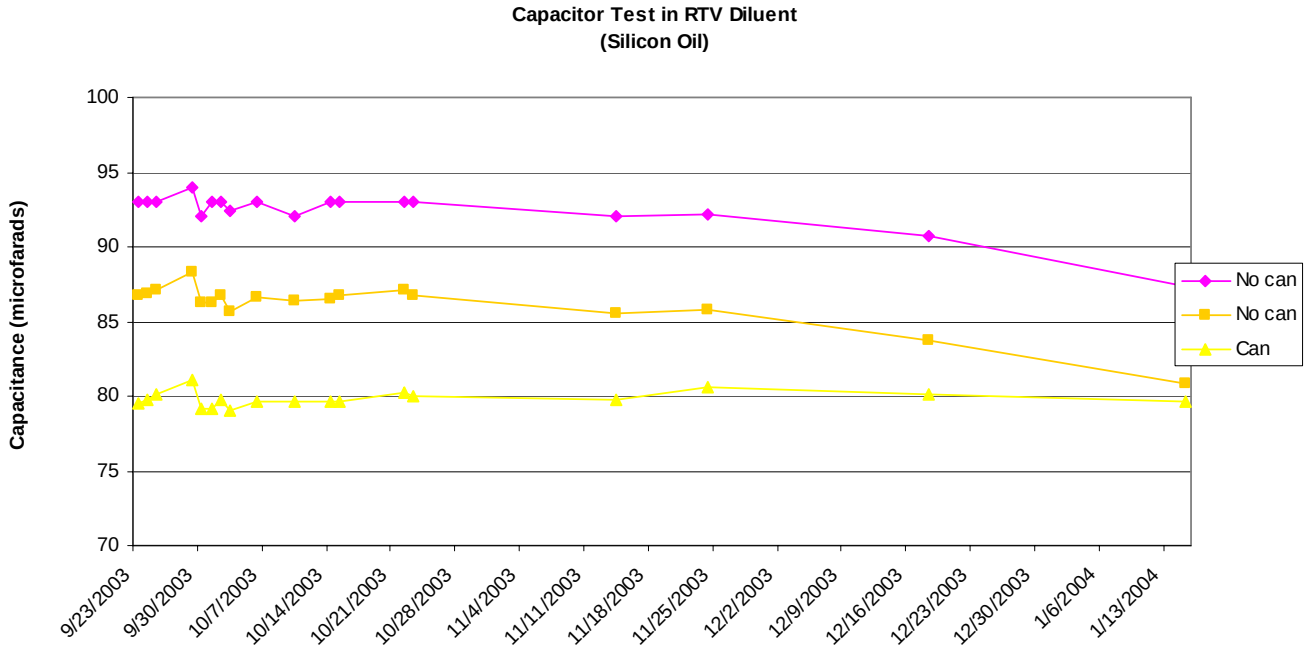

Fig. 32. Electrolytic capacitor environmental suitability test (in RTV diluent).

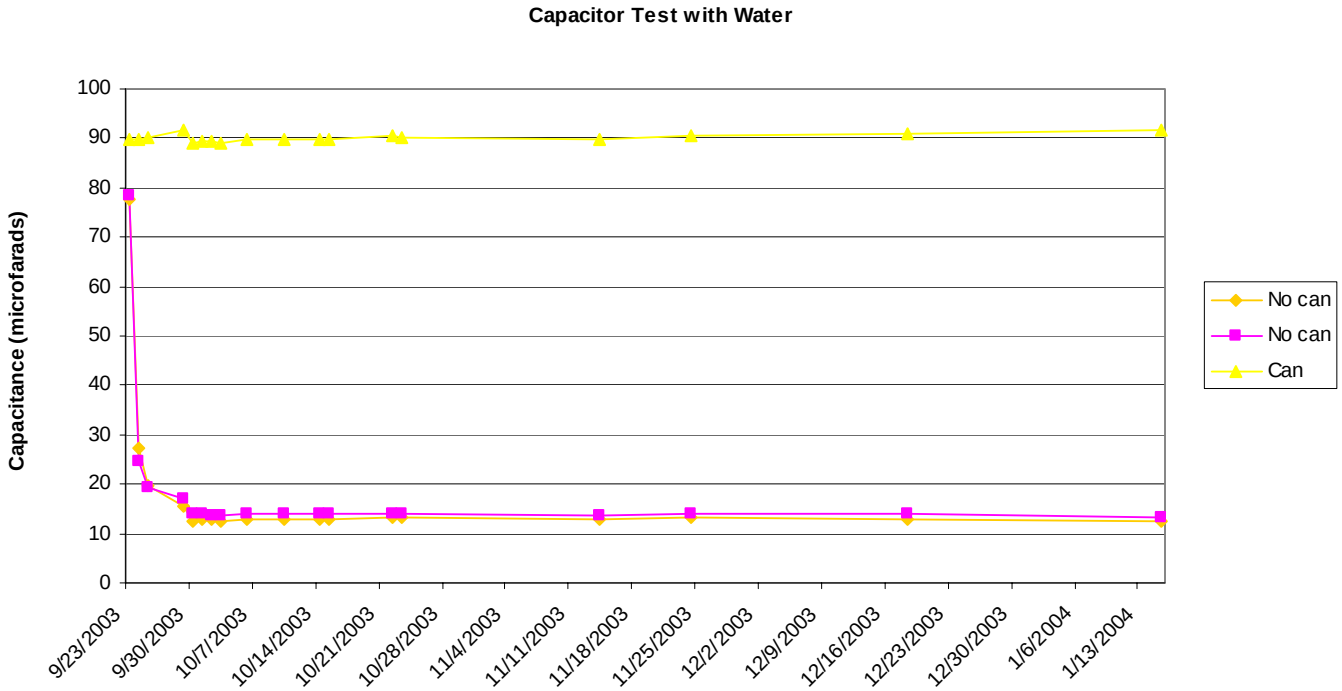

Fig. 33. Electrolytic capacitor environmental suitability test (with water).

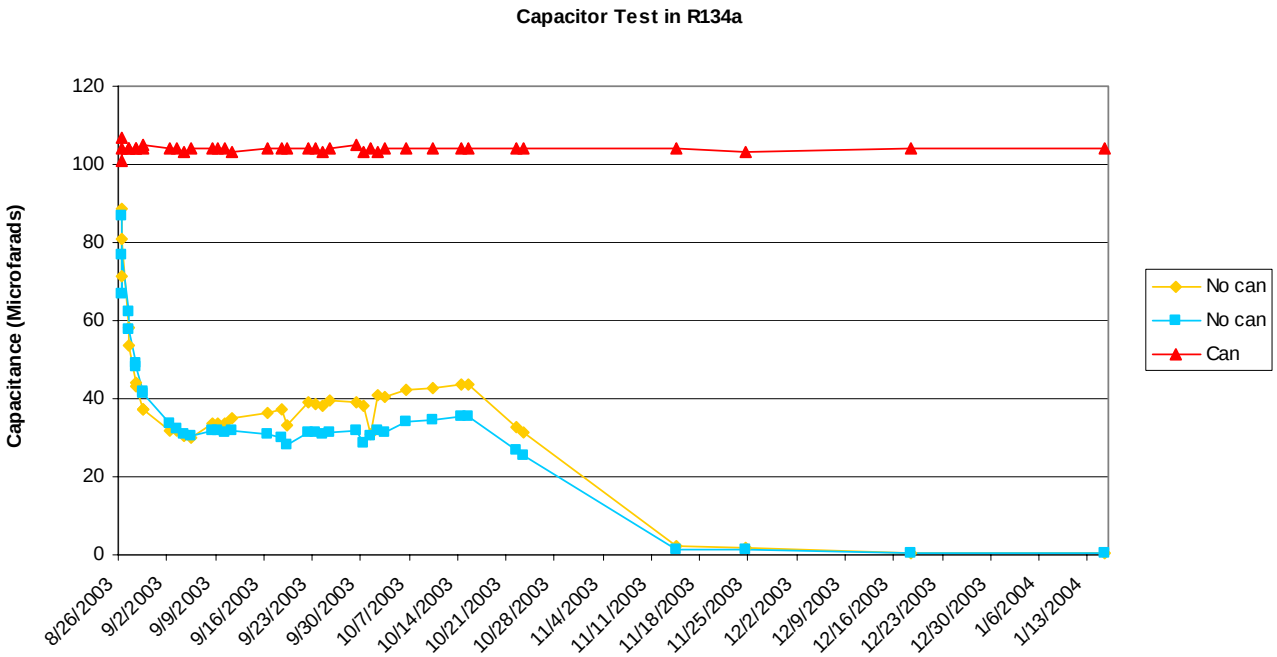

Fig. 34. Electrolytic capacitor environmental suitability test (in R134a).

The internal temperatures vs. ambient temperatures at various permissible ripple currents of a 2400-MFd, 450-V_{dc} electrolytic capacitor are shown in Fig. 35.

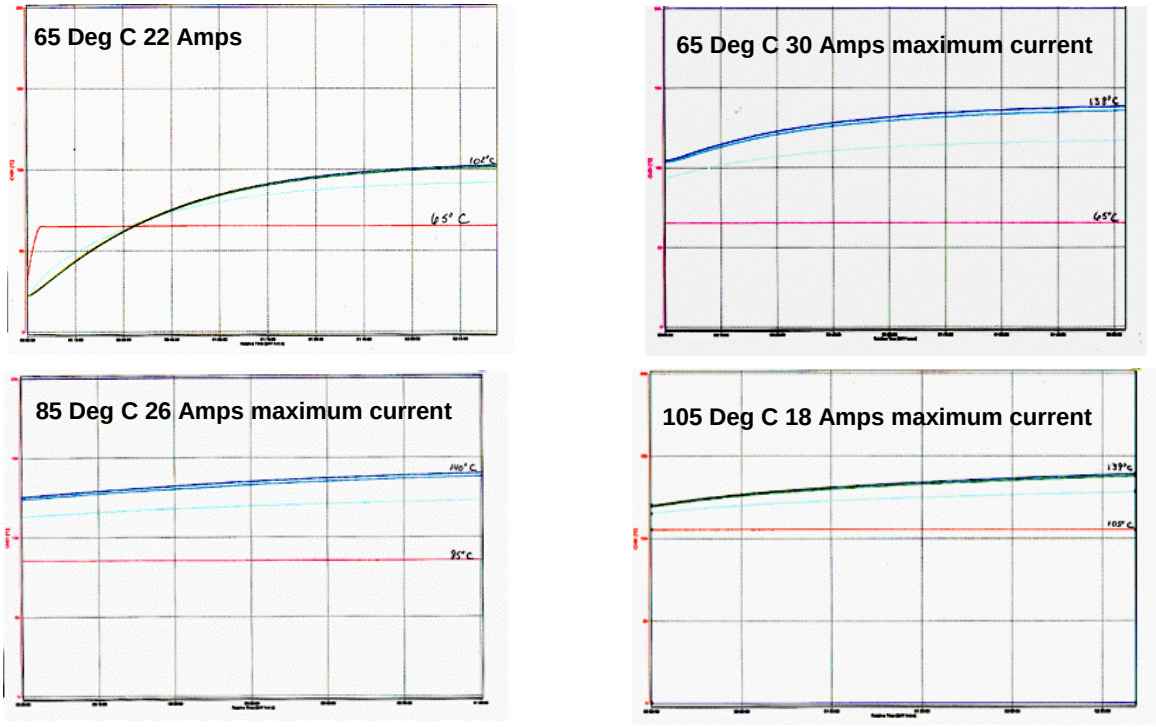

Fig. 35. Permissible ripple current vs. ambient and internal temperatures.

Figure 36 shows the relationship between the ambient temperatures and the maximum permissible ripple currents. The maximum permissible ripple currents were set by determining the internal temperature at which the capacitor would be damaged, but not failed, and then stopping just below that temperature. Damage occurred between 140 and 155°C.

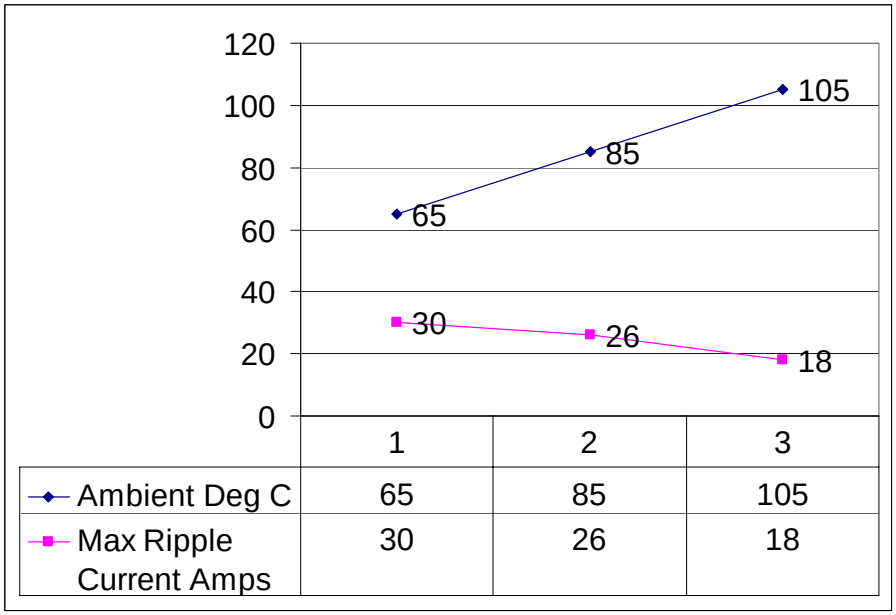

Fig. 36. Relationship between ambient temperatures and permissible maximum ripple currents.

Conclusions drawn from of the electrolytic capacitor tests were these:

- The electrolytic capacitor is not suitable to be situated inside the chamber with liquid coolants.
- The effect of thermal management on capacitor life expectancy and harmonic current capability is significant.
- Similar tests must be conducted on film and other capacitors.

Conclusions

During FY 2004, ORNL signed subcontracts with industry and university researchers for ORNL assessments of their two-phase cooling technologies. Three leading two-phase cooling technologies are being assessed. The subcontractors are ISR, Innovative Fluidics (Georgia Tech), and Rockwell Scientific Company.

ORNL invented the floating loop concept.

- For the floating loop system, initial component investigations of capacitors, die mountings, terminals, pumps, and fans were conducted.
- For the refrigerant investigation, the refrigerant dielectric properties and toxicity were studied.
- Preliminary work on motor frame design for two-phase cooling and die submerged cooling was initiated.

For FY 2005, ORNL will continue the assessment of the leading two-phase cooling technologies developed by the subcontractors. ORNL will also develop the components used in the floating

loop cooling system and integrate the motor/inverter in the floating loop. Capacitor cooling and the passive bubble ejection are part of the floating loop component investigation.

ORNL will reduce the inverter size to one-half by FY 2006 and to one-third by FY 2008.

References

1. I. Sauers, D. R. James, A. R. Ellis, C. E. Easterly, and J. S. Hsu, *Preliminary Measurements of Dielectric And Toxic Properties Of Potential Refrigerants For Two-Phase Cooling Of Power Electronics And Motors*, ORNL/TM-2004/210, Oak Ridge National Laboratory, UT-Battelle, LLC, September 2004.

3. Electric Machinery R&D

A. Radial Gap PM Motors

John W. McKeever
Oak Ridge National Laboratory
National Transportation Research Center
2360 Cherahala Boulevard
Knoxville, TN 37932
Voice: 865-946-1316; Fax: 865-946-1262; E-mail: mckeeverjw@ornl.gov

DOE Technology Development Manager: Susan A. Rogers
Voice: 202-586-8997; Fax: 202-586-1600; E-mail: Susan.Rogers@ee.doe.gov

ORNL Program Manager: Laura D. Marlino
Voice: 865-946-1245; Fax: 865-946-1262; E-mail: marlinold@ornl.gov

Objectives

- Study permanent magnet (PM) radial gap traction drive systems that could meet FreedomCAR's 2010 goals to expose weaknesses or identify superiorities.

Approach

- Study in detail three attributes—drivability, performance, and material requirements—for specific motors. Three motors selected were the commercially available 60-kW radial gap surface-mounted PM (SMPM) motor manufactured by UQM Technologies, Inc.; a hypothetical PM motor with rotor-supported magnets similar to the Honda MCF-21; and Delphi's automotive electric motor drive (AEMD) motor, whose rotor is an overhung ferromagnetic cylinder that supports the magnets on its inner surface.

Accomplishments

- Demonstrated that the axial-gap design concept could mechanically survive operation at 6600 rpm during prequalification. In this design, butted magnets are skewed one rotor tooth and held by interference in the annular region between a titanium ring and an aluminum hub, and the rotor and stator are air-cooled with an axial vane pump on the shaft.
- Demonstrated that a dual-mode inverter control (DMIC) inverter could drive the 18-pole PM motor to 6000 rpm, which corresponds to an electrical frequency of 900 Hz. Demonstrated that converter-grade silicon-controlled rectifiers (SCRs), which are less expensive than inverter-grade SCRs and can normally withstand higher voltages, could operate at this high frequency.
- Demonstrated a record constant power speed range of 11.4 with the DMIC inverter.
- Bypassed the SCRs in the DMIC inverter to achieve conventional phase advance (CPA) control and, because of the motor's large inductance, demonstrated a record constant power speed ratio (CPSR) of 11.2.

- Experienced demagnetization during the PM motor test sufficient to reduce the motor capability from 30 to 12 kW, confirming a problem that has appeared in the commercial sector.
- Assimilated equations[1] specifically for calculating the no-load spin loss eddy currents generated by the slot opening passing the magnets and the operating eddy current heat generated by harmonics, for comparing motor operation using trapezoidal and sinusoidal back-electromotive forces (emfs), for comparing measured and test results, and for estimating temperature rise in the rotor to see if eddy currents in the rotor could be responsible for demagnetization. Evaluation and comparison of the data with the equations will be conducted in FY 2005.
- Derived an equation for the inductive reactance that would minimize the current required for a fixed-supply voltage to deliver rated power for a PM synchronous motor (PMSM).
- Explored the use of finite element analysis (FEA) to evaluate the operating speed of radial gap PM motors by validating with the operating speed of the Toyota Hybrid System 2003 (THS) and 2004 (THS II) designs. Used the method to determine the operating speeds of one version using rotor-supported magnets and of an early version of an axial flux weakened/strengthened concept [three interior PMs (IPMs)]), which is supported by two bridges and two piles.

Future Direction

- Develop equations for the no-load spin loss due to heat from eddy currents in the rotor materials generated by slots passing the magnets and compare them with values measured during FY 2004 tests.
- Develop equations for the operational eddy current heat loss generated in the rotor materials by harmonics and use them to estimate the heat rise to see if this effect could be responsible for demagnetization experienced during FY 2004 tests.
- Identify an optimal magnet fraction for surface-mounted radial gap rotors that support their magnets, recognizing that the operating speed and reluctance component of torque will increase and that the magnet cost will decrease as the embedded magnet fraction decreases.
- Prepare a paper for *PE Letters* in response to a letter[2] that concluded that the DMIC is the same as a fixed inductance in each of the three phases of a PM motor, and that a winding strategy that leads to large inductance cannot benefit from DMIC control. (The response will show that the equation for the inductive reactance of the DMIC is a variable whose control defines the minimum current needed to deliver any desired power at any relative speed over 2 and that motors with larger inductances can derive significant benefit from DMIC depending on their speed.)

Publications

1. J. S. Lawler, J. M. Bailey, and J. W. McKeever, *Extended Constant Power Speed Range of the Brushless DC Motor Through Dual Mode Inverter Control*, ORNL/TM-2000/130, Oak Ridge National Laboratory, UT-Battelle, LLC, 2001.
2. J. S. Lawler, J. M. Bailey, J. W. McKeever, and J. Pinto, "Limitations of the Conventional Phase Advance Method for Constant Power Operation of the Brushless DC Motor," in *Conference Proceedings of Southeast Conference on Power Electronics Applications*, 2002.

3. J. S. Lawler, J. M. Bailey, and J. W. McKeever, "Theoretical Verification of the Infinite Constant Power Speed Range of the Brushless DC Motor Driven by Dual Mode Inverter Control," presented at the 7th IEEE Workshop on Power Electronics in Transportation, Auburn Hills, Michigan, October 24–25, 2002.
4. J. S. Lawler, J. M. Bailey, J. W. McKeever, and J. Pinto, "Extending the Constant Power Speed Range of the Brushless DC Motor through Dual-Mode Inverter Control," *IEEE Trans. on Power Electronics*, **19**(3), May 2004.

Patents

1. J. S. Lawler and J. M. Bailey, *Constant Power Speed Range Extension of Surface Mounted PM Motors*, U.S. Patent Number 6,236,179 B1, May 22, 2001.

Background

Although induction motors (IMs) have been considered the baseline for American HEV traction drives, most of the new marketable HEVs being sold by foreign sources such as Toyota and Honda are powered by PM motors. It has been difficult for U.S. suppliers to design and build a radial gap PM motor that meets FreedomCAR's 2010 goals. This task was designed to examine the source of some of these difficulties and see if solutions could be found. The approach initially proposed was to examine and compare parameters of a commercially available surface-mounted radial gap PM motor sold by UQM; a model with an external rotor whose surface-mounted magnets were secured to the inner surface, which is being developed and tested for possible commercial use by Delphi; and a model like one being proposed by Honda that has surface-mounted magnets held in place by silicon steel hooks to form an alternating magnet-silicon steel surface facing the gap. This approach had to be modified because much of the information needed for the comparison was proprietary to the vendors.

As we examined how best to continue this research, a number of problems and uncertainties arose that guided our revised approach. During discussions with the vendors and program reviews, we learned that they had encountered large heat losses during testing, which they ascribed to eddy currents induced in the rotor. Is this a problem that must be faced by all PM motors? Although there are drive systems that employ vector control to drive PMSMs, an inverter capable of employing DMIC to drive brushless dc machines, although available, had not been tested, especially for motors with large number of poles that would require the SCRs to switch at frequencies near 12 kHz. Will the DMIC work for a large pole count? Confusion surfaced about operation of the DMIC in an article in IEEE's (Institute of Electrical and Electronics Engineers, Inc.) *PE Letters*[2] that concluded that DMIC is the same as a fixed inductance in each of the three phases of a PM motor and that a winding strategy that leads to large inductance cannot benefit from DMIC control. How should the SCRs in the DMIC be truly characterized as an inductive reactance in each of the phases, and does this clarify its role in the controller? Finally, there were questions about how material properties related to the high speeds under which commercial rotors were being operated. Do the small bridges support operation at high speeds for ordinary materials? What can be learned from existing models that may be applied to future models?

The revised approach was to study the specific parameters of radial gap PM motors, drivability, performance, and material requirements. To study drivability and performance, the DMIC inverter was tested driving an 18-pole 30-kW PM motor to 6000 rpm, where the maximum electrical frequency is 900 Hz. (An axial-gap test motor with 18 poles was used because its control is identical to that of a radial gap PM motor.) Performance was also examined through analysis, which led to a derivation showing that DMIC produces any developed power with the minimum current necessary regardless of speed for relative speeds, $n = \omega/\omega_{base} \geq 2$. Material requirements were examined with FEA to determine the speed and location where yield starts and the corresponding deformations and stresses.

Testing the DMIC Inverter

The air-cooled 18-pole axial-gap PM motor was driven to 6600 rpm by the dynamometer motor and operated for a half hour to verify its mechanical stability. The 10% overspeed confirmed the integrity of the motor design, which included two significant design features. The first design feature was an annulus comprising 18 butted magnets skewed 1 slot to reduce cogging torque and held by interference between a titanium ring and an aluminum hub. The interference was sufficient to accommodate differential radial growth as the speed increased and differential radial thermal expansion as the components heated. The second design feature was a bladed cooling fan that moved outside air past the stator and rotor.

The DMIC inverter, which had been configured to drive the 18-pole PM motor at 6000 rpm, was configured for testing at a base speed of 500 rpm to a CPSR of 4 in the initial testing, and at a base speed of 500 rpm to a CPSR of 12 in the second testing. Filters were added to the gate circuit to reduce the noise to a level that allowed the motor to be driven.

Early testing sought to reach the maximum torque, 191 N-m, at 1000 rpm, which is below base speed. With the dc supply voltage at 260 V, considerably higher than the 209 V estimated, 181 N-m was applied to the load before the inverter cut off. No current measurements were taken, but the probability is that the current was about 166 A_{rms} (181 N-m/191 N-m x175 I_{rated}). The highest stator thermocouple reading was 180°F.

On the next attempt to apply 191 N-m load torque, the inverter shut off at 140 N-m. The Hall probe signals that monitor the magnet field in the gap had changed significantly, indicating that the magnets had been non-uniformly demagnetized. This was confirmed by comparing the back-emf waveform at 1500 rpm with a reference waveform taken prior to testing. The two level humps, which were initially level, had become lopsided and the peak-to-peak voltage was reduced by 10%.

To investigate the extent of demagnetization, the motor was operated at 800 rpm; that speed is below base speed, where it is more difficult for the fan to cool the motor. Torque was varied from 20 to 120 N-m in steps of 20 N-m while measuring the phase current. During testing at 155 A_{rms}, the temperature rose to 234°F, where the test was terminated. The rate of rise indicated that the stabilization temperature would have been above 312°F, which is above the recommended magnet maximum operating temperature of 302°F. This means that the motor cannot operate at rated current at or below 800 rpm. Extrapolation of the curve in Fig. 1 shows

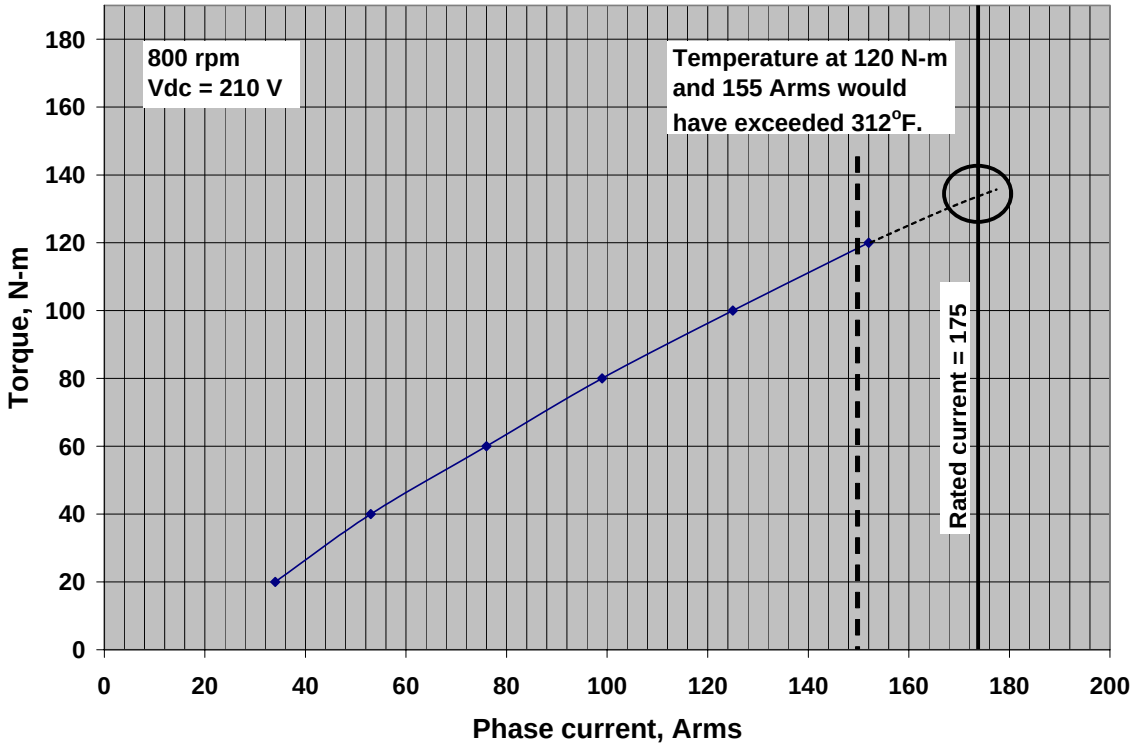

Fig. 1. Extent of motor derating caused by demagnetization.

that demagnetization has reduced the motor from 191 to 130 N-m at rated current. Our testing was conducted below 120 A_{rms} to limit stator temperature rate increase.

During this test, only the stator temperature was monitored. There was no means to measure the rotor temperature while testing. The stator temperature never rose to an alarming value. We infer, therefore, that the demagnetization resulted because of rapid temperature rise in the rotor generated by harmonics, which are plentiful because the back-emf waveform is trapezoidal. During FY 2005, we will attempt to characterize the temperature rise of the rotor caused by the harmonics. Temperature rises of this type have been experienced by UQM and by Delphi. UQM's solution was to use sinusoidal back-emfs to reduce the harmonics. Delphi's solution was to segment the magnets and back iron. Segmentation of the axial-gap motor will be very difficult; however, strategic placement of electrical insulators at the interfaces between the titanium ring, the aluminum hub, and the magnets might help. First, the order of magnitude of the problem must be estimated.The DMIC inverter was first used to drive the derated PM motor to deliver 12 kW from a base speed of 1500 rpm to 6000 rpm, demonstrating a CPSR of 4. This successful drive-up proved that the SCRs, which are converter-grade devices, could switch at the electrical frequency of 900 Hz. Converter-grade SCRs are cheaper than inverter-grade SCRs, and they are rated to withstand higher voltages. This reduces the cost that these six devices add to the inverter.

The next test sequence attempted to demonstrate a record CPSR of 12 by delivering 5-kW power from a base speed of 500 rpm to 6000 rpm. The rated power at base speed was determined by

reducing the supply voltage while delivering 80 N-m at 500 rpm until the speed began to drop. This voltage was then used through the rest of the test. Figure 2 shows how the power delivery initially rises above rated power at relatively constant current and then falls to define the CPSR at the speed where it crosses the rated power line. The value demonstrated in this test was 11.4, which is a record and is very close to our target of 12.

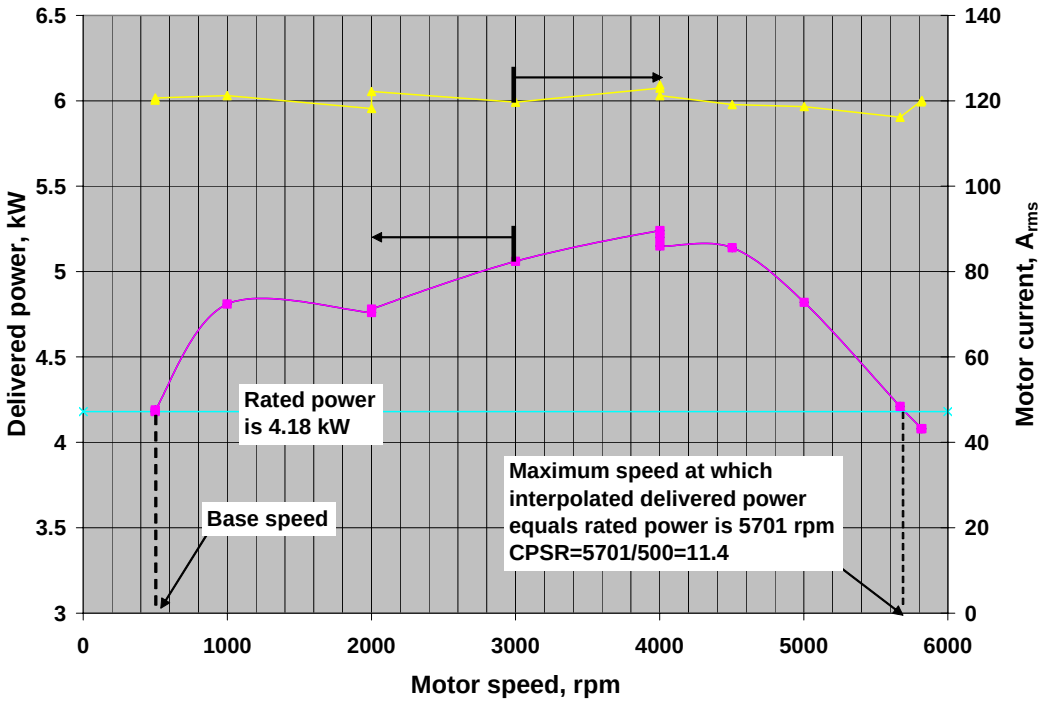

Fig. 2. Demonstration of CPSR = 11.4 using DMIC.

There was a question about the CPSR that could be achieved using only CPA. To investigate this mode of operation, the SCRs in the DMIC inverter were bypassed to enable CPA control. Because of limitations of the digital signal processor, the motor could not be operated stably above 5200 rpm; but at that speed, the power was still above rated power. As shown in Fig. 3, a linear extrapolation of the last two data points estimates a CPSR of 11.2, which is also a record.

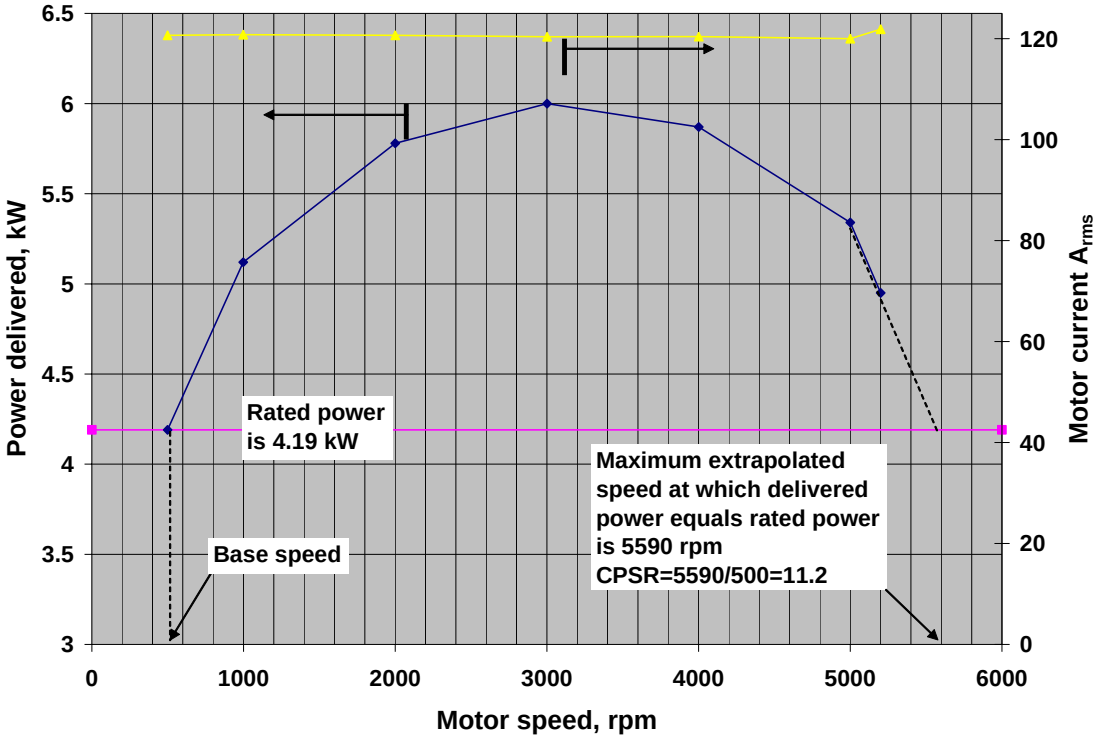

Fig. 3. Demonstration of CPSR = 11.2 using CPA control.

DMIC Minimizes Current Used by Motor

At any power level, the SCRs, which are the heart of the DMIC, enable maximum watts per rms amp control during constant power operation by minimizing rms current.[3] This feature is not possible with a motor driven by a voltage-source inverter (VSI), which has no SCRs, with a fixed inductance. In addition, losses can be substantially reduced using DMIC operation of PMSMs, whose inductance is sufficiently large for VSI control (no SCRs) to achieve infinite CPSR. This current minimization was determined in the process of answering a question: If one assumes that the supply voltage can deliver the desired useful power and neglects the resistance, is there a value of inductive reactance, $X = n\Omega_b L$, that minimizes the current? The answer is yes, and the equation for that reactance is

$$X_{min\,I} = n\Omega_b L = \frac{3V_{max}}{P}\sqrt{n^2 E_b^2 - {V_{max}}^2} \quad , \tag{1}$$

which may be solved for the inductance needed at electrical frequency, $n\Omega_b$. P is the developed power, V_{max} is the supply voltage, n is the relative mechanical speed, E_b is the back-emf, and $n\Omega_b$ is the electrical rad/s. With this optimal value of thyristor reactance, the minimum rms motor current is

$$I_{min} = \frac{P}{3V_{max}} = \frac{P}{3\sqrt{E_b^2 + (X_b I_r)^2}} \quad . \tag{2}$$

Equation (2) is independent of speed and directly proportional to developed power. If one substitutes the motor inductance for infinite CPSR, which is

$$L_{CPA\to\infty}^{CPA-PMSM} = \frac{E_b}{\Omega_b I_r} , \tag{3}$$

for X_b in Eq. (2), along with the relation for a PMSM, $P_r = 3E_b I_r$, Eq. (2) leads to the linear relation in P,

$$\frac{I_{min}}{I_r} = \frac{P}{\sqrt{2}P_r} . \tag{4}$$

It can also be shown that the motor current is in phase with the inverter voltage phasor, which means that the inverter operates at unity power factor.

Figure 4 is a comparison of the motor current under CPA control with the motor current under DMIC for a PMSM. The linear relation between current and power of Eq. (4) is plotted at the bottom. As shown in ref. [3], the equation for rms motor current,

$$I_{rms} = \frac{\sqrt{V_{max}^2 - n \cdot 2V_{max}E_b \cos\delta + n^2E_b^2}}{nX_b} , \tag{5}$$

with the inductance from Eq. (3) and the equalities, $V_{max} = E_b\sqrt{2}$, $P_{max} = P_r\sqrt{2}$, $\sin\delta = \frac{P}{P_r\sqrt{2}}$, and $\cos\delta = \sqrt{1-\sin^2\delta}$ lead to the rms motor current,

$$I = I_r\sqrt{\frac{n^2 - 2n\sqrt{2-\left(\frac{P}{P_r}\right)^2} + 2}{n^2}} . \tag{6}$$

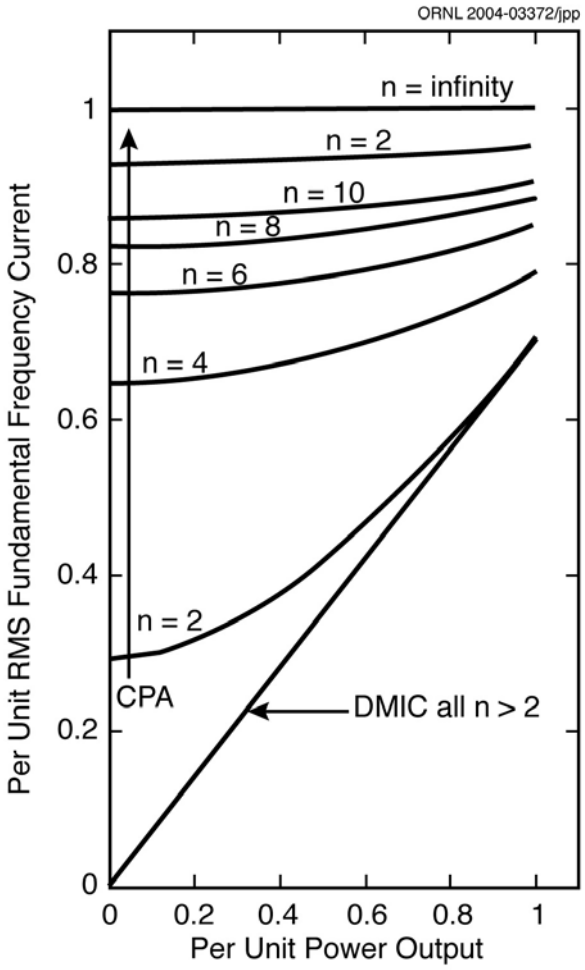

Fig. 4. Constant power operation of a PMSM comparing CPA control with DMIC.

Figure 4 is a plot of I/I_r versus P/P_r for n values of 2, 4, 6, 8, 20, and ∞. The figure shows that when $L = L_\infty$, any developed power up to the rated power can be achieved without exceeding the rms current rating of the motor. The flatness of the CPA curves indicates that the copper losses in the motor are virtually independent of the developed power. Efficiency may be poor when operating conditions require a developed power less than the rated power. The DMIC's reduction in copper losses can be applied to compensate for the increased losses in the SCRs; and when there is a net reduction in total inverter plus motor losses, that reduction can be applied over the operating life of the drive toward the added initial cost of the SCRs.

This type of analysis provides a relationship showing the current that may be saved at various operating speeds by using the DMIC controller instead of CPA or vector control, so that operational cost benefit estimates may be made based on the application's expected duty cycle. In any life-cycle cost study, this information, which is not the first or initial cost, must be included because it can provide significant benefits to the customer.

Onset of Yield Determines Maximum Operating Speed

Electric motors are designed to provide specific torque and useful power; however, a crucial question for any motor design is its maximum speed capability. Estimates may be made using force balance equations and elastic equations for rotational systems symmetric about an axis. These techniques, which may be matched to estimate circumferential stress and radial interference requirements (radial stress), provide only a rough idea of the speed capabilities of a particular configuration. In each design, the magnets generate an equiangular load that adds bending stresses to the tensile stresses; consequently, a finite element code is needed to determine a more representative picture of the stresses and deformation of the components of the motor. The PEEMRC at ORNL has used ALGOR stress analysis to examine the mechanical capabilities of the IPM motors.

Since the rotor material is ductile, if failure is generated in the rotor, an excellent way to estimate its maximum rotational speed is to adjust that speed so that the von Mises stress equals the rotor's yield strength. Yield strength is obtained from a uniaxial tensile test at the onset of plastic flow. One is tempted to use the ultimate strength, but this is not wise because plastic flow allows the components to move, which may create imbalances that will lead to failure.

For ductile materials, experience has shown that the von Mises stress provides a dependable and non-conservative estimate of failure. This approach assumes that yield, which is the onset of plastic deformation, is caused by a critical shear stress on an octahedral plane. The normal to the octahedral planes have equal direction cosines with the three axes. The expression for octahedral shear stress is

$$\tau_{oct} = \frac{1}{3}\sqrt{(\sigma_x - \sigma_y)^2 + (\sigma_y - \sigma_z)^2 + (\sigma_z - \sigma_x)^2 + 6(\tau_{xy}^2 + \tau_{yz}^2 + \tau_{zx}^2)} \,. \tag{7}$$

In the uniaxial test, all components of stress except σ_x are zero. The value of the critical octahedral shear stress may be obtained from the uniaxial test data by substituting $\sigma_{x} = \sigma_{yield}$ in Eq. (7). The result is

$$\tau_{oct} = \frac{\sqrt{2}}{3}\sigma_{yield} \,. \tag{8}$$

When more complex loading occurs for which terms in Eq. (7) are not zero, it may be set equal to Eq. (8). The result is that

$$\sigma_{yield} = \sqrt{\frac{\sqrt{(\sigma_x - \sigma_y)^2 + (\sigma_y - \sigma_z)^2 + (\sigma_z - \sigma_x)^2 + 6(\tau_{xy}^2 + \tau_{yz}^2 + \tau_{zx}^2)}}{2}} \,, \tag{9}$$

where the term on the right of Eq. (9) is known as the von Mises stress or the effective stress.

Different failure modes may require different criteria to determine maximum operating speed. For example, if the failure mode is fracture of the magnets, which are brittle materials, the criteria for operation will necessitate a Weibull distribution of the magnet's transverse fracture strength. From this distribution, a maximum stress may be determined to achieve the required probability of fracture.[4]

The IPM machines are progressing through an evolution shown in Fig. 5 that significantly increases their speed capabilities. Three types of machines, two of which are already in the market, were examined using the ALGOR finite element program. The two include the THS motor (2003) and the THS II motor (2004). A third shown in Fig. 6 has been researched by Honda and comprises surface-mounted magnets that are self-supported by the rotor steel and flush with the steel that secures them. A fourth is being investigated by ORNL as a modification of the THS II to deliver increased torque and power using the principles of the high-strength undiffused brushless motor.

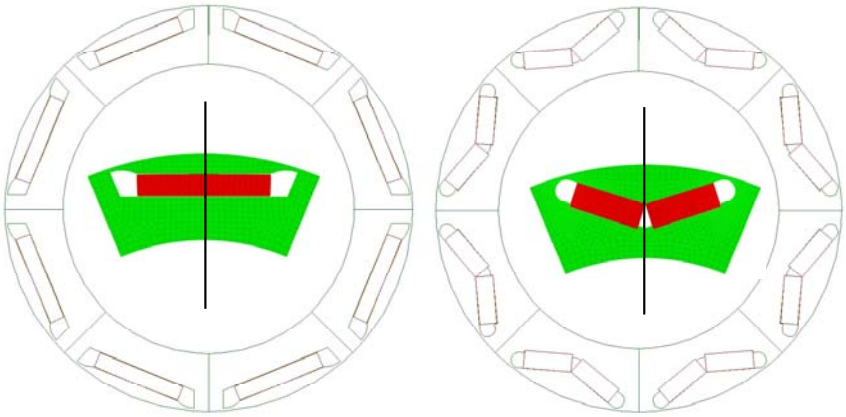

Fig. 5. Evolving IPM rotor configurations (THS left, THS II right).

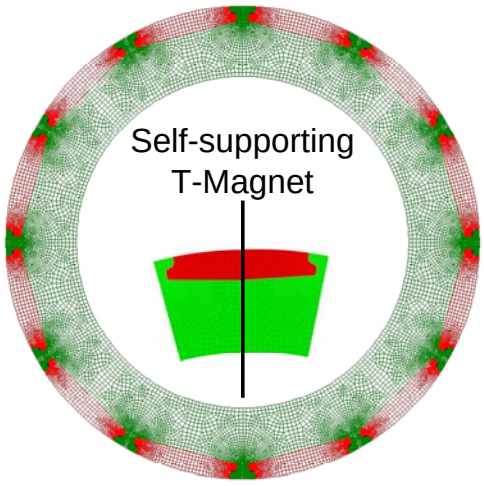

Fig. 6. Rotor-supported magnet configuration.

An IPM moves within its cocoon of M19 steel during operation. To observe how IPMs are loading the M19 with the finite element code, it is necessary to use gap elements, which come into play only when their initial dimension is reduced. Such a reduction indicates that the materials are trying to overlap. Although this is mathematically possible, it is realistically unacceptable. To prevent this from happening, stiffnesses normal to the surfaces are incorporated as part of the stiffness matrix. Since this is a non-linear calculation, the model in the configuration must be elastically stable when the first load increment is applied. This stability is provided by using spring element so soft that it will not significantly impact the final solution. After each load increment, the gap elements are checked to see which ones have diminished; and one by one, those that have diminished are added to the stiffness matrix. The load along each active gap element is calculated. The load for inactive gap elements is zero.

In each IPM model, the load of the magnets and all of the outboard material must be supported through a connection by the remaining spoke-like portions of the rotor. This connection is called the bridge. The significant mechanical contribution of the Toyota Prius THS motor is the use of two 1-mm-thick peripheral connection bridges of M19 silicon steel between the loaded region and the supporting spokes. This magnet loading is shown in Fig. 7, in which it appears that the rotor interface between the magnet and periphery bends, allowing the magnet load to be applied only at its outer edge. Because of symmetry, the total magnet load appears to be 240 lb. Figure 8 shows the onset of plastic deformation in the inner surface of the bridge near the spoke, indicating that the maximum operating speed is 5686 rpm.

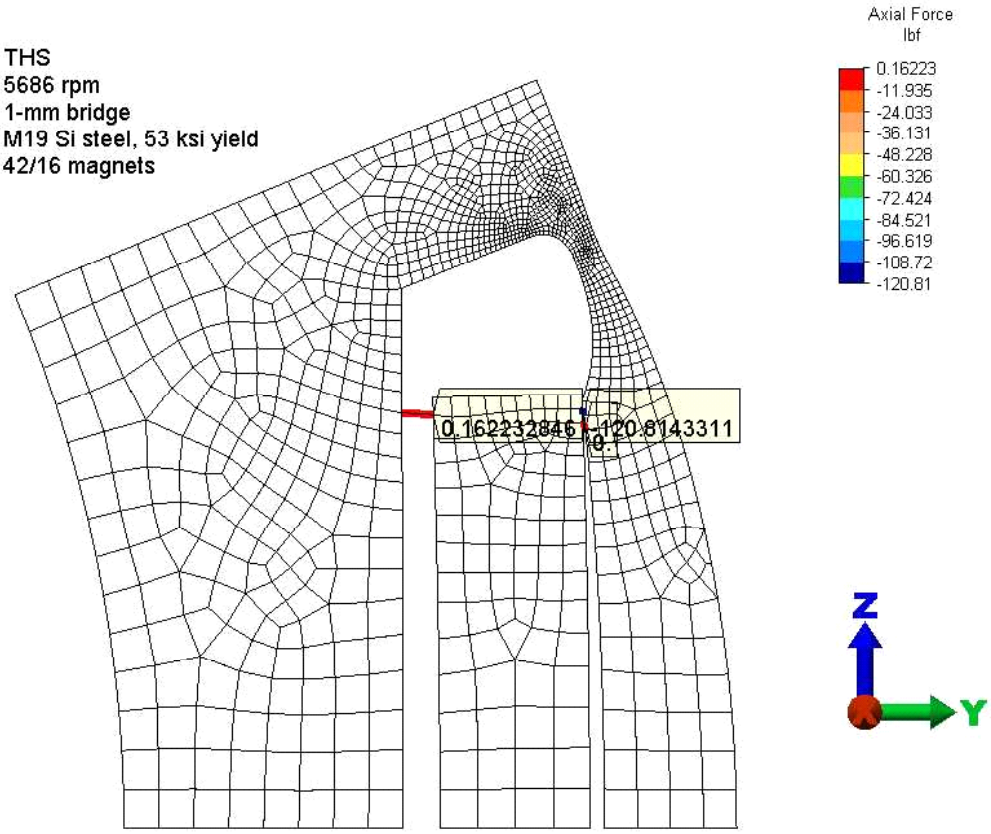

Fig. 7. Magnet loading in the THS design.

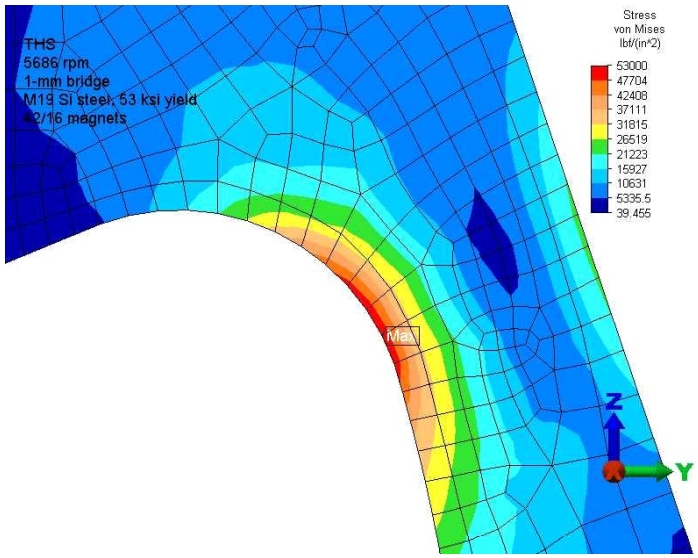

Fig. 8. Onset of plastic deformation in the THS rotor.

The impressive additional mechanical contribution of the THS II motor is the addition of a ledge on the spoke side to carry a large part of the magnet load and relieve the load on the bridge. Figure 9 shows that the magnet load supported by the ledge on the spoke side of the cocoon is 102 lb. The result of this load redistribution is that the maximum operating speed prior to the onset of plastic deformation is increased by 10% to 6231 rpm. Figure 10 shows that the stresses in the bridge at the onset of plastic deformation are similar to those of the THS motor. Results of a parametric study of the speed capability as a function of bridge thickness are shown in Fig. 11.

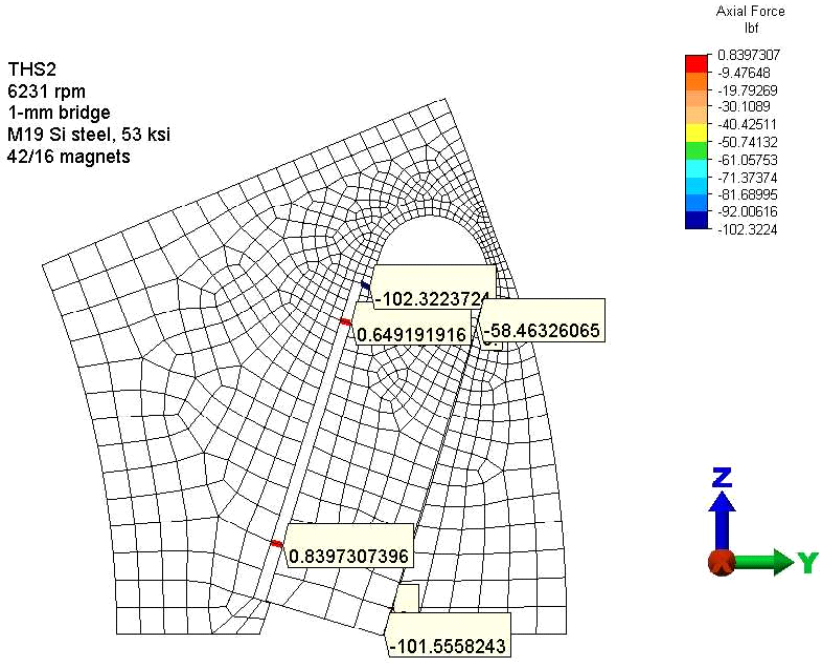

Fig. 9. Magnet load on the THS II rotor.

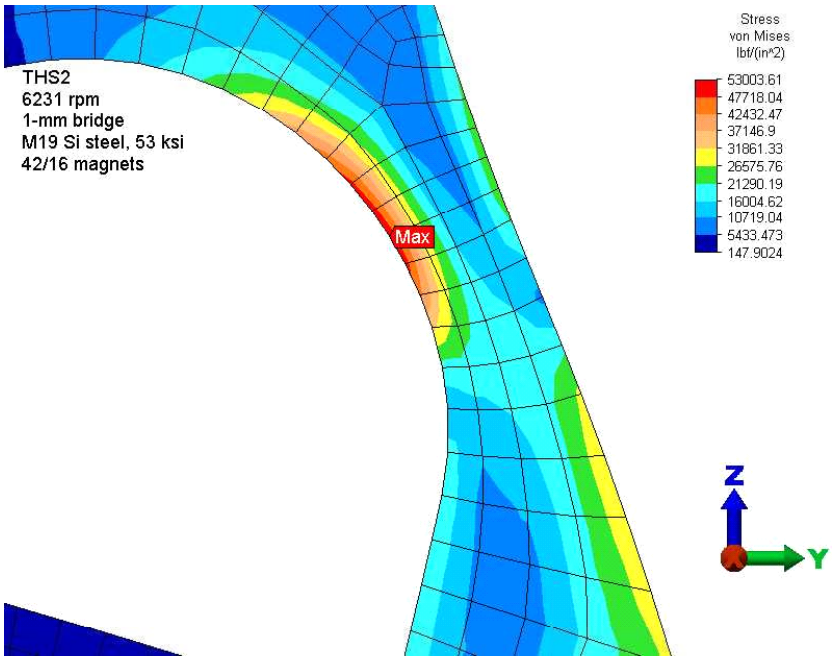

Fig. 10. Beginning of plastic deformation in the THS II rotor.

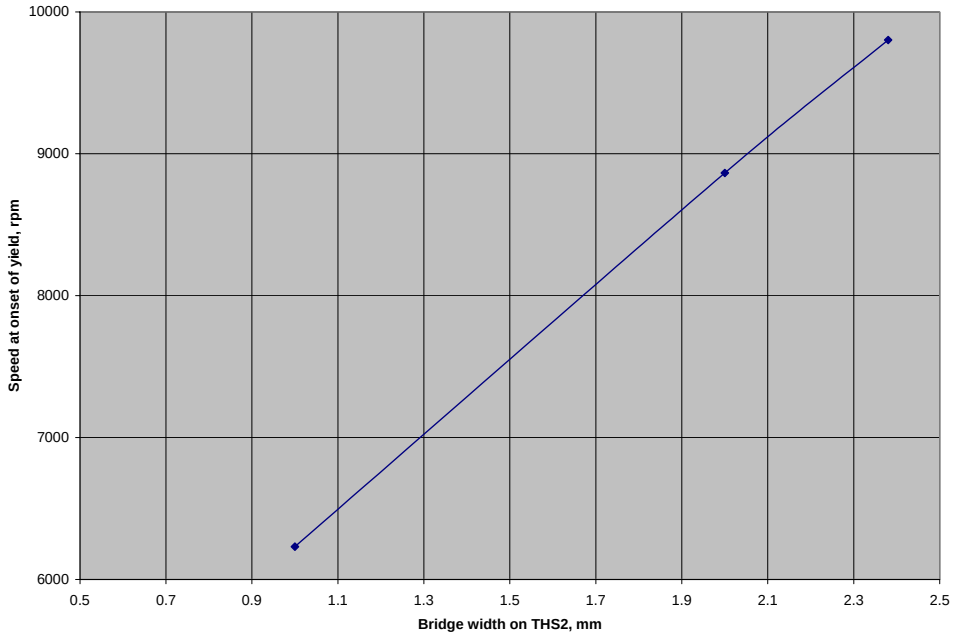

Fig. 11. THS II speed dependence on bridge thickness.

A third type of rotor being examined employs rotor-supported magnets. It has the features of a rotor with surface-mounted magnets separated by rotor steel, which uses hooks or tabs to support the magnet. Reluctance now contributes to the torque. The magnets exert a compressive load on the tabs as shown by the loads on the gap elements in Fig. 12. If the von Mises criterion is applied to this compressive load, then the failure speed is 9237 rpm, as shown in Fig. 13.

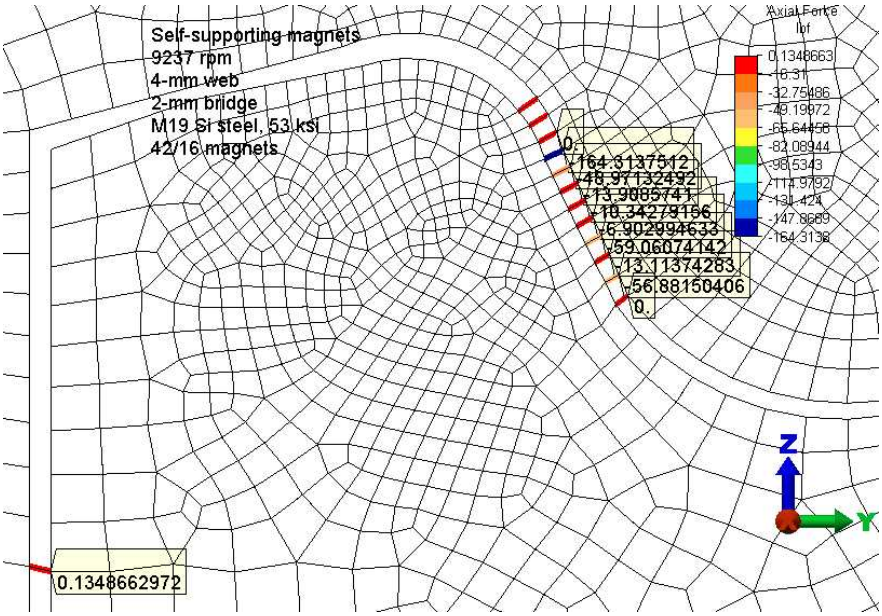

Fig. 12. Magnet load on tab of rotor-supported magnet configuration.

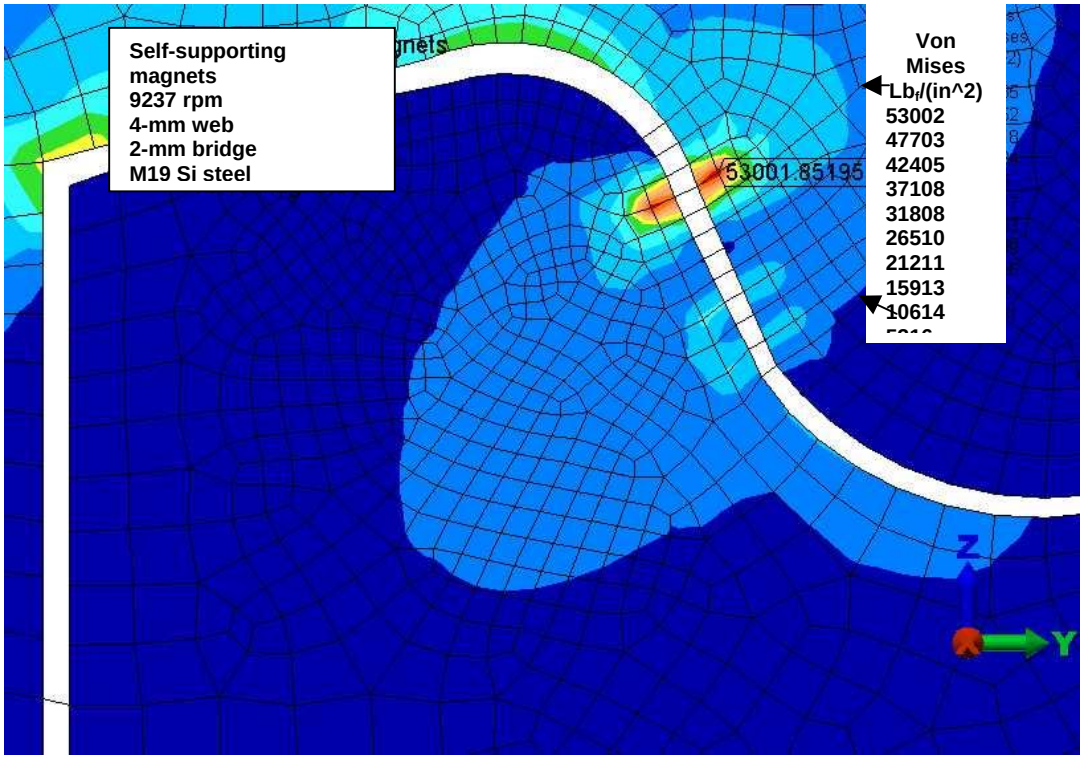

Fig. 13. Onset of plastic compression in rotor that supports its own magnets.

The fourth type of rotor proposed by ORNL is the modified THS II rotor, which uses the ledge of the THS II with the two magnets rotated into a radial orientation, adds an inner magnet to connect their inner corners, and employs a post or pile to provide additional support between each end of the inner magnet and the large region loaded by the magnets. Initial examination using the finite element approach indicated that 9715 rpm is the maximum operating speed prior to the onset of plastic deformation of the high-strength undiffused configuration using 1.2-mm bridges and 1.2-mm piles. The magnet loading on the ledge is shown in Fig. 14, and the onset of plastic deformation at the inner pile is shown in Fig. 15.

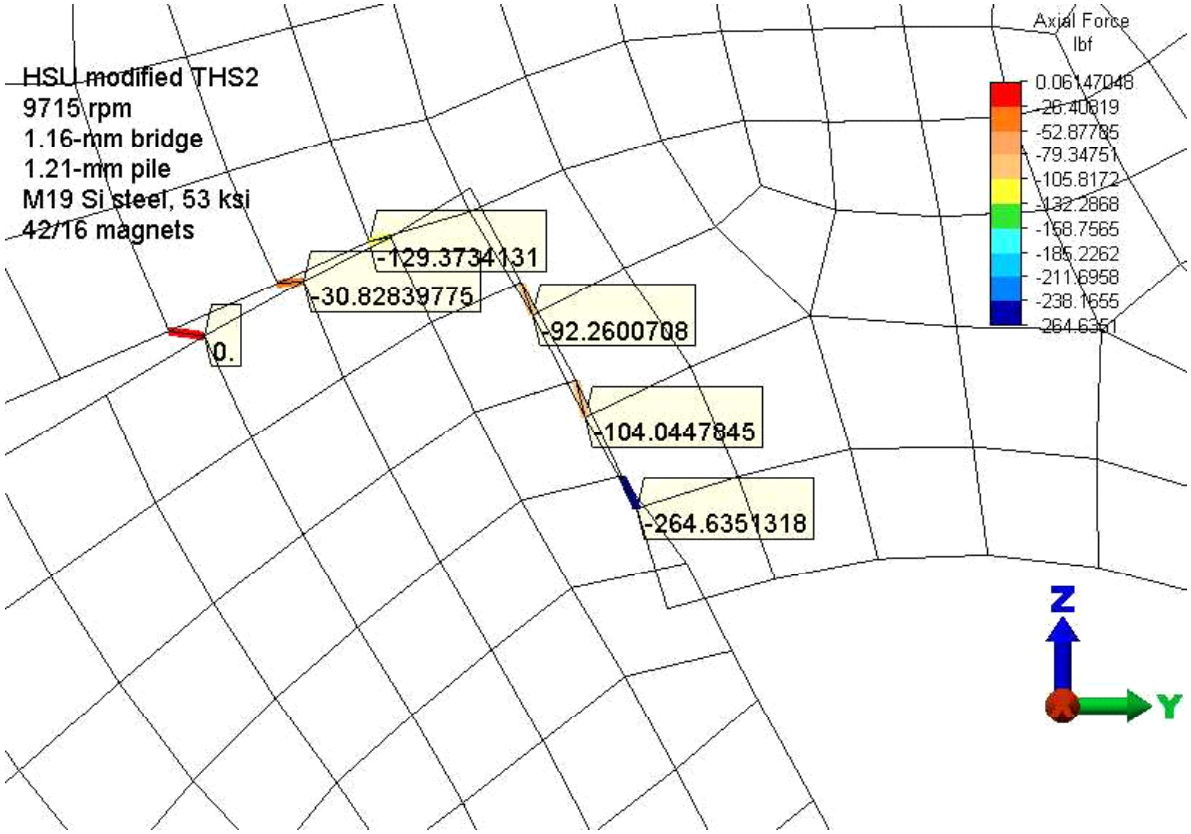

Fig. 14. Magnet load on the ledge of the modified THS II.

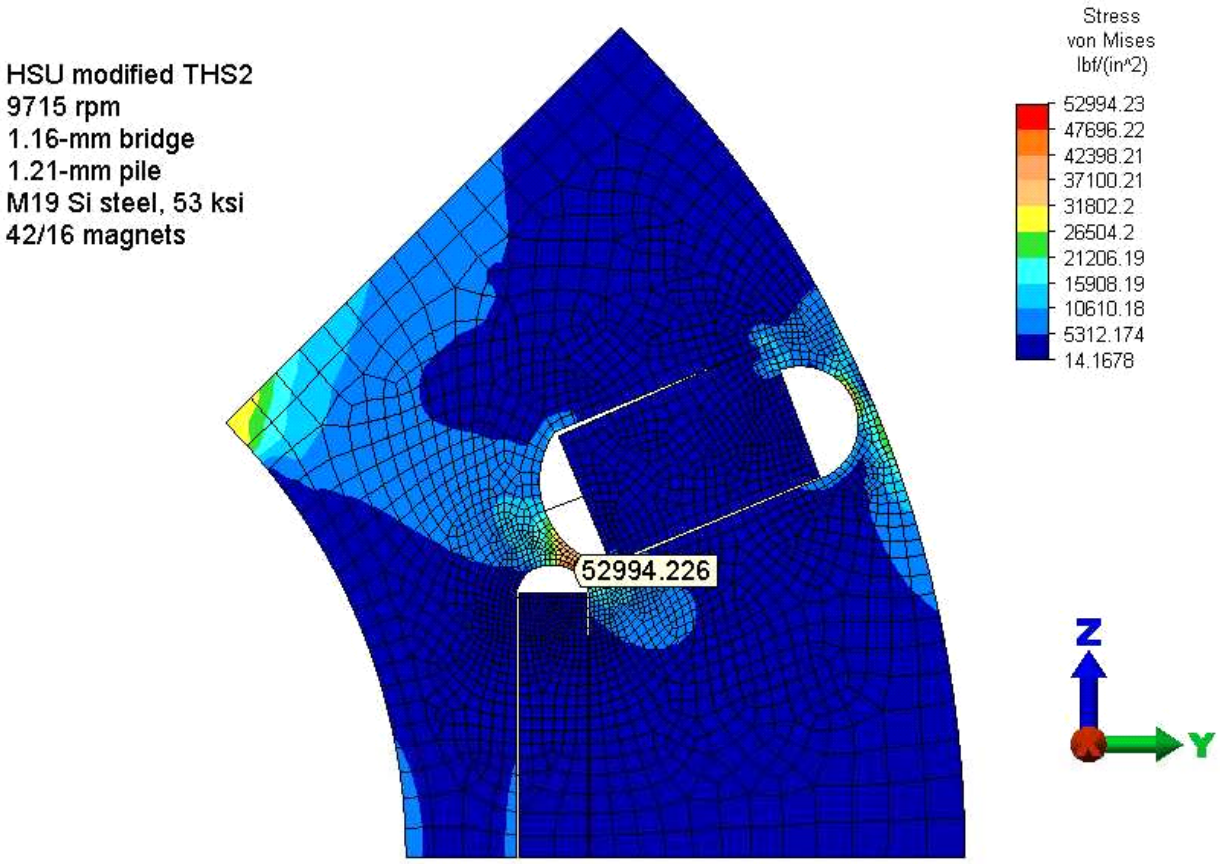

Fig. 15. Onset of plastic deformation in the modified THS II.

Conclusions and Future Work

Axial-gap motors can be constructed for high-speed operation at up to 6600 rpm, using the radial interference design concept to compensate for speed-dependent mechanical deformations and for differential thermal expansion. However, when they are driven with a trapezoidal back-emf, there are significant temperature excursions that threaten the magnets. Similar experience in the commercial sector with radial gap PM motors has promoted the use of sinusoidal back-emfs with reduction but not elimination of thermal excursions. It appears that the excursions occur as harmonics induce eddy currents in the rotor.

Maxwell's equations lead to differential equations that may be solved to determine the eddy current density in conducting elements of the rotor as a function of the perturbing B field. With no current in the motor (i.e., no load losses), magnets passing the openings of the tooth slots experience a magnetic perturbation that induces eddy currents in the magnets. With trapezoidal back-emf, harmonic currents occur in the phases that have potential to generate much larger eddy currents than the no-load eddy currents. During FY 2005, the data measured on the DMIC test will be compared with no-load loss measurements. In FY 2005, this source of heat will be investigated by estimating adiabatic temperature rise in the rotor to determine if it can definitively explain the demagnetization.

The DMIC inverter is capable of driving an 18-pole PM motor to 6000 rpm, where the electrical frequency is 900 Hz. The cheaper converter-grade SCRs are capable of soft switching at this frequency; consequently, their incremental cost impact on an inverter is more attractive to those who are considering using DMIC.

Both DMIC and CPA control were able to demonstrate legitimate record CPSRs. The excellent behavior under CPA control was a surprise because, using the derated parameters of the motor, we determined that the phase inductance should be greater than 190 uH for operation under CPA control at a CPSR of 12. The measured phase inductance of this motor was 158 uH. This will be further investigated in FY 2005.

DMIC control defines the minimum current necessary to deliver any power up to rated power at any relative speed over 2. This is significant because it quantifies the savings in current that can be attained for applications that operate for much of their lifetimes at high speeds. The PEEMRC is collaborating with a U.S. company to investigate a specific application. During FY 2005, the methodology will be developed to apply the savings derived from lower current to an application's lifetime duty cycle to estimate life-cycle cost benefit.

Small 1-mm bridges and support posts have enabled IPM rotors to operate at very high speeds. FEA is useful to quantify these speeds and to show where failure defined as the onset of plastic deformation occurs. Commercial models have exhibited splendid capabilities. Some new concepts being explored by ORNL show improved capabilities. During FY 2005, these new concepts will be further investigated.

References

1. R. L. Russell et al., "Eddy Currents and Wall Losses in Screened-rotor Induction Motors," IEEE, Paper No. 2525U, April 1958.
2. A. M. EL-Refaie, D. W. Novotny, and T. M. Jahns, "A Simple Model for Flux Weakening in Surface PM Synchronous Machines Using Back-to-Back Thyristors," *IEEE Power Electronics Letters*, **2**(2), June 2004.
3. J. S. Lawler et al., "Minimum Current Magnitude Control of Surface PM Synchronous Machines," paper in preparation responding to ref. 2.
4. Satoh et al., "Development of Traction Motor for Fuel Cell Vehicle," Paper 2004-01-05672004, SAE World Congress, Detroit, March 8–11, 2004.

B. Studies of Competitive Products

C. W. Ayers
Oak Ridge National Laboratory
National Transportation Research Center
2360 Cherahala Boulevard
Knoxville, TN 37932
Voice: 865-946-1342;Fax: 865-946-1262;E-mail: ayerscw@ornl.gov

DOE Technology Development Manager: Susan A. Rogers
Voice: 202-586-8997; Fax: 202-586-1600; E-mail: Susan.Rogers@ee.doe.gov

ORNL Program Manager: Laura D. Marlino
Voice: 865-946-1245; Fax: 865-946-1262; E-mail: marlinold@ornl.gov

Objectives

- Characterize the functional performance of the 2004 Prius THS II hybrid electric drive system.
- Understand the design methodology used in the construction of the various system components — specifically the generator, traction motor, inverter, and thermal management system.

Approach

- Conduct vehicle-level testing at the Advanced Powertrain Research Facility (APRF) at Argonne National Laboratory (ANL) and component-level testing by ORNL at the PEEMRC.
- Acquire complementary electrical and mechanical data from vehicle-level and component-level tests to gain a full understanding of 2004 Prius performance and use them to determine back-emf voltage and energy loss values over the specified operating range of the vehicle.
- Perform vehicle-level tests at the APRF with the electrical and mechanical systems installed in the original factory configuration.
- Perform component-level tests at the PEEMRC by removing the hybrid electric drive system and inverter from the vehicle and mechanically connecting the shaft to a dynamometer.

Accomplishments

- Conducted laboratory tests to evaluate the electrical and mechanical performance of the 2004 Toyota Prius and its hybrid electric drive system.
- Completed laboratory tests to measure motor and generator back-emf voltages and locked rotor torque capability, and determined gearbox-related power losses over a specified range of shaft speeds and lubricating oil temperatures.
- Initiated thermal studies on the hybrid drive under various conditions at a fixed speed (awaiting inverter/converter reconfigurations for variable speed control).
- Evaluated losses in the hybrid drive with respect to speed and system temperature.

- Documented the results.
- Studied and documented the drive train and manufacturing methods on various components by full or partial disassembly and inspection. Comparisons of the Toyota 2003 Prius and the 2004 Prius were made for some components.
- Instrumented the 2004 inverter/converter unit for full testing capability and for use in driving the hybrid drive for performance testing of those components. Control software is presently being developed at ORNL to allow the inverter to be controlled in the laboratory outside its normal in-vehicle environment.

Future Direction

- Receive the modified inverter from ANL and conduct the THS II inverter performance testing at ORNL.
- Evaluate thermal performance of the inverter under normal, full-load conditions at ORNL.
- Evaluate the THS II hybrid drive thermal performance under normal, full-load conditions using the inverter to power the system at ORNL.
- Continue the vehicle-level testing at ANL. This work will involve validating testing equipment calibration and finishing the vehicle-level performance evaluation of the THS II system. Data collected from these efforts will be compared with data taken from the component-level testing being conducted at ORNL.
- Evaluate the ANL and ORNL data sets and prepare a final report that describes the testing conducted to characterize the vehicle-level and component-level performance of the 2004 Toyota Prius.

Publications

1. J. S. Hsu, C.W. Ayers, and C.L. Coomer, *Report on Toyota/Prius Motor Design and Manufacturing Assessment*, ORNL/TM-2004/137, Oak Ridge National Laboratory, UT-Battelle, LLC, July 2004.
2. J. S. Hsu, et al., *Report on Toyota/Prius Motor Torque-Capability, Torque-Property, No-Load Back EMF, and Mechanical Losses*, ORNL/TM-2004/185, Oak Ridge National Laboratory, UT-Battelle, LLC, September 2004.
3. C. W. Ayers, J. S. Hsu, L.D. Marlino, C. W. Miller, G.W. Ott, and C.B. Oland, *Evaluation of 2004 Toyota Prius Hybrid Electric Drive System Interim Report*, ORNL/TM-2004/247, Oak Ridge National Laboratory, UT-Battelle, LLC, November 2004.

Technical Discussion

Laboratory testing of the 2004 Prius hybrid electric drive system and its components is being conducted at ANL and ORNL. The objectives of these testing programs are to characterize the functional performance of the hybrid electric drive system and to understand the design methodology used in the construction of its various components, specifically the generator, traction motor, inverter, and coolant system.

ANL Vehicle-Level Performance Tests

Beginning in early 2004, a vehicle-level performance-testing program was initiated at ANL. Objectives of this ongoing collaboration are to determine the operating characteristics and to quantify efficiencies of the 2004 Prius hybrid electric drive system as originally installed in the vehicle. The tests are being conducted at the APRF under both steady-state and dynamic conditions. To acquire the necessary electrical data, all accessible power flow points were instrumented to measure voltage and current. Power measurements were obtained between the following locations:

- Generator and inverter (Phase A current, Phase B current, A–C voltage, B–C voltage)
- Traction motor and inverter (Phase A current, Phase B current, A–C voltage, B–C voltage)
- Boost converter and battery (battery current, battery dc voltage)
- Boost converter to main inverters (dc voltage, current)

Each test run was conducted with the air-conditioner compressor inverter and the auxiliary 12-V dc-dc converter disabled. To ensure precise acceleration and speed settings during the tests, the accelerator position was remotely controlled.

The ANL chassis dynamometer is normally set up to monitor vehicle emissions under various driving cycles. Testing of a hybrid electric vehicle requires a greater monitoring effort to cover the additional electrical devices incorporated in the vehicle. In addition, the joint ANL and ORNL testing effort requires very precise power measurement to fully characterize 2004 Prius performance. The test setup for the 2004 Prius hybrid electric drive system involves current and voltage measurements at numerous points within the system. Figure 1 shows the configuration of the basic electrical components for the 2004 Prius hybrid electric drive system and the locations of the installed instrumentation.

An example time trace of data being acquired during the tests is presented in Fig. 2. It shows the power flow in different parts of the hybrid electric drive system with the vehicle speed overlaid on the graph. Review of this graph reveals that engine power is high when the vehicle is accelerating to higher speeds and drops to zero when the vehicle speed is constant, thus allowing the electric motor to propel the vehicle without assistance from the engine. At the highest speeds, however, the engine and the motor simultaneously supply power for the vehicle.

The testing is providing additional data needed to fully characterize vehicle-level performance, but calibration checks are currently being performed on the power sensing equipment to resolve possible offsets and discrepancies in the data.

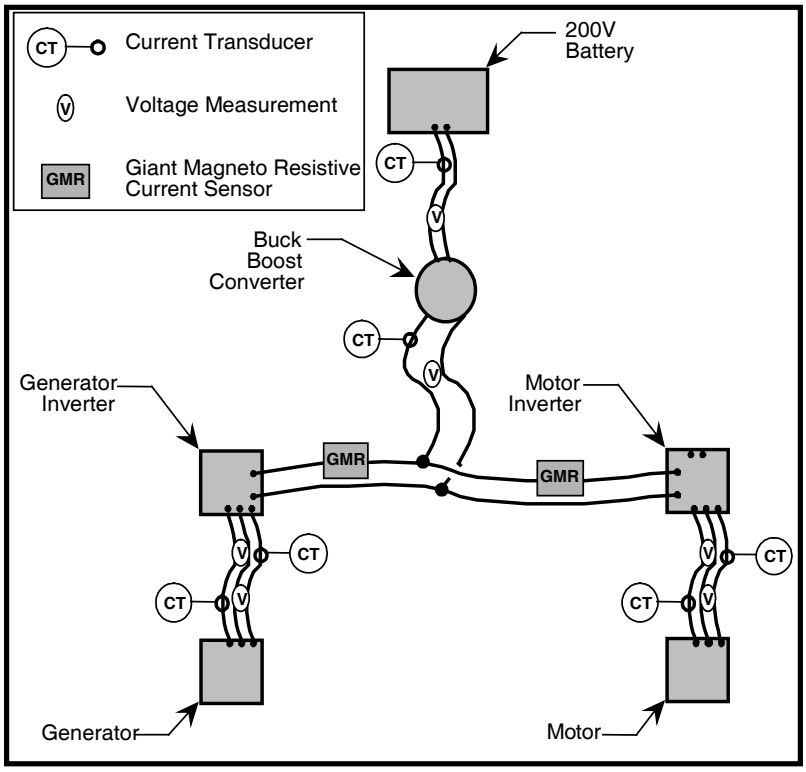

Fig. 1. Instrumentation locations for ANL testing.

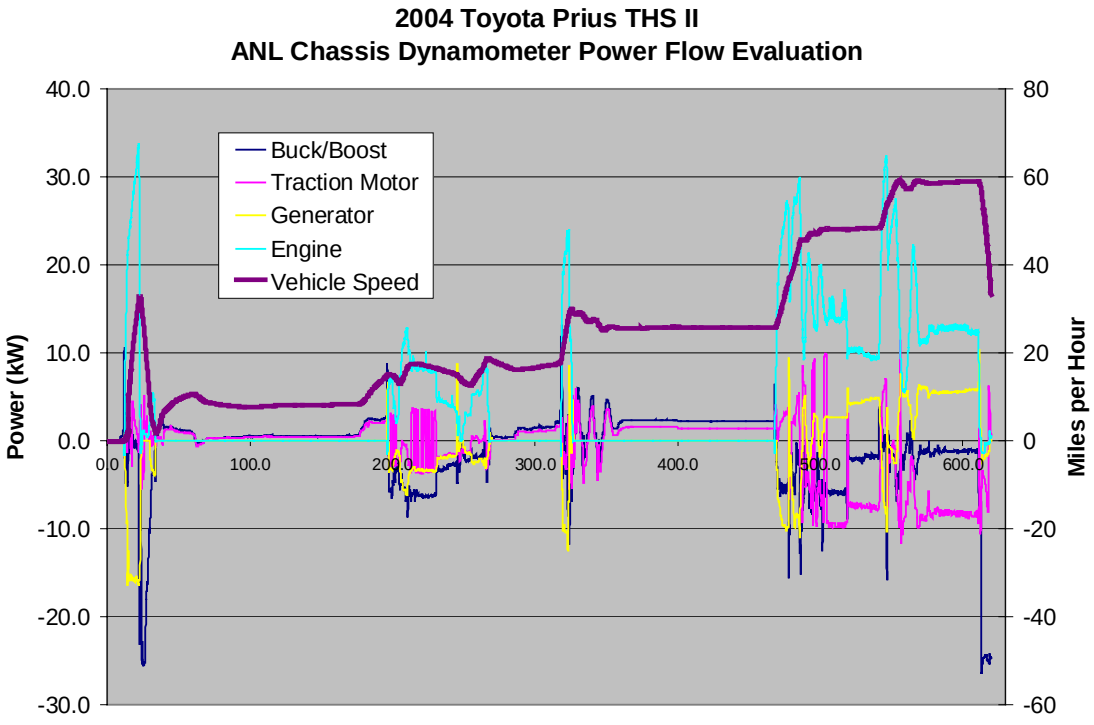

Fig. 2. Power measurements under varying speed conditions.

Another example data plot that illustrates the relationship between battery power, boost converter power, and motor power is shown in Fig. 3. These data were acquired under controlled conditions in which all auxiliary equipment was switched off (i.e., air-conditioning compressor inverter and 12-V dc-dc converter) so the battery, boost, and motor power levels would be directly related to each other. Boost power is very close to the battery power because boost converters have low losses.

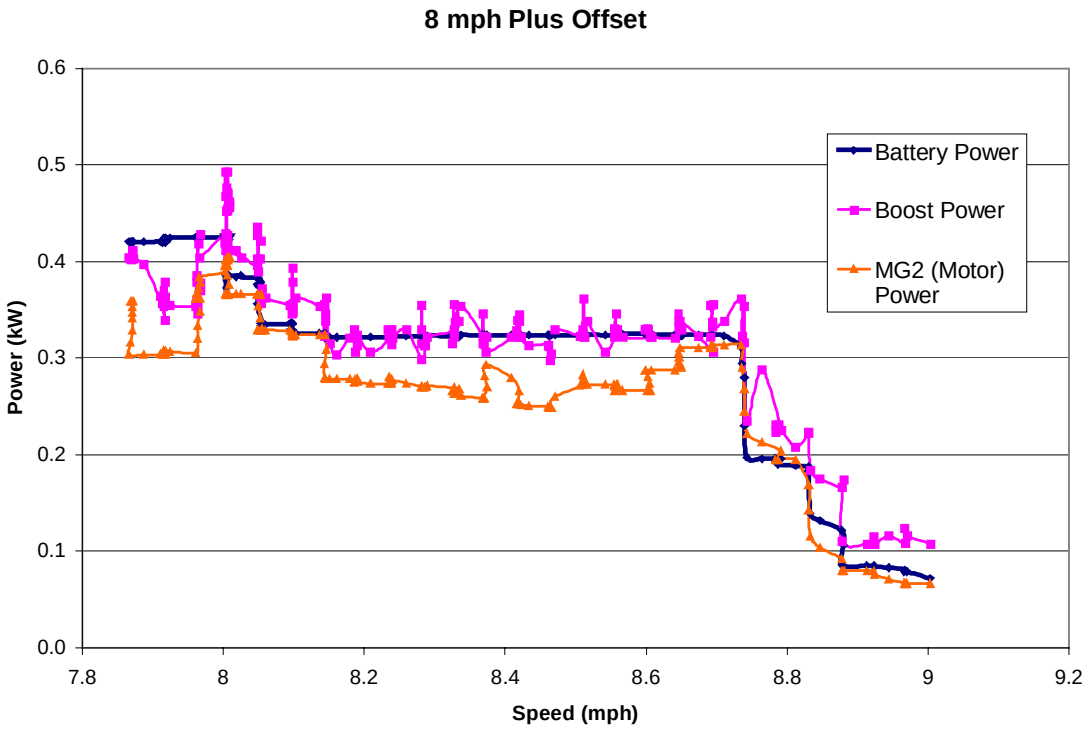

Fig. 3. Sample power measurements under controlled speed conditions.

Motor electrical power should be approximately the same but slightly lower because of efficiency losses in the motor inverter. Gross efficiencies can be inferred from this data, but more detailed efficiency results are expected as testing continues. Although this graph validates the measurement results, slight discrepancies in the data and other factors indicate the need to verify the sensor calibrations and data acquisition system settings. This verification process has been initiated and will be completed in the near future.

ORNL Component-Level Performance and Validation Tests

The hybrid electric drive system for the 2004 Prius was also tested at ORNL under a variety of operating conditions to characterize its electrical and mechanical performance. Objectives of the testing program were to measure motor and generator back-emf voltages, evaluate motor starting torque capacity, and determine gearbox-related power losses over a specified range of shaft speeds and lubricating oil temperatures.

To eliminate effects of engine friction from the evaluation, the engine was removed from the system during the tests.

Accomplishing the testing program objectives required connecting the hybrid electric drive system to a dynamometer that was capable of providing the power needed to turn the system components at specified rotational speeds. To ensure that both axles rotated at the same speed, the differential was modified so the internal gears of the differential could not rotate. By blocking rotation of these gears, it was possible to measure torque from one of the two drive wheel axles. In this modified configuration, the gear reduction ratio, which is a function of the number of gear teeth, was determined to be 4.113 motor rotations to one axle rotation.

To understand the effects of oil temperature on power loss, a system for heating the gearbox lubricating oil to a specified nominal temperature was developed and used during the tests. In this blocked differential configuration, the following measurements were obtained:

- The gear ratio from the motor shaft to the dynamometer was measured, calculated, and documented.
- The gear, windage, cogging, and other friction losses were measured without energizing the generator or the motor. Measurements were obtained with the engine spline free-spinning and with it locked.

For motor testing, the engine input spline was allowed to float, with either the motor or the dynamometer providing the driving power. During the generator tests, the engine spline was fixed from rotating, which effectively locks the planetary carrier arm. In this configuration, the planetary gear train transmitted torque to the generator shaft.

To provide a better understanding of the thermal management system, gearbox lubricating oil temperature and hybrid drive coolant system flow data were collected as part of the overall testing effort. Besides lubricating the bearings and gears, this oil also removes excess heat from the gears, motor, and generator and transfers it to the hybrid drive system coolant.

Locked Rotor Tests

A series of locked rotor tests was performed to determine the general operating capabilities of the traction motor. To perform the motor starting torque evaluation, a lever arm was devised and calibrated to a zero cogging torque position that corresponded to zero degrees. The lever arm allowed the motor shaft position to be incrementally moved in degree segments while otherwise remaining locked. Various torque values were produced by supplying current to the motor windings at varying degrees of shaft angle. The resulting data were used to produce a plot, shown in Fig. 4, that represents torque versus shaft angle at various current levels. Locked rotor torque and current were also studied to characterize the startup torque capability of the motor. Current and corresponding torque values are plotted in Fig. 5. This series of tests was effective in characterizing the starting torque capability of the 2004 Prius traction motor.

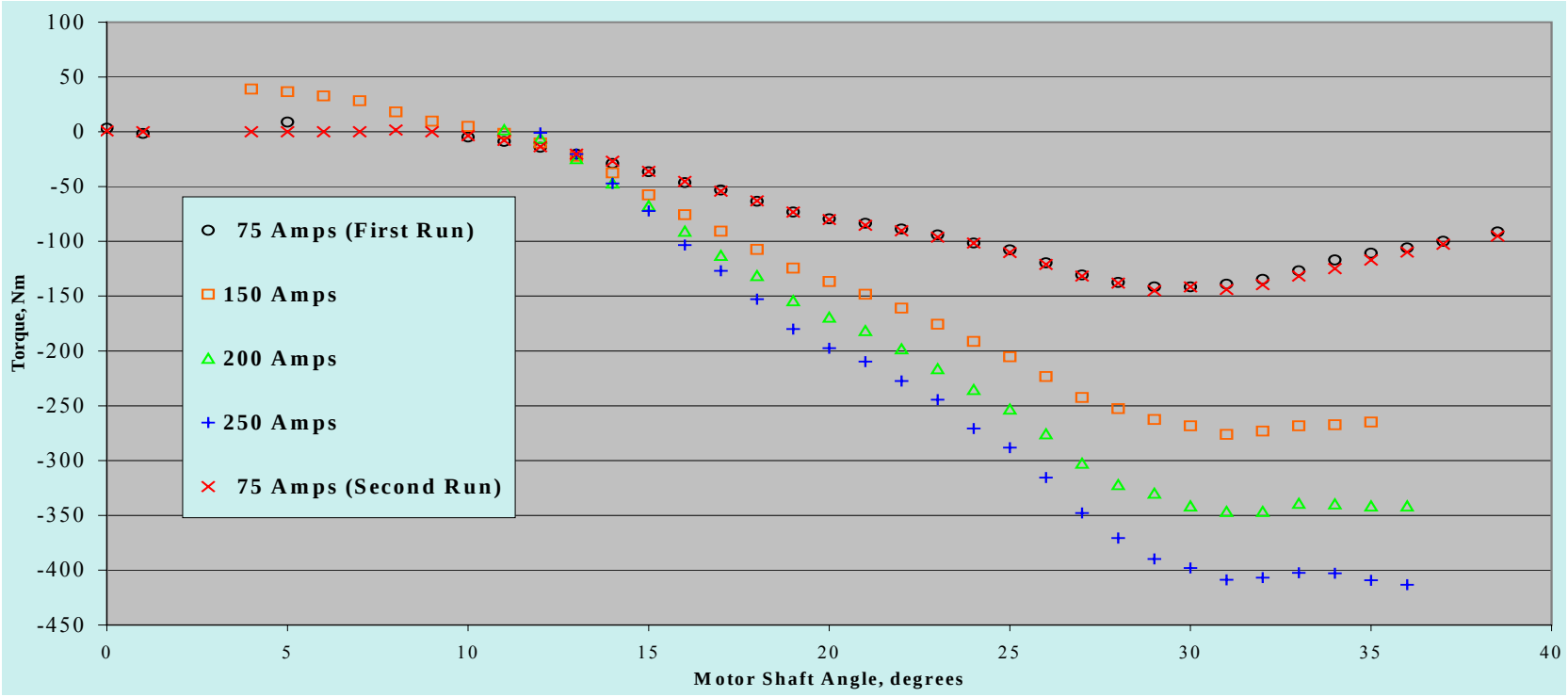

Fig. 4. Motor shaft angle vs. torque (rotor locked).

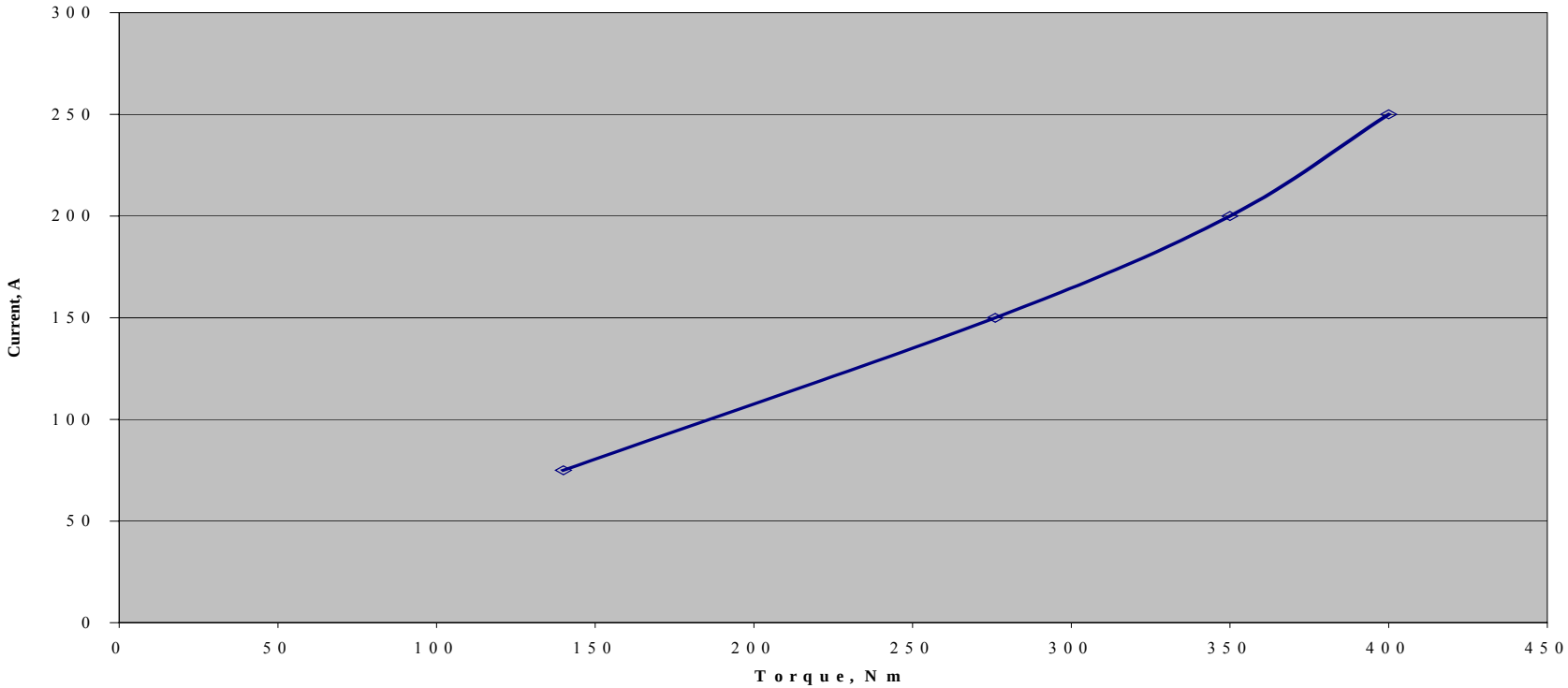

Fig. 5. Locked rotor peak torque as a function of current.

Back-EMF Tests

The back-emf voltage generated by the motor and the generator was measured using two slightly different hybrid electric drive system configurations. During the tests, an oscilloscope was used to measure both rms (Vrms) and peak (Vpeak) back-emf voltage values. Measured back-emf voltage values from the motor are plotted in Fig. 6. The lubricating oil temperature during this motor test was a nominal 25°C. Measured back-emf voltage values from the generator are plotted in Fig. 7. The lubricating oil temperature during this generator test was a nominal 80°C. In order to mechanically link the generator into the system, the engine shaft was not allowed to rotate during the tests (i.e., the planetary carrier was fixed from rotating). Using this arrangement allowed the generator to either drive or be driven by the hybrid drive gear train.

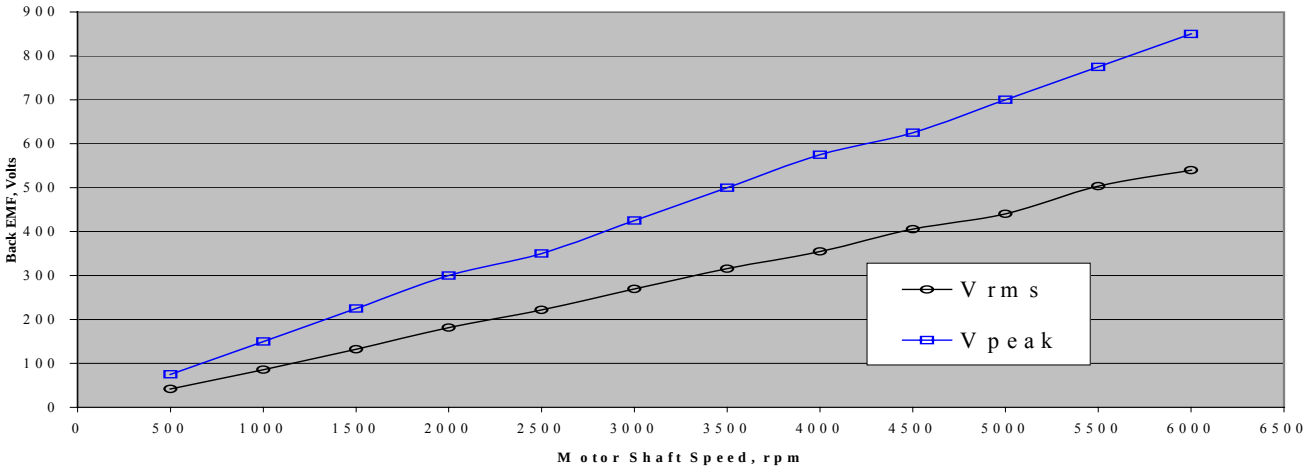

Fig. 6. Motor back-emf voltage vs. motor shaft speed.

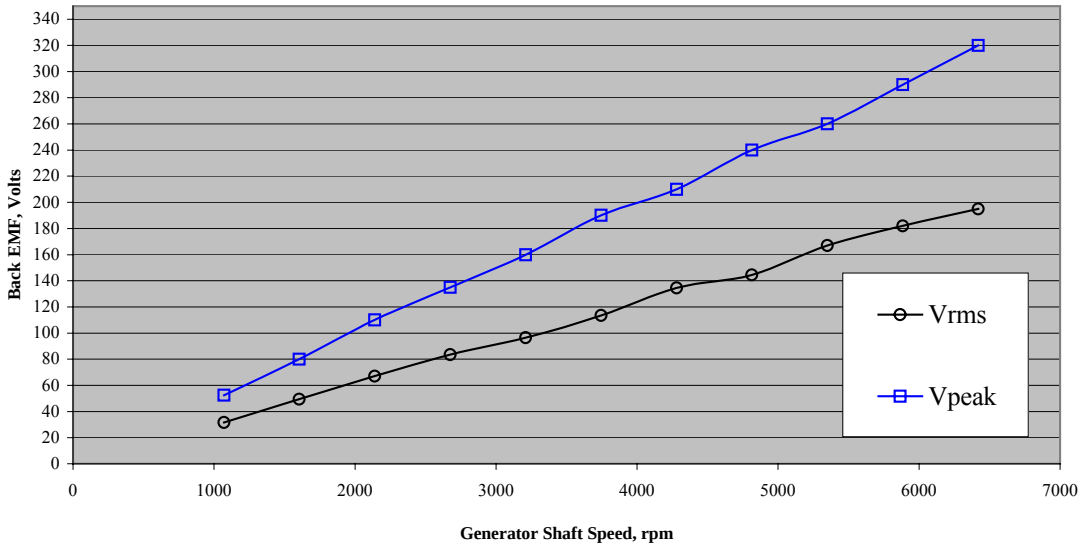

Fig. 7. Generator back-emf voltage vs. generator shaft speed.

Hybrid Drive System Losses Tests

Three types of power losses that affect the overall efficiency of the hybrid electric drive system were studied. These losses, which are reported in watts (W), include (1) gear losses; (2) motor rotor losses; and (3) planetary gears, sun gear, and generator rotor losses. The magnitude of each of these types of losses was determined by separately testing three hybrid drive system configurations at different motor shaft speeds and lubricating oil temperatures.

Overall power loss for the entire hybrid drive system was determined by testing the components in the entire hybrid gearbox. The configuration of internals in the gearbox was modified for various tests so that the subcomponents' contributions to the losses could be determined by subtraction or deduction. Loss values determined with the lubricating oil near room temperature are plotted in Fig. 8.

As Fig. 9 indicates, losses tend to decrease as the lubricating oil temperature increases.

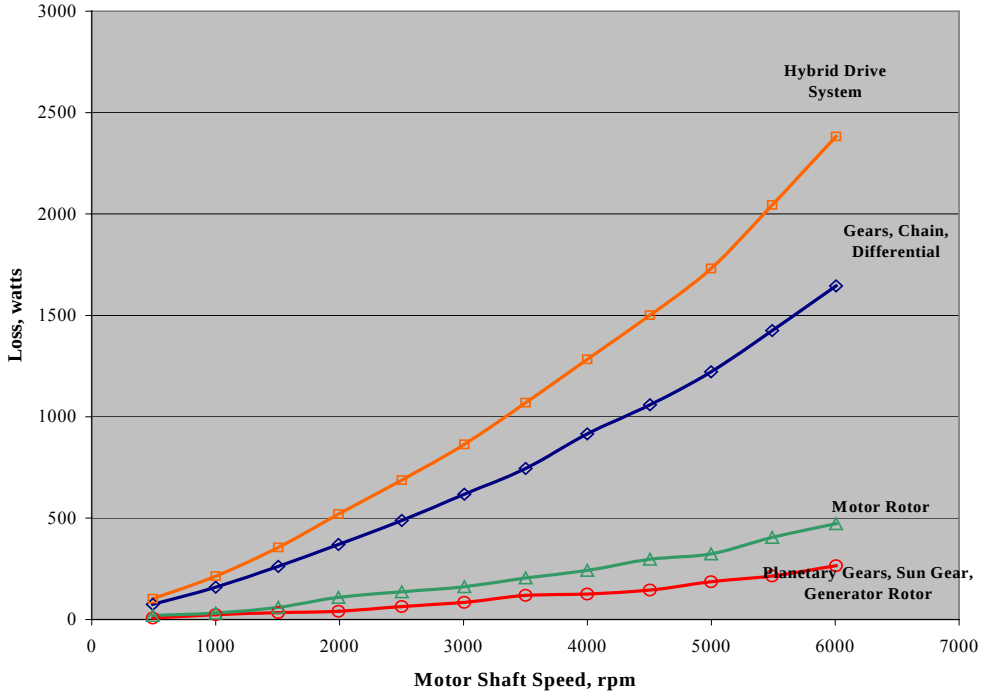

Fig. 8. Hybrid electric drive system and component losses.

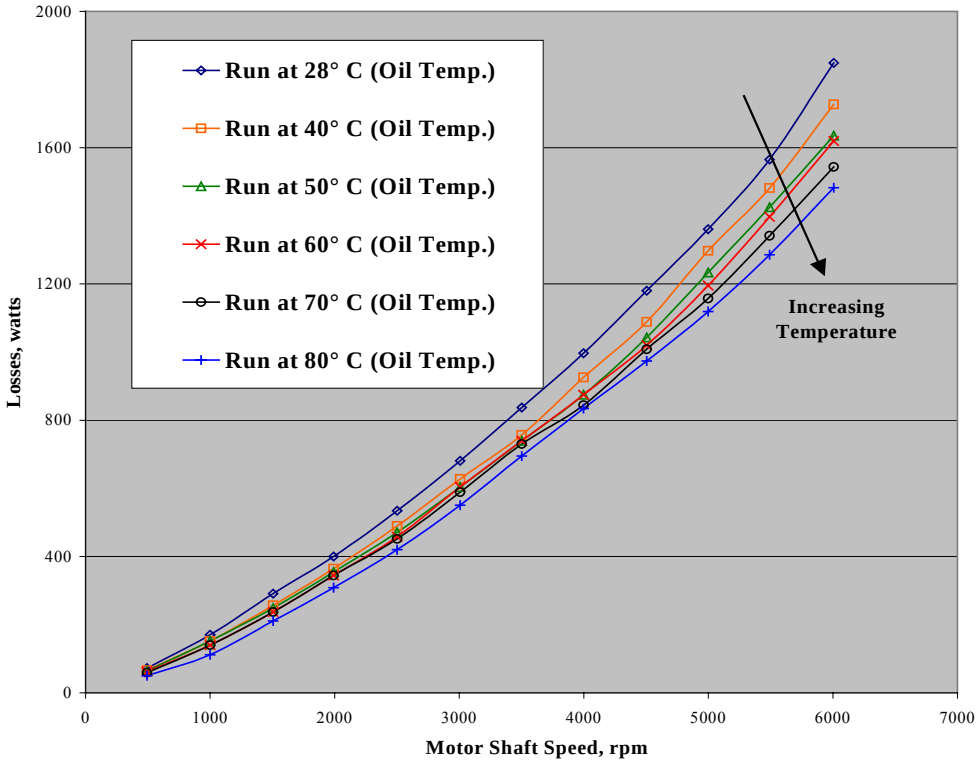

Fig. 9. Losses as a function of oil temperature.

Inverter and Converter Evaluation

The inverter that is part of the hybrid electric drive system was partially disassembled to reveal its architecture, to identify its methods of cooling, and to understand the manufacturing techniques used in its construction.

Careful study of a 2003 and a 2004 Prius inverter revealed differences between the two models. The 2004 inverter is packaged in roughly the same volume as the 2003 unit; however, the 2004 inverter contains the new buck/boost converter in addition to the motor, generator, air-conditioning compressor inverter, and dc-dc inverter and converter.

The 2004 Prius inverter is cooled using a cold plate located in the center of the package. This cold plate serves as a separator between the generator-motor-boost sections located above the plate, and the air-conditioning compressor inverter and dc-dc converter located below the plate. The cold plate transfers excess heat from the inverter to the hybrid drive system coolant as it circulates through internal passages in the cold plate. The main inverter sections (motor and generator) are packaged in one module referred to as the "12 pack." The boost converter is a separate module from the 12 pack.

The main dc link capacitors in the 2004 Prius are slightly smaller in volume than those in the 2003 Prius and are packaged in a plastic module, making them different from the commercially available can-type electrolytic capacitors used in the 2003 model. Most of the integrated circuits

in the 2004 Prius are identified with a Toyota label, compared with those in the 2003 unit that used commercially available electronic components.

Control Development

In preparing for future component-level tests, the inverter is being modified to operate and properly control the Prius traction motor and generator while outside the vehicle. Accomplishing this objective requires an understanding of the interface between the inverter and the Prius control system.

Currently, the RT-LAB real-time computing platform from OPAL-RT Technologies is being used to model and replace the Prius onboard control system. The RT-LAB system interfaces with the MATLAB SIMULINK software for quick controller development without tedious assembler programming. The system consists of a host personal computer (PC) running a user-selected operating system and two target PCs running the QNX Neutrino operating system. One of the PCs is a dual-processor computer with additional counter, encoder, and analog/digital input/output PCI boards.

The model of the Prius controller and a user interface is built in MATLAB. The software allows the control development to be flexible and versatile, with the capability of quickly making required development changes. This approach bypasses some of the more difficult hardware development efforts required to allow the inverter to be controlled outside the vehicle.
When this work is completed, inverter performance will be verified by driving simple resistive or inductive loads. After verification is completed, the inverter will then be used to operate the traction motor and generator during the component-level performance tests in a motor test cell.

Inverter Modifications at ANL

A 2004 Prius inverter is being modified at ANL with installation of instrumentation to allow control of the system and provide an effective way to monitor power flow through the inverters and converters. Currently, a preliminary version of this instrumentation is being used to perform 2004 Prius testing on the ANL chassis dynamometer. The inverter that will be used for the ORNL component-level tests is currently being modified with conventional sensors that are similar in design to those installed in the ANL inverter.

Photographs of Components

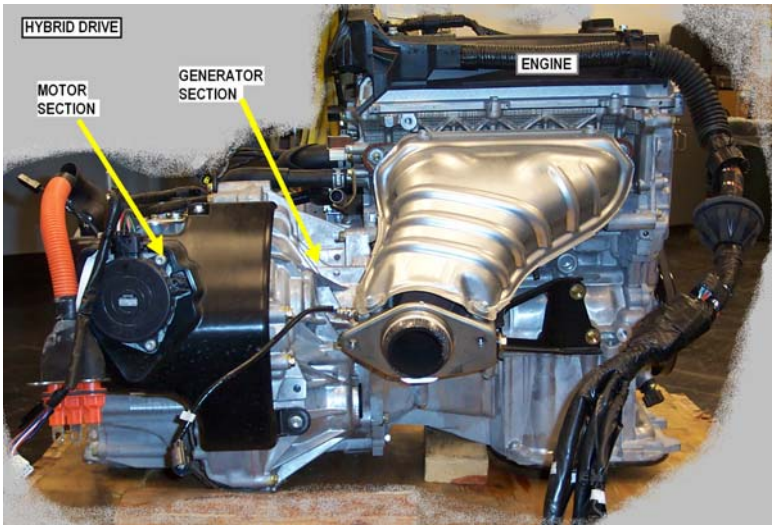

2004 Prius geartrain

2004 Prius generator rotor

2004 Prius motor rotor and stator

Prius power unit (inverter/converter)

Conclusions

ANL testing involved the following activities:

- Completion of basic instrumentation required for monitoring the inverter
- Installation of a shaft torque sensor
- Development of an interface with the onboard Toyota diagnostics computer
- Collection of initial data
- Calibration checks of the testing equipment and instrumentation

ORNL testing involved these activities:

- Characterizing overall motor performance
- Performing locked rotor tests at varying torque angles
- Collecting back-emf voltage waveforms for both the generator and traction motor
- Determining gear, bearing, and other friction losses for various operating speeds and lubricating oil temperatures

Component-level testing at ORNL revealed that gearbox-related friction losses were significant. These losses are approximately 2.4 kW at a motor speed of 6000 rpm. These losses, summarized in Table 1, were measured with the lubricating oil near room temperature (about 25°C). The tests also revealed that overall losses decreased by about 20% when the temperature of the lubricating oil increased from 27°C (2.4 kW losses) to 80°C (1.9 kW losses).

Table 1. Summary of gear train losses at 25ºC

Component	Contribution to loss (%)
Reduction gears and drive chain	68
Motor rotor	21
Generator and planetary gears	11

The following gear relationships are based on results of the gear reduction determinations (with engine spline locked):

2004 Prius motor speed = (4.113)(axle speed)

2003 Prius motor speed = (3.905)(axle speed)

2004 Prius generator speed = (10.7)(axle speed with engine spline locked)

Table 2. Summary of back-emf test results

Test conditions	Results
Motor back-emf (6000 rpm)	540 Vrms
Motor Volts/Hertz	1.33 Vrms/Hz
Generator back-emf (6420 rpm)	195 Vrms
Generator Volts/Hertz	0.46 Vrms/Hz

A series of locked rotor tests was performed to determine general operating capabilities of the traction motor. In particular, the torque and current were studied during the locked rotor tests to characterize the startup torque capability of the motor. Current and corresponding torque values are presented in Table 3.

Table 3. Summary of motor current and torque test results

Current, A	Maximum torque, Nm
75	140
150	260
250	400

C. Electric Machine R&D

John S. Hsu
Oak Ridge National Laboratory
National Transportation Research Center
2360 Cherahala Boulevard
Knoxville, Tennessee 37932-6472
Voice: (865) 946-1325; Fax: (865) 946-1262; E-mail: hsujs@ornl.gov

DOE Technology Development Manager: Susan A. Rogers
Voice: (202) 586-2314; Fax (202) 586-1600; E-mail: Susan.Rogers@hq.doe.gov

ORNL Program Manager: Laura D. Marlino
Voice: (865) 946-1245; Fax: (865) 946-1262; E-mail: marlinold@ornl.gov

---

Objectives

- Reduce the cost, weight, and volume of electric machinery.
- Improve performance.
- Simplify the system.
- Increase reliability.

Approach

- Assess various worldwide leading motor technologies.
- Design and test a radial gap interior permanent magnet (IPM) motor with brushless field excitation.
- Search for further improvement in a vehicle motor/generator.

Accomplishments

- Doubled the torque at the same full-load current after replacing the rotor of a General Electric motor with the ORNL IPM motor with brushless field excitation.
- Invented an IPM reluctance motor with brushless field excitation.
- Invented a hybrid-secondary-uncluttered PM (HSUPM) generator/motor.
- Performed Toyota Prius motor benchmarking

Future Direction

- Continue to improve the ORNL machines and integrate the motor and inverter into the ORNL floating loop.

Publications

1. J. S. Hsu, C. W. Ayers, and C. L. Coomer, *Report on Toyota/Prius Motor Design and Manufacturing Assessment*, ORNL/TM-2004/137, Oak Ridge National Laboratory**,** UT-Battelle, LLC, July 2004.
2. J. S. Hsu, C. W. Ayers, C. L. Coomer, R. H. Wiles, S. L. Campbell, K. T. Lowe, and R. T. Michelhaugh, *Report On Toyota/Prius Motor Torque Capability, Torque Property, No-Load Back Emf, And Mechanical Losses*, ORNL/TM-2004/185, Oak Ridge National Laboratory, UT-Battelle, LLC, October 2004.

Patents

1. *Motor Stator Using Corner Scraps for Additional Electrical Components*, U.S. Patent No. 6,707,222, March 16, 2004.
2. *Superconducting PM Undiffused Machines with Stationary Superconducting Coils*, U.S. Patent No. 6,700,297, March 2, 2004.
3. Provisional patent filed on AGPM reluctance motor.
4. Provisional patent filed on IPM reluctance motor with brushless field excitation.

Technical Discussion

One of the goals of FreedomCAR is that by 2010, the electric propulsion system will have a 15-year life expectancy and be capable of delivering 55 kW for 18 seconds and 30 kW continuously at a system cost of $12/kW peak. The cost target for the traction motor is $7/kW peak.

The chart in Fig. 1 indicates the current status and targets for traction motors. The chart also indicates that cost, cooling, and efficiency are the major hurdles electric motors must overcome to reach the FreedomCAR goals.

For motor R&D during FY 2004, three major tasks were conducted: studies of the Toyota/Prius motor, invention of the new radial/axial-gap IPM reluctance motors, and invention of the novel HSUPM motor.

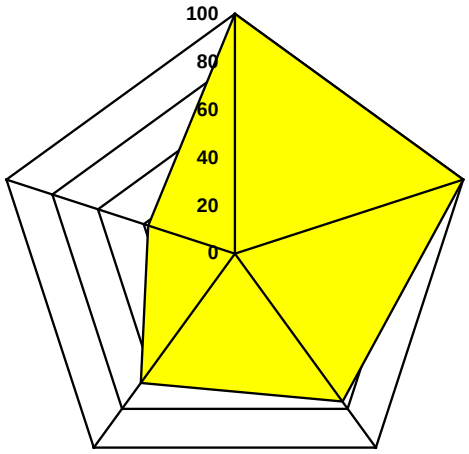

Fig. 1. Current and targeted situations for traction motor.
Source: Vijay Garg, Ford – Co Chair, Susan Rogers, DOE – Co Chair, "Electrical & Electronics Tech Team NAS Review," November 18, 2004.

Studies of Toyota/Prius Motor

The Toyota/Prius hybrid vehicle has proved itself to be a profit-making technology. An ORNL FY 2004 report on the Toyota/Prius shows that the design of the motor structure is targeted at reducing the manufacturing costs.[1] For example, the stator and rotor laminations are precisely punched and stacked for the stator and rotor cores. The cores do not go through additional machining. The non-machined cores can also reduce electromagnetic surface losses. The stator core can fit into the housing without heat shrinking and still maintain the uniform air gap between the rotor and stator. The PM assembly using polymer bonding is another cost-effective example of meeting the tolerance, insertion, protection, and magnetization requirements.

A subsequent ORNL FY 2004 report on the Toyota/Prius study presents the results of tests on the motor torque versus the load angle.[2] The tested torque is separated into two components: PM torque and reluctance torque. The reluctance torque component becomes useful when the load angle exceeds 90 electrical degrees. The Prius motor has a strong torque-production capability. The back-emf versus speed was also measured and presented in the report. These two reports contain detailed information on this benchmarking activity

The thermal management capability of the Toyota/Prius motor is being studied, and a report will be published during FY 2005.

Radial/Axial-Gap IPM Motor with Brushless Field Excitation

It is well known that motor torque is proportional to the product of its air-gap flux and stator current. If the air-gap flux is produced by a dc current, the Volt amp product is small because only the resistance contributes to the voltage drop of the dc current. On the contrary, when the air-gap flux is produced by the ac current of the stator winding, a higher Volt amp product would be produced because of both *inductance* and resistance voltage drops. This means that dc excitation requires less apparent power and consequently a smaller excitation power source. The dc excitation can be used to raise the air-gap flux density and subsequently the torque without increasing the stator current.

The required torque-speed curve of a vehicle is shown in Fig. 2. At low speed, a strong air-gap flux density can produce high torque. At high speed, a weakened air-gap flux density can increase the constant power speed range. The air-gap flux density enhancement and weakening capabilities are the innovations of the IPM motor with brushless field excitation.

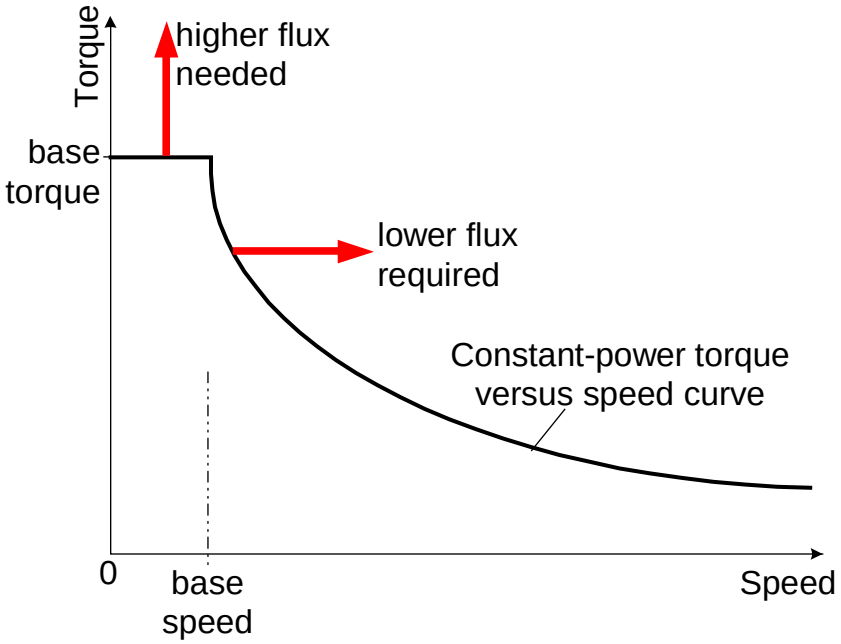

Fig. 2. Required torque/speed curve of traction motors.

In order to better understand flux control of the IPM motor through brushless field excitation, refer to Fig. 3. It shows the *series flux path* of a conventional PM machine and the *triple flux paths* of an IPM with brushless field excitation. The latter contains two parallel and one series magnetic paths.

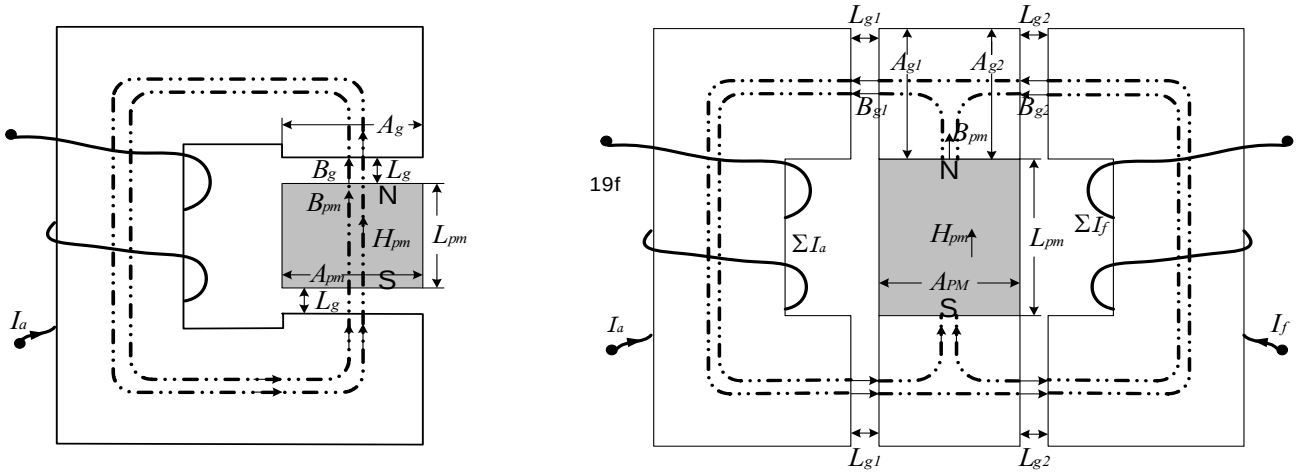

Fig. 3. Series flux path of a conventional PM machine and triple flux paths of an IPM machine with brushless field excitation.

Although the detailed derivation is not shown in this report, the results of the detailed derivations are shown in Fig. 4. The air-gap flux density of a conventional PM machine cannot be practically increased because of the saturation of the PM in a series magnetic path; that of an IPM with excitation can. Both machines exhibit field weakening.

Conclusions from Analysis

- The field enhancement of a conventional PM machine is limited by the saturation of the PMs.
- A thicker PM can better resist permanent demagnetization.
- Controlling the current of the excitation coil of the triple magnetic paths can significantly weaken and enhance the main air-gap flux.
- The leakage flux of the excitation coil through the PMs of the triple magnetic paths is blocked during field enhancement.
- No inverter demagnetization current component is needed for the field weakening of the triple magnetic paths.
- Field weakening of the triple magnetic paths never poses a demagnetization concern.
- Field enhancement can be significant with the triple magnetic paths. It is limited only by saturation of the soft magnetic core material and not by the PM.

A prototype radial gap IPM brushless excitation motor was built in FY 2004 using an existing GE motor. The rotor was rebuilt and the original stator was used in the prototype. This is shown conceptually in Fig. 5 and in greater detail in Fig. 6.

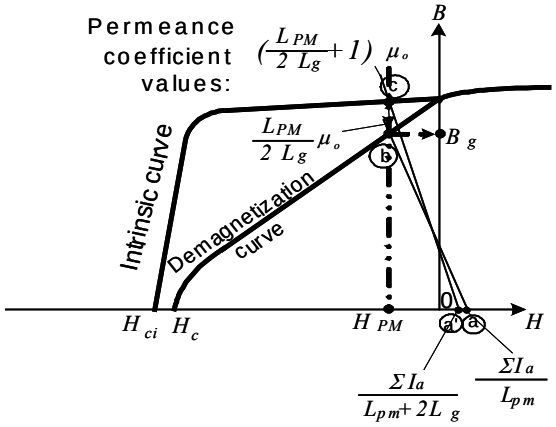

Conventional PM machine

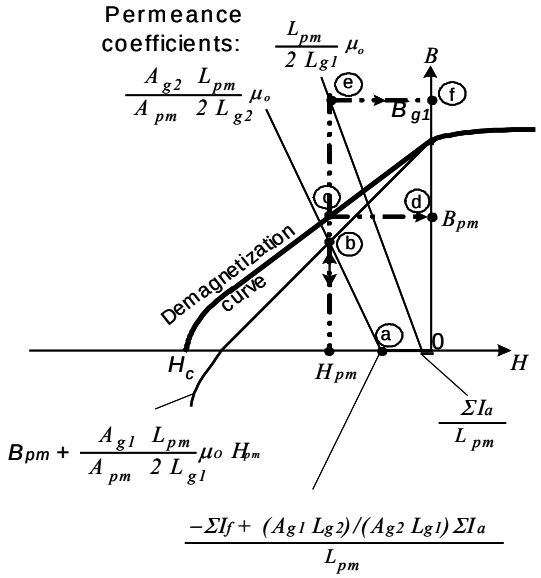

Int. PM + excitation

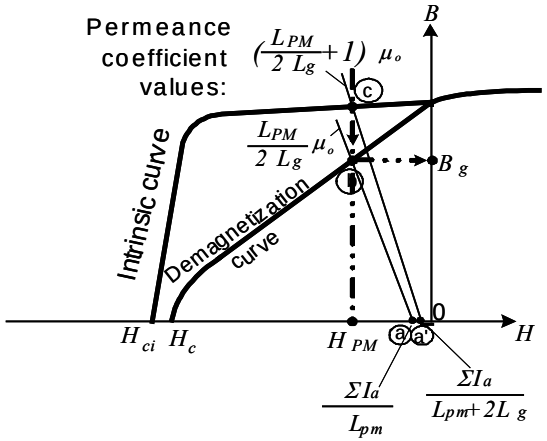

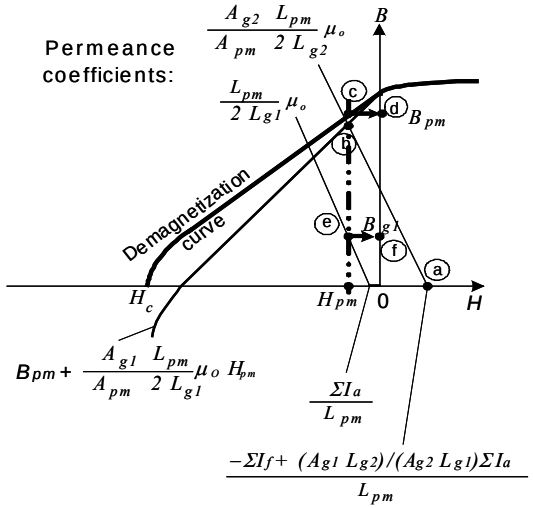

Fig. 4. Comparisons of two machines through air-gap flux densities and PM flux densities.

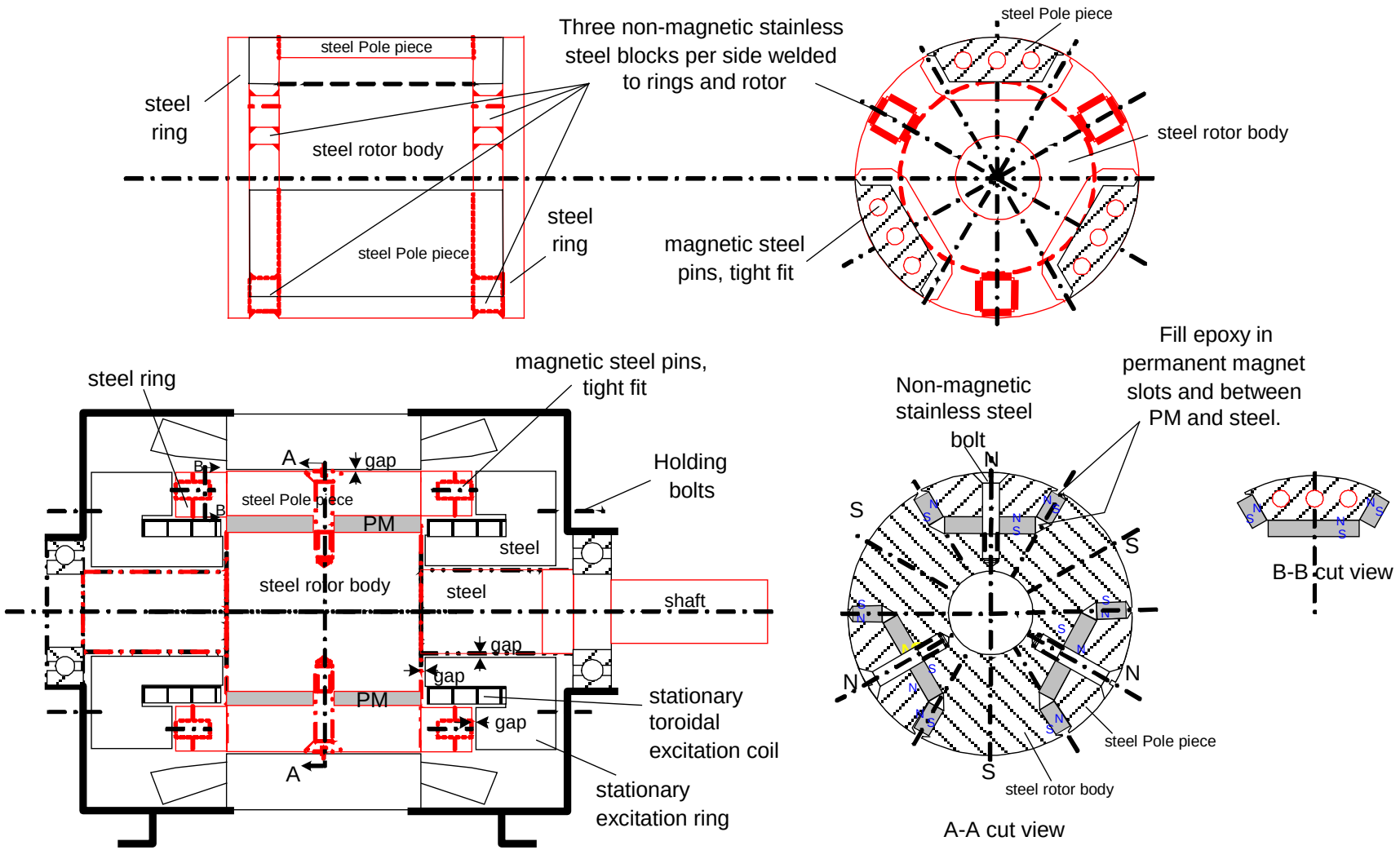

Fig. 5. A prototype radial-gap IPM machine with brushless excitation. (Modified from a GE 15-hp motor.)

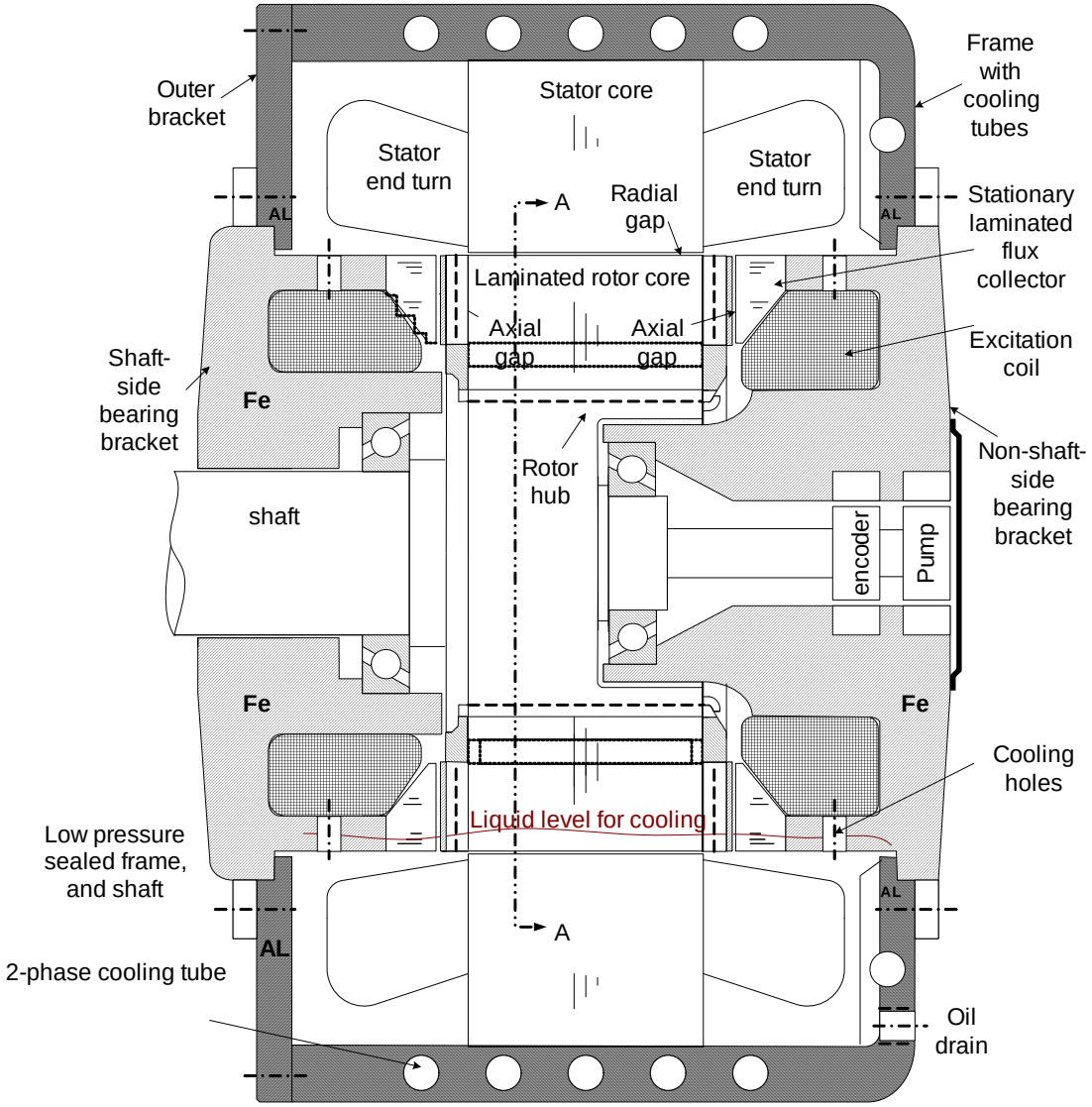

Fig. 6. A conceptual radial-gap IPM with brushless excitation and a laminated rotor.

Test Results for the Prototype Radial-Gap IPM with Brushless Excitation

During field enhancement, the prototype motor can reach 193% of the full load torque under the same full-load stator-winding current of the original unmodified motor. Because the dc flux can go through lamination punchings without causing core losses, the prototype radial-gap IPM machine with brushless excitation can be built with a laminated rotor as shown in Fig. 6.

Benefits to the FreedomCAR Program

Motor field enhancement and field weakening can increase power density and simplify power electronics. Further research for adding the reluctance path into the machine is being conducted.

HSUPM Motor

The HSUPM effort is a relatively long-term research that combines both the generator and the traction motor into one machine to reduce the drive train size. Further, additional torque coupling between the two rotors helps to boost the traction motor torque.

This task will involve two steps. Step one is to design and build the simplified hybrid-secondary-uncluttered-induction (HSUI) motor. The principle of the HSUI motor has previously been proven through tests conducted on a prototype motor (Fig. 7).

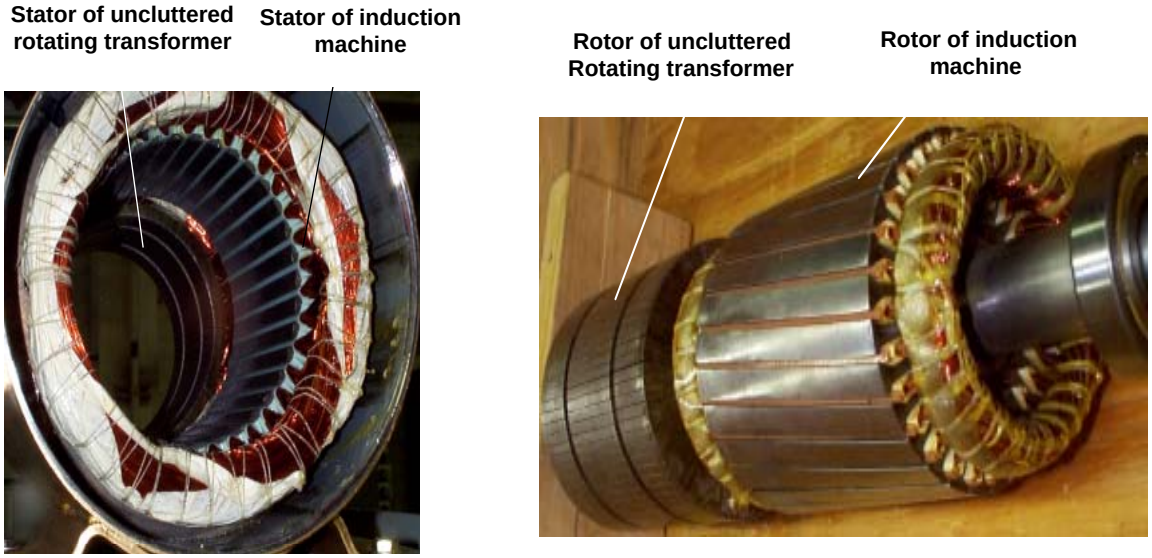

Fig. 7. Existing HSUI machine.

Further simplification can be achieved by eliminating the rotor current (or winding) as seen in the Fig. 8 pictorial. The function of the rotor current shown in Fig. 8 is only to transfer the air-gap flux of the stator and rotor on the right side of the figure to another air-gap flux of the peripheral transformer rotor and the secondary toroidal cores and coils on the left side of the figure. Therefore, the goal of this step is to develop an uncluttered rotor to transfer the flux from a cluttered content that includes the slip-frequency flux and the rotor rotating-frequency flux to an uncluttered flux that contains only the slip-frequency flux.

The result of step one will be a simplified HSUI motor as shown in Fig. 9. The uncluttered rotor does not have any windings.

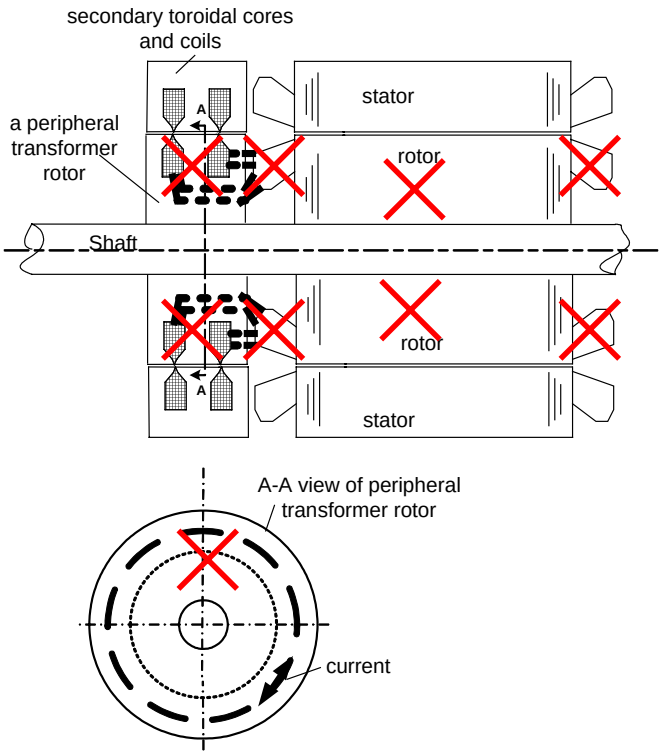

Fig. 8. Rotor current is eliminated in a simplified hybrid-secondary-uncluttered motor.

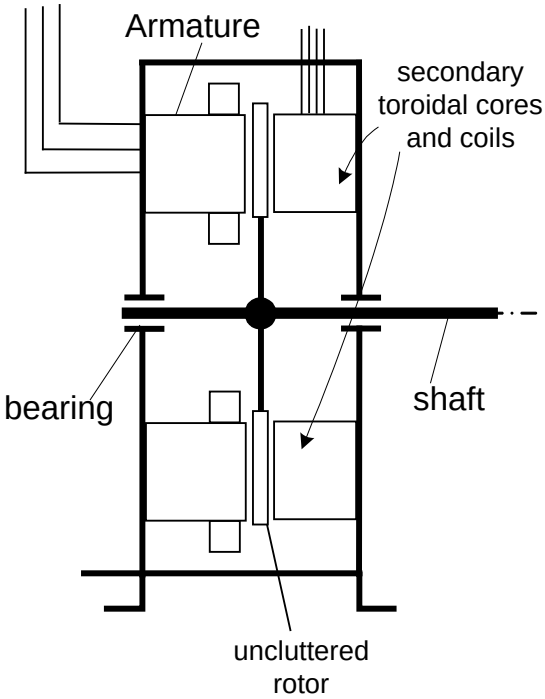

Fig. 9. Uncluttered rotor in a simplified HSUI machine.

Step two of this task is to develop an axial-gap HSUPM machine for hybrid electric vehicle applications. Figures 10(a) and 10(b) show the arrangement of the HSUPM machine, its operation modes, and its speed equations. The machine contains an uncluttered rotor and a PM rotor. The two rotors and the engine are coupled to a planetary gear set.

It can be seen that the PM rotor and the armature form a machine. The uncluttered rotor and the PM rotor forms a second machine.

When the armature drives the PM rotor to produce torque to drive the wheel, the uncluttered rotor can also drive the PM rotor for a higher wheel torque. The interesting benefit is that because of Newton's third law, the uncluttered rotor sees a reaction torque that further increases the wheel torque via the gears.

Conclusions

In FY 2004, ORNL's motor R&D efforts enveloped both short- and long-term work:

- The study of the Toyota/Prius provides an immediate assessment of the advanced technology in the market.
- The IPM motor with brushless field excitation can enhance torque, widen the speed range, and simplify the inverter.
- The relatively long-term R&D on the HSUPM machine combines the generator and motor into one machine and provides additional torque for the wheels.

The benefits of the HSUPM machine to the FreedomCAR Program are that it involves one machine instead of two, has one set of PMs, requires less space, and costs less.

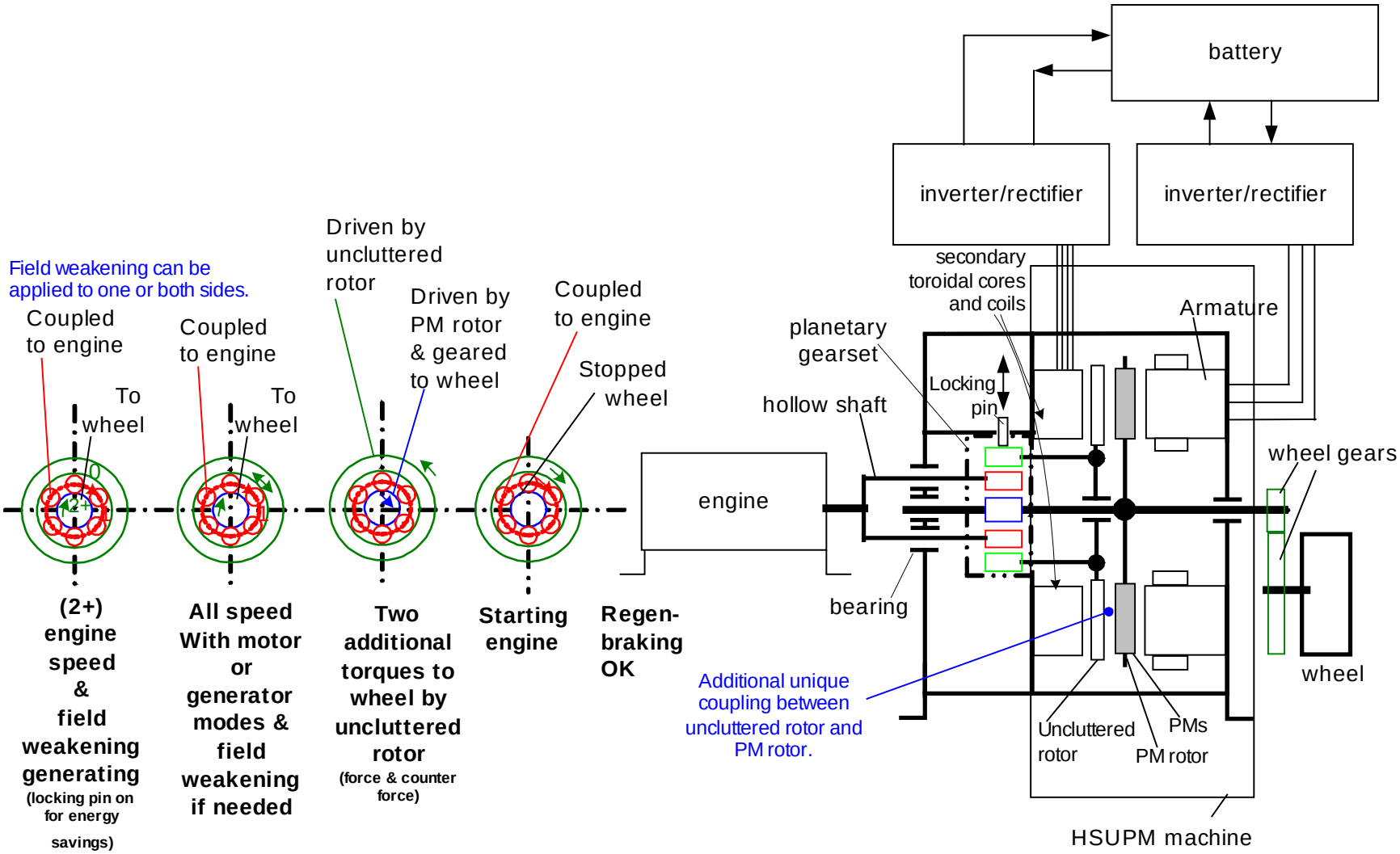

Fig. 10(a). Arrangement of the HSUPM machine and its operation modes.

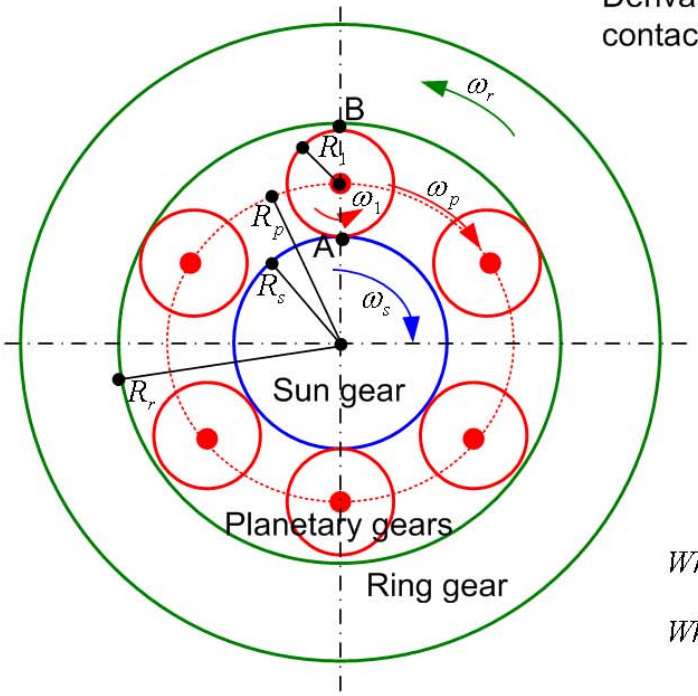

Derivation: When two gears contact each other, the speeds of contacting points have same instantaneous speed.

$$For\ point\ A: \quad \omega_s \cdot R_s = \omega_1 \cdot R_1 + \omega_p \cdot (R_p - R_1)$$

$$For\ point\ B: \quad \omega_r \cdot R_r = \omega_1 \cdot R_1 - \omega_p \cdot (R_p + R_1)$$

$$Solving\ \omega_s\ gives: \quad \omega_s = \frac{2 \cdot \omega_p \cdot R_p + \omega_r \cdot R_r}{R_s} \quad and$$

$$\omega_r = \frac{-2 \cdot \omega_p \cdot R_p + \omega_s \cdot R_s}{R_r}.$$

Speed of ω_s for wheels can be controlled by the two sides of the HSUPM machine with or without the engine running. The speeds relationship is shown by above equations.

When $\omega_s = \omega_p$, ω_r becomes $-\omega_p$. Two rotors are in sync.

When ω_s reaches:

$$\omega_s = 2 \cdot \omega_p \cdot \frac{R_p}{R_s} \qquad or \qquad \frac{\omega_s}{\omega_p} = 2 \cdot \frac{R_p}{R_s}$$

ω_s is higher than double of ω_p and $\omega_r = 0$.

a locking pin can be applied for locking ring gear.

Energy goes directly from engine to wheel at high speed, efficiency goes up.

Locking pin can be disengaged w/o force by running PM motor.

Fig. 10(b). Arrangement of the HSUPM machine and its speed equations.

D. Study of HEV Traction Motors

Samuel C. Nelson, Jr.
Oak Ridge National Laboratory
National Transportation Research Center
2360 Cherahala Boulevard
Knoxville, TN 37932
Voice: 865-946-1327; Fax: 865-946-1262; E-mail: nelsonscjr@ornl.gov

DOE Technology Development Manager: Susan A. Rogers
Voice: 202-586-8997; Fax: 202-586-1600; E-mail: Susan.Rogers@ee.doe.gov

ORNL Program Manager: Laura D. Marlino
Voice: 865-946-1245; Fax: 865-946-1262; E-mail: marlinold@ornl.gov

Objectives

- Reduce the cost, weight, and volume of electric machinery and increase the reliability.
- Analyze electric machinery designs that have potential hybrid electric vehicle (HEV) traction drive applications
- Enhance electric machinery modeling capability

Approach

- Use analytical models to characterize new electric machine designs with the performance characteristics best suited for automotive applications.
- Use lumped parameter models for the initial characterization of the machinery performance capability.
- Use finite-element analysis (FEA) to verify and/or adjust the lumped parameter models.
- Derive cost estimates for the selected machines.

Accomplishments

- Issued *PM Motor Parametric Design Analyses for Hybrid Electric Vehicles Traction Drive Application*, ORNL/TM-2004/217.

Future Direction

- Enhance and verify motor models in support of DOE's Office of FreedomCAR.

Publications

1. R. H. Staunton, S. C. Nelson, P. J. Otaduy, J. W. McKeever, J. M. Bailey, S. Das, and R. L. Smith, *PM Motor Parametric Design Analyses for Hybrid Electric Vehicles Traction Drive Application*, ORNL/TM-2004/217, the Oak Ridge National Laboratory, UT-Battelle, LLC, October 2004.

Technical Discussion

Introduction

The goal of this task is to analyze selected electric motor designs that presently show the greatest promise for use in HEV traction drive applications. Specifically, the application is for a single source of mechanical propulsion force in a fuel-cell-powered vehicle. This is a series hybrid vehicle (SHV) application, as opposed to a parallel hybrid vehicle that uses an electric motor to supplement power from an engine, primarily during acceleration.

In this task, ORNL engineers are using a number of analytical models and supplemental calculations to characterize new electric machine designs with the performance characteristics best suited for automotive applications. Physics-based models, recently developed models capable of analyzing new and innovative permanent magnet (PM) machine designs, and FEA methods are being used extensively in the study to evaluate the electric machines. In parallel with this effort, a closely coordinated cost study is developing baseline cost estimates for the selected machine designs. In the end, the study will effectively reduce the uncertainties pertaining to selected machine designs and allow the program to progress to the eventual selection and commercialization of an SHV traction motor design.

The primary focus of this work is the interior PM (IPM) machine. In IPM machines, the PMs are fully embedded (i.e., buried) in the rotor steel structure. The study is analyzing IPM machines for various design variations, using lumped parameter models to identify their key design parameters. In parallel with the IPM machine design parametric study, but with a smaller scope, analysts will evaluate other motor types. The scope of the study is limited to the motors themselves while remaining fully cognizant of the requirements of motor-inverter systems.

Background

DOE directed the automotive electric motor drive (AEMD) task efforts over several years to improve technology in many critical areas in support of the HEV. ORNL and other AEMD technical development teams were contracted to conduct research on different machine designs, primarily in the 15–30 kW range, and their progress was assessed during quarterly DOE/Technical Team meetings. As part of the DOE-AEMD contracts, axial-gap PM motors, radial-gap PM motors with an outer-rotor configuration, and induction machine designs were explored. Electric machines were researched in analytical studies, experimental prototypes were constructed, and tests were conducted for both the series and parallel HEV applications.

Several automotive original equipment manufacturers (OEMs) that are members of FreedomCAR's EETTs are recommending that analysts begin to narrow their focus to the development of IPM motors to meet FreedomCAR goals. This recommendation reflects the rapidly growing desire of the OEMs to select and commercialize a viable design in the near future. This OEM priority will be accommodated in the present study through a strong emphasis on the IPM while preserving serious consideration of other machine designs that merit the continued interest of the program.

FreedomCAR goals and specifications have been established to provide direction and guidance for the electric machine design goals set for this task. These design goals were subsequently reviewed and modified to meet the needs of both DOE and the EETTs. The specifications call for a 30-kW machine with >93% efficiency and a 15-year life, costing <$7 per kW. The full set of specifications contain several operational conditions, limitations, and performance measures that present a medium or high degree of technical challenge. Meeting the full set of specifications represents a very significant challenge, given current technology.

Priority has been assigned to certain characteristics of the electric machine based on guidance from DOE and the EETTs. For example, the cost and high-speed efficiency of the electric machine could be assigned priority. In this study, priority or emphasis will be placed on the analysis of IPM motor designs, in part because successful commercialization of this machine type has already been demonstrated successfully in the automotive industry.

IPM Machine Parametric Study

This section considers the design and modeling of (1) an 8-pole, 6000-rpm IPM machine (baseline machine), (2) a high-speed version of the baseline machine, (3) variations of a multi-layered IPM machine, and (4) two recessed-magnet machines. The analyses described in this section entailed numerous modeling runs (i.e., lumped parameter and FEA). The results of the FEAs were used to improve the accuracy of the lumped parameter model results.

For the baseline IPM machine, the stator design is a 48-slot design with 6 slots per pole. Each phase has 8 coils connected in series with 9 turns per coils. The stator ID was reduced for the high-speed IPM design. The other dimensions of the stator were adjusted in order to manage tooth flux saturation and to accommodate the required current in the slots, based on the results of lumped parameter and FEA modeling.

The rotor is the most critical design challenge for developing an IPM machine that will meet performance targets. The design must consider centrifugal forces and mechanical stresses early on, since it would make little sense to model numerous design cases when few or no rotor designs would hold together mechanically. The IPM “V-magnet” rotor baseline design is taken from a commercially produced motor and, based on the precise dimensions, the stresses were determined for the rotor at 5400 rpm. One of the first steps in scaling the IPM machine down in size to one that would operate at a higher rotor speed was to design the rotor so that it would experience the same stresses at a higher rotor speed as the baseline design at 5400 rpm. The greatest stresses in the rotor are in the bridges (i.e., a pair of thin strips of metal retaining the magnets and a triangular steel segment in the rotor structure).

Baseline IPM Machine

The results obtained from the lumped parameter model of the baseline IPM machine are summarized in Table 1. Analysis indicates that the machine, when operated at 1040 rpm, has an efficiency of 87.7% and produces 275.7 Nm of torque, of which 10.7 % is due to reluctance. When the machine operates at 5400 rpm, it has an estimated efficiency of 96.5 % and produces 53 Nm of torque, of which 29.6 % is due to reluctance.

Table 1. Selected key results of the baseline IPM machine at 1040 rpm and 5400 rpm

Selected parameter	Abbrev.	Low speed	High speed
Total machine torque, Nm	Torque	275.7	53.0
Reluctance torque, Nm	RelTorq	29.5	15.7
Mechanical power, W	Pmech	30,020	30,000
Efficiency, %	Eff	87.7	96.5
Peak current in winding, A	IWpk	225.2	77.1
RMS current in winding, A	IWrms	158.0	54.3

Numerous other simulation cases were made using the lumped parameter model to characterize machine performance over the entire specification speed range. Furthermore, subsequent to the results presented, FEA results showing significant magnetic saturation below 1200 rpm were factored into the lumped parameter model. A torque of approximately 300 Nm is constant at low speeds up to only 1000 rpm before dropping gradually with speed. The efficiency is quite high above ~1500 rpm, even exceeding 97%; however, saturation adversely affects efficiency at low speeds. Power is constant beginning at 1000 rpm. The high current at low speeds results in significant levels of magnet saturation in the stator teeth. Figure 1 shows the torque capability (total and reluctance) for the baseline machine.

The first goal of the FEA modeling effort was to model the same IPM machine for which the lumped parameter model had produced results to determine how well the two models agree and to resolve differences. The resolving of differences can include different activities, including (1) making double checks and identifying errors, (2) assessing phenomena that the lumped parameter model either does not account for or does not thoroughly account for, and/or (3) taking the results of the FEA to fine-tune the lumped parameter model. This last activity generally amounts to telling the lumped parameter model how badly the permeability of the steel is being affected by saturation and helping the lumped parameter model account for other losses. Once this is accomplished, the lumped parameter model can be used with greater confidence to quickly evaluate other, similar motor designs.

The FEA model estimated that a peak current of 250 A in each phase line would produce a total machine torque of 304 Nm. This shows good agreement with the lumped parameter model estimate of a 250.9-A peak producing a torque of 308.2 Nm. The FEA model estimated that a peak current of 50 A would produce a total torque of 80 Nm. The lumped parameter model estimated that a peak current of 55.9 A would produce a total machine torque of 75.5 Nm. Figure 2 plots the expected torque with magnets of varying strength in the baseline IPM rotor. The baseline IPM machine has 1.12-T magnets. The range of magnet strength (B_r) includes 0.2-,

0.4-, 0.6-, 0.8-, and 1.12-T magnets. The torque constant (i.e., torque/amperes) in general decreases with increasing currents as a result of the saturation effects of the machine.

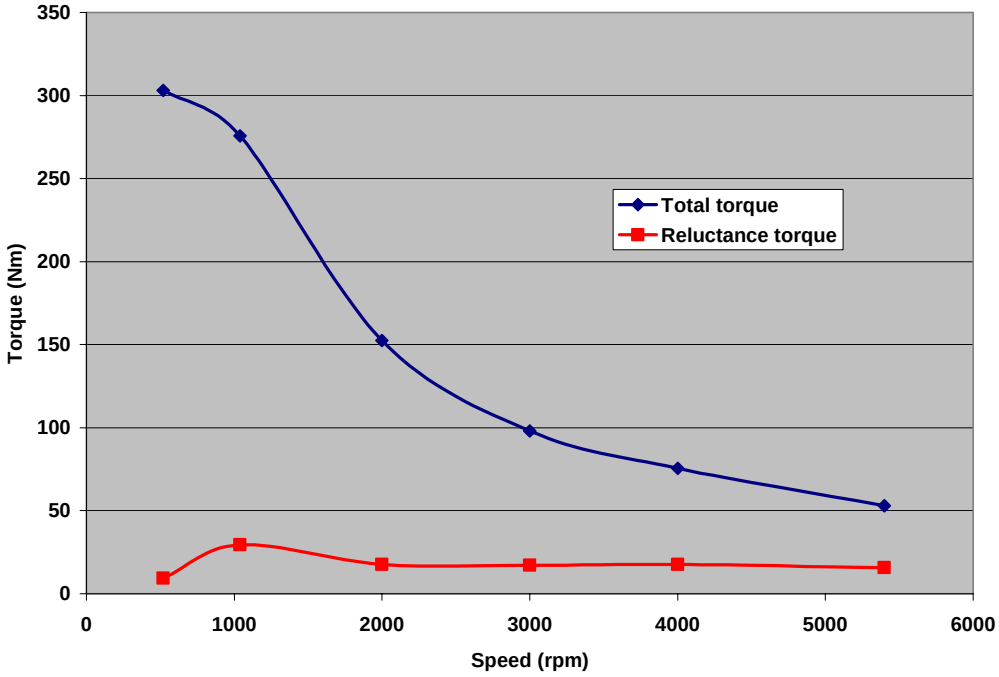

Fig. 1. Torque vs. machine speed for the baseline IPM machine.

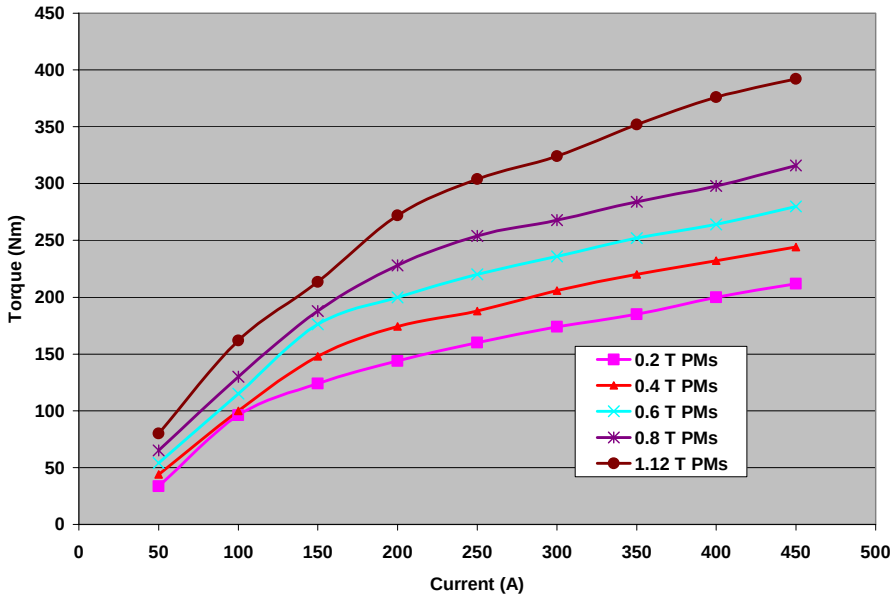

Fig. 2. Torque vs. current for magnets of varying strength for baseline IPM machine.

High-Speed IPM Machine

The high-speed IPM machine is similar to the baseline case except that it is scaled down to allow higher-speed operation. The rotor and shaft were scaled by approximately 0.8 to maintain the same stresses at 8000 rpm as the baseline machine experienced at 5400 rpm. The stator was scaled down to a lesser extent in order to manage tooth flux saturation and to accommodate the required current in the slots. The results obtained from the lumped parameter model are summarized in Table 2 for the high-speed IPM machine. The model indicates that when operated at 2000 rpm, the machine had an efficiency of 97.5% and produced 146.6 Nm of torque. When the machine operated at 8000 rpm, it had an efficiency of 95.3 % and produced 40.4 Nm of torque.

Table 2. Selected lumped-parameter results of the high-speed IPM machine at 2000 and 8000 rpm

Selected parameter	Abbrev.	Low speed	High speed
Total machine torque, Nm	Torque	163.6	40.4
Mechanical power, W	Pmech	34,260	33,890
Efficiency, %	Eff	97.6	95.3
Peak current in winding, A	IWpk	98	94.6
RMS current in winding, A	IWrms	70.2	64.9

FEA was performed for the high-speed machine at 2000 rpm and 8000 rpm, and a brief summary of the expected capability of the machine is presented in Table 3. The torque and power capability of the high-speed IPM are lower based on the FEA compared with the lumped parameter model.

Table 3. Selected FEA results of the high-speed IPM machine at 2000 and 8000 rpm

Selected parameter	Abbrev.	Low speed	High speed
Total machine torque, Nm	Torque	147.5	36.0
Mechanical power, W	Pmech	30,900	30,160

Multi-Layered IPM Machine

A multi-layered IPM machine configuration with three layers of PMs in the rotor is analyzed in this task. Variations to the basic multi-layered IPM machine that are considered include (1) machine without center posts, (2) machine with steel center posts, (3) machine with bi-state metal bridges and center posts, and (4) machine with two layers of PMs.

The basic geometry of the multi-layered IPM machine that is evaluated is shown in Fig. 3. The relative performance capability of the multi-layered IPM machine is compared with the baseline IPM machine discussed earlier. The strength of the PMs (i.e., residual induction, B_r) in the multi-layered machine is varied so that the contribution of magnet strength to machine performance can be quantified.

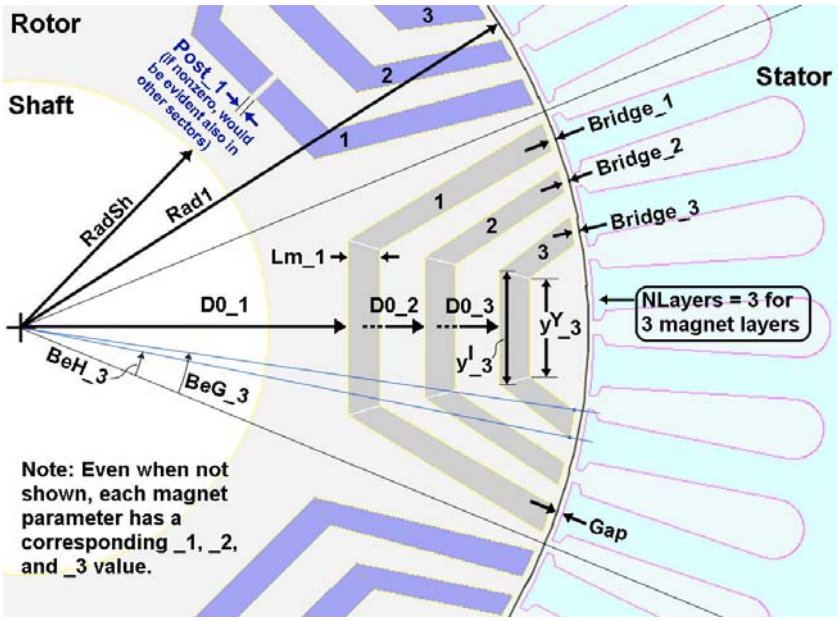

Fig. 3. Multi-layered IPM machine geometry.

The outside radius of the multi-layered rotor is the same as in the baseline IPM machine (i.e., 134.62 mm). The multi-layered machine is 80.57 mm long, 3 mm shorter than the baseline IPM machine. The baseline stator configuration was used in the models to drive the multi-layered rotor to allow comparison to the baseline machine.

Multi-layered machine configurations are modeled with and without center posts to investigate the effect of steel center posts on machine performance. Center posts will increase the mechanical strength of the rotor, allowing operation at higher speeds, but will result in additional flux losses in the center post.

The multi-layered machine configuration allows weaker-strength PMs to be utilized, which may reduce the cost of the machine. The multi-layered IPM machine's rotor can be injected with a mixture of powered magnetic material and an organic or inorganic binder material that can be cured in the rotor cavities. The injected magnets are not capable of obtaining the magnetic strengths associated with sintered magnets, but the magnet strengths can be customized for the needed application by varying the percentage of magnet and binder material. Another potential advantage is that the weaker magnets may have characteristics that are better suited for the expected 160 to 180ºC temperature of the rotor. Cost versus performance tradeoffs will determine the attractiveness of the multi-layered machine.

Variations to the baseline stator configuration should be considered in future work to optimize the stator design for the multi-layered rotor configuration.

FEA Model and Results for Multi-Layered IPM Machine

FEA models were created based on the geometry of the multi-layered machine rotor with and without 1-mm center posts. The baseline IPM stator was used for the multi-layered machine FEA model. A stack length of 80.57 mm was used for the multi-layered machine. Phase currents were varied from 50 to 450 A in steps of 50 A, and the strength of the PMs (i.e., flux density, B_r) was varied from 0.2 to 1.2 T in steps of 0.2 T. The peak torque capability of each machine configuration was estimated based on the FEA model.

FEA Modeling Results for Multi-Layered IPM Machine without Center Posts

Figure 4 shows the estimated torque capability vs. current for the multi-layered IPM machine without center posts, while Fig. 5 shows the estimated torque constants (i.e., torque/ampere) for the same conditions. In general, the torque constant reaches a peak at about 100 A and decreases at higher currents as a result of saturation effects in the ferromagnetic materials. Figure 6 compares the torque capability of the multi-layered machine without center posts (i.e.,0.6-T, 0.8-T, and 1.0-T magnets) with that of the baseline IPM machine. The baseline and the multi-layered IPM machine without center posts (and 0.6-T PMs) have about the same torque capability at 275 A.

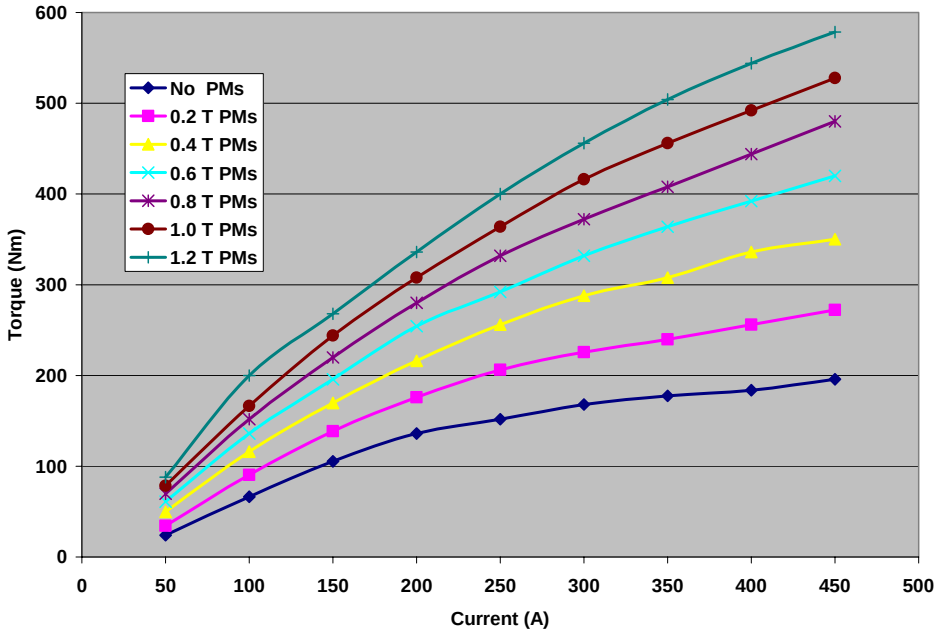

Fig. 4. Torque vs. phase current for multi-layered IPM machine without center posts.

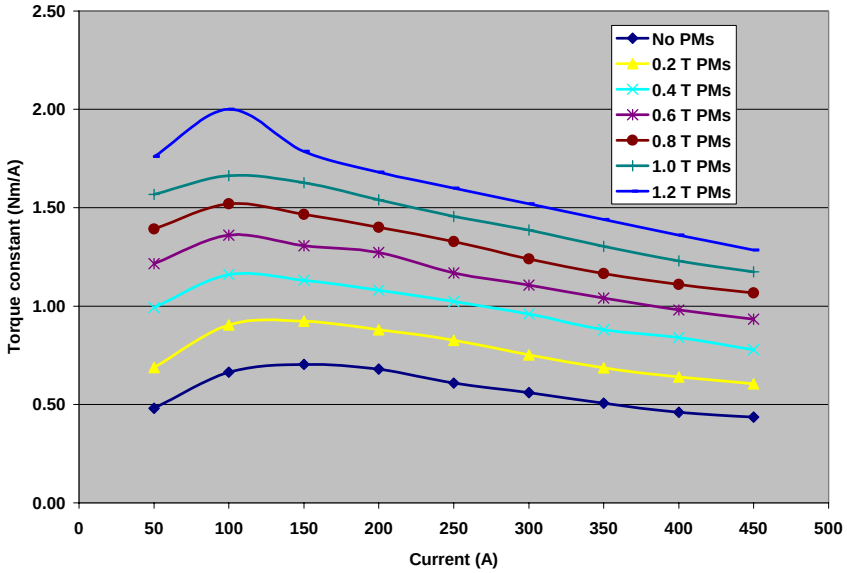

Fig. 5. Torque constant vs. phase currents for multi-layered IPM machine without center posts.

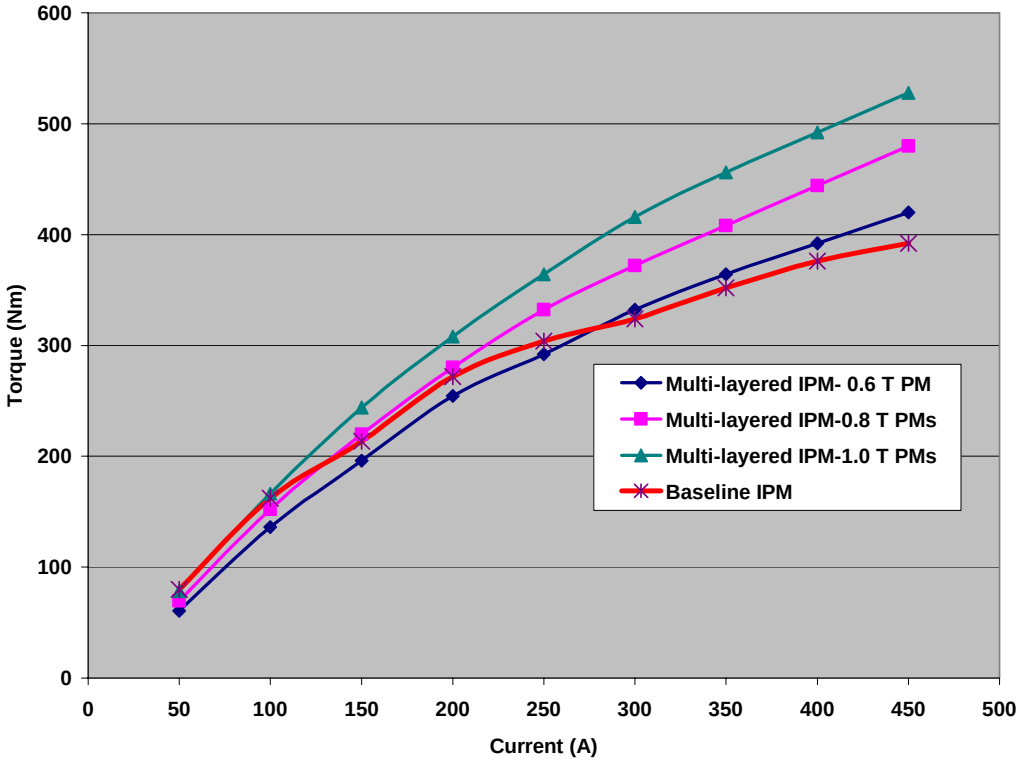

Fig. 6. Torque capability of baseline and multi-layered IPM machine without center posts.

FEA Modeling Results for Multi-Layered IPM with Steel Center Posts

Figure 7 shows the estimated torque capability vs. current for the multi-layered IPM machine with steel center posts. The torque capability is reduced as a result of the flux leakage at the center posts. The baseline and the multi-layered IPM machine with steel center posts (and 0.6-T PMs) have about the same torque capability at about 300 A.

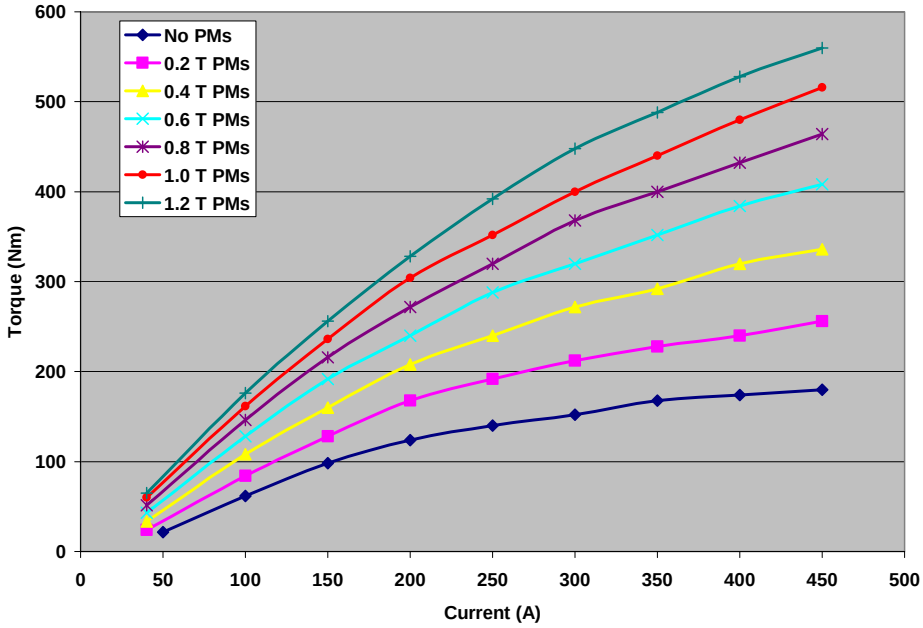

Fig. 7. Torque vs. phase currents for multi-layered IPM machine with steel center posts.

Figure 8 compares the torque capability of the multi-layered IPM with 0.4-T PMs with and without steel center posts. The rotor configuration without center posts has a higher torque capability. The multi-layered IPM machine with steel center posts experiences a noticeable loss of torque capability as a result of the steel center posts. The machine experiences about a 30% loss in torque capability with a 50-A phase current because the center posts are not saturated at this low current. During higher-current operation, the loss is much less severe, typically 5% or less.

FEA Modeling Results for Bi-State Center Posts and Bridges

Research has shown that bi-state material can have its normally high magnetic permeability permanently reduced in localized regions to that of air by means of heat treatment. Most of the rotor lamination could retain the high magnetic permeability that is desired, while localized regions could be changed to a low permeability state. IPM machine center posts and bridges are two regions that could greatly benefit from the incorporation of bi-state material. Figure 9 compares the torque capability of multi-layered IPM machines with 0.4-T PMs with bi-state and steel bridges and center posts. At 50 A, a significant increase of 50% in torque capability of the machine is estimated, owing to the reduced flux leakage in steel bridges and center posts at low

saturation conditions. When the current (and saturation of the ferromagnetic materials) is increased, the increase in torque is in the 10 to 18% range.

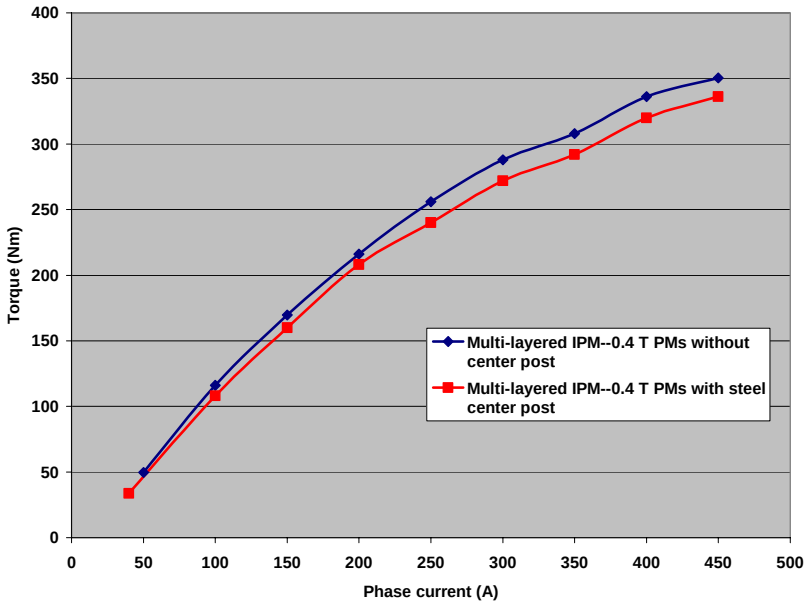

Fig. 8. Torque comparison of multi-layered IPM machine with 0.4-T PMs with and without steel center posts.

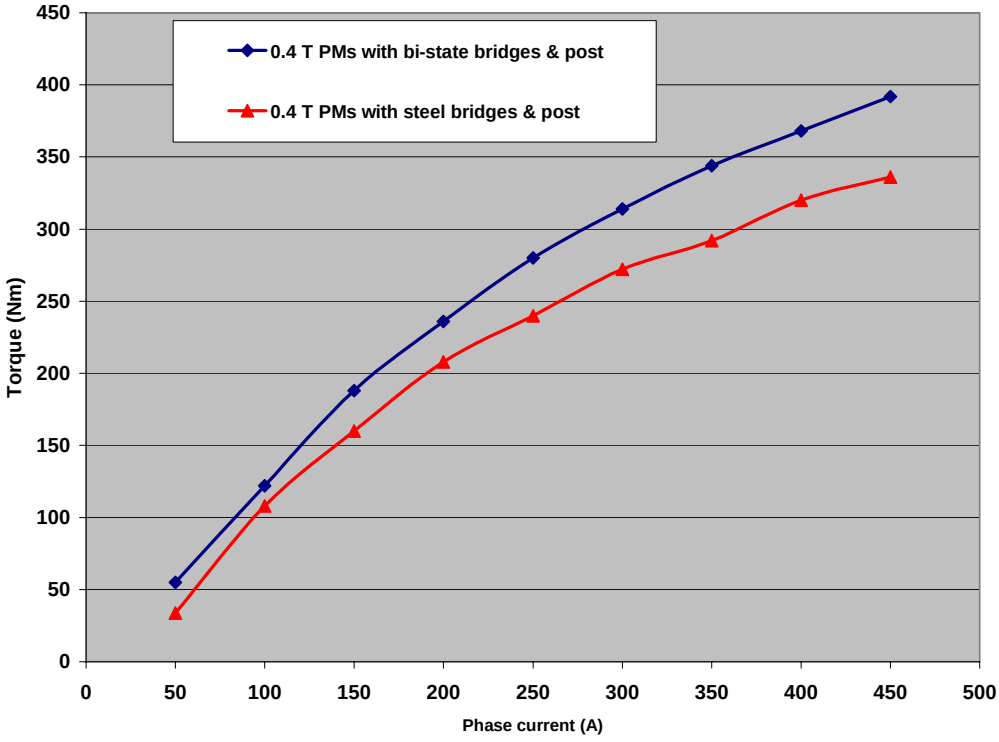

Fig. 9. Torque comparison of multi-layered IPM with 0.4-T PMs with bi-state and steel bridges and center posts.

Cost Analysis

Methodology and Assumptions

The focus of this cost analysis is to examine the relative cost-effectiveness of alternative motor designs. Other major electric drive components, such as the controller and gear drive, have not been included in this analysis. A spreadsheet-based cost modeling framework was developed for electric motor cost estimation that would allow an examination of performance vs. cost trade-offs among the competing alternative designs. This framework is designed so that it also allows adjustments at the component level for changes in material prices, substitutions, or design changes to further refine the estimate and to test the sensitivity of overall motor cost to changes in component costs. Although the initial focus of the cost estimation was at the major component level, additional design details such as different magnet shape and strength have also been incorporated as designs progressed.

The cost estimation in this study assumes a bottom-up approach in a large-scale motor manufacturing facility. The cost structure for a motor manufacturing facility was developed based on conversations held with a few brushless PM machine manufacturers. Each motor is broken down into *seven* main constituent elements that include magnets, rotor lamination, rotor shaft, stator lamination, copper windings, housings, and cooling. Housings mainly include rotor end caps, motor frame, and frame end caps. Since different magnet design configurations have been the focus for an examination of the IPM machine design, magnet cost estimates were done at a detailed level and data were obtained directly from a limited number of magnet suppliers still operating in the United States today. Motor component sizing information obtained from lumped parameter model runs is used as essential input for the cost estimation.

It is assumed that the production of these components takes place under realistic, favorable economic conditions with volumes high enough to justify a significant level of automation and full realization of raw-material volume discounts. Raw materials for various motor components are purchased from suppliers, and they are assembled in a motor manufacturing facility. Laminations are usually sold as a set for both rotors and stators, and cost in this case is mostly dictated by the stator size, number of slots, and magnet poles. Although lamination dies made of carbide materials are expensive, in the range of ~ $200K, a long die life of about 70 million parts results in this cost being a relatively small fraction of the overall lamination cost. Rotor shaft material is assumed to be cold drawn steel. The motor frame and end caps are manufactured from extruded aluminum and die-cast aluminum, respectively. The cost of motor cooling has not been determined explicitly, but it is estimated to be 10% of the total manufacturing cost. Labor and overhead are assumed to take into account the cost of machining operations necessary for the motor housing and end caps. Thus the manufacturing cost of the complete motor is determined by adding the individual element costs plus the labor and overhead, which includes the cost of assembly and testing and is estimated to represent ~25% of the total motor component material costs. Finally, the OEM cost is estimated by adding a profit margin of 10% for a large-scale production volume to the manufacturing cost.

Cost Estimates for Alternative IPM Machine Configurations

The Prius 2004 IPM motor design is considered as the baseline design having V-shaped magnets, against which two alternative IPM machine designs are compared. One of the alternative IPM machine designs considers three layers of magnet arcs (the multi-layer design discussed earlier), whereas the other is a "high-speed" design having motor dimensions significantly smaller than those of the baseline design. In addition, the motor cost sensitivity was examined; but it was limited only to the multi-layer design by varying the magnet strength, considering the in-situ magnets as the alternative magnet manufacturing option, and having the option of steel center posts of 1-mm width in magnets, as discussed earlier. The magnetic strengths for the multi-layer design were varied in the range of 0.2–1.2 T and in increments of 0.2 T. The in-situ magnet manufacturing technique has the advantage of fewer processing steps because both fabrication and magnetization are done directly in the rotor slot, and because magnetization is much easier since the magnets are hot; but it offers certain disadvantages that may increase the overall magnet manufacturing cost. These disadvantages include higher tooling costs, slower cycle time, a design that is more costly to modify because of larger equipment requirements, and higher scrap rates. There exists a trade-off between higher output (under conventional technology) and higher capital cost (under the in-situ technology). Steel center posts in magnets were considered as one of the sensitivity analysis parameters to improve mechanical magnet stability. Since magnet cost contributes the major share of motor cost, besides consideration of specific magnet designs, we examine magnet cost in detail at first, followed by the total motor cost and sensitivity analyses.

PM Cost

The cost of the PMs is a formidable barrier to the market acceptance of IPM motors, requiring that PM material be used in reduced amounts and strength in electric propulsion systems. Until recently, the raw material cost accounted for less than half of the price of finished neodymium iron boron (NdFeB) magnets. With some of the key process patents for manufacturing NdFeB magnets beginning to expire in 2004, new suppliers are pressing to significantly reduce the price of components not related to the raw materials. In addition, the recent aggressive entry and expansion of Chinese manufacturers into the rare-earth magnet marketplace has helped lower magnet costs. China has the natural advantage of rich deposits of rare-earth materials that are now being more fully exploited to make Chinese manufacturers major players in the high-strength PM market. Because of fierce price competition, most U.S. PM suppliers have either shut down or moved overseas. (The prominent one is Magnequench, the original developer of NdFeB magnet material, which has divested all of its businesses and moved completely to offshore Asia).

Depending on the required PM strength, three manufacturing methods (injection molding, compression molding, and sintering) are generally used. The first two methods produce bonded magnets that are composite materials produced by mixing isotropic magnetic powder with a polymer binder (generally nylon and epoxy for injection and compression molding, respectively), then forming a shaped magnet part in which magnetic particles are interspersed within the bonding matrix. Many different types of binders and forming methods can be used, and this high degree of flexibility is one of the most important advantages of bonded magnets. It

offers significant opportunities for high-volume, low-cost net-shape manufacturing of magnetic parts or assemblies. Remanence and energy product of a bonded magnet are directly linked to the amount of binder used, typically 2 wt % in compression-molded magnets and 8–15 wt % in injection-molded magnets. Magnetization is done after the bonded magnet is formed, thereby providing tremendous flexibility in terms of the magnetization patterns and orientations that can be created. Of the two molded magnet types, compression-molded magnets have a higher remanence because of the improved loading when blended with epoxy resin. This molding technique also produces better magnetic properties than does injection molding, yielding a magnet with higher energy density.

Sintered magnets require microcrystalline anisotropic powders (unlike nanocrystalline isotropic powders for bonded magnets). By modifying alloy composition and manufacturing conditions, different needs for magnetic properties can be satisfied. A conventional sintering route is used in this case, starting with ingot casting, followed by pulverization with a coarse grind and then jet-milling for the initial powder preparation. The resulting powder is then aligned in a magnetic field and pressed into a partially dense compact. Generally, the dense compacts are sintered, followed by a post-sinter heat to refine the grain boundary texture and relieve internal stresses. Cylinders, arcs, and rectangular bars are typical shapes for sintered components. Sintering is fundamentally limited in its ability to produce net-shape components, as the green compacts can lose up to 25% in volume through shrinkage during sintering. In addition, they require machining to the desired dimensions and coating with a protective layer of nickel (for higher-value magnetic parts), zinc (for lower-cost applications), aluminum, or epoxy. Compared with bonded magnets, sintered magnets are heavier, higher in strength, and consequently more expensive.

The particular alloy selection under each scenario was based on meeting the typical automotive operating temperature range of 160–180^{o}C, and magnet cost quotes were obtained directly from the suppliers and based on a large annual production volume of 100,000 pieces. For higher-strength magnets (i.e., about 1.12 T), assumed for all three scenarios are sintered NdFeB magnets. The raw material for these sintered magnets is assumed to be Vacodym 655AP with a density of 7.67 gm/cm^3, obtained from the European supplier Vacuumschmelze (known as VAC Magnetics in the United States). For the magnet strength sensitivity analysis of the multi-layered design, we assume injection molding for lower-strength magnet scenarios (i.e., less than 0.7 T) using MQP-B+ powders produced by Magnequench as the raw material, which provides the best compromise between the range of magnet strength and operating temperature requirements. This is an isotropic Nd-Fe-Co-B alloy composition magnet powder that is rapidly solidified into a thin metal ribbon and milled into powder, where the Co content is 5 wt %, suitable for the manufacture of bonded magnets. The compounded magnet powder cost is assumed to be $48/kg, which includes the cost of mixing with the binder. This powder has a remanance of 0.9 T and Curie temperature of 360°C, so it is suitable for our automotive applications, which are limited to 0.7 T. The 0.4–0.6 T range of magnet strength used for this material is obtained by adjusting the magnet powder weight loading. In the case of a lower magnet strength of 0.2 T, ferrite material of 88 wt % loading at a cost of $6.05/kg is assumed.

Sintered NdFeB magnets for higher strength are commercially available at only around 1.2 T today. To achieve a magnet strength in the range of 0.8–1.0 T, considered in the magnet strength sensitivity analysis of the multi-layered design, either samarium-cobalt type rare earth alloys or

additions of dysprosium and terbium rare earth metals to NdFeB magnets can be used. Dysprosium and terbium additions lower the magnet remanence but also improve the temperature stability for magnets. Both samarium-cobalt alloys and dysprosium and terbium are expensive alternatives until they are used commercially in the future. Vacomax 145S and Vacodym 688AP from VAC Magnetics were used for the 0.8-T and 1.0-T sintered magnets, respectively, considered for the sensitivity analysis of the multi-layered design. Vacomax 145S is a samarium-cobalt alloy with the chemical composition of $SmCo_5$ and density of 8.47 gm/cm^3, whereas the other is based on NDFeB-based alloys with a density of around 7.76 gm/cm^3.

Alternative IPM Motor Design Cost

Table 4 shows the mass and cost of distribution of three alternative 50-kW (peak) motor designs under consideration in this phase of this study. The relatively small size of the high-speed IPM motor design, results in a low manufacturing cost, about $300, compared with the 2004 Prius cost. The motor cost in terms of $/kW is estimated to be 8.6 and 6.0 for the 2004 Prius and the high-speed IPM designs, respectively. These costs are considerably higher than the desired <$2.2/kW AEMD motor specification. Not only is the manufacturing cost the least for the high-speed motor design, but also its various lower component weights provide an opportunity for fuel economy. The magnet cost is one of the dominant motor cost components, as shown in Table 4; and the wide fluctuation in costs in the marketplace creates increased uncertainty in estimating motor cost.

Table 4. Motor mass and cost distribution of three alternative IPM designs

Motor components	Prius 04		High-speed		Multi-layered	
	Mass (lb)	Cost ($)	Mass (lb)	Cost ($)	Mass (lb)	Cost ($)
Magnets	2.2	89	1.3	53	5.2	122
Rotor lamination	11.7	16	7.0	9	13.5	18
Rotor shaft	25.5	46	15.1	27	25.5	46
Stator lamination	39.4	52	30.8	42	37.9	51
Copper windings	13.2	44	12.0	39	13.2	44
Housing	16.7	38	11.7	28	16.2	37
Cooling	n/a	36	n/a	25	n/a	40
Labor and overhead	n/a	71	n/a	50	n/a	79
Mfg. cost	n/a	392	n/a	273	n/a	436
Profit margin	n/a	39	n/a	27	n/a	44
OEM price		432		300		480

The multi-layered design is the most expensive option considered here, more than three times the cost of the baseline design. Except for the rotor, all other component design parameters of the former are similar to those of the latter. Although the expensive sintered magnet type has been considered for all three designs, the quantity it requires because of the three magnet layers and its intricate design cause the magnet cost to jump significantly higher in the case of multi-layered design. Because of higher rotor weight, its potential for fuel economy in automotive traction drive applications will also be limited. Improvement in fuel efficiency due to a reduction in

current with improved motor design is estimated to be 0.04 mpg/A.[1] As discussed in the following section, the power capability of the multi-layered design due to higher magnet content is likely to be significantly higher than for the other two designs considered here. It is appropriate, then, that cost comparisons for alternative designs be made based on an equivalent performance level. The gear drive cost was not included in the analysis because program targets did not require that it be included.

Conclusions

The IPM machine appears to be well suited for traction drive applications. In high-power-density IPM machines, it is unavoidable that both the rotor and stator operate at or near saturated conditions in many regions, specifically during peak power operation, which creates electromagnetic design issues. The high current at low speeds results in significant levels of magnetic saturation in the stator teeth, and the rotor bridge is designed to operate at saturated conditions to prevent flux leakage. A noticeable percentage of total torque produced by a IPM machine is reluctant torque. R&D efforts in HEV traction drive motors should continue, with a focus on machines that have reluctant torque capability. In addition to the high-strength PM machines, such as the baseline machine, lower-strength PM machines should be considered in future research for their cost reduction potential. Research in the area of bi-state materials should be considered for applications such as center posts.

As rotor speed increases, mechanical balance at all possible load and cooling conditions becomes more critical. In addition, magnetic losses in the rotor become more important because of the high frequencies (HFs), and thus high-quality steel and laminated construction become imperative. In high-speed PM machines, rotor magnet retention and rotor structural integrity are critical and must be adequately addressed. In the IPM design, the greatest mechanical stresses in the rotor are in the bridge areas. Increasing the width of the bridge reduces the mechanical stress, but it increases the amount of magnetic energy leaking through it (up to 25% of the magnetic potential may be lost.) Alternative ways to hold the magnets and polar cap in place may have to be considered.

A multi-layered IPM machine configuration with three layers of PMs in the rotor was analyzed in the report, and some variations to the basic multi-layered IPM machine were considered. The strength of the PMs (i.e., flux density) was varied from 0.2 to 1.2 T in steps of 0.2 T, and the performance capability of the machine was analyzed with varying phase currents. FEA was used extensively to analyze the torque capability of the multi-layered IPM machine. The torque capability of a multi-layered IPM with 0.6-T PMs without steel center posts is very comparable to that of the baseline IPM machine. Further research should be considered for multi-layered IPM machines with 0.4-T and 0.6-T PMs. Optimization of the geometry of the rotor, number of layers of PMs, geometry (i.e., thickness and length) of the layers of PMs, and stator design should be considered for future research.

As expected, the cost of magnets dominates the overall motor material cost distribution. The baseline and high-speed machines used sintered magnets at a price of about $40/lb, while the multi-layered machine used 0.6-T bonded magnets with a cost of about $23/lb. Material types for the full-size and high-speed IPM machine components were assumed to be similar in both cases,

but most component weights of the high-speed IPM design are less because of the reduced rotor size. While the high-speed IPM has potential to be the less expensive option, magnetic saturation of the machine is a major design barrier.

References

1. A. C. Morcos and P. Campbell, "Neo Magnets Boost Fuel Economy," *Machine Design*, September 5, 2002.

4. Power Electronics Research and Technology Development

A. Wide Bandgap Semiconductors

Burak Ozpineci, Madhu S. Chinthavali, and Leon M. Tolbert
Oak Ridge National Laboratory
National Transportation Research Center
2360 Cherahala Boulevard
Knoxville, TN 37932
Voice: 865-946-1329; Fax: 865-946-1262; e-mail: ozpinecib@ornl.gov

DOE Technology Development Manager: Susan A. Rogers
Voice: 202-586-8997; Fax: 202-586-1600; e-mail: susan.rogers@ee.doe.gov

ORNL Program Manager: Laura D. Marlino
Voice: 865-946-1245; Fax: 865-946-1262; e-mail: marlinold@ornl.gov

Objectives

- Assess the impact of replacing silicon (Si) power devices in transportation applications with devices based on wide-bandgap (WBG) semiconductors, especially silicon carbide (SiC) – based power devices.
- Develop reasonable simulation tools for these new devices and use them to predict the expected performance gains and determine the areas of the greatest impact.
- Build, test, and model SiC-based power converters for hybrid electric vehicles (HEVs) to validate the predictions.

Approach

- Update the state of the art in WBG semiconductors
- Develop and reiterate models of WBG semiconductor devices, especially SiC diodes, junction field-effect transistors (JFETs), and metal oxide semiconductor field-effect transistors (MOSFETs).
- Revise the system models.
- Simulate the performance of an HEV traction drive and dc-dc converter using these device models.
- Test, characterize, and model a 55-kW Si-SiC hybrid [Si insulated gate bipolar transistor (IGBT), SiC Schottky diodes] traction inverter and compare it with a similar all-Si traction inverter. A 7.5-kW all-SiC inverter will also be tested, characterized, and modeled to compare with an all-Si and an Si-SiC hybrid inverter and to validate the system models and demonstrate the system-level benefits.

Accomplishments

- Acquired several SiC Schottky diodes, vertical JFETs (VJFETs), and MOSFETs. Some of these devices are at the experimental stage.
- Tested, characterized, and modeled SiC Schottky diodes, VJFETs, and MOSFETs.
- Designed and built a gate driver for SiC VJFETs, which can also be used for SiC MOSFETs. This gate driver is different from all the few other SiC switch gate drivers in that it uses an Si switch gate driver chip modified to drive SiC switches.
- Placed and managed two subcontracts, one with CREE, Inc. and the other one with Rockwell Scientific.
- Took delivery of 600-V/75-A diodes from CREE as a result of its subcontract.

Future Direction

FY 2006–2007: Conduct research in high-temperature packaging for SiC power devices, as present device packaging cannot handle the temperatures at which SiC devices are capable of operating. External collaboration will be required.

FY 2007–2008: Provided the test results show the 7.5-kW all-SiC inverter demonstrates significant advantages over a similar all-Si inverter, and high-power SiC devices are available, build a 55-kW all-SiC inverter to compare an all-SiC inverter with an all-Si inverter at full scale.

FY 2006–2008: Continue acquiring, testing, characterizing, and modeling new SiC devices.

Publications

1. M. Chinthavali, B. Ozpineci, and L. M. Tolbert, "High Temperature and High Frequency Performance Evaluation of 4H-SiC VJFET and Schottky Diodes" accepted to be presented at IEEE Annual Applied Power Electronics Conference and Exposition, Austin, Texas, March 6–10, 2005.
2. M. Chinthavali, B. Ozpineci, and L. M. Tolbert, "Enhancing Power Electronic Devices with Wide Bandgap Semiconductors," accepted to be presented at Advanced Workshop on 'Frontiers of Electronics' (WOFE '04), Aruba, December 17–22, 2004.
3. M. Hasanuzzaman, S. K. Islam, L. M. Tolbert, and B. Ozpineci, "Design, Modeling, Testing, and SPICE Parameter Extraction of DIMOS Transistor in 4H-Silicon Carbide," accepted to be presented at Advanced Workshop on 'Frontiers of Electronics' (WOFE '04), Aruba, December 17–22, 2004/
4. M. Chinthavali, B. Ozpineci, L. M. Tolbert, "High Temperature Characterization of SiC Power Electronic Devices" presented at IEEE Workshop on Power Electronics in Transportation, Novi, Michigan, October 21–22, 2002.

Technical Discussion

There is a growing demand for more efficient, higher-power, and higher-temperature operation in the transportation industry. In spite of the advanced technology, Si power devices have been saturated in terms of higher-temperature and higher-power operation by virtue of their physical properties. SiC has been identified as a material with the potential to replace Si devices because

of its superior material advantages, such as large bandgap, high thermal conductivity, and high critical breakdown field strength. SiC devices are capable of operating at H.V.s, HFs, and higher junction temperatures. Significant reductions in the weight and size of SiC power converters and an increase in the efficiency is projected.[1–4]

SiC unipolar devices such as Schottky diodes, VJFETs, and MOSFETs have much higher breakdown voltages compared with their Si counterparts, which makes it possible for them to be used in traction drives. The power devices in traction applications should be able to handle extreme environments, which include a wide range of operating temperatures. In the following sections, the performance of some commercially available SiC Schottky diodes and experimental samples of SiC VJFETs will be presented.

SiC Schottky Diodes

SiC Schottky diodes make up the majority of carrier devices and are attractive for HF applications, as they have lower switching losses than pn diodes. However, the Schottky diodes have higher leakage currents, which affect the breakdown voltage rating of the device, and higher on-state resistance, which results in higher conduction losses. SiC Schottky diodes tested in FY 2004 are the S1 (1200 V, 7.5A), S2 (600 V, 4A), S3 (600 V, 10 A), and S4 (300 V, 10A) diodes.

1. Static Characteristics

The static characteristics of different SiC Schottky diodes at room temperature are shown in Fig. 1. The threshold voltage or the knee voltage and the on-state resistance are different for the diodes because of differences in device dimensions for different ratings. Their static characteristics for a temperature range of -50°C to 175°C are shown in Fig. 2 for one of the devices S1 (600 V, 7.5A). The on-state voltage drop of a Schottky diode is dependent on barrier height and the on-state resistance. Both the parameters vary with temperature and hence contribute to the temperature dependence of forward characteristics.

At lower current levels, the built-in potential (barrier potential) decreases with increasing temperature owing to reduction in barrier height. As the temperatures increases, the thermal energy of electrons increases, causing lowering of the barrier height. The variation in V_d with temperature is plotted in Fig. 3.

At higher current levels, the voltage drop is mainly due to the series resistance of the diode. The on-state resistance is one of the critical parameters that determine the performance of the device and is a temperature-sensitive parameter. $R_{on,sp}$ increases with temperature as a result of a decrease in mobility at higher temperatures. The positive temperature coefficient characteristic increases the conduction losses at high temperatures; however, this is advantageous for current sharing and paralleling.

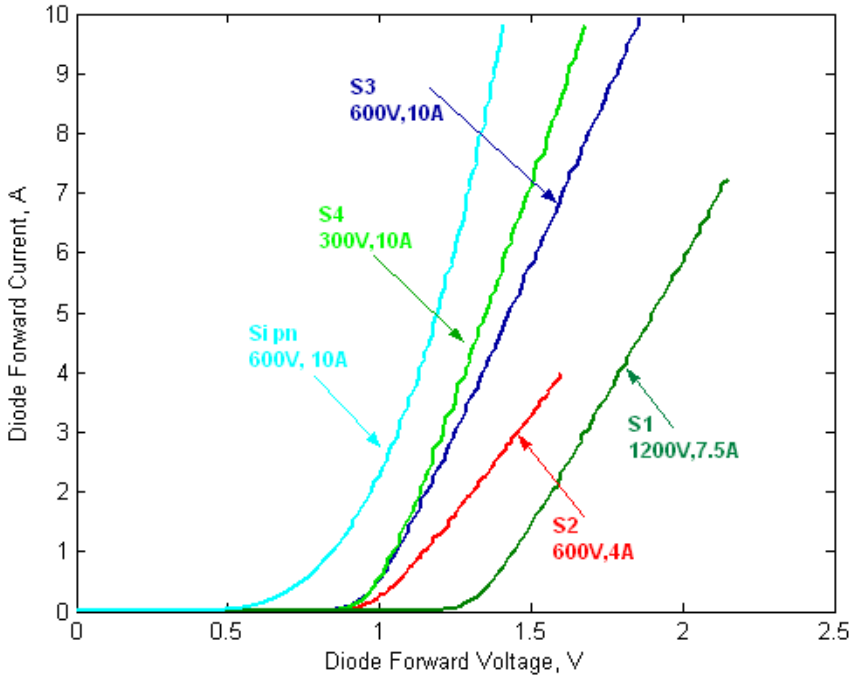

Fig. 1. *i-v* characteristics of Si pn and SiC Schottky diodes.

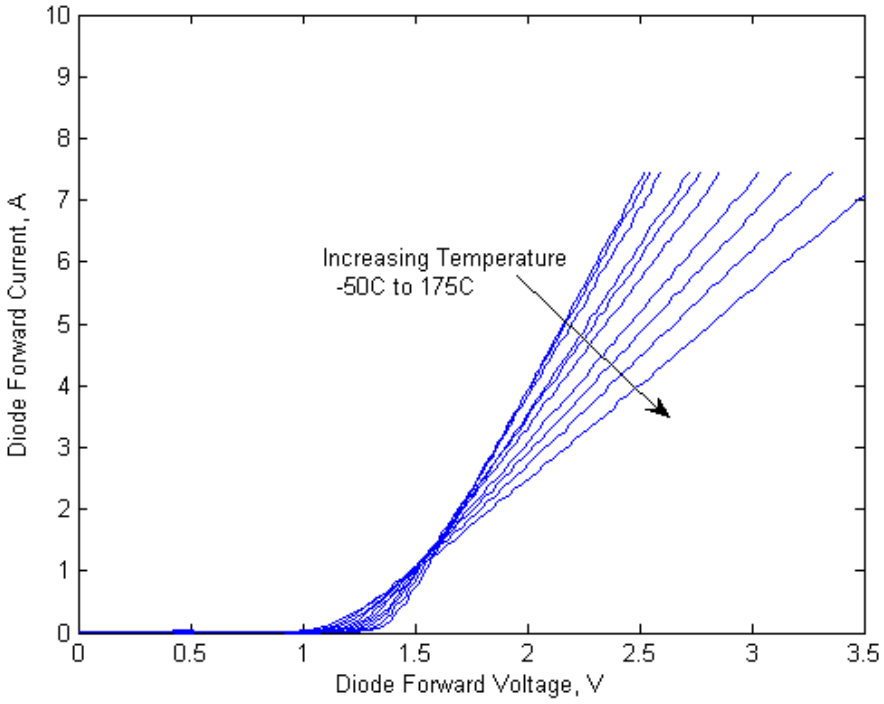

Fig. 2. *i-v* characteristics of S1 at different operating temperatures.

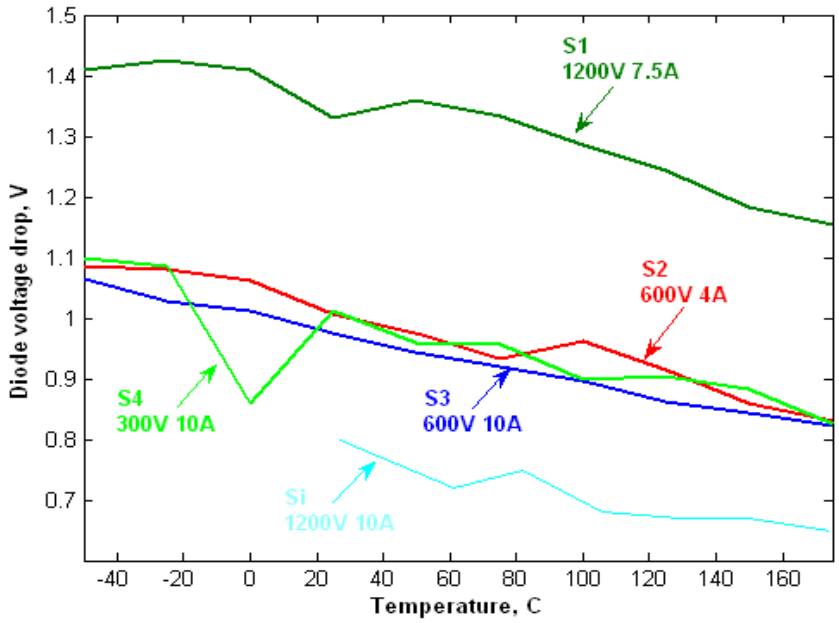

Fig. 3. V_d for Si and SiC diodes at different operating temperatures.

The $R_{on,sp}$ for the diodes is calculated from the slope of the *i-v* characteristics and is plotted for different temperatures shown in Fig. 4. The on-state resistance varies for each diode because of the difference in blocking voltages. The $R_{on,sp}$ for majority carrier devices can be expressed as a function of breakdown voltage and critical electric field:

$$R_{on,sp} = \frac{4V_B^2}{\varepsilon (E_c)^3 \mu_n}, \quad (1)$$

where ε is the permittivity (C/V·cm), E_c is the breakdown field (V/cm), and μ_n is the electron mobility(cm^2/V·s). To withstand high breakdown voltages, blocking layer thickness is increased and doping concentrations are reduced. These changes result in increased series resistance of the diode. Hence, device S1 rated at 1200 V, 7.5A has more on-resistance than S3 and S4. The resistance varies with forward current density and the area of the device. It is evident from Fig. 5(a) and 5(b) that S2 and S3 with the same voltage and different current ratings have different on-state resistances.

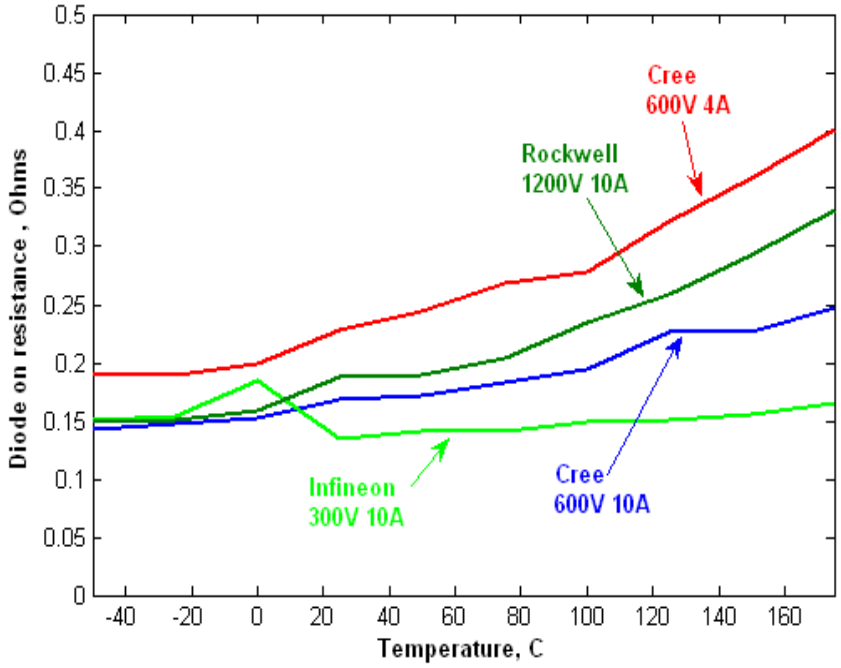

Fig. 4. R_d for Si and SiC diodes at different operating temperatures.

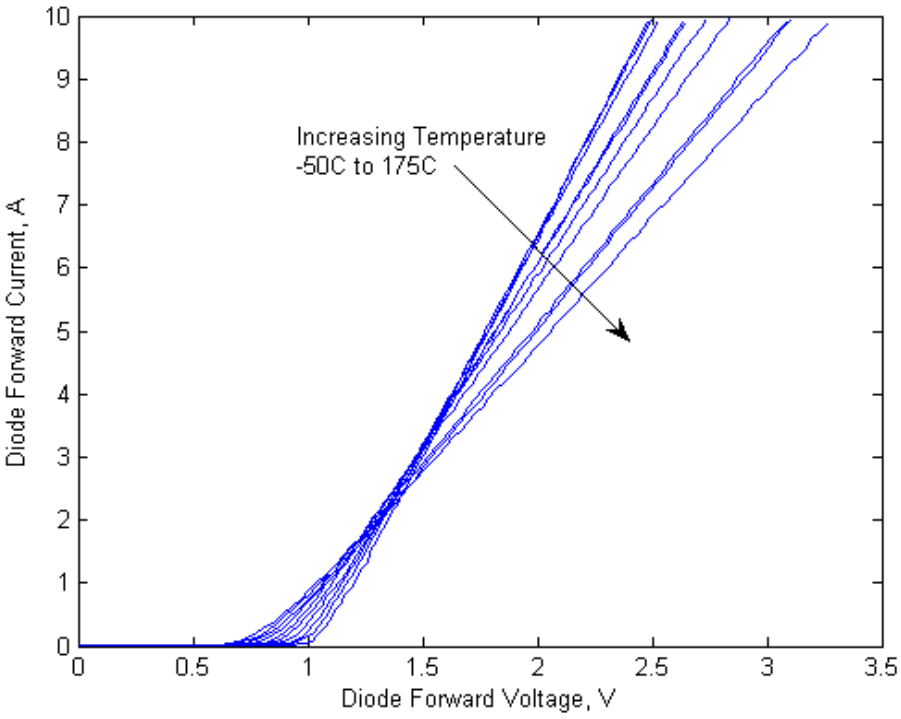

Fig. 5(a). *i-v* characteristics of S3 at different operating temperatures.

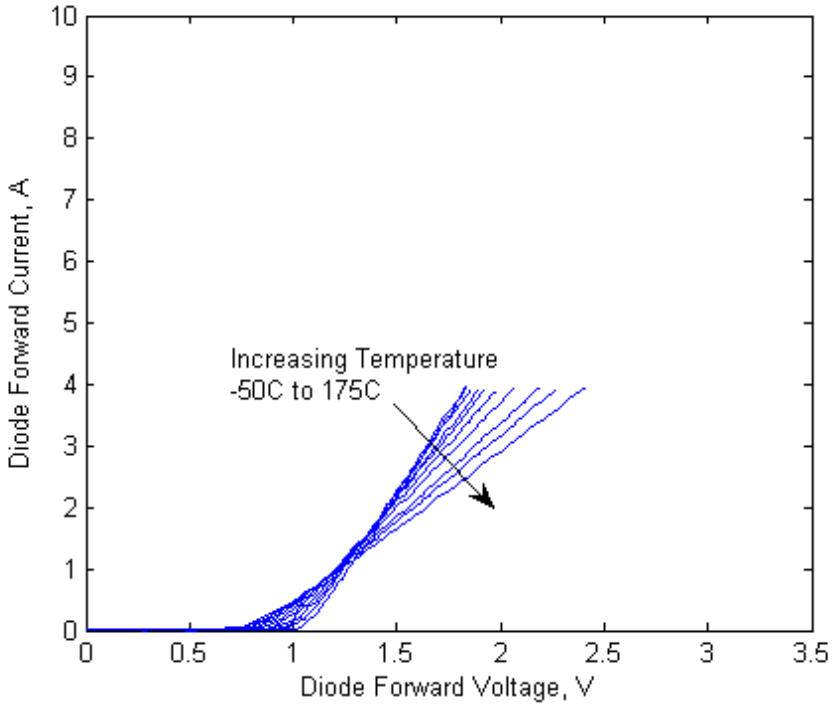

Fig. 5(b). *i-v* characteristics of S2 at different operating temperatures.

2. Dynamic Characteristics

A buck chopper with a clamped inductive load was built for evaluating the switching characteristics of the diodes. An IGBT was used as the main switch; it was switched at 1 kHz with a 30% duty ratio.

The energy losses for various forward peak currents and different temperatures are shown for an Si diode and diode S4 in Fig. 6. The energy losses for the Si diode increase with temperature as a result of the increase in peak reverse recovery current. The switching losses for diode S4 are almost independent of the change in temperature. The reverse recovery current is dependent on the charge stored in the drift region. A SiC Schottky diode has no stored charge, as it is a majority carrier device, and hence has virtually constant turn-on energy loss for a wide temperature range. The negligible reverse recovery current reduces the oscillation due to ringing and eliminates the use of a snubber for limiting the reverse recovery. The result is increased efficiency as the losses are minimized. In addition, the reduced blocking layer thickness, due to the wide bandgap of the SiC material, contributes to the low switching losses of the SiC diode.

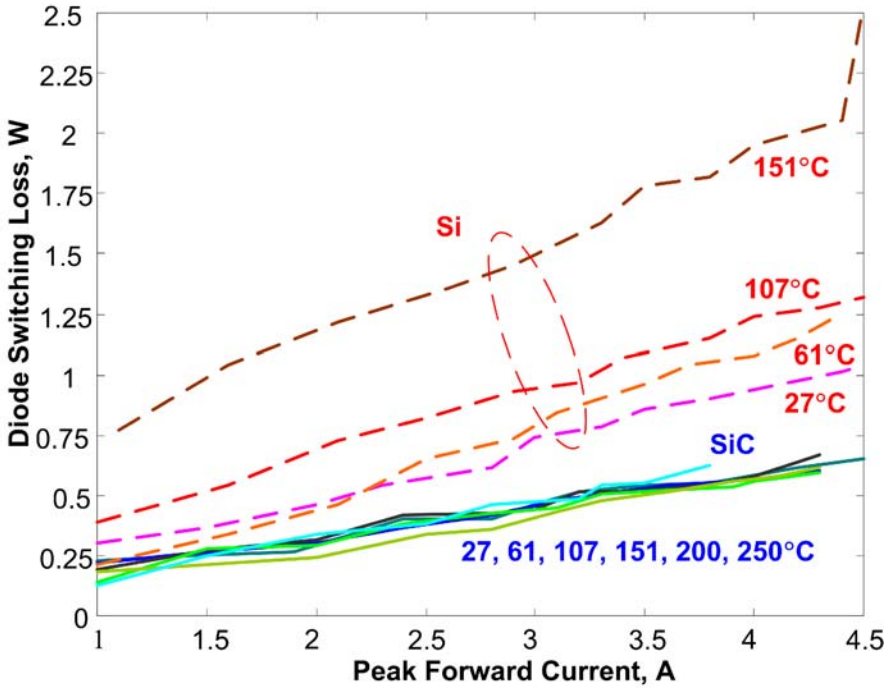

Fig. 6. Peak reverse recovery values with respect to forward current at different operating temperatures.

SiC VJFET

1. Static Characteristics

A JFET is a unipolar device and has several advantages compared with other FET devices. A JFET has low voltage drop and higher switching speeds. A JFET is free from gate oxide interface problems like MOSFETs. JFETs are normally-on devices and conduct even though no gate voltage is applied. Thus a JFET requires a protection circuit for system power failures to prevent a short circuit. These diodes are faster, as they are SiC diodes; however, these diodes have significant forward voltage drop as a result of the WBG of SiC. The VJFET can be used in high-current and H.V. applications, unlike Si JFETs, because of the vertical structure and because of the intrinsic properties of SiC. A normally-on SiC VJFET rated at 1200 V and 2 A was tested to study the high-temperature behavior of the device. The forward characteristics for different temperatures are also shown in Fig. 7. The on-resistance of the VJFET increases from 0.36 at −50ºC to 1.4 at 175ºC, as shown in Fig. 8. The values of the on-resistance are high. However, these devices have a positive temperature coefficient, which enables easy paralleling of devices. The on-state resistance would decrease with parallel devices.

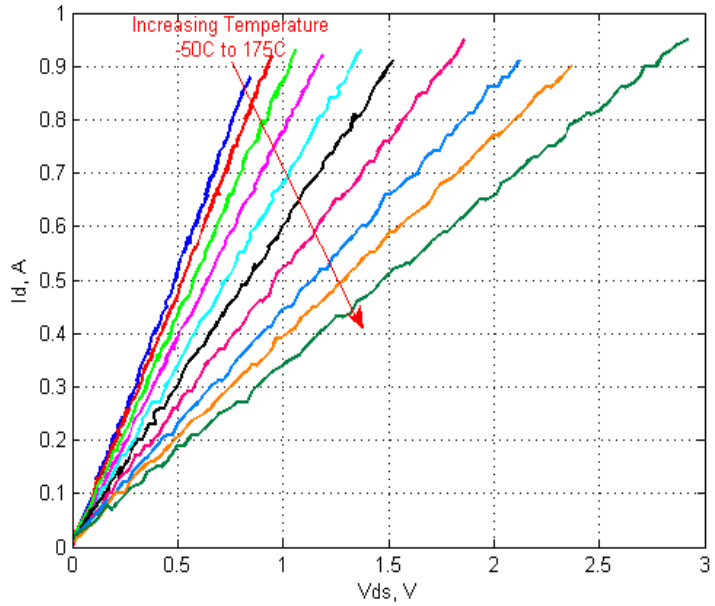

Fig. 7. *i-v* characteristics of SiC VJFET at different temperatures.

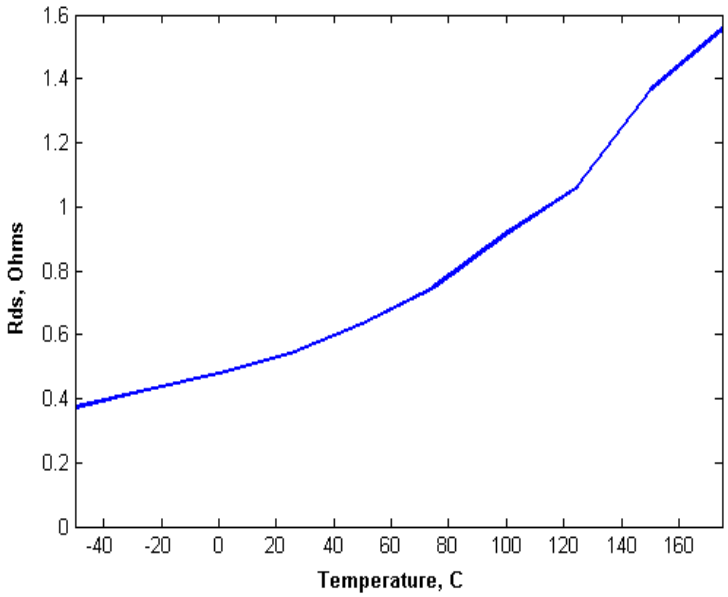

Fig. 8. On resistance of SiC VJFET at different temperatures.

2. Transfer Characteristics

The transfer characteristics of different VJFET samples are shown in Fig. 9. The negative gate pinch-off voltage required to turn off the device does not vary much with an increase in drain-to-source voltage, V_{ds}. This pinch-off voltage determines the voltage requirement of the gate drive circuit. A gate drive was developed for the VJFET for HF and high-temperature operation. Based

on the transfer characteristics, the gate drive was designed for a voltage of –30 V, and 250-kHz operation was achieved for peak gate currents of 0.8 A.

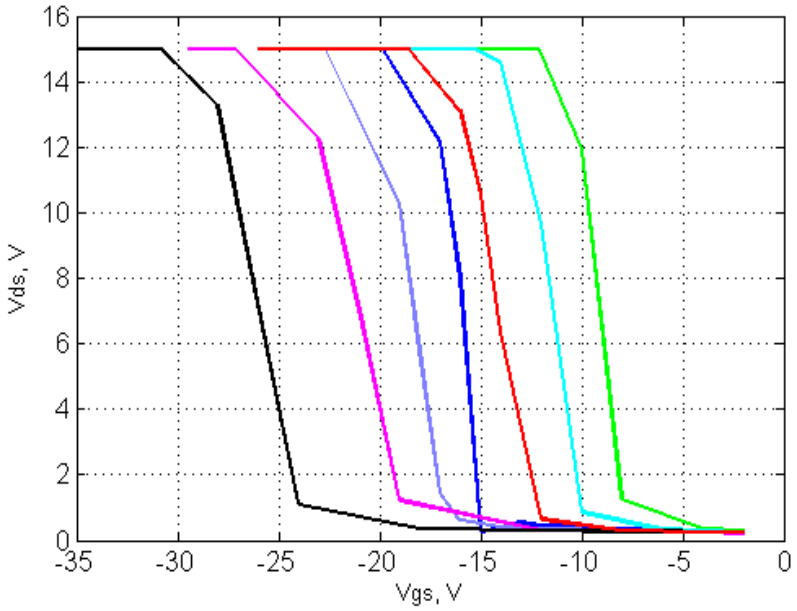

Fig. 9. Transfer characteristics of SiC VJFET.

3. Gate Drive Requirements

SiC VJFET switches can be operated at higher switching frequencies and higher temperatures; therefore, they have different gate drive requirements than traditional Si power switches. Since SiC VJFETs are normally-on devices, they can be turned off by applying a negative voltage that is higher than what a typical Si switch requires. One of the important parameters in gate drive design for VJFETs is that they have a large stray capacitance between the gate and the other terminals. The total input capacitance of a VJFET, C_{iss}, determines the current required by the gate and the rate at which the applied gate voltage is built across the gate and source terminals. These capacitances are caused by the geometrical design of the device and by the parasitic body diode. Therefore, the circuit that drives the gate terminal should be capable of supplying a reasonable current so the stray capacitance can be charged up as quickly as possible. The gate drive was tested with several capacitors as loads before the driver circuit was tested with the device. When these are operated at HFs, they also need high-peak gate currents. Total input capacitance, C_{iss}, of a VJFET determines the current required by the gate and the rate at which the applied gate voltage is built across the gate and source terminals.

A SiC VJFET gate driver was built to satisfy these conditions and to use most of the SiC device benefits. The main objective of the project was to build a gate driver using commercially available gate driver chips. Based on transfer characteristics, the gate drive was designed for a voltage of –30 V because the pinch-off voltage for most of the samples tested was –20 V. The gate series resistance was changed to achieve HF operation. A 250-kHz operation was achieved with a resistance of 5.4 ohms and a peak gate current of 0.8A. There are several gate drive circuits designed for SiC VJFETs using discrete devices. In this circuit design, a commercial gate

drive, IC chip IXDD414, is used, making it more reliable in operation. These gate drives can also be applied to SiC MOSFETs by redesigning the passive components and modifying the output voltage polarity. The gate voltage and current waveforms are shown in Fig. 10. The switching waveforms of the VJFET are shown in Fig. 11.

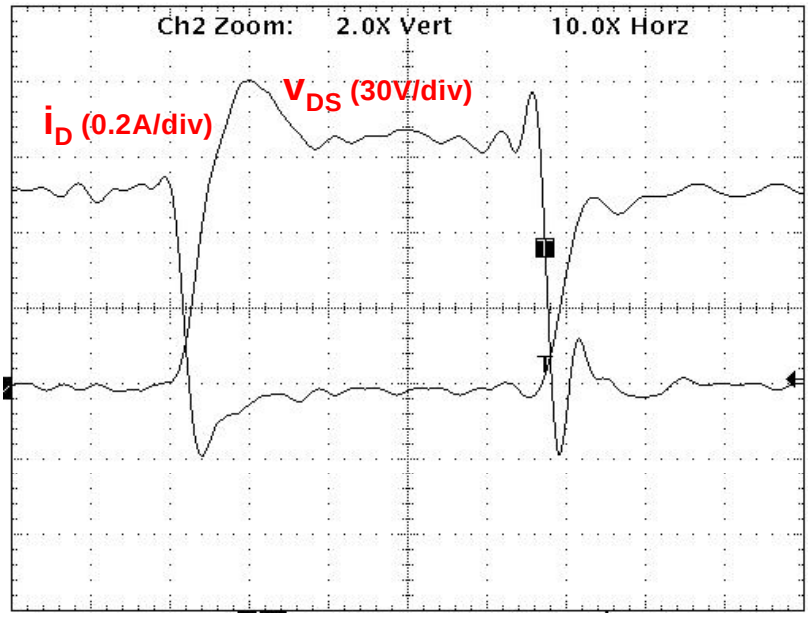

Fig. 10. Switching waveforms of SiC VJFET at 250 kHz.

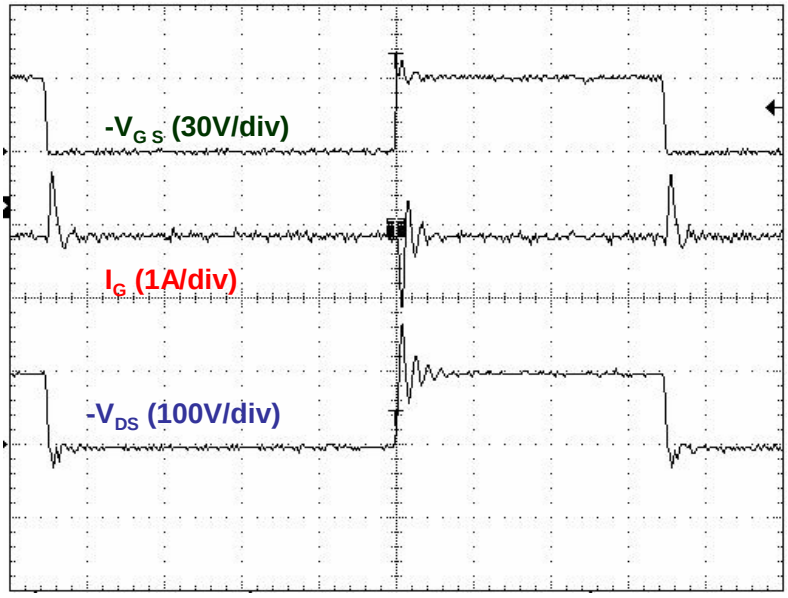

Fig. 11. Gate voltage and current waveforms at 250 kHz.

Subcontracts

In concert with this project, two subcontracts were awarded, one to CREE and one to Rockwell Scientific.

1. CREE Subcontract

CREE has built 600-V/75-A SiC Schottky diodes on 4-SiC wafers and has delivered 100 of them to Semikron to replace the Si pn diodes in the AIPM. The rest of the diodes have been sent to ORNL for further testing. Figure 12 shows one of the wafers. Figure 13 shows one of these diodes packaged by CREE.

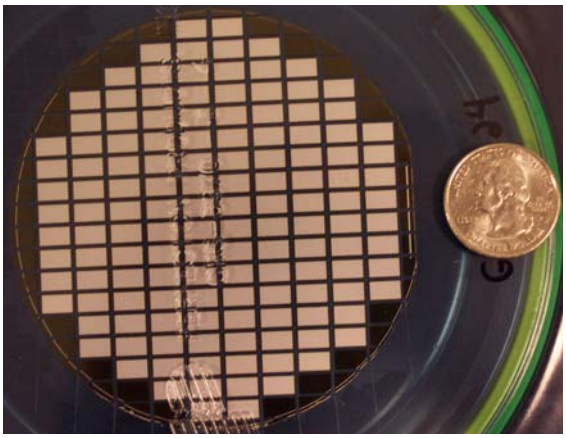

Fig. 12. 600 V/75A SiC Schottky diodes on a wafer next to a quarter.

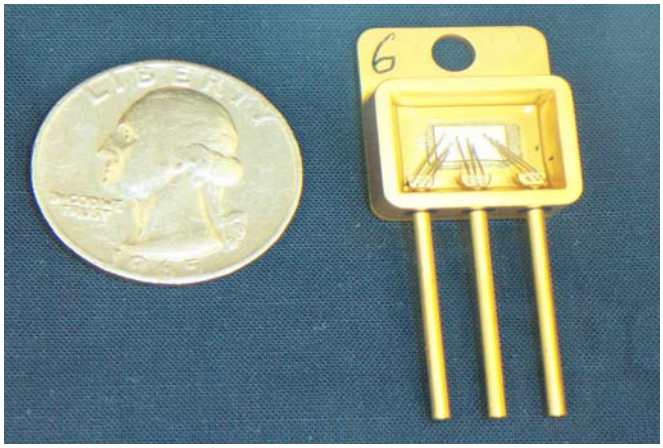

Fig. 13. A 600-V/75-A SiC Schottky diode next to a quarter.

2. Rockwell Scientific Subcontract

Rockwell Scientific is building a 7.5-kW all-SiC inverter to be delivered to ORNL in December 2004. The inverter will consist of SiC VJFETs and Schottky diodes. The resulting all-SiC inverter will be compared with similar all-Si inverters to show the impact of SiC power devices.

Figure 14 shows an all-SiC Rockwell Scientific inverter that is similar to the one to be delivered to ORNL.

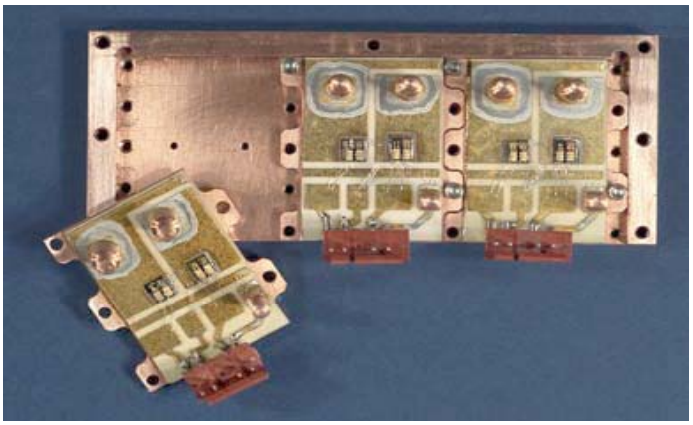

Fig. 14. All-SiC Rockwell Scientific inverter.

Conclusions

The performances of some SiC Schottky diodes and an SiC JFET have been characterized within a temperature range. These characteristics will eventually be used to develop more realistic system-level models to show the system-level benefits of SiC devices.

SiC switching devices such as the SiC JFET have different gate driver requirements. This work, as opposed to the other work in the literature, has identified a commercially available gate driver chip for Si MOSFETs and IGBTs and has shown how to modify it to drive SiC VJFETs. However, further research is required for higher-temperature operation of these gate drivers.

B. Integrated dc-dc Converter for Multi-Voltage Bus Systems in HEVs and Fuel Cell Vehicles

Gui-Jia Su
Oak Ridge National Laboratory
National Transportation Research Center
2360 Cherahala Boulevard
Knoxville, TN 37932
Voice: 865-946-1330; Fax: 865-946-1262; E-mail: sugj@ornl.gov

DOE Technology Development Manager: Susan A. Rogers
Voice: 202-586-8997; Fax: 202-586-1600; E-mail: Susan.Rogers@ee.doe.gov

ORNL Program Manager: Laura D. Marlino
Voice: 865-946-1245; Fax: 865-946-1262; E-mail: marlinold@ornl.gov

Objectives

- Develop low-cost, integrated dc-dc converter topologies for 14-V/42-V/H.V. (200–500 V) bus systems for hybrid electric vehicles (HEVs) and fuel cell vehicle applications.
- Demonstrate prototypes and provide testing data for performance and cost evaluation.
- Analytically and experimentally investigate the latest commercially available power devices to evaluate the benefits that they can bring to dc-dc converters.

Approach

- Employ an integrated converter topology to minimize the number of switches.
- Employ soft switching and synchronous rectification techniques to improve efficiency and reduce electromagnetic interference (EMI).
- Increase switching frequency using the latest metal oxide semiconductor field effect transistors (MOSFETs) and insulated gate bipolar transistors (IGBTs) and reduce the number of switches to reduce volume and increase power density.

Accomplishments

- Developed an integrated dc-dc converter topology that employs only four switches while providing a triple voltage bus (14-V/42-V/H.V.).
- Designed and fabricated a 2-kW prototype converter.
- Through simulation study, validated the duty ratio and phase-angle–based power flow control and confirmed it by preliminary testing results.

Future Direction

- To further reduce cost, examine modified topologies with fewer components and then design, fabricate, and test new prototypes.
- Investigate alternative power circuit assembly techniques to address fabrication issues.

- Continuously monitor the latest power devices, including H.V. MOSFETs with significantly reduced on-resistance and high-speed IGBTs, update the device database, and evaluate the benefits that they bring to dc-dc converters.

Publications

1. "A New ZVS Bi-directional DC-DC Converter for Fuel Cell and Battery Applications," pp. 54–65 in *IEEE Trans. on Power Electronics*, **19**(1), January 2004.
2. "A Low Cost, Triple-Voltage Bus DC/DC Converter for Automotive Applications," accepted to the *IEEE Applied Power Electronics Conference and Exposition* (APEC) in Austin, Texas, March 6–10, 2005.

Technical Discussion

Introduction

The 14-V electrical system currently used in automobiles has reached its limits of capability and cannot meet the demands of future electrical loads or satisfy the desire for replacing more engine-driven mechanical and hydraulic systems with electrical systems to increase efficiency. Therefore, 42-V systems have been proposed to cope with increasing electrical loads. During the transition to the 42-V system, most automobiles are expected to employ a 14-V/42-V dual-level voltage system, in which a bi-directional dc-dc converter is required to connect the two voltage networks. Additionally, most battery-powered HEVs employ a HV (200–500 V) bus for the traction motor drive. In HEVs with a 42-V alternator, a dc-dc converter supplied from the 42-V bus may be used to charge the HV battery as shown in Fig.1(a). Also, for HEVs having a generator directly connected on the HV bus, a dc-dc converter is typically required to charge the 14-V and/or 42-V batteries.

Fuel-cell–powered vehicles will require a bi-directional dc-dc converter to interconnect the fuel-cell–powered HV bus and the low-voltage buses for vehicle auxiliary loads. For these reasons, both the 14-V and 42-V buses may be employed to power vehicle accessory loads, as shown in Fig.1(b). An energy storage device is also required for fuel cell start-up and for storing the energy captured by regenerative braking, because the fuel cells lack energy storage capability. One way to accomplish this is to use the vehicle 14-V or 42-V battery with a bi-directional dc-dc converter. During vehicle starting, the HV bus is boosted to around 300 V by the dc-dc converter drawing power from the 14-V or 42-V battery. This HV bus then supplies power for the fuel cell compressor motor expanding unit controller and brings up the fuel cell voltage, which in turn feeds back to the HV bus to release loading from the battery.

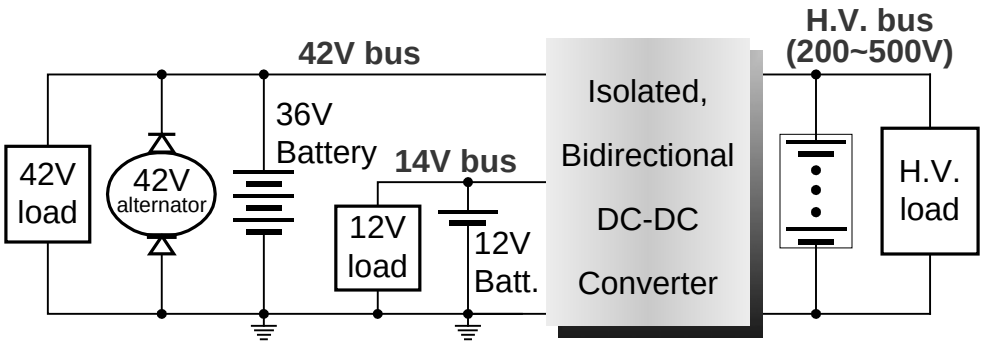

(a) HEVs

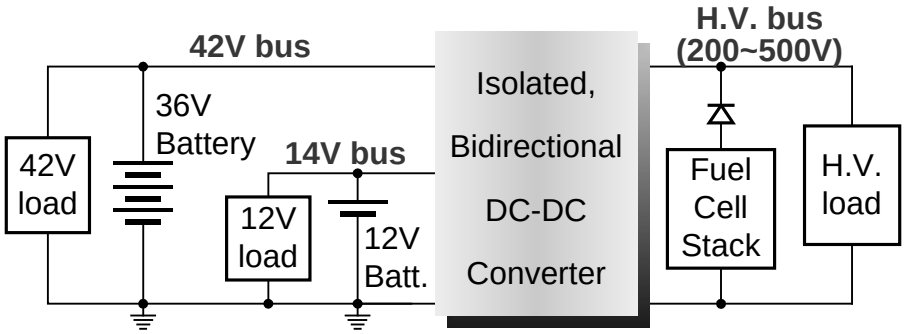

(b) Fuel cell powered vehicles

Fig. 1. A dc-dc converter interconnecting 14-V/42-V/H.V. bus nets in HEVs and fuel cell-powered vehicles.

In summary, a triple-voltage bus (14-V/42-V/H.V.) system will likely be employed in HEVs and fuel-cell–powered vehicles, as shown in Fig.1, before all vehicle auxiliary electrical components are moved to the 42-V bus. While dc-dc converters are available to interconnect any two of the buses, to reduce component count, size, cost, and volume, it is desirable to employ an integrated dc-dc converter to interconnect the three voltage buses instead of using two separate converters. Aside from bi-directional power control capability, the converter needs to provide galvanic isolation between the low-voltage and HV buses to meet safety requirements. Further, soft switching is preferred over hard switching because of the reduced level of EMI and switching losses.

In this project, a low-cost, soft-switched, isolated bi-directional dc-dc converter is developed for interconnecting the three bus nets. The converter is a modified version of the dual half-bridge topology proposed in previous development programs. It uses snubber capacitors and transformer leakage inductance to achieve zero-voltage-switching (ZVS). Therefore, no extra resonant components are required for ZVS, further reducing component count. The inherent soft-switching capability and the low component count of the converter allow high power density, efficient power conversion, and compact packaging. A novel power flow control scheme based on a combined duty ratio and phase shift angle control are also presented. A 2-kW prototype has been designed, built, and tested. Simulation study and preliminary experimental data have verified the proposed power flow control scheme. Extensive testing is planned to provide data for performance and cost evaluation.

dc-dc Converter for Triple Voltage Buses

Description of the dc-dc Converter

Figure 2 shows a schematic of the dc-dc converter, which mainly consists of dual half-bridge inverters/converters and a HF transformer, *Tr*. The HF transformer provides the required galvanic isolation and voltage level matching between the 14-V and 42-V buses and the HV bus, while the 14-V and 42-V buses share a common ground. The leakage inductance of the transformer is used as the intermediate energy storing and transferring element between the two low-voltage buses and the HV net. The snubber capacitors, C_{r1}~C_{r4}, resonate with the transformer leakage inductance to provide ZVS.

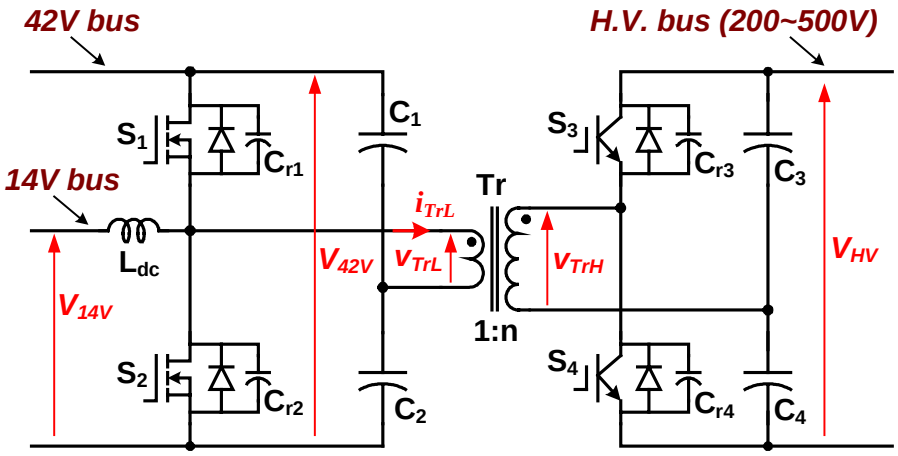

Fig. 2. Schematic of the soft-switched bi-directional dc-dc converter.

Duty ratio control is used for power flow control between the 14-V and 42-V buses, making the two bus voltages, V_{14V} and V_{42V}, track each other by $V_{14V} = d \bullet V_{42V}$, where d is the duty ratio of the switches S_1 and S_3. For 14-V/42-V systems, the duty ratio is fixed at $d = 1/3$ for normal operation and can be changed to adjust the state of charge of the low-voltage batteries if necessary. In addition, a phase shift angle, ϕ, between the transformer primary and secondary voltages is employed for power flow control between the 42-V and HV buses (Fig.3), where d = 1/3. The power transferred through the transformer can be expressed by

$$P = \frac{V_{42v} V_{HV}}{n} \cdot \frac{\phi}{2\pi f_{sw} L_s} \cdot [\frac{2}{9} - \frac{\phi}{4\pi}] \ , \tag{1}$$

where n = transformer turns ratio, Ls = transformer leakage inductance, fsw = switching frequency.

For a given design, the maximum power is determined by

$$P_{\max} = \frac{V_{42v} V_{HV}}{n} \cdot \frac{2}{81 f_{sw} L_s} \text{ at } \phi_{P_{\max}} = \frac{4\pi}{9} \ . \tag{2}$$

Figure 4 plots the power versus the phase shift angle at different voltage levels of $V_{H.V.}$ with n = 8, Ls = 0.16µH, fsw = 40 kHz, V_{42v} = 42-V for a prototype design.

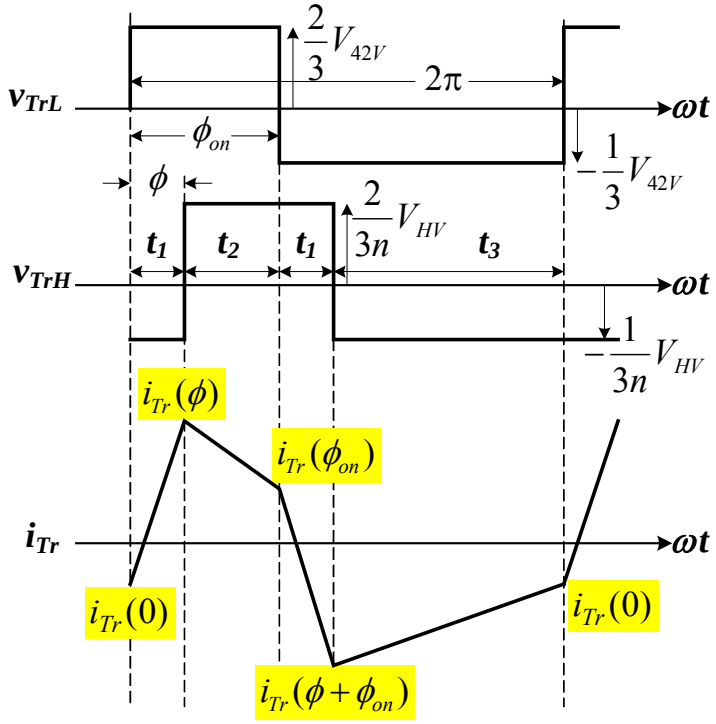

Fig. 3. Ideal transformer voltage and current waveforms illustrating power flow control between the 42-V and HV buses at d = 1/3.

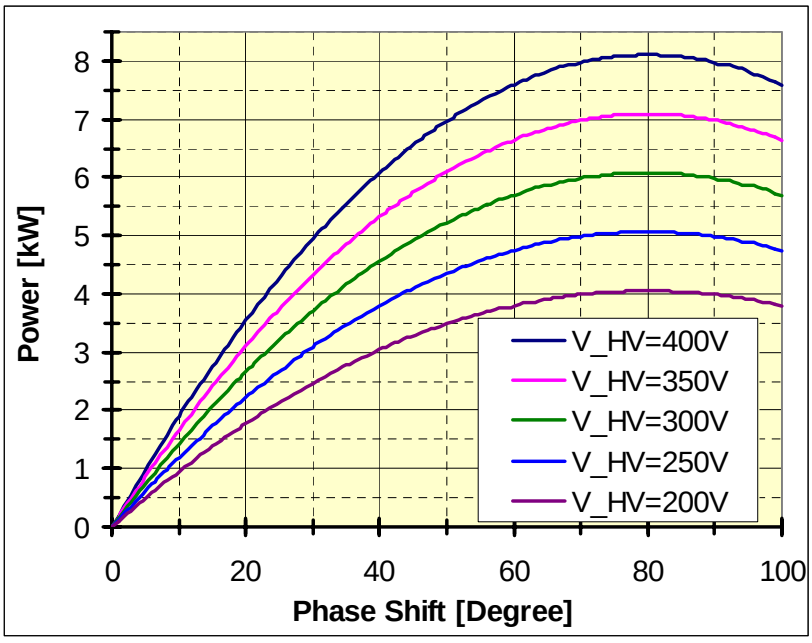

Fig. 4. Power vs. phase shift angle at various levels of $V_{H.V.}$ (n = 8, Ls = 0.16µH, fsw = 40 kHz, V_{42v} = 42V).

Simulation and Experimental Results

A 2-kW prototype was designed, built and tested to verify the power flow control scheme and to evaluate its performance. Specifications of the prototype are listed below.

- Rating: 2 kW continous/5 kW maximum
- Efficiency: >92% over a wide load range
- Targeted switching frequency: 40–50 kHz

A detailed circuit simulation was first performed to verify the design goal, which is to guarantee at least 2 kW power can be transferred through the transformer at a voltage range of 200–400 V from the HV bus. Figure 5(a) and (b) shows simulation results where power is transferred from the low-voltage buses to the HV net; in 5(a) at $V_{H.V.}$ = 200-V, 2.1 kW is provide to the HV bus, while in 5(b) at $V_{H.V.}$ = 400-V, power is increased to 5.1 kW. Figure 6(a) and (b) shows simulated waveforms when the power flow is reversed. The simulation results confirm the design goal of the power ratings.

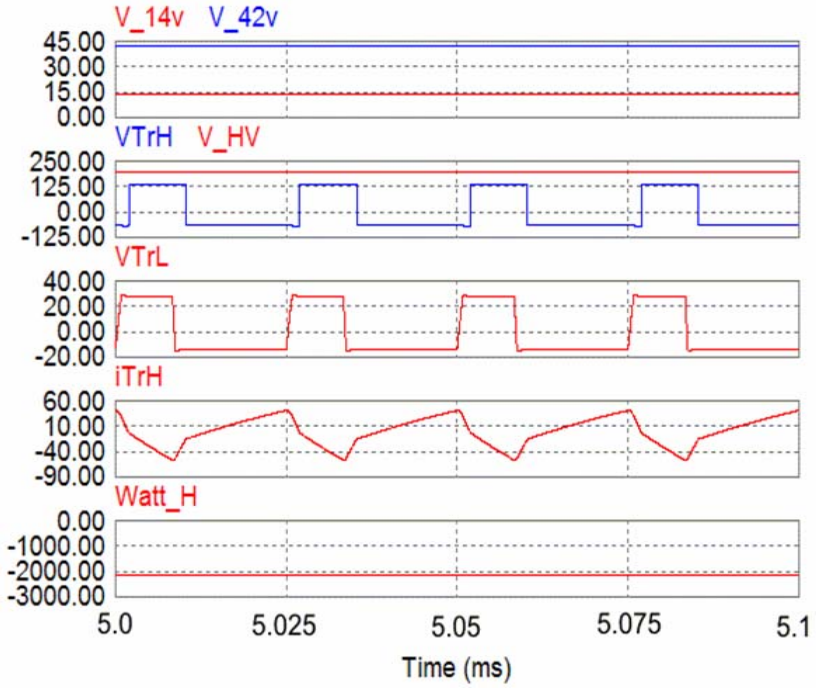

(a) $V_{H.V.}$ = 200-V, power transferred to the H.V. bus: 2.1 kW.

Fig. 5. Simulation results showing power is transferred from the low-voltage buses to the H.V. net.

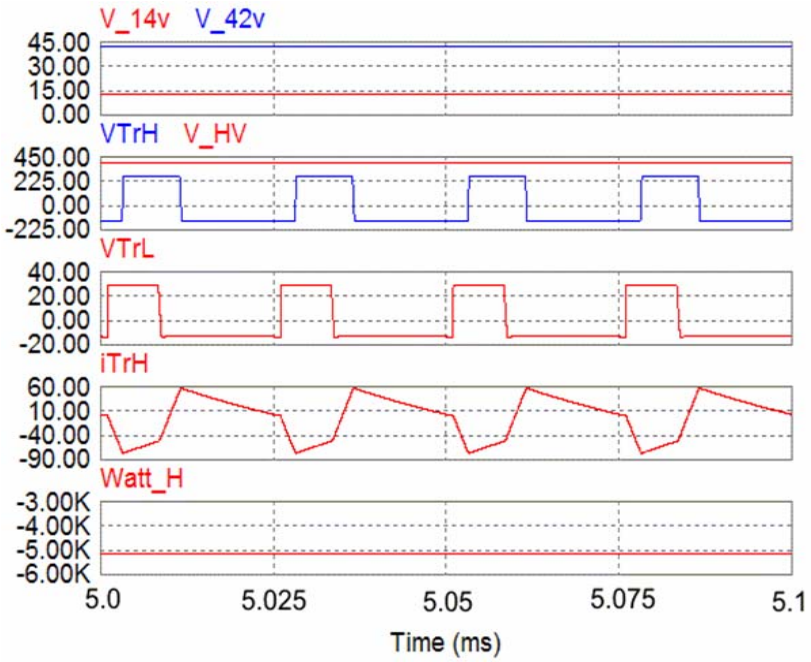

(b) $V_{H.V.}$ = 400-V, power transferred to the H.V. bus: 5.1 kW.

Fig. 5. Simulation results showing power is transferred from the low-voltage buses to the H.V. net (cont'd).

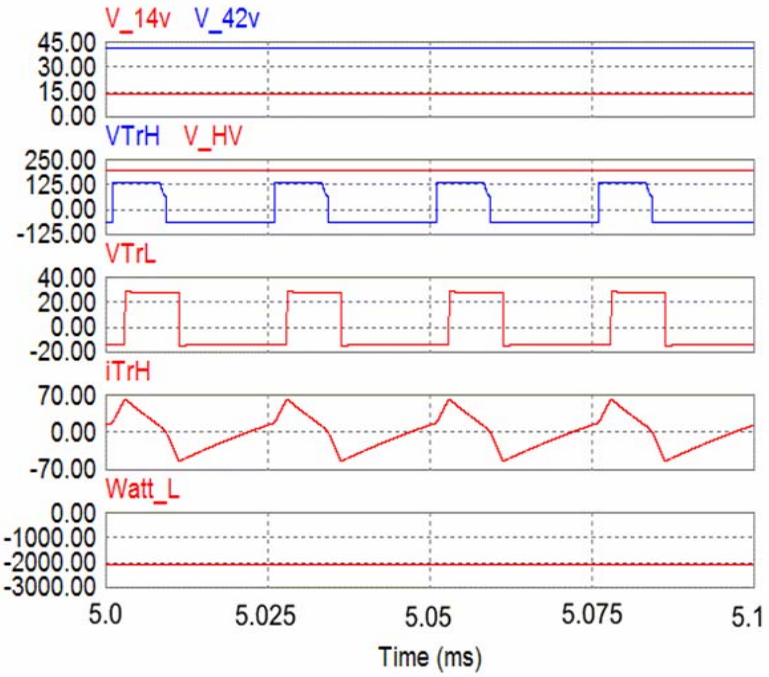

(a) $V_{H.V.}$ = 200-V, power transferred to the low-voltage buses: 2.0 kW.

Fig. 6. Simulation results illustrating power is transferred from the H.V. net to the low-voltage buses.

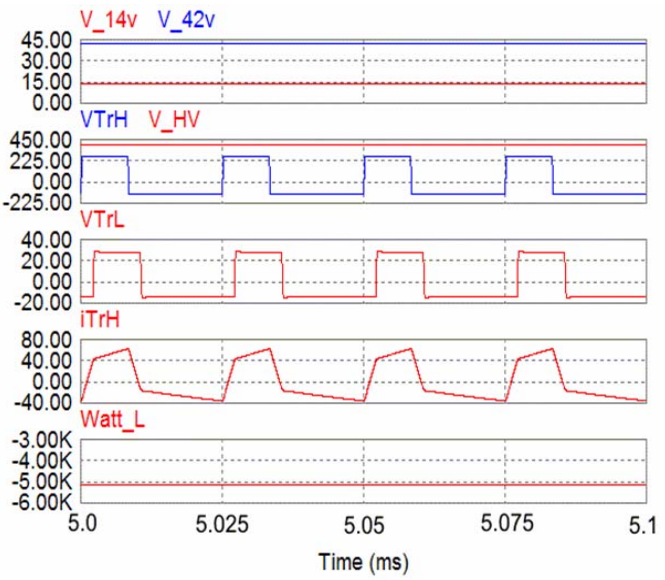

(b) $V_{H.V.}$ = 400-V, power transferred to the low-voltage buses: 5.1 kW.

Fig. 6. Simulation results illustrating power is transferred from the H.V. net to the low-voltage buses (cont'd).

To prove the concept of the combined duty ratio and phase shift angle control scheme for power flow management among the three buses, initial testing was conducted using the existing dual voltage (14-V/300-V) converter developed in previous projects. The test was done at 60% of the rated power with a switching frequency of 20 kHz towing to a limited coolant flow. Figure 7 shows an oscillogram of the test results for a duty ratio about 60%. Because the duty ratio is not equal to 50 %, the positive and negative voltage amplitude of the transformer voltages, v_{TrL} and v_{TrH}, not the same, clearly confirming the duty ratio control scheme.

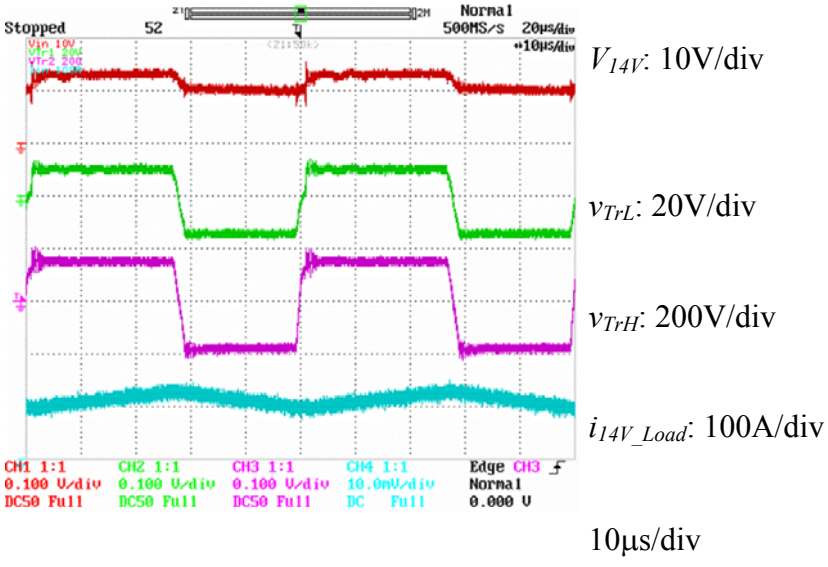

Fig. 7. Proof-of-concept testing waveforms at a load power of 1.2 kW in high-to-low power transfer using the existing dual-voltage (14-V/300-V) converter developed in previous projects.

A 2-kW prototype was designed and built based on the analytical simulation and preliminary proof-of-concept testing results. Figure 8 shows a photo of the prototype, which is laid on a 0.375-in. liquid-cooled heat sink with a footprint 7.5 in. wide by 13.5 in. long. It was intentionally laid loosely to provide easy probing access.

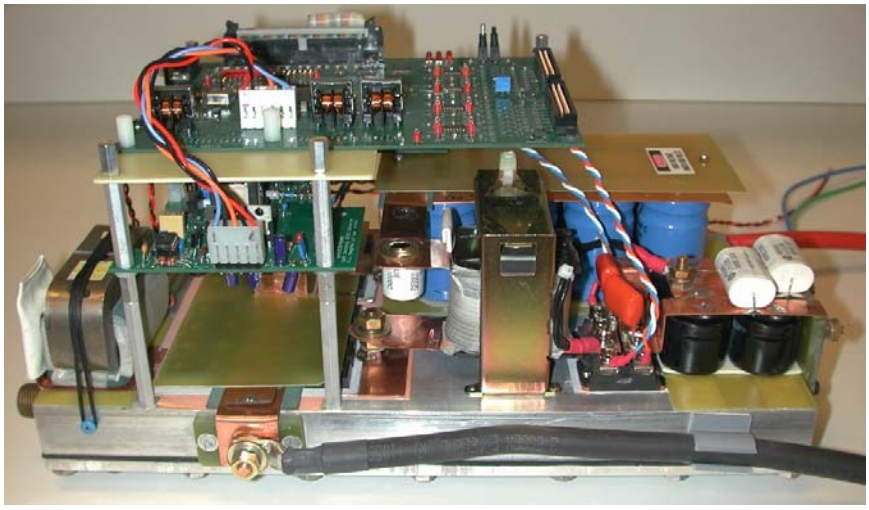

Fig. 8. Photo of the prototype.

The HV switches are implemented with two CoolMOS MOSFETs made by IXYS, which are rated at 600 V/50 A with an on-resistance of 35 mΩ. High-speed IGBTs will also be tested. The low-voltage switches are MOSFETs made by International Rectifier, rated at 75 V/90 A with an on-resistance of 4.5 mΩ.

The inductor was fabricated using a Metglas^{TM} amorphous, C-core (AMCC-32) with the following specifications:

- Winding: 16-mil-thick copper foil
- Inductance: 10 μH
- Current rating: 100 A

The HF transformer was fabricated using Ferroxcube E-cores, E65/32/27. Two different grades of soft ferrite, 3F3 and 3C94, will be tested for the transformer core. The primary winding uses a 10-mil-thick copper foil and has 2 turns, while the secondary winding uses 3 litz wires of 16 AWG in parallel and has 16 turns. The two windings are interleaved to minimize the leakage inductance.

Figure 9 shows an initial test result for 42-V to 14-V and HV power transfer, where the duty ratio is set at 1/3 and the switching frequency at 40 kHz. More extensive testing is under way.

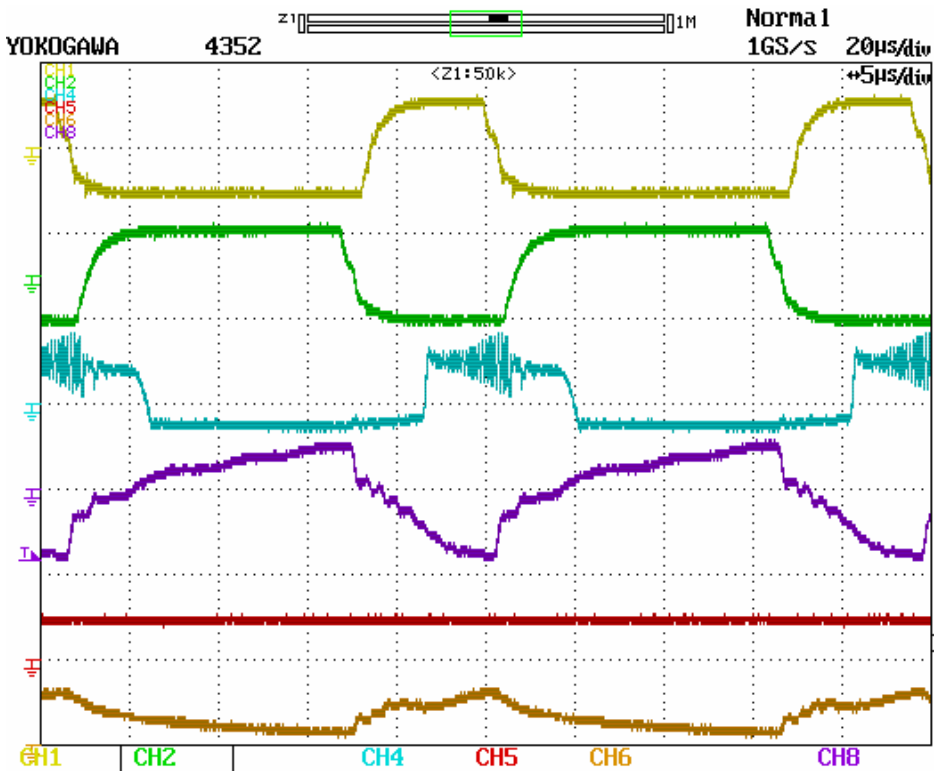

Fig. 9. Initial testing waveforms for 42-V to 14-V and H.V. power transfer.

Conclusions

The proposed integrated dc-dc converter for triple-voltage-bus (14-V/42-V/H.V.) systems for HEVs and fuel cell vehicles applications has the following features:

- Uses only four switching devices, leading to significant cost savings and higher power density.
- Has soft switching and synchronous rectification, contributing to high efficiency and low EMI.
- Requires no auxiliary circuit or complex control for soft switching.
- Has flexible power flow management owing to the capability for power transfer among all three-voltage buses, employing the combined duty ratio and phase shift angle control scheme.

Simulation and preliminary testing results on a 2-kW prototype confirmed the operating principles of the converter. Additional extensive testing will provide data for performance and cost analysis.

C. Integrated Inverter for HEVs and Fuel Cell-Powered Vehicles

Gui-Jia Su
Oak Ridge National Laboratory
National Transportation Research Center
2360 Cherahala Boulevard
Knoxville, TN 37932
Voice: 865-946-1330; Fax: 865-946-1262; E-mail: sugj@ornl.gov

DOE Technology Development Manager: Susan A. Rogers
Voice: 202-586-8997; Fax: 202-586-1600; E-mail: susan.rogers@ee.doe.gov

ORNL Program Manager: Laura D. Marlino
Voice: 865-946-1245; Fax: 865-946-1262; E-mail: marlinold@ornl.gov

Objectives

- Develop integrated power conversion topologies to reduce the component count, size and cost of power electronics systems for traction drive and compressor motor drives in HEVs and fuel cell–powered vehicles.
- Produce inverter hardware and testing data that will enable quantitative evaluation of the integrated inverter drive system's ability to further reduce the cost and volume of the power electronics system beyond meeting FreedomCAR electric propulsion system technical goals.

Approach

- The compressor drive is integrated into the traction motor drive to reduce cost by reducing the number of components. Components are shared with the main inverter, the switching power semiconductor devices, dc bus filter capacitors, gate drive power supplies, and control circuit.

Accomplishments

- Developed an integrated traction and compressor drive system employing a five-leg inverter.
- Designed, fabricated, and successfully tested a prototype inverter with a three-phase induction motor (IM) and a two-phase compressor motor.
- For the compressor drive, reduced the inverter components including semiconductor switches and gate drive circuits by more than one-third.
- Incorporated the compressor drive into the traction motor controller through software, rather than having a separate control circuit, further reducing the cost.

Future Direction

- Design, fabricate, and test a new inverter prototype for PM motors.
- Develop low-cost position sensorless control of two-phase brushless dc (BLDC) motors for compressor drives to eliminate position sensors.

Publications

1. "A Five-Leg Inverter for Driving a Traction Motor and a Compressor Motor," pp. 117–123 in *Proceedings of the 8th IEEE Workshop on Power Electronics in Transportation* (WPET2004), Novi, Michigan, October 21–22, 2004.
2. "An Integrated Traction and Compressor Drive System for EV/HEV Applications," accepted to the *IEEE Applied Power Electronics Conference and Exposition* (APEC) in Austin, Texas, March 6–10, 2005.

Patents

1. *Integrated Inverter for Driving Multiple Motors/Generators*, ORNL Invention Disclosure—ID 1316, S-101905.

Technical Discussion

Background

Because of their superior performance over the conventional engine belt-driven counterparts, electric motor-driven compressors for heating, ventilating, and air-conditioning (HVAC) are being deployed in automobiles with a 42-V power net and in HEVs where a H.V. bus is readily available. The advantages of electrically driven HVAC compressors are (1) highly efficient operation as the compressor speed can be adjusted independently of engine speed, unlike the conventional belt-driven unit, (2) flexible packaging, such as the installation location, is not restricted to the accessory drive side of the engine and, (3) leakage of the refrigerant into atmosphere is reduced because of the elimination of the rotating seals. In addition, the electric compressor enables HEVs to shut off the engine during vehicle stops or at low vehicle speeds when the engine power is not required. Moreover, fuel cell-powered vehicles require an electrically driven HVAC compressor.

To reduce the cost of the automotive accessory drives, two-phase inverter-fed IM drives were used to replace wound-field or PM dc motors for heating, ventilating, demisting, engine-cooling, and water-pumping applications in the automotive industry. Compared to a three-phase motor fed by a three-phase inverter, which typically requires six switches, a two-phase motor can be controlled by a lower-cost, two-leg inverter plus a split-capacitor leg as illustrated in Fig. 1. Unlike a semiconductor switch leg, the split-capacitor leg does not need an additional gate drive or control circuits. However, capacitors have their own drawbacks such as lower reliability and a short service lifespan. These drawbacks become aggravated by the harsh environments expected in EV/HEV applications. It is therefore desirable to eliminate the split-capacitor leg.

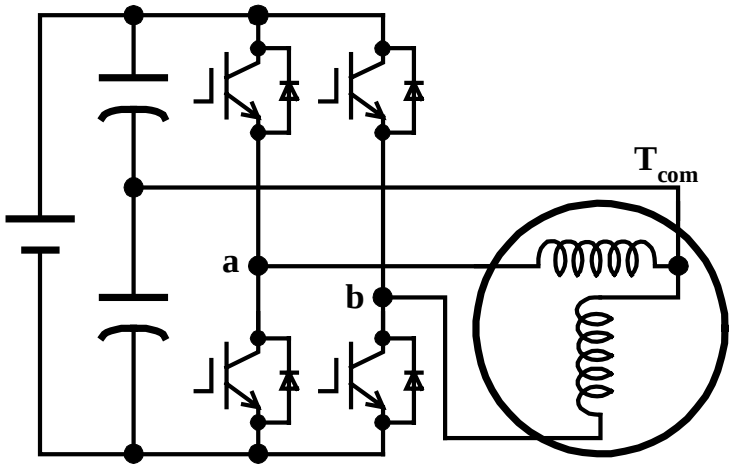

Fig. 1. A low-cost, two-phase motor drive using four switches and two capacitors.

In this project, an integrated inverter of five legs is developed for speed control of a three-phase traction motor and a two-phase compressor motor to further reduce the compressor drive cost. The two-phase inverter is first integrated into the three-phase inverter for the traction motor, so that dc bus filter capacitors, gate drive power supplies, and control circuit can be shared. Furthermore, the split-capacitor leg is eliminated by tying the common terminal of the two-phase motor to the neutral point of the three-phase traction motor. Integrating the compressor drive into the traction motor drive results in a lower-cost, smaller-volume drive system. Both simulation study and prototype testing are conducted to verify that the speed of the two motors can be controlled independently from each other.

Integrated Inverter Topology

Description of the Intergrated Inverter

Figure 2 shows the proposed five-leg integrated inverter for driving a three-phase traction motor and a two-phase compressor motor. The inverter consists of a dc source, V_{dc}, a filter capacitor, C_1, and five phase legs, *U*, *V*, and *W* for feeding the traction motor, and *a* and *b* for the compressor motor. The two-phase motor has two windings, phase-*a* and phase-*b*, and the two-phase windings are connected at one end to form a common terminal, T_{com}, with the other ends remaining separated to form two independent phase terminals, T_a and T_b.

The first three legs of the inverter, *U*, *V*, and *W* consisting of the switches S_1~S_6 form a three-phase main inverter, which through pulse-width modulation (PWM) provides three sinusoidal currents to the three-phase motor. The remaining two legs, *a* and *b*, are connected to the independent phase terminals of the two-phase motor, Ta and Tb, respectively, forming an auxiliary two-phase inverter. In addition, the common terminal, T_{com}, is connected to the neutral point, *N*, of the three-phase motor to eliminate the otherwise required split-capacitor phase leg. The two phase legs, *a* and *b*, provide two sinusoidal currents by PWM with a phase shift of 90 electrical degrees to the two-phase motor. The sum of the two-phase currents, i_a and i_b, will split evenly into three parts, and each part flows through one of the phase windings of the three-phase motor and the associated phase leg of the three-phase inverter as the return paths.

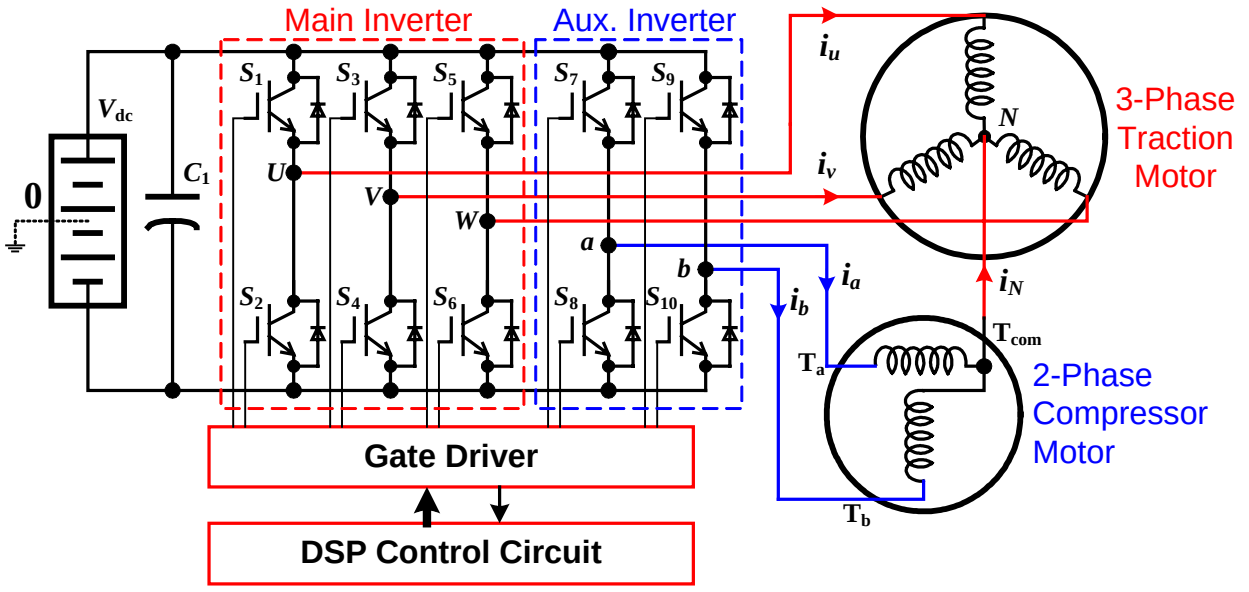

Fig. 2. Proposed integrated inverter for driving a three-phase traction motor and a two-phase compressor motor.

Figure 3(a) shows an equivalent circuit of the integrated drive system, in which the inverter is represented by five voltage sources, v_u, v_v, v_w, v_a and v_b, corresponding to the five phase legs, *U*, *V*, *W*, *a* and *b*, respectively. All the voltage sources are referenced to the midpoint of the dc source, V_{dc}. By connecting the common terminal, T_{com}, to the neutral point, *N*, of the three-phase motor, the sum of the two-phase currents, i_N (= i_a + i_b), will split evenly into three parts, and each part will flow through one of the phase windings of the three-phase motor and the associated phase leg of the three-phase inverter as the return paths, assuming a symmetrical three-phase motor and inverter. The two-phase motor currents are therefore zero-sequence components flowing in the three-phase stator and will have no effect on the operation of the three-phase motor because the zero-sequence currents will not produce torque, as shown in Fig. 3(b). In other words, the torque-producing currents of the two motors can be controlled independently.

In Fig. 3(b), the zero-sequence circuit (ZSC) of the three-phase stator is separated from the positive and negative sequence circuits, where R_{ms} and L_{m0s} represent the resistance and inductance of the ZSC, and v_0 is the zero-sequence component of the three-phase voltage sources, v_u, v_v, and v_w, which may or may not exist, depending on the PWM scheme. The zero-sequence voltage, v_0, can be calculated by

$$v_0 = \frac{v_u + v_v + v_w}{3}, \tag{1}$$

v_{us}, v_{vs}, and v_{ws} are the phase voltages referenced to the zero-sequence voltage, of the three phases, *U*, *V*, and *W*, respectively, and are expressed by

$$\begin{cases} v_{us} = v_u - v_0 \\ v_{vs} = v_v - v_0 \\ v_{ws} = v_w - v_0 \end{cases} . \tag{2}$$

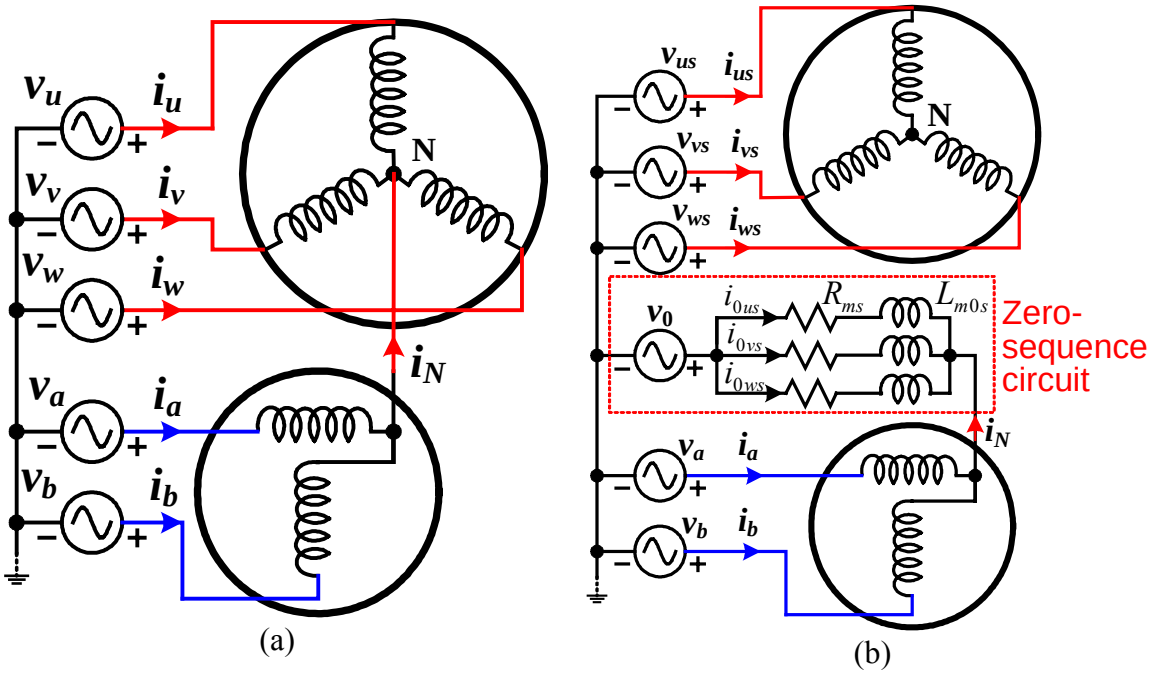

Fig. 3. Equivalent circuits: (a) inverter phase legs as voltage sources; (b) zero-sequence circuit of the main motor as the current return path of the two-phase motor.

The zero-sequence voltage component, v_0, which could be generated by certain PWM strategies such as the space vector modulation schemes, can be cancelled by injecting the same component into the modulation signals for the two-phase inverter so that v_0 will not produce current in the circuit, as will be shown in the simulation and experimental results.

Effects on the Current Rating of the Main Motor

Because the stator windings of the three-phase motor are utilized as the current return paths of the two-phase motor, the stator current rating may need to be increased to accommodate the two-phase motor currents. However, the increase of the main motor current is negligible if the two-phase motor current is sufficiently small compared to that of the main motor, which is typical in the intended automotive applications, as shown below.

The phase-*U* current of the main motor, i_u, can be expressed by

$$i_u = i_{us} - \frac{i_a + i_b}{3}, \tag{3}$$

where i_{us} is the required current if the three-phase motor is operated alone without connection to the two-phase motor. Because the two motor currents will usually have different frequencies, the rms value of the main motor phase current, i_u, can therefore be calculated by

$$I_{u,rms} = \sqrt{I_{us,rms}^2 + \frac{2I_{a,rms}^2}{9}}, \quad (4)$$

where $I_{a,rms}$ is the required rms current of the two-phase motor. For instance, given a 350 A_{rms} traction motor and a 25 A_{rms} compressor motor, i.e., $I_{us,rms}$ = 350A and $I_{a,rms}$ = 25A, the resulting traction motor current is

$$I_{u,rms} = \sqrt{350^2 + \frac{2 \times 25^2}{9}}, \quad (5)$$
$$= 350.2\text{Arms}$$

giving a negligible increase of 0.2A, less than 0.06%.

Components Count Reduction

Compared to a conventional system consisting of two separate three-phase inverters, one phase-leg including two switches and their associated gate drivers can be eliminated. Moreover, it is apparent that by integrating the two-phase auxiliary inverter into the main three-phase inverter, the dc bus filter capacitor and gate-drive power supplies can be shared between the two inverters. Furthermore, a single control circuit typically based on a microprocessor or DSP with built-in motor control hardware, such as A/D converters, PWM counters and encoder interface circuitry can be used to execute control algorithms for the two motors. With a proper control algorithm, the motors can be run in either motoring mode, i.e., providing power to the motor shaft, or operating in the generating mode, in which power is transferred from the motor shaft to the inverter dc source. In short, for the compressor drive, the inverter component count (including semiconductor switches and gate drive circuits) can be reduced by more than one-third.

Simulation and Experimental Results

Detailed circuit simulation and extensive testing were conducted to verify the proposed integated drive operations.

Simulations

Figure 4 shows an equivalent circuit of the motors on the stator d-q frame for simulation, where the ZSC of the three-phase stator is separated from its positive/negative sequence counterparts and is inserted into the current path of the two-phase motor. A detailed derivation of the equivalent circuit and the simulation work will be described in a future publication.

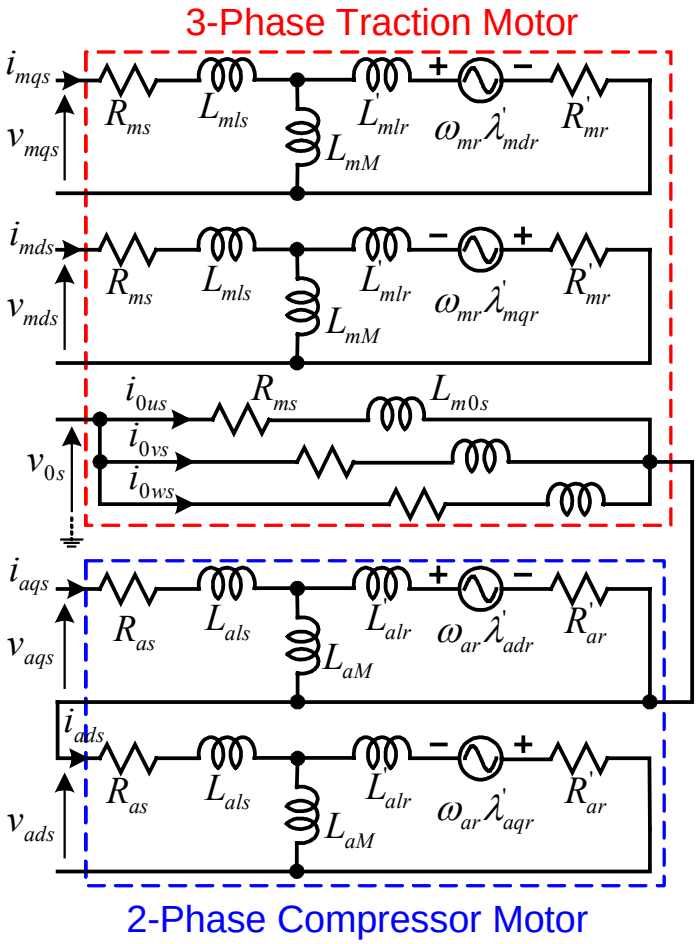

Fig. 4. An equivalent circuit on stator d-q frame for simulation.

Figure 5 shows simulated motor current waveforms when the two motors operate at different speeds, where *Vu** and *Va** are modulation signals for the three-phase motor phase-*U* and the two-phase motor phase-*a*, respectively. In Fig. 5 (a), a sine-triangle comparison PWM scheme is used without third-harmonic injection, and thus there are no zero-sequence components in the three-phase voltages, (i.e., $v_0 = 0$). In contrast, a third harmonic is added to the modulation signals for the three-phase inverter in (b), resulting in a zero-sequence voltage component (i.e., $v_0 \neq 0$). By injecting the same third-harmonic component into the two-phase modulation signals, v_0 can be cancelled and no third-harmonic current is produced.

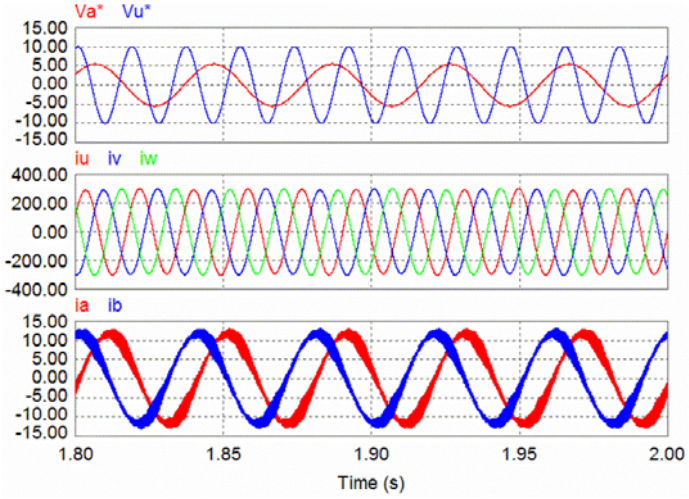

(a) $v_0 = 0$.

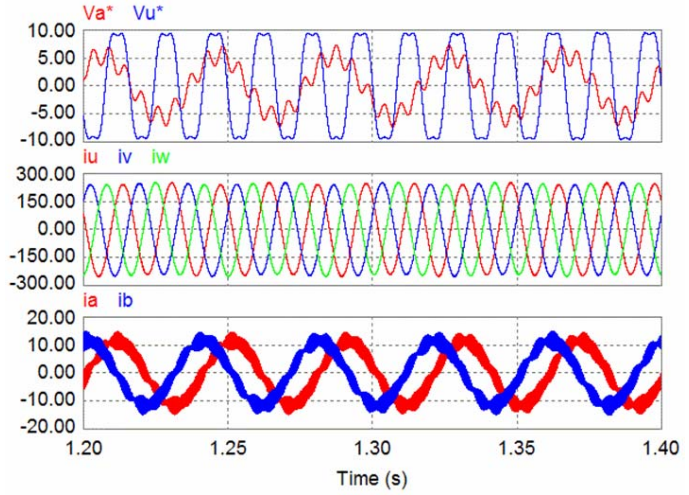

(b) $v_0 \neq 0$.

Fig. 5. Simulation results.

Experimental Setup

A prototype inverter was designed and fabricated, which consists of three 600 V/600 A dual-pack IGBT modules for driving the traction motor and two 600 V/50 A dual-pack IGBTs for driving the two-phase compressor motor. Figure 6 shows photos of the inverter and motors. For testing, a 15 HP, 230/460-V, six-pole, three-phase IM was used as the traction motor. The motor has two sets of stator windings that can be connected in series for 460-V or in parallel for 230-V operation. All winding terminals are accessible because it is intended to use a Y connection for starting and then a Δ-connection for normal running. In our testing, each winding set is wired as a Y connection and the two sets are connected in parallel. For the compressor motor, a 2-HP, 230/460-V, three-phase, two-pole motor, which also has two sets of stator windings, was modified to form a two-phase motor as shown in Fig. 7 (a). To reduce the dc bus voltage requirement, the two phase-*a* windings are connected in parallel, and each of the phase-*b* and phase-*c* windings are connected in series and then in parallel. This connection is the equivalent of an asymmetrical two-phase motor of two orthogonal windings with a turns ratio of $\sqrt{3}:1$, as can be seen from the magnetomotive force vectors shown in Fig. 7 (b).

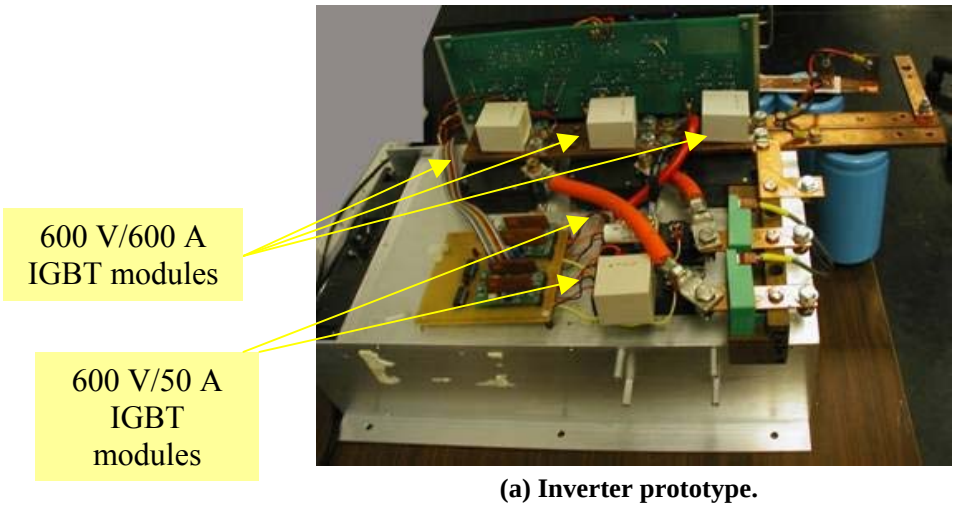

(a) Inverter prototype.

(b) Main motor 230/460 V, 6 poles, 15-HP, 2-sets of stator windings, Δ/Y connections, 3-phase.

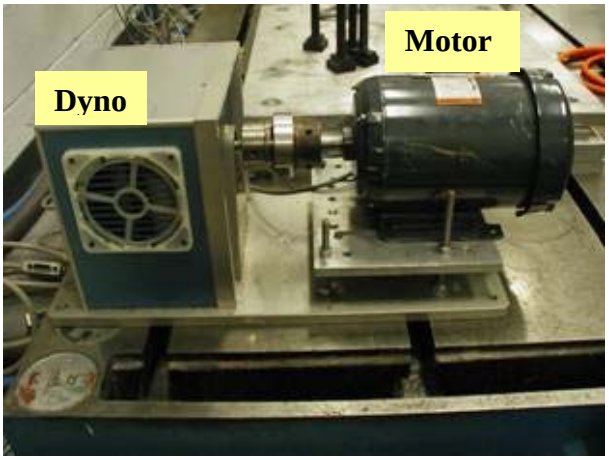

(c) Two-phase motor and dyno modified from a 2-HP 3-phase motor: 230/460 V, 2-sets of stator windings, 2 poles, Y-connections.

Fig. 6. Photos of the inverter and motors.

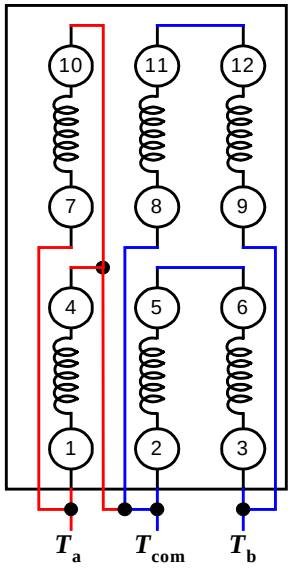

(a) Stator winding connection.

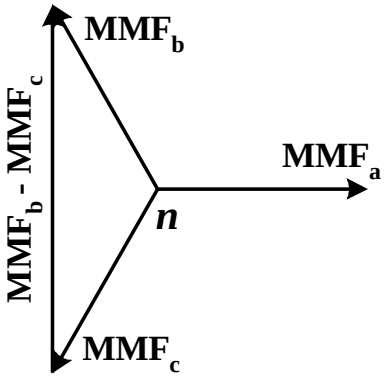

(b) Magnetomotive force vectors.

Fig. 7. Wiring connection of a three-phase motor for producing a two-phase motor.

Experimental Results

Figure 8(a)–(f) give testing waveforms at various load conditions and without the zero-sequence components in the three-phase voltages, i.e., $v_0 = 0$, which clearly shows that the speed of the two motors can be controlled independently. In (a), the main motor was not running while the two-phase motor was loaded with 220 oz.·in. (1.55 N·m) at 1000 rpm. In (b), the main motor was loaded with 65 N·m at 610 rpm, and the two-phase motor was not running. In (c), the main motor was loaded with 65 N·m at 610 rpm while the two-phase motor ran at 1100 rpm with no load. In (d), the main motor ran at 1000 rpm with no load, while the two-phase motor was loaded with 220 oz·in. (1.55 N·m) at 992 rpm. In (e), the main motor was loaded with 65.1 N·m at 610 rpm, while the two-phase motor was loaded with 221 oz·in. (1.56 N·m) at 898 rpm. In (f) the main motor was loaded with 91 N·m at 541 rpm, while the two-phase motor was loaded with 325 oz·in. (2.30 N·m) at 963 rpm. Because of their asymmetrical windings, the two-phase motor currents, i_a and i_b, are not equal.

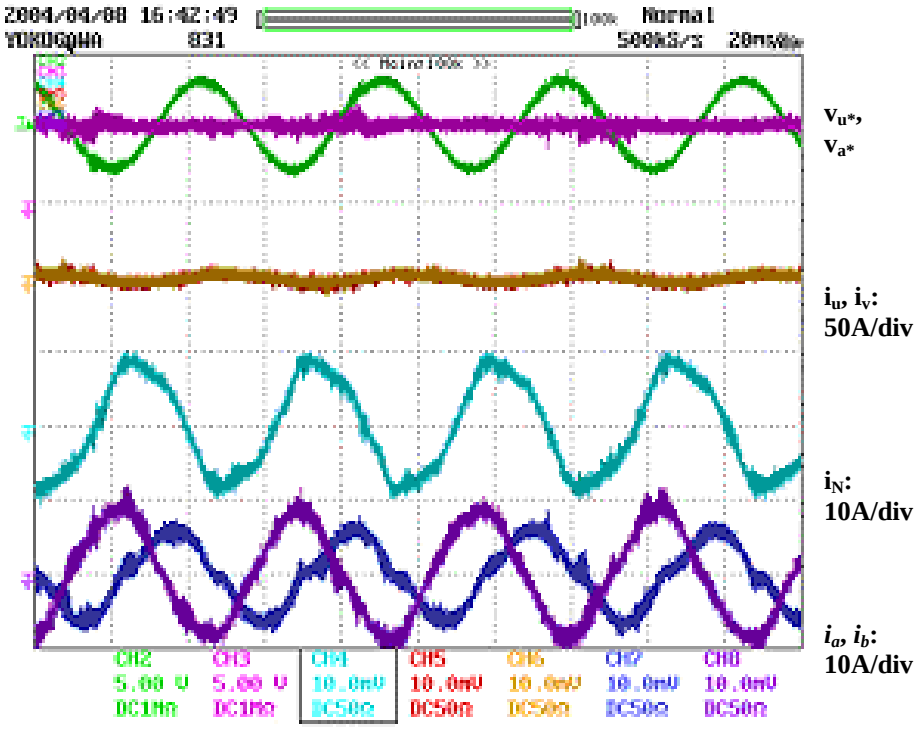

(a) Main motor is not running while 2-phase motor is loaded with 220 oz·in. (1.55 N·m) at 1000 rpm. 20ms/div

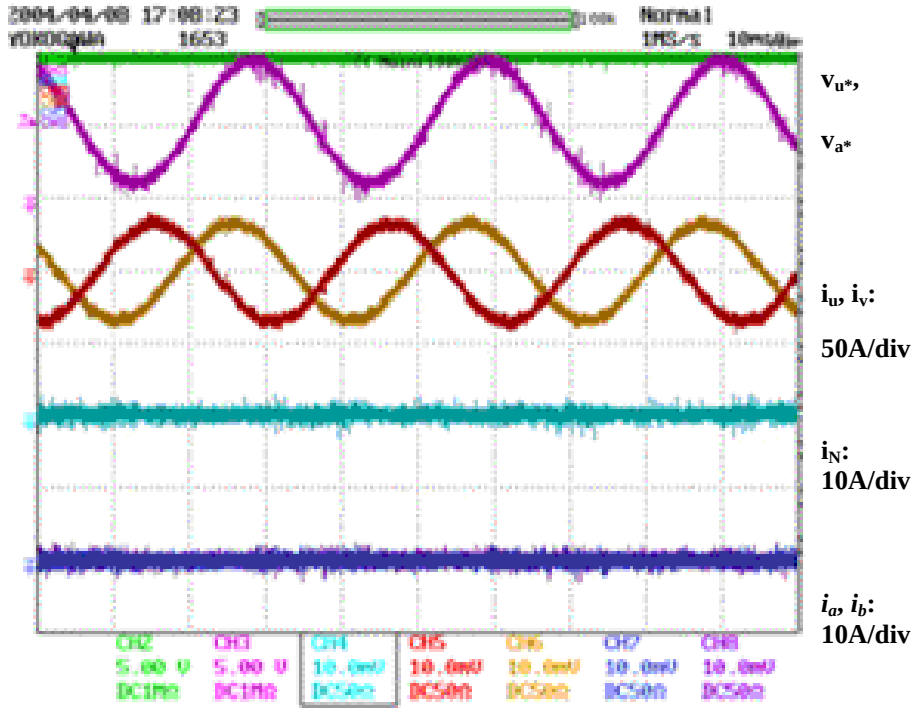

(b) Main motor is loaded with 65 N·m at 610 rpm, while 2-phase motor is not running. 10ms/div

Fig. 8. Testing waveforms at various load conditions showing that the speed of the two motors can be controlled independently.

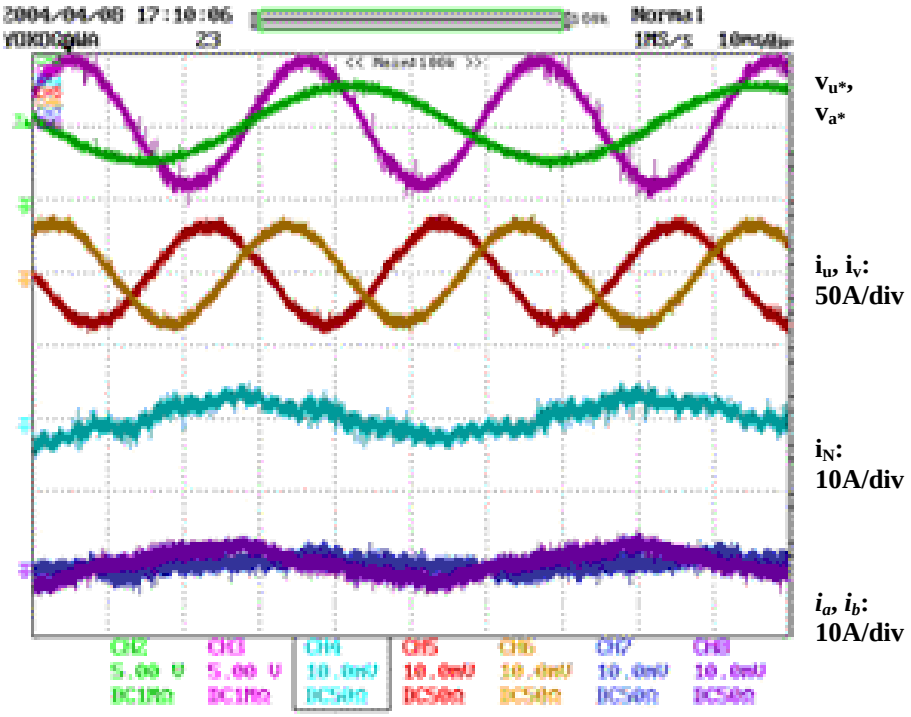

(c) Main motor is loaded with 65 N·m at 610 rpm, 2-phase motor at 1100 rpm has no load. 10ms/div

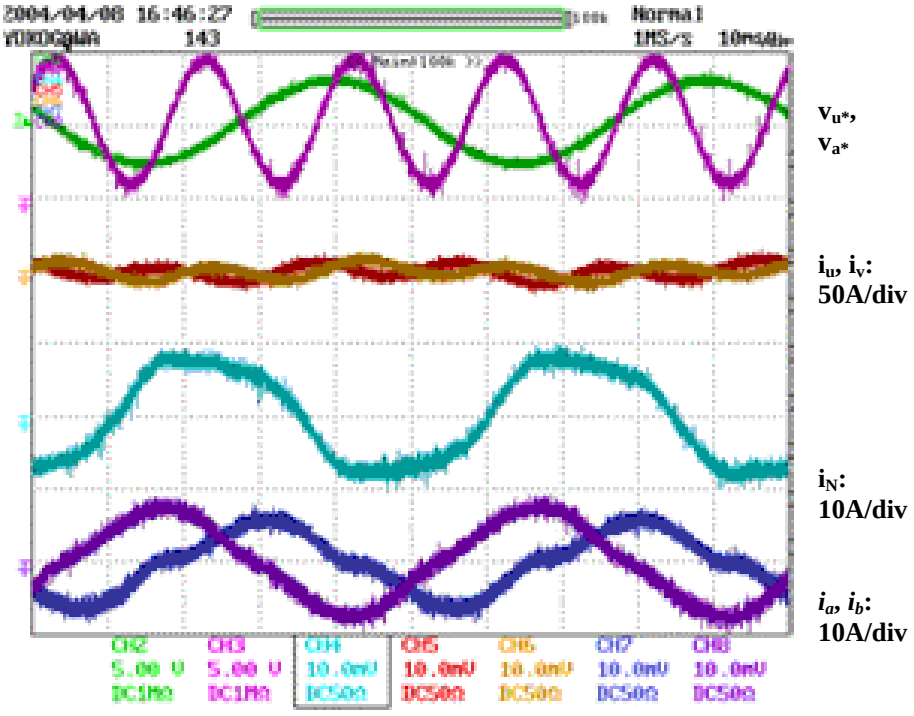

(d) Main motor at 1000 rpm with no load; 2-phase motor is loaded with 220 oz·in. (1.55 N·m) at 992 rpm. 10ms/div

Fig. 8. Testing waveforms at various load conditions showing that the speed of the two motors can be controlled independently (cont.).

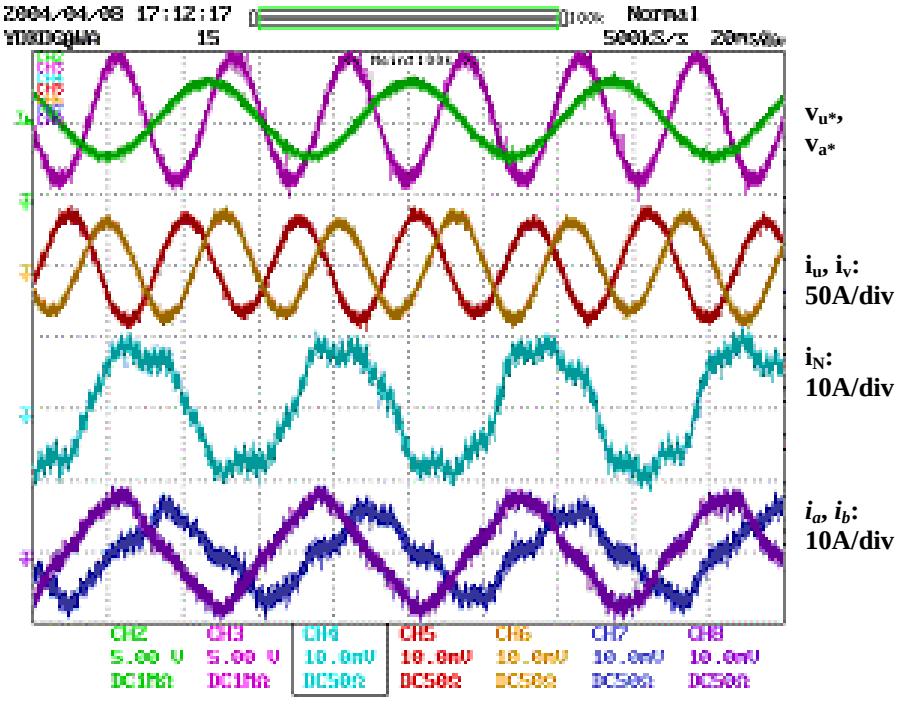

(e) Main motor is loaded with 65.1 N·m at 610 rpm; 2-phase motor is loaded with 221 oz·in. (1.56 N·m) at 898 rpm. 20ms/div

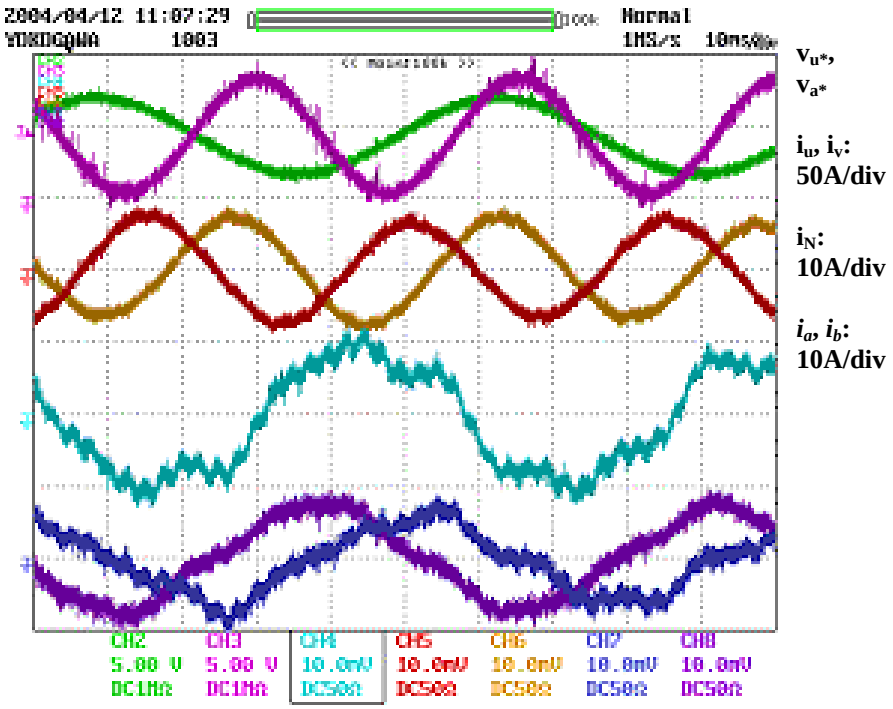

(f) Main motor is loaded with 91 N·m at 541 rpm; 2-phase motor is loaded with 325 oz·in. (2.30 N·m) at 963 rpm. 10ms/div

Fig. 8. Testing waveforms at various load conditions, showing that the speed of the two motors can be controlled independently (cont.).

A third-harmonic current was generated when the three-phase modulation signals contained a third harmonic, which is a zero-sequence component, i.e., $v_0 \neq 0$. This is shown in Fig. 9 (a), where the main motor was loaded with 85 N·m at 544 rpm and the two-phase motor was loaded with 221 oz·in. (1.56 N·m) at 1040 rpm. By adding the same third harmonic to the two-phase modulation signals, no third-harmonic current was produced, as illustrated in 9(b), where the main motor was loaded with 91 N·m at 542 rpm and the two-phase motor was loaded with 325 oz·in. (2.30 N·m) at 966 rpm.

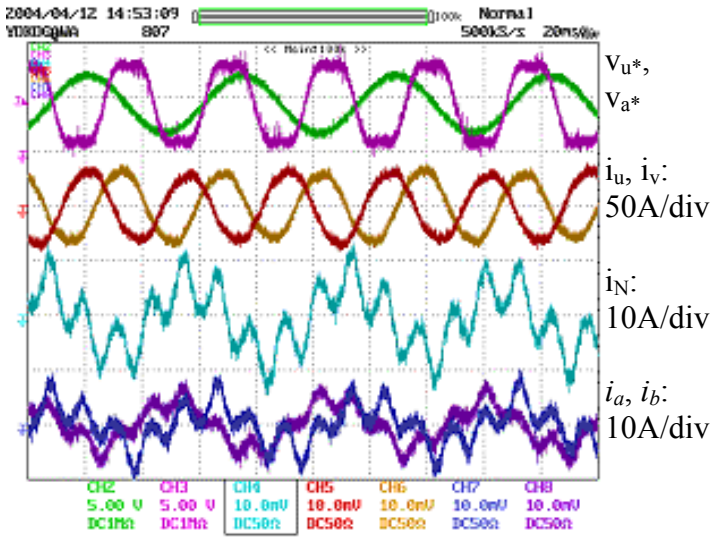

(a) Main motor is loaded with 85 N·m at 544 rpm; 2-phase motor is loaded with 221 oz·in. (1.56 N·m) at 1040 rpm. 20ms/div

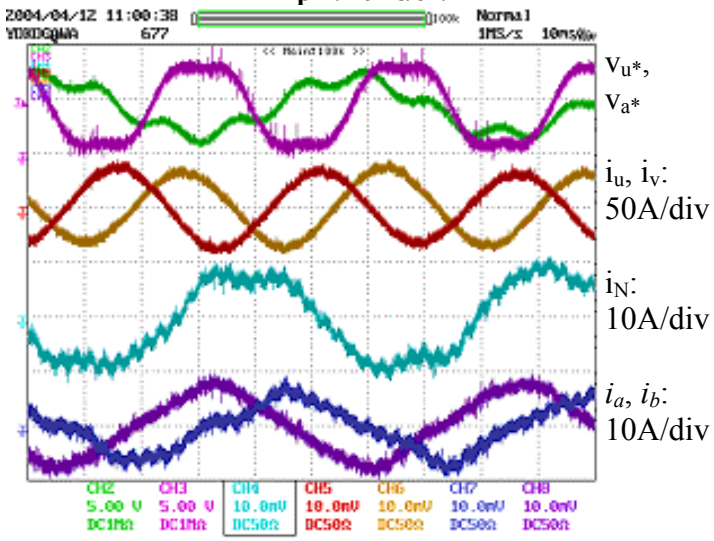

(b) Main motor is loaded with 91 N·m at 542 rpm; 2-phase motor is loaded with 325 oz·in (2.30 N·m) at 966 rpm. 10ms/div

Fig. 9. Testing waveforms show that third-harmonic components in the three-phase voltages can be prevented from producing current.

Conclusions

The proposed integrated traction and compressor motor drive using a five-leg inverter can significantly reduce the cost of the compressor motor drive in EV/HEV applications. For the compressor drive, the inverter components (including semiconductor switches and gate drive circuits) can be reduced by more than one-third. Additional cost savings are due to the fact that the compressor drive does not require a separate control circuit; it is incorporated into the traction motor controller through software.

The simulation and testing results show that

- The split-dc bus capacitors for a two-phase compressor motor drive can be eliminated by using the traction motor stator windings as the current return paths.
- The increase in the current rating of the main inverter switches and the traction motor due to the two-phase motor current is negligible.
- The speed of the traction and compressor motors can be controlled independently from each other. The test results on the independent control characteristics of the two motors and on the voltage waveforms agree fully with the analytical predictions.
- The fundamental components of the two motors have no influence on each other.

While IMs were tested in 2004 and are discussed in this paper, the proposed inverter is applicable to ac synchronous PM machines and brushless dc motors.

D. DMIC Cost Study

John W. McKeever
Oak Ridge National Laboratory
National Transportation Research Center
2360 Cherahala Boulevard
Knoxville, TN 37932
Voice: 865-946-1316; Fax: 865-946-1262; E-mail: mckeeverjw@ornl.gov

DOE Technology Development Manager: Susan A. Rogers
Voice: 202-586-8997; Fax: 202-586-1600; E-mail: susan.rogers@ee.doe.gov

ORNL Program Manager: Laura D. Marlino
Voice: 865-946-1245; Fax: 865-946-1262; E-mail: marlinold@ornl.gov

Objectives

- Determine if there is an initial cost benefit sufficient to compensate for the additional cost of six thyristors introduced by duel-mode inverter controller (DMIC) circuitry when a permanent magnet (PM) motor is driven under DMIC rather than under conventional phase advance (CPA) control.

Approach

- Develop formulas to determine the inductance range over which BLDC motors [brushless dc machines (BDCMs)] and PM synchronous motors (PMSMs) may be controlled to deliver rated power without exceeding rated current under CPA control and DMIC.
- Examine a matrix of motors designed to cover a wide range of inductances and select two for CPA cost analysis and two for DMIC cost analysis. Determine the cost of these motors.
- Prepare the list of inverter components whose costs represent the inverter cost, size the components with respect to voltage and current to match each motor, and contact commercial sources to determine the cost of the components when they are purchased in lots of 10,000.
- Examine the differences between the CPA and DMIC inverter drives for consistency.
- Examine the possibility of a methodology to determine an incremental life cycle cost benefit between CPA control and DMIC if the lifetime duty cycle of the application is known.

Accomplishments

- Derived equations for the limiting inductances of BDCMs with trapezoidal back-emfs and PMSMs with sinusoidal back-emfs when driven with CPA and with DMIC.
- Designed two PM motors whose inductances called for CPA control and two PM motors whose inductances called for DMIC control based on the equations derived for limiting inductances for a PM motor.
- Determined the cost of the motors based on current material prices.
- Sized the inverter components with respect to voltage and current for each motor, contacted vendors for price data, and estimated the inverter costs.

- Showed that it is possible to "break even" when using DMIC by compensating for increased motor and silicon-controlled rectifier (SCR) costs with a H.V., lower-current motor so cheaper IGBTs may be used.
- Developed an equation for the current differential between CPA operation and DMIC operation of a PMSM at relative speeds greater than or equal to 2 for any power up to rated power. This is the basis for a life-cycle cost analysis.
- (Beyond this task): Began a cooperative R&D agreement (CRADA) collaboration with a U.S. manufacturer to explore initial and life-cycle cost benefits of DMIC for a specific commercial application.

Publications

1. J. S. Lawler, J. M. Bailey, and J. W. McKeever, *Extended Constant Power Speed Range of the Brushless DC Motor Through Dual Mode Inverter Control*, ORNL/TM-2000/130, Oak Ridge National Laboratory, UT-Battelle, LLC, 2001.
2. J. S. Lawler, J. M. Bailey, J. W. McKeever, and J. Pinto, "Limitations of the Conventional Phase Advance Method for Constant Power Operation of the Brushless DC Motor," in *Conference Proceedings of Southeast Conference on Power Electronics Applications*, 2002.
3. J. S. Lawler, J. M. Bailey, and J. W. McKeever, "Theoretical Verification of the Infinite Constant Power Speed Range of the Brushless DC Motor Driven by Dual Mode Inverter Control," presented at the 7th IEEE Workshop on Power Electronics in Transportation, Auburn Hills, Michigan, October 24–25, 2002.
4. J. S. Lawler, J. M. Bailey, J. W. McKeever, and J. Pinto, "Extending the Constant Power Speed Range of the Brushless DC Motor through Dual-Mode Inverter Control," *IEEE Trans. on Power Electronics*, **19**(3), May 2004.

Patents

1. J. S. Lawler and J. M. Bailey, *Constant Power Speed Range Extension of Surface Mounted PM Motors*, U.S. Patent Number 6,236,179 B1, May 22, 2001.

Future Direction

- Complete a CRADA collaboration with a U.S. manufacturer for a specific application to explore initial and life-cycle cost benefits.

Background

In 1999, the Power Electronics and Electric Machines Research Center (PEEMRC) at ORNL started a program to investigate alternate "field weakening" schemes for PM motors. "Alternate" refers to the fact that the research emphasizes motors with interior-mounted PMs (IMPMs). The PEEMRC emphasis was placed on motors with SMPMs because of the relative ease of manufacturing suface-mounted PM (SMPM) motors compared with PM motors.

This task was to find ways to drive PM motors that inherently have low inductance at high speeds where their back-emf exceeds the supply voltage. ORNL developed and demonstrated the DMIC[1,2] method of field weakening for SMPM motors. The predecessor of DMIC is CPA,

which was developed by UQM, Inc.[3] ORNL's initial analyses of CPA and DMIC were based on driving motors with trapezoidal back-emfs[4–6] obtained using double-layer, lapped, stator windings with one slot per pole per phase. A PM motor with a sinusoidal back-emf obtained with two poles per slot per phase has been analyzed under DMIC operation as a University of Tennessee, Knoxville, doctoral dissertation.[7] In the process of this research, ORNL has completed analysis that explains and quantifies the role of inductance in these methods of control.

PM motors inherently have a lower inductance as a result of the increase in effective air gap caused by the magnet, which is in the denominator of the equation for L_{gap}. L_{gap} accounts for about half of the phase inductance. Because of the low inductance, there is a propensity for currents to exceed the motor's rated value. DMIC solves this problem for "low inductance" PM motors and, in addition, provides a number of safety features that protect against uncontrolled generator mode operation;[8,9] however, the DMIC topology adds a pair of anti-parallel thyristors in each of the three phases, introducing additional silicon costs as well as additional voltage drops during operation. Therefore, it is important to determine under what conditions the beneficial features of DMIC can offset its additional silicon cost and voltage drop losses.

Role of Self-Inductance in Performance and Control of PM Motors

The armature windings of PM motors with surface-mounted magnets can be positioned to achieve a trapezoidal back-emf or a sinusoidal back-emf. A machine with a trapezoidal back-emf is called a BDCM; one with a sinusoidal back-emf is commonly referred to as a PMSM. Because of the back-emf waveform, the power density of the BDCM is 1.15 times that of the PMSM;[10] however, the harmonic content of the trapezoidal waveform is much higher. Recent laboratory tests at the PEEMRC suggest that these harmonics generate sufficient heat in the rotor to cause demagnetization. This problem, which has also been encountered in the commercial sector, is being investigated at ORNL.

A motor's developed power is inversely proportional to the inductance of the stator coil. The rated current, which is a control parameter of the motor that should not be exceeded, is also inversely proportional to the inductance. Rated power defines the upper bound for the inductance because any larger inductance cannot deliver rated power. Rated current, if exceeded, defines the lower bound for inductance overheating, and demagnetization may occur.

For both the BDCM and PMSM, the primary factor limiting their ability to operate at high constant power speed ratios (CPSRs) is the armature winding inductance. The field weakening of these two types of motors differs and is discussed later. Explicit formulae are developed for each machine type to show the limitation that inductance places on CPSR. The analysis neglects second-order effects such as speed-sensitive losses that include friction, windage, hysteresis, eddy currents, and skin effect in winding resistance. These speed-sensitive losses will limit the CPSR of any practical motor to a finite value.

Inductance Bounds for the BDCM (Trapezoidal Back-emf)

Two control methods have been developed to drive the BDCM through a wide CPSR. The first method, CPA, was developed for UQM Technologies. It uses the conventional voltage-source inverter (VSI) to drive the motor. The second method, DMIC, was developed at ORNL. The DMIC uses a special inverter configuration, which interfaces the common VSI output to the motor through an ac voltage controller composed of six SCRs (two anti-parallel devices in each of three phases). Between zero speed and base speed, there is very little functional difference between the two methods. Both use well-established current regulation at low speed. Above base speed, the two methods differ substantially in how the motor current is controlled. The DMIC method works well for low-inductance motors, while CPA is applicable for high-inductance motors. High-speed operation of each method is summarized, and formulas are given to show the dependence of CPSR capability on inductance.

Bounding Inductances for CPA

When the analysis of CPA is based on a per-phase fundamental phasor model shown in Fig. 1, the equation for power delivered is

$$P = \frac{36 V_{dc} E_b}{\pi^3 \Omega_b L} \sin \delta \tag{1}$$

where V_{dc} is the dc supply voltage,
E_b is the back-emf,
Ω_b is the base speed in electrical radians/s,
L is the inductance, and
δ is the inverter lead angle related to the advance angle, θ_a, by $\delta = \theta_a - 30^o$.

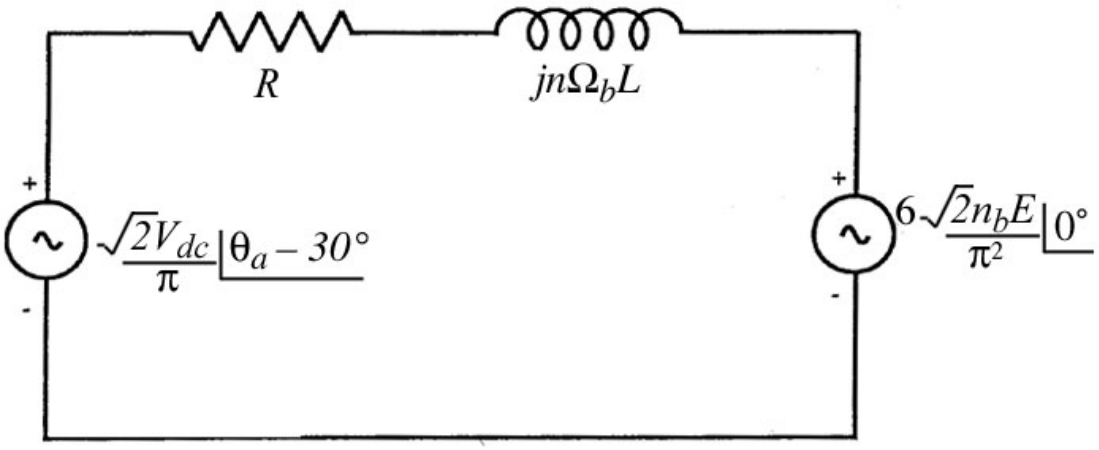

Fig. 1. Per-phase fundamental phasor model of trapezoidal back-emf used to analyze CPA at high speed.

Equation (1) may be solved for the inverter lead angle that will yield rated power as

$$\delta = \sin^{-1}\left[\frac{\pi^3 \Omega_b L P_r}{36 V_{dc} E_b}\right] \quad . \tag{2}$$

Regeneration requirements may necessitate a power higher than rated power so that the right side of Eq. (1) must exceed P_r. This leads directly to the upper bound on inductance,

$$L_{\max}^{CPA-BDCM} = \frac{36 V_{dc} E_b}{\pi^3 \Omega_b P_r} . \tag{3}$$

The rated current, I_r, imposes a significant constraint on the motor inductance by the equation,

$$I_r \geq \frac{\sqrt{\frac{2V_{dc}^2}{CPSR^2} + \frac{72E_b^2}{\pi^2} - \frac{24E_b V_{dc}}{\pi CPSR}\cos\delta}}{\pi \Omega_b L} \quad , \tag{4}$$

This leads directly to a lower bound for the inductance,

$$L_{\min}^{CPA-BDCM} \geq \frac{\sqrt{\frac{2V_{dc}^2}{CPSR^2} + \frac{72E_b^2}{\pi^2} - \frac{24E_b V_{dc}}{\pi CPSR}\cos\delta}}{\pi \Omega_b I_r} . \tag{5}$$

At high speeds where CPSR $\rightarrow \infty$, an infinite CPSR is achieved when the inductance is greater than

$$L_{CPSR\rightarrow\infty}^{CPA-BDCM} = \frac{6\sqrt{2} E_b}{\pi^2 \Omega_b I_r} \quad . \tag{6}$$

For V_{dc} = 190 V, E_b = 74.2 V, I_r = 203 A, $\Omega_b = 1634$ electrical rad/sec, and P_r = 37000 W, the values of L_{max}= 269 uH and L_{∞}= 192 uH may be calculated directly from Eqs. (3) and (6). The value of L_{min} = 164 uH may be calculated by iterating between Eqs. (2) and (5).

Bounding Inductances for DMIC

The differential equations that govern the BDCM when driven by DMIC have been solved analytically[1] for CPSR ≥ 2. This analytic solution led to the formulae for the average motor power and the rms motor current,

$$P = \frac{2 V_{dc} E_b}{\pi^2 \Omega_b L}\left[\theta_a^3 + \pi\theta_a^2 + \frac{\pi^2}{3}\theta_a - \frac{2\pi^3}{27}\right] \quad , \tag{7}$$

and $$I_{rms} = \frac{E_b}{\Omega_b L}\sqrt{\frac{8}{5\pi^3}\theta_a^5 + \frac{8}{3\pi_2}\theta_a^4 + \frac{16}{9\pi}\theta_a^3 + \frac{4}{27}\theta_a^2 - \frac{16\pi}{81}\theta_a + \frac{23\pi^2}{1215}} \quad , \tag{8}$$

where θ_a is the advance thyristor firing angle measured from the intersection of the dc voltage with the line-to-neutral back-emf, as shown in Fig. 2. Note that I_{rms} is independent of the dc supply voltage and motor speed. This means that after the advance is determined to deliver power, the same advance is used to calculate a fixed rms current that delivers that power for all speeds above CPSR ≥ 2. The advance that delivers rated power also determines the rated rms current, which will support that power delivery regardless of speed range from CPSR = 2 to infinite CPSR under DMIC. Of course, resistance and losses determine the actual CPSR.

The smallest advance, $\theta_a = \pi/6$, determines the lower bound of inductance as

$$L_{\min}^{DMIC-BDCM} = \frac{\pi E_b}{\Omega_b I_r \sqrt{1620}} \quad . \tag{9}$$

The largest advance, $\theta_a = \pi/3$, determines the upper bound of inductance as

$$L_{\max}^{DMIC-BDCM} = \frac{\pi E_b}{\Omega_b I_r} \sqrt{\frac{91}{1215}} \quad . \tag{10}$$

The ratio of L_{max} to L_{min} is 11.0, which gives the motor designer a wide target for the inductance range.

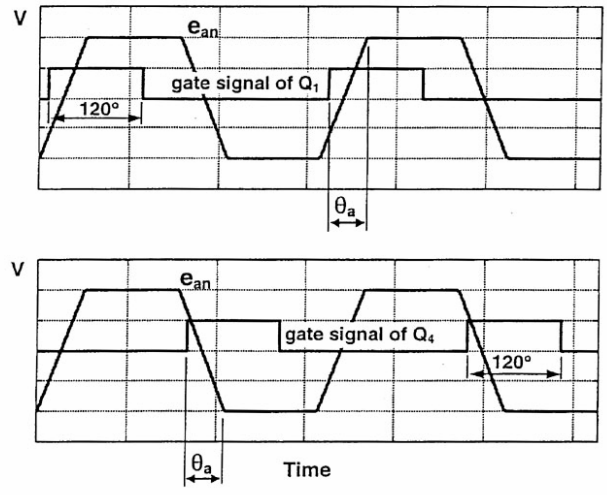

Fig. 2. Transistor firing scheme and definition of θ_a.

If one substitutes the same parameters used to calculate the CPA inductances, V_{dc} = 190 V, E_b = 74.2 V, I_r = 203 A, Ω_b = 1634 electrical rad/s, and P_r = 37000 W, the values of L_{min}= 17.5 uH and L_{max}= 192 uH may be calculated directly from Eqs. (11) and (12).

Bounding Inductances for the PMSM (Sinusoidal Back-emf)

When the analysis of CPA is based on the per-phase phasor model for sinusoidal voltage waveforms shown in Fig. 3, the equation for power delivered is

$$P = \frac{3V_{\max}E_b}{\Omega_b L}\sin\delta \quad . \tag{11}$$

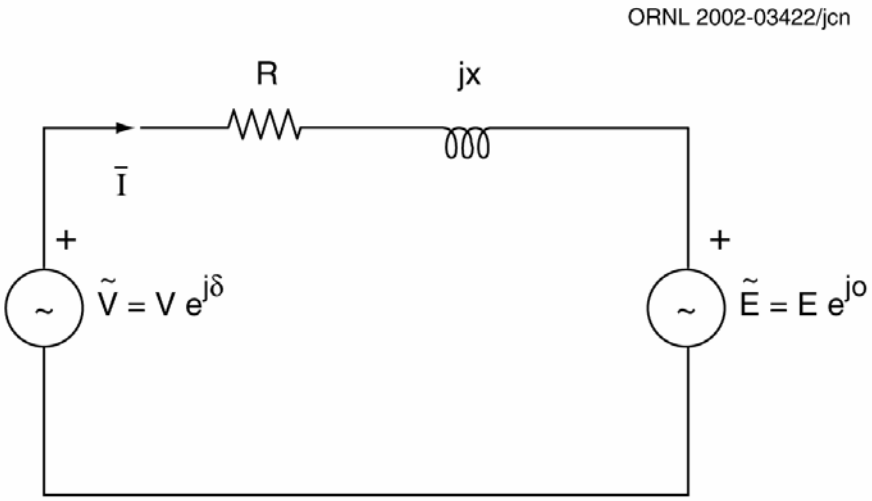

Fig. 3. Per-phase phasor model of sinusoidal back-emf used to analyze CPA at high speed.

The value of V in the model is $V_{max,}$ and it is related to V_{dc} if over-modulation is allowed by $V_{dc} = \frac{\pi}{\sqrt{2}}V_{\max}$.

The expression for power shows that it is easy to control the motor to deliver required power above base speed, just as it did for the BDCM. All that is necessary is that the inverter lead angle, δ, be held fixed so that the required power is delivered. The equation is

$$\delta = \sin^{-1}\left(\frac{X_b P}{3V_{\max}E_b}\right) = \cos^{-1}\left(\frac{E_b}{V_{\max}}\right) \quad , \tag{12}$$

where X_b is the inductive reactance, $\Omega_b L$. The expression on the far right of Eq. (12) is obtained by substituting the equality,

$$P_r = 3E_b I_r \, , \tag{13}$$

in the center expression of Eq. (12) and recognizing that E_b is 90° out of phase with the inductor voltage. Equation (13) is true because, at base speed, the sum of the power developed in each phase at rated current is the rated power of the motor; and the current is in phase with the back-emf.

While constant lead angle control allows the PMSM to operate at constant power above base speed, it is not a certainty that that it will operate within the rated current. Neglecting the armature resistance, the equation for phasor current for Fig. 3 is

$$\bar{I} = \frac{V_{\max} e^{j\delta} - E_b}{jnX_b} \quad , \tag{14}$$

which has rms magnitude

$$I_{rms} = \frac{\sqrt{V_{\max}^2 - n \cdot 2V_{\max} E_b \cos\delta + n^2 E_b^2}}{nX_b} \quad . \tag{15}$$

Recall that n is the ratio,

$$n = N/N_b, \tag{16}$$

where N is the mechanical angular speed, rpm, and
N_b is the mechanical angular base speed in rpm.

Equation (15) gives the rms motor current, I_{rms}, when operating at any speed above base speed. Substituting the lead angle from the right side of Eq. (12) so that rated power is produced, and requiring that the rms current be less than the rated current at maximum speed where n equals the CPSR, leads to the equation for bounding current,

$$I_r \geq \frac{\sqrt{V_{\max}^2 + CPSR(CPSR-2)E_b^2}}{CPSR * \Omega_b L} \quad . \tag{17}$$

Equation (17) may be solved directly for the lower bound on inductance to satisfy the rated current limit,

$$L_{\min}^{CPA-PMSM} \geq \frac{\sqrt{V_{\max}^2 + CPSR(CPSR-2)E_b^2}}{CPSR * \Omega_b I_r} \quad . \tag{18}$$

The limit of Eq. (18) as CPSR approaches infinity shows that an infinite CPSR can be achieved provided that the motor inductance is greater than

$$L_{CPSR\to\infty}^{CPA-PMSM} \geq \frac{E_b}{\Omega_b I_r} \quad . \tag{19}$$

The upper bound is obtained by recognizing that the lead angle in Eq. (11) cannot exceed 90°. Again, by using the equality of Eq. (13), one may calculate the upper bound to inductance,

$$L_{\max} = \frac{3V_{\max}E_b}{P_r\Omega_b} = \frac{V_{\max}}{\Omega_b I_r} \quad . \tag{20}$$

If one substitutes the values V_{dc} = 190 V, so that V_{max} = 85.54 V (assuming over-modulation), $E_b = 74.2/\sqrt{2}$ V, I_r = 203 A, $\Omega_b = 1634$ electrical rad/s, P_r = 37000 W, and CPSR = 9, the values of L_{min} = 142 uH, L_∞ = 158 uH, and L_{max} = 164 uH may be calculated directly from Eqs. (18), (19), and (20).

DMIC Minimizes Current in PMS as well as BDCM

Recent analysis has shown that at any power level, the SCRs, which are the heart of the DMIC, enable maximum watts per rms amp control during constant power operation by minimizing rms current. This feature is not possible with a VSI-driven motor, which has no SCRs, with a fixed inductance. In addition, losses can be substantially reduced using DMIC operation of PMSMs whose inductance is sufficiently large for VSI control (no SCRs) to achieve infinite CPSR. This current minimization was determined by addressing the question, "if one assumes that the supply voltage can deliver the desired useful power and neglects the resistance, is there a value of inductive reactance, $X_b = n\Omega_b L$, that minimizes the current?" The answer is yes, and the equation for that inductive reactance is

$$X_{\min I} = n\Omega_b L = \frac{3V_{\max}}{P}\sqrt{n^2 {E_b}^2 - {V_{\max}}^2} \quad , \tag{21}$$

which may be solved for the inductance needed at that electrical frequency, $n\Omega_b$. P is the developed power, V_{max} is the supply voltage, n is the relative mechanical speed, and Ω_b is the electrical rad/s. With the optimal value of thyristor reactance, the minimum rms motor current is

$$I_{\min} = \frac{P}{3V_{\max}} = \frac{P}{3\sqrt{E_b^2 + \left(X_b I_r\right)^2}} \quad . \tag{22}$$

Equation (22) is independent of speed and directly proportional to developed power. If one substitutes the equality from Eq. (13) and the motor inductance for infinite CPSR from Eq. (19) for X_b into Eq. (22), a linear relationship in P emerges,

$$\frac{I_{\min}}{I_r} = \frac{P}{\sqrt{2}P_r} \quad . \tag{23}$$

It can also be shown that the motor current is in phase with the inverter voltage phasor, which means that the inverter operates at unity power factor.

Figure 4 compares the motor current under CPA control with the motor current under DMIC. The linear relation between current and power of Eq. (23) is plotted at the bottom. As shown in ref [11], Eq. (17) with the inductance for infinite CPSR from Eq. (19), $V_{max}=E_b\sqrt{2}$, $P_{max}=P_r\sqrt{2}$, $\sin\delta = P/(P_r\sqrt{2})$, and $\cos\delta = \sqrt{1-\sin^2\delta}$ lead to the rms motor current equation,

$$I = I_r\sqrt{\frac{n^2 - 2n\sqrt{2-\left(\frac{P}{P_r}\right)^2} + 2}{n^2}} \quad . \tag{24}$$

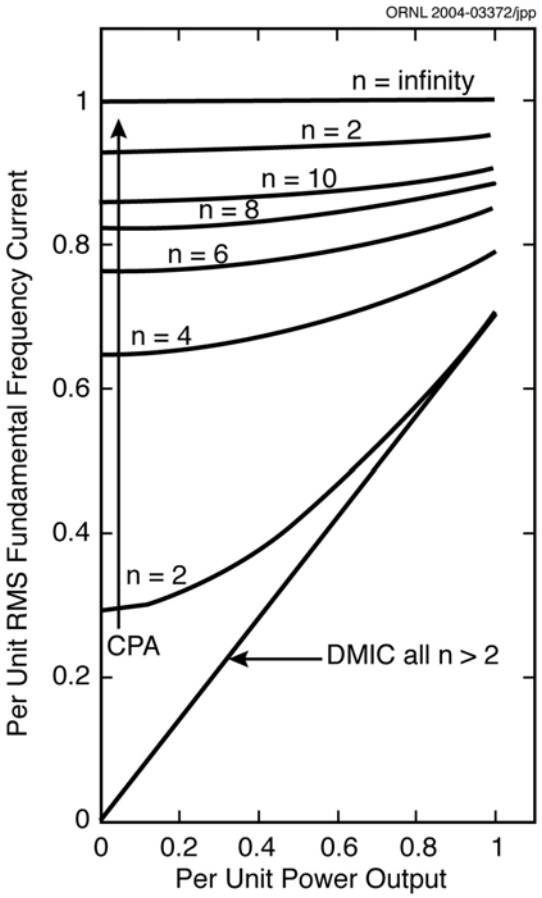

Fig. 4. Constant power operation of a PMSM motor comparing CPA control with DMIC.

Figure 4 is a plot of Eq. (24) in the form of I/I_{rated} versus P/P_r for n values of 2, 4, 6, 8, 20, and ∞. Figure 4 shows that when $L = L_{\infty,}$ any developed power up to the rated power can be achieved without exceeding the rms current rating of the motor. The flatness of the CPA curves indicates that the copper losses in the motor are virtually independent of the developed power. Efficiency may be poor when operating conditions require a developed power less than the rated power. The

DMIC's reduction in copper losses can be applied to compensate for the increased losses in the SCRs, and when there is a net reduction in total inverter plus motor losses, that reduction can be applied over the operating life of the drive toward the added initial cost of the SCRs.

This type of analysis provides a relationship showing the current that may be saved at various operating speeds by using one controller (DMIC) instead of another (CPA or vector control) so that operational cost benefit estimates may be made based on the application's expected duty cycle. In any life cycle cost study, this information, which is not the first or initial cost, must be included because it can provide significant benefits to the customer.

Motor and Inverter Cost Study

There are several ways to increase the inductance, *L*, of a PM motor. One, which is clumsy and wasteful, is to add an inductor in each of the three phases. Justifying the additional cost of the six thyristors required by the DMIC vs. the cost penalty of adding inductors in each phase, is not difficult. A second method is to attempt to increase the inductance in the stator windings of the design. The University of Wisconsin, Madison (T. Jahns) and ORNL (J. M. Bailey) are conducting research to increase the inductance by means of concentrated windings; however, by using ORNL's radial-gap design tool for radial-gap PM motors, we found that a reasonable range of inductance could be designed into the PM motors.

Seven motor designs that use the design code with phase inductances ranging from 1270 μH to 97 μH are summarized in Table 1. Each motor was designed to deliver 30 kW at 1500 rpm with the maximum current density in the wires held at about 13 A/mm^2. Two equations illustrate the internal consistency of Table 1. The first is the equation for torque, which is

$$T = \frac{30 \bullet 2E_b I^{peak}}{\pi \Omega_{rpm}} \quad , \tag{25}$$

and the second is for back-emf, which is

$$E_b = N_m B_g n_s L_{st} \frac{2\pi\Omega_{rpm}}{60} R_{ro} \quad , \tag{26}$$

where N_m is the number of poles,
B_g is the magnetic field strength,
L_{st} is the length of the stator,
I^{peak} is the maximum current,
Ω_{rpm} is the mechanical rotational speed, and
R_{ro} is the outer radius of the rotor.

Case 2 reduces Case 1's inductance by cutting the turns per slot in half, which reduces the back-emf. The current must be doubled to maintain torque. This requires that the conducting area be doubled to maintain the current density. Reduction of wire length and increase in area should reduce the wire resistance by 1/4. Case 3 doubles the stator length, which doubles the back-emf.

Current must decrease by 1/2 to maintain torque. This requires that the conducting area be decreased by 1/2 to maintain the current density. Recognizing that doubling the stator length is roughly like increasing the wire length by 4/3 (not 2 because of the end turns), one may estimate the increase in resistance as the product of 4/3 by 2 from the area reduction. Case 4 relates to Case 3 like Case 2 relates to Case 1. Cases 5, 6, and 9, which are not used in the cost study, are all at the same length and show the effect on inductance as turns per slot variation is compensated by wires per turn to maintain current density. Note that the stator radius of the last three cases is larger, which is responsible for their higher costs.

Additional important design outputs beyond the calculations summarized in Table 1 are the volume and weight of the rotor steel laminates, the stator steel laminates, the magnets, and the copper from which material costs are estimated. Two 0.5-in-thick steel disks connected the rotor to a 1.5-in.-diam steel shaft. The shaft extended beyond the stack length by 4 in. A 0.5-in.-thick cylindrical aluminum housing extended 0.5 in. beyond the stator at each end and was enclosed at each end by equally thick aluminum end disks flush with the edge of the cylinder. The number of 0.0185-in.-thick steel laminates was determined by dividing the stacking factor corrected length by the thickness of a laminate. Since the rotor and stator are punched from a single laminate, cost per laminate was apportioned to the rotor and stator by weight fraction. Table 2 shows the material weight of the magnets, rotor laminates, shaft, connecting disks, stator laminates, copper wire, and aluminum housing.

Table 3 summarizes the SMPM motor costs. It includes material, labor and overhead (25% of material cost), and cooling system penalty cost (10% of material plus labor plus overhead) as the major elements of manufacturing costs. The original equipment manufacturer price adds 10% for profit margin to the manufacturing cost.

Table 1. Motor designs investigated for motor cost study

Case	#1	#2	#3	#4		#5	#6	#9
Power, W	30000	30000	30000	30000		30000	30000	30000
Torque, N-m	191	191	191	191		191	191	191
Speed, rpm	1500	1500	1500	1500		1500	1500	1500
OR stator R_{so}, in	5	5	5	5		6.5	6.5	6.5
OR rotor, R_{ro}, in.	3	3	3	3		3	3	3
IR rotor, R_{ri}, in.	2.453	2.453	2.453	2.453		2.009	2.009	2.009
Stack length, L_{st}, in.	1.969	1.969	3.938	3.938		3.938	3.938	3.938
Terminal voltage, V	308	154	305	152		290	146	73
Lawler V_{dc}, V	529.31	264.26	412.81	205.77		417.79	209.26	104.65
No. magnets	18	18	18	18		8	8	8
Omega$_b$, electrical rad/s	**1413.72**	**1413.72**	**1413.72**	**1413.72**		**628.3**	**628.3**	**628.3**
T_c, turns/coil	8	4	4	2		8	4	2
T_s, turns/slot	16	8	8	4		16	8	4
line-to-neutral back-emf at base speed, E_b	**147.06**	**73.53**	**147.06**	**73.38**		**138.52**	**69.26**	**34.63**
$I_{peak}=P/(2E_b)$, A	102	204	102	204.42		108.29	216.58	433.15
I_{rms}=sqrt(2/3)I_{peak}	**83.28**	**166.56**	**83.28**	**166.90**		**88.42**	**176.83**	**353.67**
Phase Inductance, L, uH	**1270**	**316**	**624**	**156**		**1560**	**390**	**97**
Phase resistance, R, ohms	0.0673	0.0168	0.0497	0.0115		0.0592	0.0159	0.004
wire gage	16	16	16	16		16	16	16
wires per turn	6	12	6	13		7	13	26
wire area, mm^2	1.308	1.308	1.308	1.308		1.308	1.308	1.308
Copper area in slot, mm^2	133	133	79	69		151	140	140
Current Density, A/mm^2	13.00	13.00	13.25	12.25		12.02	12.84	12.94
L^{DMIC}_{min}, uH	97	24	97	24		195	49	12
$L^{DMIC}_{no\ cont.\ cur}$, uH	839	210	839	209		1674	419	105
L^{DMIC}_{max}, uH	1074	268	1074	267		2144	536	134
The following inductance bounds use Lawler's Vdc which is best when L>LDMICmax								
L^{CPA}_{min}, uH for CPSR=4	568	142	679	169		1297	324	81
$L^{CPA}_{inf.}$, uH	1074	268	1074	267		2144	536	134
L^{CPA}_{max}, uH	2131	532	1662	413		3565	893	223

Table 2. Weight of components in motor cost study

Case	#1	#2	#3	#4		#5	#6	#9
Magnet mass, lb	2.15	2.15	4.30	4.29		4.45	4.45	4.45
Rotor laminates, lb	2.79	2.79	5.58	5.57		12.38	12.38	12.38
1.5-in.-dia steel shaft, lb.	2.93	2.93	3.90	3.90		3.90	3.90	3.90
Two 0.5-in. thick steel connecting disks, lb	4.76	4.76	4.76	4.76		3.03	3.03	3.03
Stator laminates, lb	14.90	14.90	29.80	29.74		66.30	66.30	66.30
Copper, lb	13.90	13.90	10.28	11.12		16.64	15.45	15.45
0.5-in.thick Al cyl housing, lb	4.90	4.90	8.14	8.14		10.47	10.47	10.47
Two 0.5-in Al end disks, lb	7.68	7.68	7.68	7.68		13.10	13.10	13.10

Table 3. Cost comparison of PM motors with surface-mounted magnets

cost/lb or %	Case	#1	#2	#3	#4		#5	#6	#9
	Cost per laminate, $	0.41	0.41	0.41	0.41		0.63	0.63	0.63
$14.50	Magnet matl., $/lb	$31.18	$31.18	$62.35	$62.21		$64.53	$64.53	$64.53
	0.0185-in. M19 rotor lamins.	$6.68	$6.68	$13.35	$13.35		$20.47	$20.47	$20.47
$1.80	Rotor shaft, $/lb	$5.27	$5.27	$7.01	$7.01		$7.01	$7.01	$7.01
$0.50	Rotor support disks, $/lb	$2.38	$2.38	$2.38	$2.38		$1.52	$1.52	$1.52
	0.0185-in. M19 stator lamins.	$35.65	$35.65	$71.30	$71.30		$109.61	$109.61	$109.61
$3.07	Copper wire, $/lb	$42.67	$42.67	$31.56	$34.14		$51.08	$47.43	$47.43
$2.50	Cyl aluminum frame, $/lb	$12.24	$12.24	$20.36	$20.36		$26.18	$26.18	$26.18
$3.00	Aluminum end caps, $/lb	$23.03	$23.03	$23.03	$23.03		$39.29	$39.29	$39.29
25%	Labor & Overhead	$39.78	$39.78	$57.84	$58.45		$79.92	$79.01	$79.01
10%	Cooling	$19.89	$19.89	$28.92	$29.22		$39.96	$39.50	$39.50
	Mfg. Cost	$218.77	$218.77	$318.11	$321.45		$439.57	$434.55	$434.55
10%	Profit Margin	$21.88	$21.88	$31.81	$32.15		$43.96	$43.45	$43.45
	OEM Price	**$240.64**	**$240.64**	**$349.92**	**$353.60**		**$483.53**	**$478.00**	**$478.00**

The cost of the motor is most tied to magnet and copper costs. It was essential to hold the current density constant by reducing the wire-packing factor for the low-inductance motors. Otherwise much more copper was added to the motor costs, resulting in an additional $50 penalty. Increasing the length adds to the magnet materials, which is probably the most significant contributor to the additional cost of the low-inductance motors.

A simulation of the first four cases was completed to verify that the desired power could be delivered by the model and to guide selection of the inverter devices. The simulation provided information about the current in the motor and in the inverter while being driven by CPA and by DMIC. In addition to the voltage requirements obtained during the motor design study, current requirements are also necessary for selection of the inverter components. Table 4 summarizes the peak, rms, and average currents that pass through the inverter's transistors and bypass diodes and through the motor, as well as the peak and rms currents that pass through the motor and dc source during CPA operation. It then summarizes the peak, rms, and average current that passes through the transistors and, for cases 3 and 4, through the thyristors, recognizing that there is no

current back through the bypass diodes in the IGBT package during DMIC operation. Finally, it presents the peak and rms currents through the motor and dc source under DMIC operation.

Table 4. Inverter and motor currents under CPA and DMIC for selection of devices in cost study

Case	#1	#2	#3	#4
V_{dc}	529	264	413	206
Back-emf line-to-line	1176	588	1176	587
P_{CPA_avg}	29351	29190	29224	28373
$I_{CPA\_transistor\_peak}$	67.50	135.00	141.70	281.50
$I_{CPA\_transistor\_rms}$	33.70	67.20	63.10	125.00
$I_{CPA\_transistor\_avg}$	20.20	40.30	34.10	67.70
$I_{CPA\_bypass\_diode\_peak}$	28.00	57.50	107.20	213.80
$I_{CPA\_bypass\_diode\_rms}$	5.00	10.50	27.40	55.10
$I_{CPA\_bypass\_diode\_avg}$	1.30	2.80	9.60	19.50
$I_{CPA\_motor\_peak}$	67.50	135.00	141.70	281.50
$I_{CPA\_motor\_rms}$	48.00	96.30	97.40	193.30
$I_{CPA\_dcsource\_rms}$	56.30	113.70	79.90	157.40
$I_{CPA\_dcsource\_peak}$	57.00	112.40	73.30	144.20
$E_{CPA}(n=4)$	0.9722	0.9599	0.9325	0.9136
P_{DMIC_avg}	28973	29202	29901	28903
$I_{DMIC\_transistor\_peak}$	58.00	117.00	77.80	150.50
$I_{DMIC\_transistor\_rms}$	30.10	60.60	41.30	79.80
$I_{DMIC\_transistor\_avg}$	18.50	37.20	24.60	47.50
$I_{DMIC\_bypass\_diode\_peak}$	0.00	0.00	0.00	0.00
$I_{DMIC\_bypass\_diode\_rms}$	0.00	0.00	0.00	0.00
$I_{DMIC\_bypass\_diode\_avg}$	0.00	0.00	0.00	0.00
$I_{DMIC\_motor\_peak}$	58.00	117.00	77.80	150.50
$I_{DMIC\_motor\_rms}$	42.70	85.60	58.00	113.10
$I_{DMIC\_dcsource\_rms}$	56.00	111.60	73.60	143.10
$I_{DMIC\_dcsource\_peak}$	56.00	111.60	73.50	143.00
$E_{DMIC}(n=4)$	0.9709	0.9551	0.9625	0.9437

Table 5 summarizes the size of the more expensive components based on the voltages in Table 1 and the currents in Table 4. Finally, Table 6 presents the total inverter costs based on a production volume of 10,000 units, along with indications of the sources that provided these cost estimates. It is likely that with larger volume demand in the future, the inverter costs will decline substantially. These numbers lead to a cost per unit power of about $70/kW, which is quite high compared with the target value of $20/kW.

Table 5. Selection of expensive inverter components based on motor design voltages and simulation currents

	Typical	Case 1	Case 2	Case 3	Case 4
Part name	**specifications**				
IGBT module	Dual 600V/600A	Dual 800V/200A	Dual 450V/450A	Dual 600V/200A	Dual 350V/450A
DC bus Capacitor	5000μF/250 V_{dc}	4000μF/660V_{dc}	5000μF/350V_{dc}	4000μF/500V_{dc}	5000μF/250V_{dc}
IGBT snubber capacitor	9.0μF/600 V_{dc}	6.0μF/900V_{dc}	9.0μF/600V_{dc}	6.0μF/600V_{dc}	9.0μF/600V_{dc}
dc current transfomer	400AT/4 V_{dc}, 0-650AT dc	200AT/4 V_{dc}	400AT/4V_{dc}, 0-650AT dc	200AT/4V_{dc}	400AT/4V_{dc}, 0-650AT dc
SCR module	Dual 2000V/430A	NA	NA	Dual 2200V/80A	Dual 1100V/160A
SCR snubber resistance	10 ohm 2W	NA	NA		
SCR snubber capacitor	0.22μF 250 VAC	NA	NA	0.22μF 1550 VAC	0.22μF 800 VAC

Table 6. Inverter costs for production volume of 10,000 units

	Qty.	Case 1	Case 2	Case 3	Case 4	Comments
Part name						
IGBT module	6	$562	$562	$401	$562	Traci Rutherford, Newark
DC bus capacitor	3	$90	$26	$23	$26	Karen, Carlton Bates
IGBT snubber capacitor	3	$285	$316	$158	$109	Don Atkins, Industrial Electronics
dc current transformer	2	$40	$40	$40	$40	LEM USA
Gate drive board	1	$93	$93	$93	$93	Original estimate reduced for high production volume
Interface drive board	1	$13	$13	$13	$13	Original estimate reduced for high production volume
Digital signal processing board	1	$250	$250	$250	$250	Spectrum Digital
Industrial functions	3	$84	$84	$84	$84	ComAir RotronMX2B1 – Newark
Heat exchanger	1	$127	$127	$175	$175	Electronic Precept (CPA) & CHH Technology for DMIC
Bus structure	1	$40	$40	$40	$40	Based on AIPM estimate by Silicon Power Corporation
Control power supply	1	$35	$35	$35	$35	Joyce, Astrodyne
DMIC control	1	X	X	$16	$16	Original estimate reduced for high production volume
SCR module	6	X	X	$128	$286	Jenn Andrus/DigiKey – 5/18 & 5/19
SCR snubber resistance	3	X	X	$1	$1	Original estimate
SCR snubber capacitor	3	X	X	$35	$18	Stuart Deliduke – provided by Gui-Jia Su
SCR control board	1	X	X	$41	$41	Original estimate reduced for high production volume
Enclosure	1	$25	$25	$25	$25	Based on AIPM estimate by Silicon Power Corporation
Labor & overhead		$406	$398	$385	$448	24.7% of material cost
TOTAL		$2,049	$2,008	$1,942	$2,261	

Estimating Life Cycle Cost Benefits

Intuitively, one might believe that since the DMIC involves six added semiconductors, specifically the SCRs, the DMIC is necessarily at a disadvantage relative to the initial cost of CPA. Moreover, since the SCRs introduce an additional loss mechanism, it would appear that the DMIC would be at a further disadvantage relative to efficiency. It is reasonable to ask whether there is any economic benefit to using the DMIC. This section uses the results of this study to show that the DMIC is not at a disadvantage relative to initial cost. We also preview a life-cycle cost analysis, being conducted by ORNL for an industrial partner, that we expect will show that DMIC has significant life-cycle cost benefits because of reduced total losses in the traction drive.

One conclusion of this study is that it is not difficult to design a SMPM machine having high internal inductance. This is true for the sinusoidal back-emf PMSM as well as the trapezoidal back-emf BDCM. High-inductance machines do not require the DMIC in order to operate over an extended CPSR. However, high-inductance machines do require a larger dc supply voltage in order to sustain rated power at the base speed condition, and the dc supply voltage affects the voltage rating of inverter components. Consider high-inductance "motor 1" in Table 3 and the companion CPA inverter components of "case 1" in Table 6. The total initial cost of this drive is $2290. Alternatively, the lower-inductance motor 3 in Table 3 and the companion DMIC inverter components of case 3 in Table 6 have a total initial cost of $2292. Thus, it is not necessarily true that there is an initial cost penalty associated with the application of DMIC.

Recent research summarized earlier has shown that the DMIC can reduce motor current magnitude during high-speed operation even for a high-inductance motor. Figure 4 shows that during high-speed operation, the rms motor current magnitude at any developed power level is lower for a high-inductance PMSM using DMIC than with the same motor driven by CPA. Reduced-magnitude motor current reduces copper losses, which vary with the square of motor current, and reduces the losses in the inverter, which vary with the first power of motor current. Despite the additional loss mechanism introduced by the SCRs, an overall reduction in total losses can occur when the DMIC is used. ORNL is conducting a study to compare the total energy in the losses of CPA and DMIC over the life of the drive. Total losses depend on speed and power level; consequently, an accurate model of the duty cycle of the drive is essential to performing the analysis. The model being developed includes motor copper losses as well as inverter loss mechanisms, including semiconductor conduction losses, switching losses, and reverse recovery losses. It is expected that the model developed will be sufficiently parametric to allow easy evaluation of the total energy losses over the drive lifetime for a variety of applications.

Conclusions and Future Work

Equations for maximum and minimum inductance limits have been derived for BDCMs with trapezoidal back-emfs when driven with CPA and with DMIC. Similar equations for maximum and minimum inductance limits have been derived for PMSMs with sinusoidal back-emfs. The upper limit must not be exceeded, or the rated power may not be reached. The lower limit, if exceeded, allows the current to rise above the rated limit.

With the copper packing fraction adjusted to maintain constant current density, adjustment of the number of turns per slot and the motor length led to four designs: cases 1 through 4, for surface-mounted radial gap PM motors. These motors covered the required range of inductances from 156 to 1270 uH to compare CPA-controlled and DMIC drive-system costs. Based on the equations for inductance limits, cases 1 and 2 were for CPA control and cases 3 and 4 were for DMIC control. The design code used was ORNL's radial gap design tool.

The original equipment manufacturer cost of the motor and inverter for four cases, based on communication with vendors and current material costs, was completed, showing an average inverter cost of $2065 and an average motor cost of $296. The ratio of inverter cost to motor cost is 7:1. Current technical lore is that this ratio is about 10:1. This does confirm that efforts to reduce converter costs have more room for impact than efforts to reduce motor costs.

A counterintuitive result of the motor cost study was that the cost of cases 3 and 4 with reduced inductance added $111 to the cost. To maintain power and torque, the reduction in the number of turns had to be accompanied by an increase in length, which influences material costs. Refinements can probably lower the cost of cases 3 and 4 slightly, which would raise the inverter-to–motor cost ratio above 7.

The cost of the thyristor-associated components for the DMIC was $221 for case 3 and $362 for case 4. The difference in cost was caused by the large increase in current in case 4 because of the lower back-emf of case 4 with corresponding lower voltage requirements and higher current requirements. Because of higher voltage and lower current, the added SCR costs (DMIC) in the case 3 inverter were compensated by the reduced cost of the IGBTs. The result is that the case 3 DMIC drive system cost, $2292, was only $2 more than the case 1 CPA drive system cost. This suggests that the potential exists to compensate for added SCR costs by carefully sizing the drive system, in this case to have increased voltage. It also attaches a penalty to higher-current systems.

An analysis using a phasor model of a PMSM has provided a relationship showing the amount of current that may be saved at power levels up to rated power and relative speeds over 2 by using the DMIC controller instead of CPA. This information, along with the lifetime duty cycle map of a given application, may be used to estimate cost benefit over the life of a vehicle. This may provide an incentive to employ DMIC.

ORNL and a commercial manufacturer are collaborating through a CRADA to examine both cost and performance justifications for using a traction drive that employs DMIC. The vendor's access to extensive cost information and its experience in cost-benefit analysis, for both initial cost and life-cycle cost, will be focused on a specific application. It will be interesting to compare their conclusions with the conclusions of this analysis.

References

1. J. S. Lawler, J. M. Bailey, and J. W. McKeever, *Extended Constant Power Speed Range of the Brushless DC Motor Through Dual Mode Inverter Control*, ORNL/TM-2000/130, Oak Ridge National Laboratory, UT-Battelle, LLC, 2001.
2. J. S. Lawler and J. M. Bailey, *Constant Power Speed Range Extension of Surface Mounted PM Motors*, U.S. Patent Number 6,236,179 B1, May 22, 2001.
3. Cambier et al., *Brushless DC Motor Using Phase Timing Advancement,* U.S. Patent Number 5,677,605, October 14, 1997.
4. J. S. Lawler, J. M. Bailey, J. W. McKeever, and J. Pinto, "Limitations of the Conventional Phase Advance Method for Constant Power Operation of the Brushless DC Motor," *Conference Proceedings of Southeast Conference on Power Electronics Applications*, 2002.
5. J. S. Lawler, J. M. Bailey, and J. W. McKeever, "Theoretical Verification of the Infinite Constant Power Speed Range of the Brushless DC Motor Driven by Dual Mode Inverter Control," presented at the 7th IEEE Workshop on Power Electronics in Transportation, Auburn Hills, Michigan, October 24–25, 2002.
6. J. S. Lawler, J. M. Bailey, J. W. McKeever, and J. Pinto, "Extending the constant Power Speed Range of the Brushless DC Motor through Dual-Mode Inverter Control," *IEEE Trans.actionser Electronics*, **19**(3) May 2004.
7. J. Pinto, "Analysis of Extended Constant Power Speed Range of the Permanent Magnet Synchronous Machine Driven by Dual Mode Inverter Control," Ph.D. Dissertation, The University of Tennessee, Knoxville, Tennessee, August 2001.
8. T. M. Jahns and V. Caliskan, "Uncontrolled Generator Operation of Interior PM Synchronous Machines Following High-Speed Inverter Shutdown," pp 1347–1357 in *IEEE Trans. Industry Applications*, **35**(6), November/December 1999.
9. J. W. McKeever, "Inverter Control for High CPSR, System Design, Safety, and Extra Power Delivery," DOE Office of FreedomCAR and Vehicle Technologies Program and ORNL Power Electronics and Electric Machinery Research Center Merit Review, June 5, 2003.
10. P. Pillay and R. Krishman, "Application Characteristics of Permanent Magnet Synchronous Motors and Brushless DC Motors for Servo Drives," pp.380–390 in *Proceedings of the 1987 IEEE Annual Meeting*, Atlanta, Georgia, October 19–23, 1987.
11. D. C. Hanselman, *Brushless Permanent-Magnet Motor Design,* McGraw-Hill, Inc., New York ISBN 0-07-026025-7, 1994.

E. Z-Source Power Converter

Donald J. Adams
Oak Ridge National Laboratory
National Transportation Research Center
2360 Cherahala Boulevard
Knoxville, Tennessee 37932
Voice: (865) 946-1321; Fax: (865) 946-1262; adamsdj@ornl.gov

DOE Technology Development Manager: Susan A. Rogers
Voice: 202-586-8997; Fax: 202-586-1600; E-mail: susan.rogers@ee.doe.gov

ORNL Program Manager: Laura D. Marlino
Voice: 865-946-1245; Fax: 865-946-1262; E-mail: marlinold@ornl.gov

Objectives

- Develop and demonstrate a low-cost, high-efficiency, reliable inverter for traction drives of hybrid electric and fuel-cell–powered vehicles.

Approach

- Investigate the current inverter systems for traction drives and propose a new Z-source inverter traction drive system.
- Perform a comprehensive comparison, model development, and computer simulation of the existing topologies versus the new Z-source inverter.
- Design and prototype a 50-kW Z-source inverter for induction motor (IM) traction drive to prove the concept.
- Perform testing and a performance study of the Z-source inverter prototype

Accomplishments

- Developed detailed specifications for a Z-source inverter prototype for hybrid vehicle traction drive applications. A comprehensive cost comparison, model development, and computer simulation were performed and a report was issued.
- Began parts procurement and assembly of the 55-kW prototype.

Future Direction

- Evaluate the prototype initially at Michigan State University (MSU) and then more fully at ORNL.

Publications

1. Fang. Z. Peng, “Z-source Inverter for Adjustable Speed Drives,” presented at the IEEE/PESC Aachen, 2004.
2. Fang. Z. Peng, Miaosen Shen, and Zhaoming Qian, “Maximum Boost Control of the Z-

Source Inverter," presented at the IEEE/PESC Aachen, 2004.
3. Xupeng. Fang, Zhaoming Qian, Qi Gao, Bin Gu, Fang. Z. Peng, and Xiaoming Yuan, "Current Mode Z-Source Inverter-Fed ASD System," presented at the IEEE/PESC Aachen, 2004.
4. Miaosen Shen, Jin Wang, Alan Joseph, Fang Z. Peng, Leon M. Tolbert, and Donald J. Adams, "Maximum Constant Boost Control of the Z-Source Inverter," presented at the IEEE/IAS Seattle, 2004.
5. Miaosen Shen, Alan Joseph, Jin Wang, Fang Z. Peng, and Donald J. Adams, "Comparison of Ttraditional Inverter and Z-Source Inverter for Fuel Cell Applications," submitted to IEEE WPET, 2004.
6. Fang. Z. Peng, *Z-Source Inverter for Hybrid Electric and Fuel Cell Vehicles Tasks 1 & 2 Report: Development of Specifications and Comparison of Z-Source versus Existing Inverters*, Task Completion Report, March 31, 2004.

Patents

The Z-Source converter intellectual property predates this project and is owned by MSU. The patent application was filed on June 10, 2003, assigned application number 10/458,564 and is titled "Impedance Source Power Converter."

Technical Discussion

The goal of this work is to develop and demonstrate a low-cost, high-efficiency, reliable inverter for traction drives of hybrid electric and fuel-cell–powered vehicles. This goal is being pursued with the development of the Z-source power converter as a viable means of combining a dc-dc converter and an inverter.

A new converter topology and theory called the Z-source power converter was recently invented at MSU. The Z-source converter comprises an impedance network to couple the main converter circuit to the power source or load. The unique feature offered by the Z-source network is that unlike the traditional V-source or I-source, it can be open- and short-circuited, which provides a mechanism for the main converter circuit to step up or step down voltage as desired. The Z-source network provides great flexibility for the source, main circuit, and load. ORNL funded MSU in FY 2004 to further develop, design, fabricate, and evaluate a 55-kW Z-source converter, which will be completed in late FY 2005.

Currently, two existing inverter topologies exist that are used for hybrid electric and fuel cell vehicles: the conventional three-phase pulse width modulation (PWM) inverter and three-phase PWM inverter with a dc-dc boost front end. Because of a wide voltage change and the limited voltage level of the battery and/or fuel cell stack, the conventional PWM inverter topology imposes high stresses to the switching devices and motor and limits to the motor's constant power speed ratio (CPSR). The dc-dc boosted PWM inverter topology can alleviate the stresses and limitations, but it suffers from problems such as high cost and complexity associated with the two-stage power conversion. This project is to investigate and develop a new inverter topology called the Z-source inverter for hybrid electric and fuel cell vehicles. The three topologies are shown in Fig. 1.

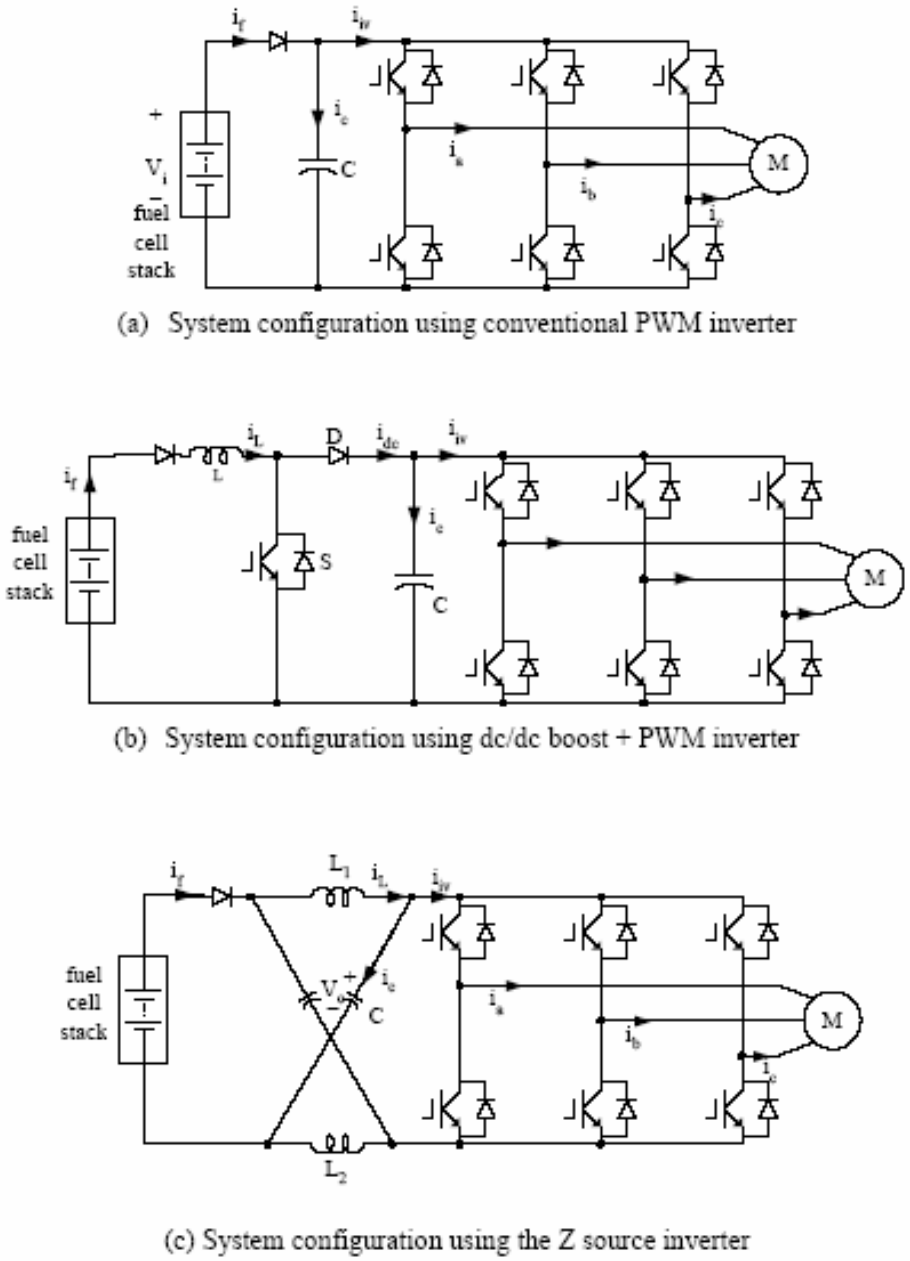

(a) System configuration using conventional PWM inverter

(b) System configuration using dc/dc boost + PWM inverter

(c) System configuration using the Z source inverter

Fig. 1. Three inverter system configurations for comparison.

As the first phase of the project, ORNL has identified and developed detailed specifications of a fuel cell vehicle for this investigation. Specifications include input V-I characteristics (Fig. 2) and output voltage, stator current, and output power characteristics with respect to output frequency (Fig. 3 shows the motor to be used for the traction drive).

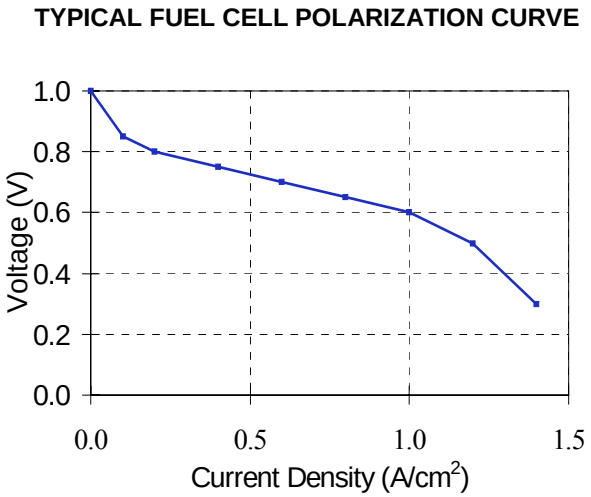

Fig. 2. Fuel cell characteristic curve.

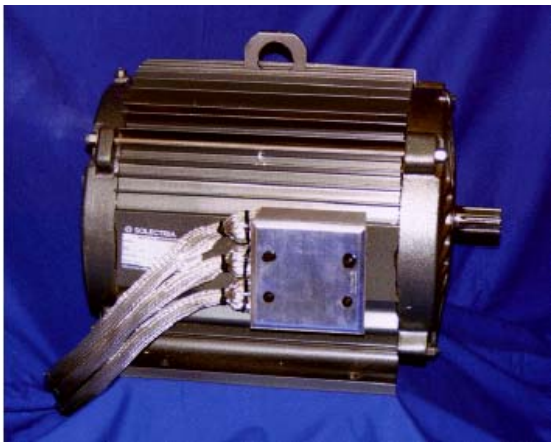

Fig. 3. Inverter load: Solectria AC55 IM.

A comprehensive comparison was made of the conventional PWM inverter, the PWM inverter plus dc-dc boost, and the Z-source inverter—in terms of switch device power (SDP), cost, efficiency, and CPSR—using computer simulations of each topology. The comparison results obtained show that Z-source inverter

- Improves inverter conversion efficiency by 1% over the two existing inverters (Fig. 4) and inverter/motor system efficiency by 2 to 15% over the conventional PWM inverter (Fig. 5).
- Reduces the average current SDP by 15%, which leads to cost reduction (Table 1). The actual price quote from a distributor also demonstrates the cost reduction.
- Extends CPSR by 1.68 times over the system driven by the conventional PWM inverter.
- Has high reliability due to a lack of shoot-through problem.

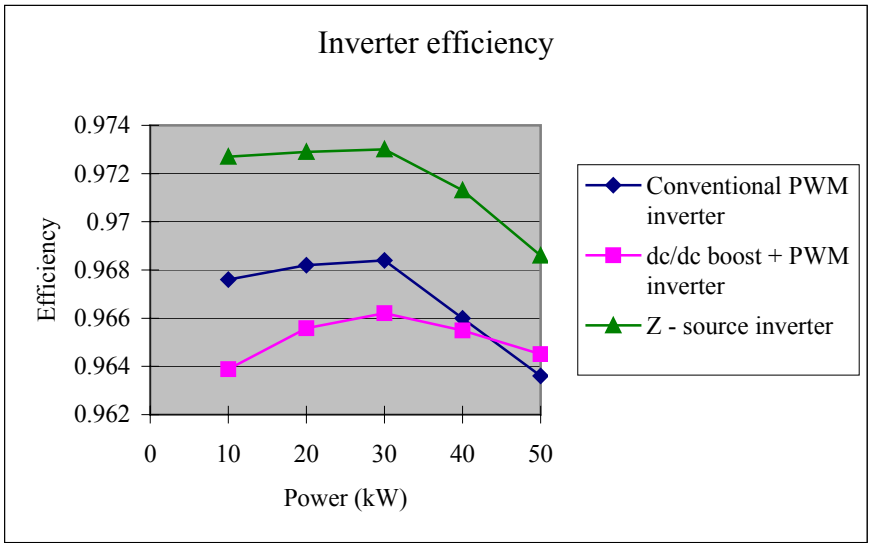

Fig. 4. Inverter efficiency comparison.

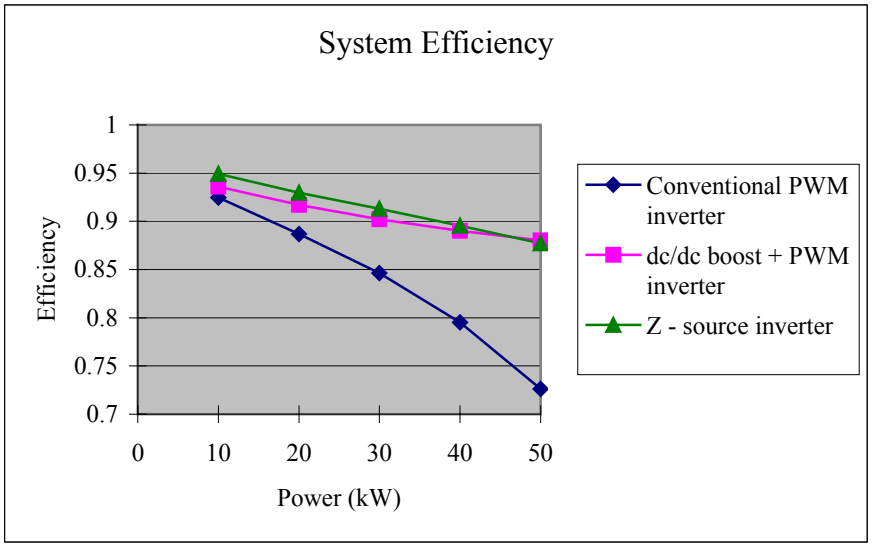

Fig. 5. Inverter and motor system efficiency comparison.

Table. 1. Inverter systems SDP and actual price comparison

Inverter systems	Total average SDP (kVA)	Total peak SDP (kVA)	Actual device price
Conventional PWM inverter	238	747	$808.8
dc-dc boost plus PWM inverter	225	528	$509.6
Z-source inverter	199	605	$308.88

Conclusions

The progress report issued in March contains much more detail and indicates that the Z-Source holds promise as a buck-boost drive for hybrid vehicle applications. The full-scale prototype has been designed, parts are being procured, and assembly is under way. Evaluation tests will then be conducted initially at MSU and then at ORNL. The project is proceeding according to the original schedule and cost and is planned to conclude at the end of FY 2005.

F. AEMD Validation Testing and Contract Support

Samuel C. Nelson, Jr.
Oak Ridge National Laboratory
National Transportation Research Center
2360 Cherahala Boulevard
Knoxville, TN 37932
Voice: 865-946-1327; Fax: 865-946-1262; E-mail: nelsonscjr @ornl.gov

DOE Technology Development Manager: Susan A. Rogers
Voice: 202-586-8997; Fax: 202-586-1600; E-mail: susan.rogers@ee.doe.gov

ORNL Program Manager: Laura D. Marlino
Voice: 865-946-1245; Fax: 865-946-1262; E-mail: marlinold@ornl.gov

Objectives

- Reduce the cost, weight, and volume of electric machinery and increase the reliability.
- Provide technical support to the automotive electric motor drive (AEMD) contracts manager.
- Plan and organize the testing phases of the AEMD program.

Approach

- Assess the conformance to established standards and use the results to determine the suitability of the AEMD technology for automotive applications.

Accomplishments

- Developed a series and a parallel machine for traction drive applications.

Future Direction

- Define new tasks and provide ORNL support in response to future technical needs at the DOE Office of FreedomCAR.

Publications

1. S. C. Nelson, *Performance Testing the Series Machine from Delphi—April 2004*, ORNL/TM-2004/136, Oak Ridge National Laboratory, UT-Battelle, LLC, August 2004.
2. S. C. Nelson, *Performance Testing the Series Machine from Delphi—October 2003*, ORNL/TM-2003/271, Oak Ridge National Laboratory, UT-Battelle, LLC, December 2003.

Technical Discussion

Introduction

The AEMD subtask supports DOE's Program effort to research, develop, and demonstrate a traction motor for use in advanced hybrid electric vehicles that meets the goals and schedule of Office of FreedomCAR. To achieve these goals, the traction motor must meet the following requirements: reductions in size, weight, and manufacturing cost and improvements in efficiency and reliability.

ORNL's role for the AEMD project was to provide technical support to DOE, plan and organize the testing phases of the AEMD program, and validate the technology's conformance with the AEMD specification requirements. ORNL has produced a plan for testing of the AEMD pre-production prototypes according to the specifications and standard test procedures called out in the solicitation. ORNL has specified the equipment and instrumentation required to meet the needs of the test plan. The most cost-effective methods of testing the AEMDs was considered in the decision to purchase test equipment, leverage the use of equipment from related work, or use facilities elsewhere. A large portion of the testing facilities and procedures was leveraged from the automotive integrated power module project.

2004 Activities

During FY 2004, the series electric machine was tested to verify performance capability. The electric motor is a 12-pole, three-phase permanent magnet machine with an outer-rotor configuration. The machine has a nominal voltage rating of 325 V, a continuous power rating of 30 kW, and a peak power rating of 55 kW. The AEMD unit operates at a base speed of 6000 rpm with a maximum rated speed of 12000 rpm. The motor is liquid cooled and has a thermistor embedded in the stator to allow the stator temperature to be monitored. The insulation of the electric motor is Class H and is rated up to 180°C. Figure 1 shows Delphi's deliverable series machine.

The series electric (motor only) machine without the gear assembly and lubrication was tested October 20–24, 2004 at Delphi. The efficiency of the electric machine during continuous power tests was in the 94 to 97% range. Continuous power tests were performed with 70ºC coolant with a flow rate of 2 gallons per minute. The efficiency of the machine decreased at higher speeds with low loads, as would be expected. The stator temperature stabilized in the 100 to 140ºC range during most of the continuous power tests. The test results are documented in ORNL/TM-2003/271, *Performance Testing the Series Electric Machine from Delphi—October 2003*.

Testing of the deliverable series electric machine was performed at the development dynamometer test cell at Delphi during April 2004. The configuration of the series electric machine that was tested included a reduction gear assembly and lubrication fluid. Torque versus speed mapping of the machine was performed with dc link voltages of 325 and 200 V_{dc}. The machine was tested from 500 rpm to 12,000 rpm in interval of 500 rpm with torque loads of 100, 80, 60, 40, and 20%, and at 10% of rated torque.

The deliverable series machine produced continuous and peak mechanical power from 3000 to 12,000 rpm with the minimal dc link voltage, 200 V_{dc}. The machine developed at least 590 Nm from approximately 500 to 2500 rpm during the tests with the minimal dc link voltage. The machine demonstrated efficiencies of ≥93% from 2997 to 6003 rpm with mechanical loads ≥30 kW, and from 3500 to 6001 rpm with mechanical power levels ≥55 kW with the minimal dc link voltage. The machine has slightly higher efficiencies when operated with a dc link voltage of 325 V_{dc}. At mechanical power levels ≥55 kW, the machine demonstrated efficiencies of ≥93% from 3511 to 7507 rpm and of ≥90% from 2496 to 9528 rpm with a dc link voltage of 325 V_{dc}.

Fig. 1. Deliverable series machine from Delphi.

Table 1 presents the measured parameters of the Delphi motor along with the FCVT goals, with a column indicating whether those goals were achieved.

Table 1. Comparison of goals vs. actual for Delphi series PM motor

Parameters	Goal	Actual	Meet goal
Continuous power (kW)	30	30	Yes
Peak power (kW)	53	53	Yes
Cost ($)	$450	$477	No
Volume (l)	11	9.7	Yes
Weight (kg)	35	38.9	No
Power density (kW/kg)	1.5	1.4	No
Efficiency (%)	93	85	No

5. CONTRACTED COMMERCIAL DEVELOPMENT OF NEW TECHNOLOGIES

A. dc-to-dc Converter (Ballard Subcontract)

R. L. Smith
Oak Ridge National Laboratory
National Transportation Research Center
2360 Cherahala Boulevard
Knoxville, TN 37932
Voice: 865-946-1205; Fax: 865-946-1214; E-mail: smithrl4@ornl.gov

DOE Technology Development Manager: Susan A. Rogers
Voice: 202-586-8997; Fax: 202-586-1600; E-mail: susan.rogers@ee.doe.gov

ORNL Program Manager: Laura D. Marlino
Voice: 865-946-1245; Fax: 865-946-1262; E-mail: marlinold@ornl.gov

Objectives

- Provide the functional and performance requirements for a dc-dc converter in a broad range of applications such as hybrid and fuel cell-based vehicles.

- Identify the key barriers in the existing design approach and address them with appropriate topology, employing innovative design methodology, and developing process technology.

- Develop a novel dc-dc converter topology that can handle high current and high coolant temperature and that achieves high packaging density.

- Design and build a 5-kW dc-dc buck converter for a hybrid or fuel cell vehicle.

Approach

- Perform a detailed design study to identify the key requirements for achieving DOE's objectives:
  – Higher efficiency
  – High coolant and ambient temperature capability
  – High reliability
  – Smaller volume and lower weight
  – Lower cost

- Pursue three major technology development areas: converter topology; integrated, module-based dc-dc converter; and planar magnetics with enhanced cooling

Accomplishments

- Conducted computer simulations that indicate that the target efficiency can be achieved and that smaller passive components can be used because of the advantages (such as interleaving) of the selected topology.

- Developed a segmented technology to prove the concept.

- Built a segmented prototype and conducted preliminary tests. The preliminary results suggest that (1) the segmented topology works, (2) the process technology needed for a module-based dc-dc converter is well developed, and (3) the innovative planar magnetics technology developed in this program functions well.

Future Direction

- Characterize this segmented prototype in detail and select key components for the final DOE design.
- Initiate a detailed cost study to assess the cost for high-volume production of this product.
- Build and test the final prototype.

Introduction

DOE's Office of FreedomCAR and Vehicle Technologies supports R&D efforts for advanced vehicles to reduce a growing dependency on oil and to reduce pollution levels. The dc-dc converter is an integral electronic part/subsystem of both hybrid and fuel cell vehicles, and advancement in this technology to increase efficiency and power density is critical in achieving DOE's goal. This work is being done in close coordination with domestic automotive companies in order to develop technologies that can be implemented at low production costs.

This work subcontracted to Ballard Power Systems provided the functional and performance requirements for a dc-dc converter in a broad range of applications such as hybrid and fuel cell-based vehicles.

The present dc-dc converter technology is built using multiple discrete power devices soldered onto the printed circuit board (PCB), traditional bulky transformers, inductors, and a large number of interconnects. This design approach results in a converter with poor performance, reduced reliability, and high manufacturing cost. The automotive industry cannot mass-produce hybrid and fuel cell vehicles unless these converters can become modular, compact, efficient, reliable, and cheap. The present proposal to design and built a 5-kW dc-dc buck converter for a hybrid and fuel cell vehicle identifies the key barriers in the existing design approach and breaks those barriers by applying appropriate topology, employing innovative design methodology, and developing process technology. A novel topology of the dc-dc converter is being developed that can handle high current and high coolant temperature. The proposed topology achieves high packaging density by integrating key components into a insert-molded housing construction, by eliminating unnecessary components, and by reducing the total component count. In addition to those advantages, the new dc-dc converter can be manufactured at high volume, eliminating

costly manual assembly time. Because the design is modular, changing the building blocks of the converter without major change in the architecture can alter the power.

Technical Discussion

- A detailed design study was conducted to identify the key requirements for achieving DOE's objectives for the dc-dc converter. They were identified as
  – High efficiency (92%)
  – High coolant and ambient temperature capability
  – High reliability (15 years/150,000 miles)
  – Small volume (5 L) and low weight (6 Kg)
  – Low cost ($75/kW)

The study concluded that these stringent requirements cannot be achieved using the traditional approach and technology. Three major technology development areas have been proposed to accomplish DOE's goals:

1. Converter topology

- High-power application
- Lower components rms current stress through the use of interleaving
- Reduced ripple current on capacitors through the use of interleaving
- Lower power loss through the use of soft-switching and bare dies
- Smaller magnetics through the use of high switching frequency
- Low electromagnetic interference owing to use of integrated power devices and magnetics

2. Integrated module-based dc-dc converter

- Enhanced thermal performance
- Reduced number of devices
- Increased reliability
- Increased integration

3. Planar magnetics with enhanced cooling

- Higher power density due to enhanced cooling
- Some power devices integrated with transformer winding
- Optimized HF loop
- Well-controlled leakage inductance

The proposed topology and its advantages are illustrated in Fig. 1.

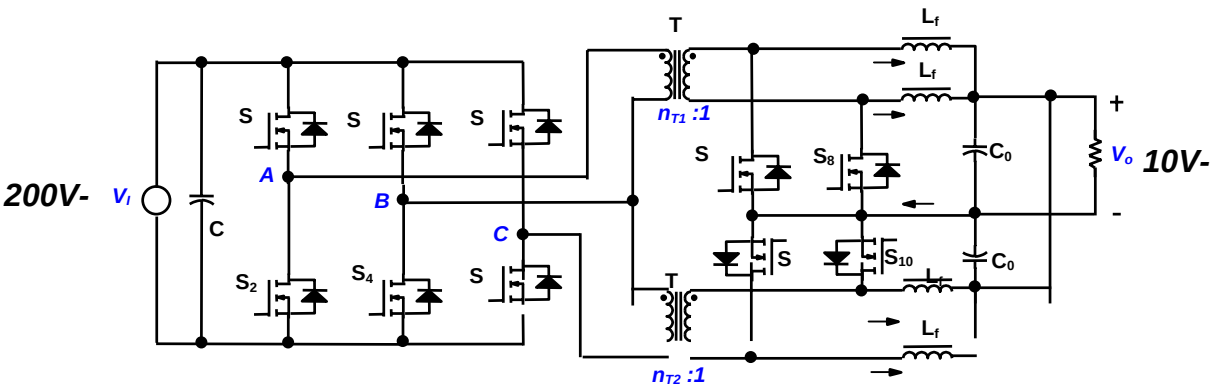

Fig. 1. The proposed dc-dc converter topology and its advantages.

Advantages of the Topology

1. The power rating for transformer T is half that of option 1.
2. Current rating for inductor Lf1–Lf4 is a quarter of the load current.
3. Ripple current on filter capacitors Ci and Co is small.
4. Packaging for metal oxide semiconductor field effect transistor (MOSFET) switches S5–S8 (current doubler) is robust because the drain of the MOSFET can be directly soldered onto the DBC-based transformer winding.
5. The disadvantage of the current doubler rectifier is that 100-V MOSFETs are needed instead of 50-V MOSFETs in option 1. But dealing with voltage is easier than dealing with current for silicon device packaging for the same power rating.

A packaging drawing of the proposed dc-dc converter is shown in Fig. 2.

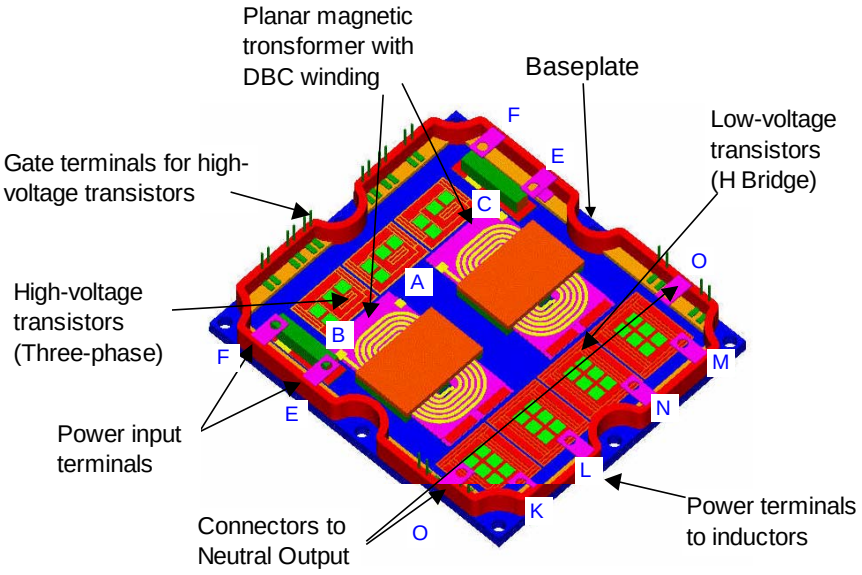

Fig. 2. Packaging drawing of the dc-dc converter.

Preliminary simulation results for the selected topology indicate that the target efficiency can be achieved. The simulation results also proved that smaller passive components can be used owing to the advantages of the selected topology (such as interleaving). To prove the concept, a segmented topology (approximately half the power with one transformer, two inductors, four H.V. switches and two low voltage switches) has been developed. The objectives are to verify that the key technologies work, the interaction among different components is well understood, and design trade-offs are identified. After this stage is accomplished, the final design can progress with selected components with greater confidence.

We built a segmented prototype in November 2004, and we conducted some preliminary tests. The test results are explained in progress report 5B. The preliminary results suggest that (1) the segmented topology works, (2) the process technology needed for module-based dc-dc is well developed, and (3) the innovative planar magnetics technology developed in this program functions well.

B. System on a Chip (Automotive Integrated Electronics Corporation Subcontract)

R. L. Smith
Oak Ridge National Laboratory
National Transportation Research Center
2360 Cherahala Boulevard
Knoxville, TN 37932
Voice: 865-946-1205; Fax: 865-946-1214; E-mail: smithrl4@ornl.gov

DOE Technology Development Manager: Susan A. Rogers
Voice: 202-586-8997; Fax: 202-586-1600; E-mail: susan.rogers@ee.doe.gov

ORNL Program Manager: Laura D. Marlino
Voice: 865-946-1245; Fax: 865-946-1262; E-mail: marlinold@ornl.gov

Objectives

- Provide the functional and performance requirements for a system-on-a-chip (SoC) dual motor controller for use in a broad range of applications such as hybrid and fuel cell-based vehicles.
- Reduce cost through the integration of functions and inclusion of necessary external circuitry within a single semiconductor device and the development of a flexible modular control system suitable for use with drive systems of varying power levels.
- Through the reduction in parts count and manufacturing efforts, realize a cost reduction of 40 to 60% in high-volume production.

Approach

- Initiate a comprehensive study on how the motor controller semiconductor will be designed and fabricated to meet the technical requirements.
- Identify a process and foundry capable of manufacturing the die to the specifications presented and in the quantity required.
- Identify and make arrangements to secure or develop macros necessary for the selected process.
- Determine packaging options and assess physical issues involved with packaging and layout.
- Develop a design flow plan and determine test methodologies.
- Perform a detailed cost study to satisfactorily demonstrate the seller's ability to reach cost targets.

Accomplishments

- Showed that the development of an SoC for meeting the technical objectives is feasible.
- Conducted a detailed cost study that projected a cost of less than $30/unit, exceeding the cost target of $90/unit However, the non-recurring engineering costs are estimated at over $2 million.
- Established a proposed schedule of the development effort, along with major milestones.

Future Direction

- Determine whether to pursue Phase II development of the SoC.

Publications

1. R. J. Gauer and R. F. Emnett, *Research & Development of Fuel Cell & Advanced Vehicle Power Electronics & Machinery Applications*, Final Report, Automotive Integrated Electronics Corporation, September 23, 2004.

Introduction

DOE's Office of FreedomCAR and Vehicle Technologies supports R&D efforts for advanced vehicles to reduce a growing dependency on oil and continually elevating pollution levels. This work is being done in close coordination with the domestic automotive industry with the goal of developing and demonstrating significant technological advancements at low production costs.

This work, subcontracted to Automated Integrated Electronics Corp. (AIEC), provided the functional and performance requirements for an SoC dual motor controller for use in a broad range of applications such as hybrid and fuel cell-based vehicles.

Current motor controller technology revolves around commercially available digital signal processors (DSPs). These chips are able to perform the complicated high-speed mathematical functions necessary for motor control. In some cases, DSP manufacturers have included additional circuitry within the chip, specifically for use in control applications. However, external circuitry is still required to accomplish all the functions necessary for efficient motor control. This activity outlines the functional and performance requirements for a dual traction motor controller SoC (see Fig. 1). The proposed architecture is intended to achieve cost reduction through the integration of functions and the inclusion of necessary external circuitry within a single semiconductor device. Additionally, cost reduction will be realized by the development of a flexible modular control system suitable for use with drive systems of varying power levels

Through the reduction in parts count and manufacturing efforts, it is hoped a cost reduction of 40 to 60% can be realized in high-volume production.

Technical Discussion

A comprehensive study was initiated on how the motor controller semiconductor will be designed and fabricated to meet the technical requirements. Technical barriers were discussed along with potential solutions. Any issues concerning the use of the proposed technology relevant to a HEV application were also identified.

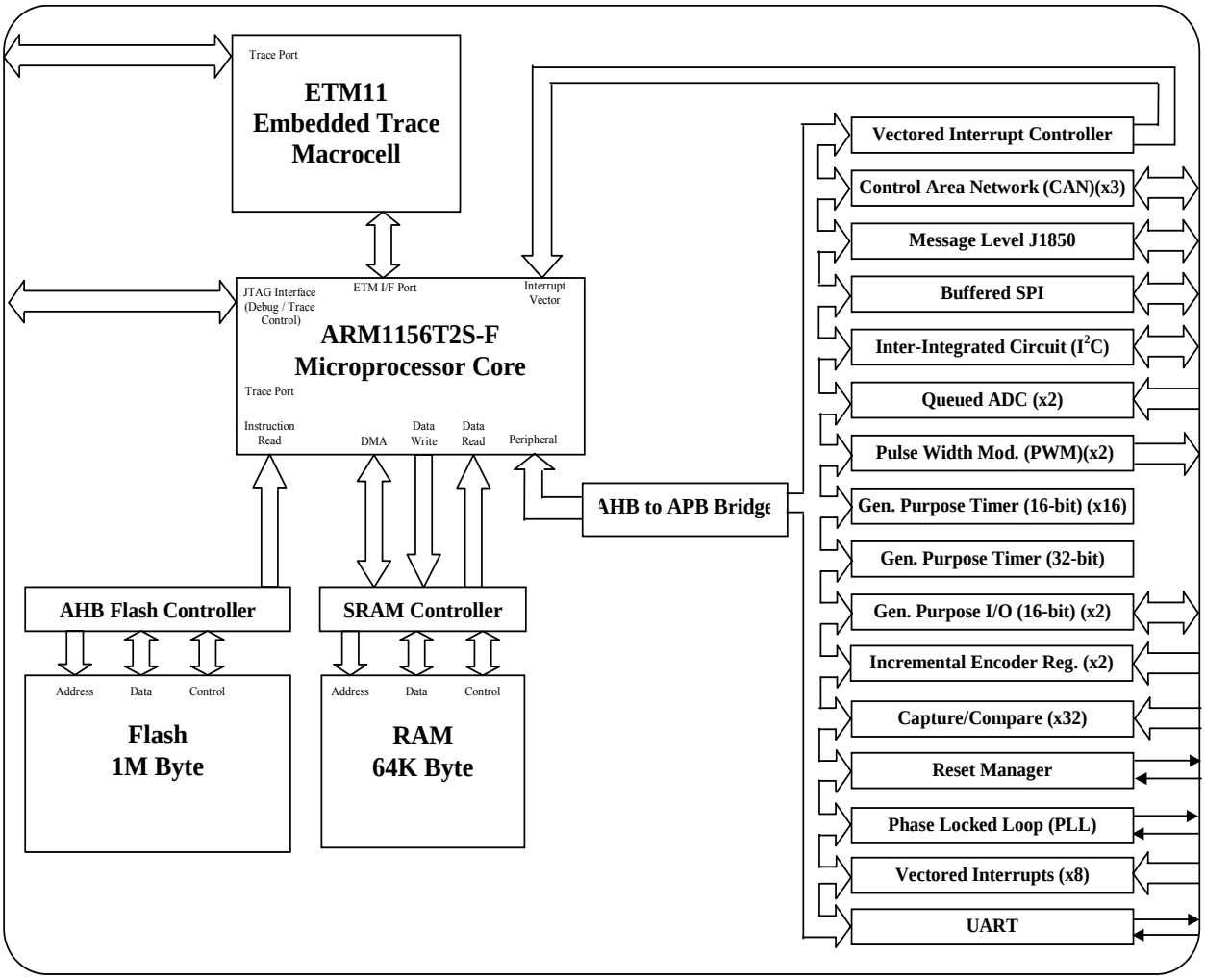

Fig. 1. Top-level diagram of the AIEC SoC motor controller.

A proposed schedule of the development effort has been established along with major milestones.

This work has shown that the development of an SoC for meeting the technical objectives is feasible. Furthermore, this work has shown that the unit cost for a SoC far exceeds cost expectations targeted at $90/unit with a projected cost of less than $30/unit. However, the non-recurring engineering (NRE) costs are estimated at over $2 million.

A process and foundry capable of manufacturing the die to the specifications presented and the quantity required were identified. All hard macros necessary for the selected process were identified, and arrangements were made to secure necessary macros, either through the foundry or via third parties. Any macros that need to be developed in house were identified and time was allotted in the scheduling plan. The elevated operating temperatures required for this chip may necessitate remodeling of macros. These considerations were included in the development study. A tentative power estimate was made, and specific packaging options have been presented. If packaging is done ‘out of house’ potential subcontractors will be identified. Any physical issues

involved with packaging and layout will be assessed. A design flow plan will be developed, and test methodologies will be determined (Fig. 2).

A detailed cost study was performed to satisfactorily demonstrate the seller's ability to reach cost targets. The study identified critical or key costing issues. Viable methods of dealing with barriers in order to meet cost goals were proposed. The study included projections of costs for annual production volumes of 100,000, 500,000, and 1,000,000.

This work has shown that the development of a SoC for meeting the technical objectives is feasible. Furthermore, this work has shown that the unit cost for a SoC far exceeds cost expectations targeted at $90/unit with a projected cost of less than $30/unit. However, the non-recurring engineering (NRE) costs are estimated at over $2 million.

Future Direction

A determination must be made whether to pursue the Phase II development of the SoC.

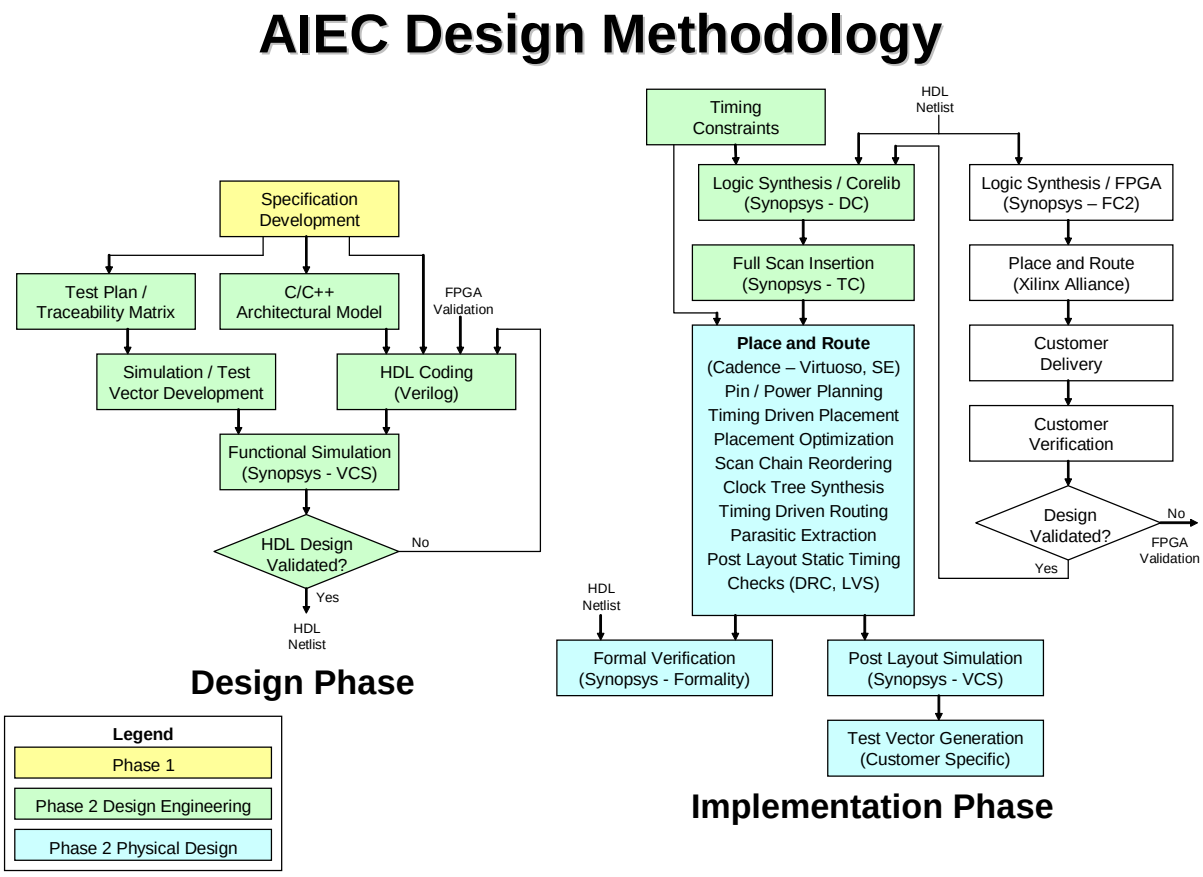

Fig. 2. Design flow diagram for the SoC motor controller.

6. POWER ELECTRONICS CROSSCUT ACTIVITIES FOR EERE AND OETD

R. L. Smith
Oak Ridge National Laboratory
National Transportation Research Center
2360 Cherahala Boulevard
Knoxville, TN 37932
Voice: 865-946-1205; Fax: 865-946-1214; E-mail: smithrl4@ornl.gov

DOE Technology Development Manager: Susan A. Rogers
Voice: 202-586-8997; Fax: 202-586-1600; E-mail: susan.rogers@ee.doe.gov

ORNL Program Manager: Laura D. Marlino
Voice: 865-946-1245; Fax: 865-946-1262; E-mail: marlinold@ornl.gov

Objectives

- Review, explore, discuss, and promote the best practices in power electronics science and technology to enhance the ability of DOE Energy Efficiency and Renewable Energy (EERE) and Office of Electric Transmission and Distribution (OETD) program offices to reach their energy security and environmental goals while
  - Limiting duplication of effort to reduce R&D costs
  - Establishing direction for future power electronics projects
  - Identifying opportunities for collaboration
  - Adopting successful technologies quickly
  - Assisting program offices in staying abreast of worldwide power electronics innovations
  - Building synergism for future collaboration on
    - High-impact technology (e.g., silicon carbide, manufacturability)
    - Global issues (e.g., cost and weight reduction, U.S. leadership)
    - Workshops
    - Interfaces, codes, and standards
    - Identifying best practices and capabilities
    - Establishing a website

Approach

- Set up a Power Electronics Crosscut Team to examine the issues and identify technology requirements, gaps, and areas of common interest among EERE and OETD. The team met periodically during the year as a group to
  - Catalog DOE projects with power electronics activities
  - Identify power electronics technology, facility, equipment, and skill gaps in order to guide DOE investments
  - Conduct in-depth reviews of selected projects for solar inverters, motors, power semiconductors, thermal management technologies, and similar power devices
  - Visit national laboratories with power electronics capabilities

Accomplishments

- Held four crosscut meetings in Washington, D.C., where representatives from the EERE and OETD offices discussed opportunities for collaboration, and heard special presentations on
  - DOE System-Driven Approach Inverter Workshop—Dan Ton (DOE) and Ward Bower (Sandia National Laboratories),
  - Power electronics, electrical machinery, and thermal management—Laura Marlino (ORNL),
  - EERE and OETD power electronics activities—all representatives participating
  - WBG materials—Burak Ozpineci (ORNL).

- Participated in crosscut meetings at the National Renewable Energy Laboratory and discussed collaboration activities with researchers from
  - Solar Energy Research Facility
  - Thermal Test Facility
  - Photovoltaic Outdoor Test Facility
  - National Wind Technology Center

- Visited the Sandia National Laboratories to discuss
  - Power electronics
  - Battery testing
  - Polymer film capacitors
  - GaN transistors
  - Inverter certification and reliablity

- Based on the discussions from the various meetings and reviews, identified four categories of potential interest and focus:
  - Power conversion and conditioning—includes inverters, dc-dc converters
  - Electric machines and magnetics—includes motors, generators, alternators, magnets
  - Semiconductor devices and packaging—includes power semiconductors, switches, capacitors
  - Sensors and controls for monitoring and control of electric power, voltage, current, fluid velocity, temperature, etc.

Future Direction

- Identify potential power electronics research topics that are exploratory, long-term, and shorter-term and identify strategies for implementing these topics.
- Focus on identifying opportunities for jointly funding projects among the EERE and OETD offices.
- Identify extreme parameters (e.g., voltage, current, power) and environmental conditions (e.g., temperature) for EERE and OETD applications.
- Identify best practices in power electronics.
- Establish a web site.

- Hold a workshop.
- Identify and replicate good strategies from other crosscut activities.

Publication

1. R. L. Smith and R. J. Kevala (Sentech, Inc.), *Power Electronics Crosscut Activities for EERE and OETD: Final Report*, September 30, 2004.

Participants

The Power Electronics Crosscut Team included representatives from several DOE programs and offices.

Energy Efficiency and Renewable Energy
- Biomass—Doug Kaempf, John Ferell
- Building Technologies—Jim Rannels, Jim Broderick
- Distributed Energy—Pat Hoffman
- FreedomCAR and Vehicle Technologies—Susan Rogers, Laura Marlino, Graham Hagey, Russ Kevala, Richard Smith, Mike Lloyd, Ray Fesslor, Mike Laughlin, Dick Ziegler
- Hydrogen, Fuel Cells, and Infrastructure Technologies—Pat Davis, Valri Lightner
- Industrial Technologies—Buddy Garland, Jim Quinn, Gideon Varga, Isaac Chen, Peter Salmon
- Geothermal—Ray LaSala
- Solar—Dan Ton, Alec Bulawka
- Wind and Hydropower—Stan Calvert, Charles Newcomb

Office of Electric Transmission and Distribution
- Electric Power Systems R&D—Bill Parks, Imre Gyuk

Background

Figure 1 shows that the voltage and power needs of the power electronics activities vary over a very wide range. Therefore, more in-depth analysis is needed to find areas of collaboration for the development of power semiconductors, heat dissipation devices, and sensors and controls that may be applicable over wider ranges or that are amenable to being packaged in modules that can be cascaded or connected in series to obtain the required performance.

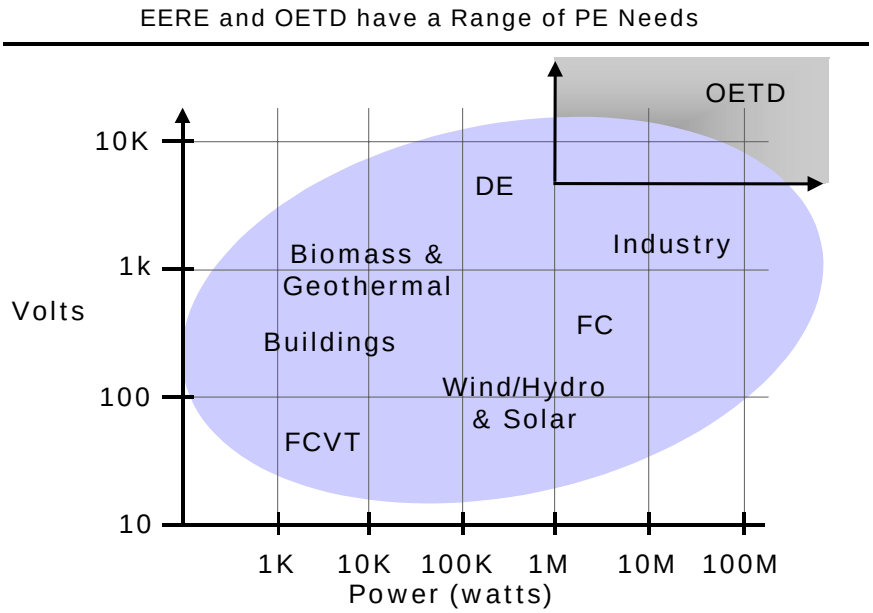

Fig. 1. Range of voltage and power needs.

Figure 2 shows that there are areas of overlap in the voltage and power needs of the power electronics activities within various programs. These areas of overlap should be examined carefully to explore collaboration of effort and funding to obtain synergies.

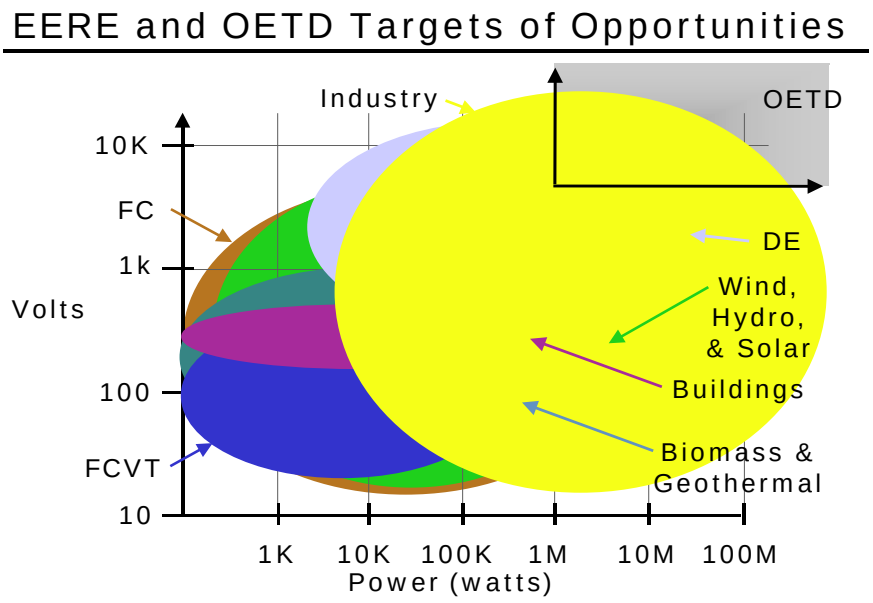

Fig. 2. Overlaps in voltage and power needs.

7. TECHNOLOGY ASSESSMENTS

Kathleen Gambrell
Oak Ridge National Laboratory
National Transportation Research Center
2360 Cherahala Boulevard
Knoxville, TN 37932
Voice: 865-946-1286; Fax: 865-946-1381; E-mail: gambrelkp@ornl.gov

DOE Technology Development Manager: Susan A. Rogers
Voice: 202-586-8997; Fax: 202-586-1600; E-mail: susan.rogers@ee.doe.gov

ORNL Program Manager: Laura D. Marlino
Voice: 865-946-1245; Fax: 865-946-1262; E-mail: marlinold@ornl.gov

Objectives

- Assess technologies for power electronics and machinery that improve performance and dramatically decrease system costs for light and heavy vehicles. Specifically,
  - reducing the size of passive components of inverters
  - reducing permanent magnet (PM) manufacturing costs
  - addressing vehicle system and subsystem interactions with power electronics
  - establishing the feasibility and reliability of high-temperature power/control electronics for hybrid electric vehicles (HEVs)

Approach

- Request assistance from 12 assessors from the private sector and academia in developing assessments of various technologies that are critical to DOE's mission. Each assessment had the following components:
  - Summary of the state of the art for that technology.
  - Technical options that should be considered to meet the FreedomCAR requirements.
  - Technological gaps that currently present barriers to the use of those options.
  - R&D approaches that could overcome those barriers, including estimates of the challenges, risks, amount of effort, cost, and time that will be required.

Accomplishments

- Received assessments from the organizations listed. This report is a summary of the full reports submitted by each assessor. For more details, full reports are available from the ORNL program manager.
  - Clarkson University—Pragasen Pillay
  - Kevin Kennedy and Associates, Inc.—John Miller
  - Jason Lai
  - LoPel Corporation—Krishnan Shenai
  - Motorsoft, Inc.—James Hendershot

– W. G. Odendaal
– Pennsylvania State University—Mike Lanagan
– Texas A&M University—Prasad Enjeti
– University of Illinois—Phil Krein
– University of Maryland—Patrick McCluskey
– University of Wisconsin—Thomas M. Jahns
– Yeadon Energy Systems, Inc.—William Yeadon

Future Direction

Task 1. Reducing the Size of Passive Components of Inverters

Clarkson University—Pillay
Focus additional research on the different topologies that can be used in the power electronic converter that interfaces between the ultracapacitor and dc link.

Penn State—Lanagan
Address the long-term reliability of newly developed dielectric materials for dc bus capacitor applications.

Future Dielectric Materials Development Paths

Polymers
- High-temperature
- Process integration
- Crystal/amorphous

Oxide Films
- Scale-up process
- Increase voltage
- Cost analysis

Glass Ceramics
- Graceful failure
- Thinner dielectric
- Process scale-up

Global R&D Topics
- Dielectric breakdown strength and graceful failure
- Permittivity characterization (E-field, frequency, temperature)
- Electrode/dielectric interfaces
- Reliability over 10 years at high temperature

Task 2. Reducing PM Manufacturing Costs

University of Wisconsin—Jahns
- Since experience with the large-scale production of interior-mounted PM (IMPM) machines is very limited in North America, there is a significant need to establish the necessary manufacturing technology to make automated manufacturing feasible and efficient.

Candidate techniques include injection molding of the NdFeB-bonded magnets directly into the IMPM machine rotor.

- The available design tools for minimizing the cost of the magnets and their assembly into IMPM machine rotors are still limited and inaccurate. Since magnets play such a key role in determining the cost of PM machines, every effort should be made to develop optimized rotor designs that achieve the required performance levels with the minimum amount of magnet material.
- The magnets buried inside the IMPM machine rotors are typically held in place by thin steel bridges that must provide sufficient structural strength at high rotor speeds without magnetically shorting the magnets. Clever mechanical design and careful structural analysis are required to determine and verify the best available solutions.
- The segmented stator configuration offers opportunities for reducing manufacturing costs for large-scale production. However, these savings will be realized only if sufficient engineering attention is devoted to developing the manufacturing techniques that will capitalize on the cost-reduction opportunities.
- The suitability of high-performance synchronous SPM machines for electric propulsion applications depends on the machine's ability to deliver wide speed ranges of constant-power operation. Although the underlying theory has been established, considerable engineering effort is still required to experimentally verify the key concepts and optimize the resulting machine designs for high performance and low cost.
- Given the appealing performance features of the IMPM machine and the opportunities for stator cost reduction using segmented concentrated winding configurations, the possibility of combining both into the same PM machine is very intriguing. However, significant design issues are raised by such a machine configuration, including its ultimate feasibility. The payoff is sufficiently high to justify an R&D effort to seek successful development of such a machine.

Motorsoft—Hendershot

- Further integration of inverters should be pursued, using power bridge modules, gate drivers, current transducers and microprocessors that also allow sensorless commutation.
- Sensorless commutation should be pursued for reliability improvement and cost reduction.
- Rotor manufacturing processes for internal type PM rotors need to be improved, possibly injecting neodymium magnet material in place to reduce cost.
- Use of and possible improvement in bi-state magnetic materials used in the rotor lamination should be pursued. Their use can improve the structural integrity of the rotor. Possibly, the relative permeability of the material in its highest permeability state can be improved from 900 to closer to 8000 (the permeability of M19 lamination steel).
- Development of a highly thermally conductive plastic is needed for injection molding for impregnating stator windings.
- Engineered thermoplastics should be developed for molding of the end bells, end frame, or cooling jacket to eliminate or reduce machining. The end frame and one end bell possibly could be molded as one piece.
- Losses in the machine need to be identified. It has long been accepted that that the sources of heat in the machine are the copper losses or I square R, iron lamination eddy current, and hysteresis losses. Work is needed to look at the skin effect, proximity effect, ac impedance

losses in mutual current distribution in parallel conductors, and their effect on losses. These are usually eliminated by conductor transposition.
- New lower-cost and iron-loss lamination material for laminations should be developed.

Yeadon Energy Systems—Yeadon
- Overall, the switched reluctance motor has the best chance of making us free of foreign control of materials. There is enough copper and iron in the United States to completely free us from reliance on rare earth magnet materials. The Upper Peninsula of Michigan alone has iron and copper reserves that would last more than 1000 years. Additional research into motor and drive characteristics is warranted.
- Based on this information, additional research is recommended to improve the flux density capabilities of steel. Materials are currently available—with the trade names Vanadium, Permendur, and Hyperco—that increase flux densities by 30%. But they contain about 48% cobalt, which raises the cost and is itself a rare foreign-controlled material. Finding an alternative that would produce the same results as adding cobalt would provide a motor similar in size to the rare earth PM brushless dc (BLDC) motors. It would also help reduce the size of BLDC and PM dc motors.
- Michigan Technological University should be employed to determine a low-cost extraction method for ore, as well as to develop improved magnetic steels. Since this university has both mining and metallurgy programs, a collaboration project is feasible.
- Applying the kind of research effort to brush/commutator materials that has been used for capacitors should yield additional life and make the PM dc motor a contender for this application because of its lower drive cost.

Task 3. Vehicle System and Subsystem Interactions with Power Electronics

Lai
- Efficiency: There is a strong need for high-efficiency power conversion systems.
- Voltage level: H.V. levels for traction and ancillary drives need to be investigated.
- Motor type: Increased reluctance torque on PM machines needs to be achieved.
- dc-dc converter: There is a need for high–efficiency, compact, high-power bidirectional dc-dc converters
- System integration: There are sensor, inverter, and motor integration needs.
- Electromagnetic interference (EMI): Methods are needed to achieve reductions with advanced modulation soft-switching technologies.
- Energy storage: Evaluation is needed of ultracapacitor energy density and life cycling effects.
- dc bus capacitor: High current requirements need to be met.
- Advanced inverters: Specifically on the Z-source inverter and soft-switching inverters should be pursued.
- Advance Motors: PM machines with constant power range extension need to be developed.

Texas A&M—Enjeti
Government funding of some of the critical research needs is essential and can effectively shorten the technology development. Funded projects to stimulate university/industry cooperation should be pursued, and there should be increased cooperation between national laboratories and universities.

- There is a strong need for a power device that combines the metal oxide semiconductor (MOS) gate control characteristics with the current-carrying capability and voltage drop characteristics of a thyristor-type structure. The device forward voltage drop even at higher currents (>400 A) must be less than 2 V and at the same time must be capable of being operated at switching frequencies higher than 10 kHz. In addition to the switching device, there is a need for development of a new power diode with superior dynamic characteristics. Research on silicon carbide (SiC) needs to be accelerated to enable its application to high-power switching devices at higher operating temperatures. The devices and the rest of the components need to withstand thermal cycling and extreme vibrations. Research should fully test a hardware prototype of a high-temperature dc-dc converter and the inverter with SiC devices. Some R&D could also study the design aspects of power electronic systems that need to withstand extreme vibrations.
- The technologies related to device packaging need to be investigated for developing a power switch. Wire bonding and device interconnections are barriers to development of high-current-density power units. Currently, the package resistance is about 20% of the total MOS field effect transistor (MOSFET) resistance. The other 80% is the chip contribution. In the future, with decreasing specific on-resistances (Rds(on) × area), the package share would be easily be 50% without further developments in assembly technology. Depending on the bonding configuration, the current rating of a MOSFET is limited either by the chip itself or by the bonding. Technologies such as topside power connection without wire bonds (copper strap) need to be investigated. The advantage of copper strap is that it has a larger cross-section used to carry the current, and the surface connection with the source area leads to reduced package Rds(on) and higher current capability. Also, device packaging technologies such as heat-sinking on both sides of the die and interconnect solutions for large-scale manufacturing need to be investigated.
- Capacitors with HF and H.V. operation, low equivalent series resistance (ESR), high operating temperature, and high ripple current capability need to be further developed. Hence, improved dielectric materials need to be investigated. The technology of laminated bus bars with high isolation voltage and low inductance needs further work to meet the automotive operating environment. To meet the packaging goals, the components must be designed to operate over a much higher temperature range.
- A novel way of cooling the entire power conditioning unit needs to be examined to quickly take away the heat from the devices. The current heat management techniques seem inadequate to dissipate heat in high-power-density systems.
- Research into improving and/or enhancing ultracapacitor technology with increased power density and lowering manufacturing needs to be accelerated. The development of ultracapacitors is important for the development of both internal combustion engine–hybrids and fuel cell 19 vehicles. It is envisioned that ultracapacitors alone can meet future automobile energy storage needs.
- Although soft-switching inverters have the advantage of lower switching losses and low EMI, they need more components, higher-operating-voltage devices (depending on the topology), and complicated control compared with hard-switched inverters. Hence the soft-switched inverter application is limited to very special types of needs. There is a need to develop an inverter topology to achieve the performance of soft-switched inverters with fewer components and simplified control. Topologies need to be developed with two or more integrated functions, such as the inverter, charger, and dc-dc converter, and with minimum

use of capacitors. More effort needs to be directed at packaging of the Z-source inverter and its dc-link bus bar design to improve performance and to reduce voltage excursions due to stray inductance.

- Integrated EMI filters for control of EMI generated as a result of switching of the devices need to be part of the inverter/converter topology. Fault-tolerant topologies and control techniques need further investigation. The system needs to be fault-tolerant and provide emergency capability.
- In the area of propulsion motor and other motor-control technologies, methods to eliminate the speed/position sensors, inverter current sensors, etc., have been under investigation for several years. These technologies have not yet proved to be practical for automotive applications. The technology development effort needs to be focused on speed sensorless operation of electric machines and reduction or elimination of current sensors in the inverters. The usage of single dc-link current sensor in the inverter to control the current within a three-phase motor is feasible and need to be explored further. The controllers need to be developed for robust operation.
- Development of low-cost and high-temperature magnets would lead to widespread use of PM motors. PM motors have higher efficiency and need lower current to obtain the same torque than other machines. This would reduce the cost of power devices also.
- The cost of developing new manufacturing processes and packaging techniques is prohibitive for low production volumes. The units have to be rugged and reliable for a 150,000-mile vehicle lifetime.

University of Illinois—Krein

Based on the three vehicle configurations and on more general design considerations for hybrid vehicles, a number of important research needs are identified. Significant issues include

- Low-cost semiconductor packages for insulated gate bipolar transistors (IGBTs).
- Soft magnetic composite (SMC) materials with improved permeability and reduced loss.
- Extension of polymer electrolyte capacitors to full dc bus ranges.
- Tradeoffs for fuel cell voltage.
- Controls and circuits that support reduced converter complexity.
- Better methods for bidirectional conversion.
- Low-cost gearboxes that use motor control for synchronized shifting.
- Fundamental understanding of dynamic capabilities and dynamic energy tradeoffs in fuel cells.
- Package and device integration.
- Controls that support “soft-bus” designs.
- Dynamic system simulation that identifies specific losses and short-term energy tradeoffs.

Task 4. Feasibility and Reliability of High-Temperature Power/Control Electronics for HEVs

Kevin Kennedy Associates—Miller

Recommendations made in the full report are translated into R&D community technology needs for 300°C control and power electronics.

- Resistors: Laboratory work is ongoing now to develop thin film resistors for 300°C applications. Auburn University is looking at new materials in lieu of nichrome thin film, but more R&D is needed.
- Capacitors: The U.S. high-temperature electronics industry needs a fundamental materials breakthrough or a fundamentally new concept for high-dielectric-constant and H.V. capacitors that will not have the capacitance tolerance problems of X7R ceramics. R&D should focus first on the conductive ceramics.
- Active devices: The high-temperature semiconductor industry has available a limited suite of SiC diodes—bipolar junction transistors, vertical junction FETs, and soon, MOSFETs and IGBTs—available for 225°C and higher continuous operation. R&D is needed to solve the issues with gate oxide, metalization, and electromigration issues and ion impurities. Gallium nitride devices can be tailored to power and should receive more R&D. Commercial companies such as CREE, ExFab, Siced GmbH, and others are pushing the technology, but a U.S. national focus is needed.
- High-temperature control and power electronics: DOE and ORNL should promote the creation of a center on extreme environmental electronics funded by the National Science Foundation. This follows from recommendation No. 1 of this report section, and uses CPES, the model used at the Virginia State and Polytechnic University center for power electronics systems, as the model. CPES was primarily a components center, but in recent years it has risen to a systems center. This model should be applied to the proposed center for extreme environmental electronics.
- Stretch recommendation—How to "leap-frog" Toyota and Honda: Two trends are emerging from this study that are precursors to a roadmap on how the United States might profit from the lessons learned by Toyota and Honda HEV products and technologically "leap-frog" them to wider applications. The two trends are that high-temperature power electronics devices are inherently H.V. components. Both SiC and gallium nitride have excellent H.V. capability.

Lopel Corporation—Shenai

Currently, the power electronics industry is fragmented. What is needed is a concerted effort from component and system providers working in tandem with automotive manufacturers. A well-focused collaborative effort that includes university, industrial, and governmental organizations within a newly formed research infrastructure is needed to rapidly develop and commercialize breakthrough disruptive technologies. With this perspective in mind, a non-profit research center dedicated to the development and rapid commercialization of strategic breakthrough technologies is recommended, as shown in Fig. 1.

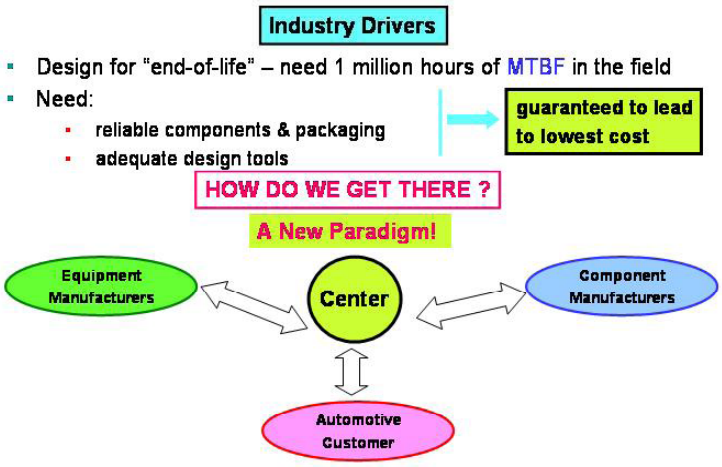

Fig. 1. Recommended platform for technology development and commercialization.

Odendaal

Several challenges must be met to achieve reliable, cost-effective, high-temperature power electronics systems for HEVs. High-temperature solutions have to be found for each of the constituent technologies of power electronics if a complete high-temperature solution is sought using HEVs. Failure in one key constituent technology will affect the entire system. Pursuing a technological solution that depends on a chain of successes in a short term, therefore, presents a high-risk.

A better strategy would be to invest in a research roadmap aiming at parallel technological advances that would each produce an incremental benefit, but that are not dependent on one another for an improved systems solution.

University of Maryland—McCluskey

The desire to increase the fuel cell baseplate temperatures to temperatures that will cause junction temperatures to exceed 150°C requires research be focused in the following areas:

- SiC IGBT device research
- SiC-SiO2 interface research (for high-temperature power MOSFETs)
- Integrated circuits containing SOI control and SiC power devices
- Failure mechanism modeling for SiC power devices, including oxide breakdown in MOSFETs
- Research into electromigration and metallization stability for SiC devices
- Capacitor ceramic dielectric development for higher power density
- Nanocrystalline magnetic materials for lower core losses
- Characterization of fatigue in high-temperature, lead-free die attach and substrate attach materials
- Development of die attaches through sintered nanopowders or other solid state diffusion methods

- Modeling of fatigue and fracture in DBC, HTCC, and LTCC ceramic substrates
- Development of new interconnection schemes for integrated packaging of power electronics
- Modeling of reliability of interconnect structures in power electronics, focusing on wire bonds and flip chips

---

Technical Discussion

DOE's Office of FreedomCAR and Vehicle Technologies supports R&D to understand and develop technologies that will ensure the nation's transportation energy and environmental future. As part of that program, the Advanced Power Electronics and Electric Machine activity seeks to develop power electronics and machinery technologies that improve performance and dramatically decrease system costs for light and heavy vehicles. With a focus on fuel-cell–powered vehicles and HEVs, the R&D will emphasize the development of component technologies for such items as inverters, dc-dc converters, controllers, and motors. The specific goal for FY 2010 is to develop an integrated electronics system that costs no more than $12/kW peak and can deliver at least 55 kW power for 18 seconds and 30 kW of continuous power. The operational life of the propulsion system should be at least 15 years or 150,000 miles. In support of this goal, the following four areas were investigated.

Task 1. Reducing the Size of Passive Components of Inverters
As the silicon die and its associated cooling requirements shrink, dc-link capacitors are steadily becoming a larger percentage of the physical size of the inverter. In order to reduce the total size of an inverter that will meet the FreedomCAR expectations (i.e., low cost, minimum of 15-year life, high efficiency, easy maintenance, and small size), the size of the dc-link capacitors and other passive components needs to be significantly reduced. This study analyzed various capacitor technologies and drew conclusions as to where the gaps are in obtaining components that will fulfill the FreedomCAR goals.

Task 2. Reducing PM Manufacturing Costs
As the raw material costs, for all practical purposes, are fixed or beyond the control of motor manufacturers, manufacturing issues remain the only viable method to decrease the cost of the magnets, which remain by far the high-dollar item in a PM motor. This assessment involved examining manufacturing issues to reduce the cost of the magnets for PM motors. It investigated the current state of the art in rare earth magnets and examined the advantages, disadvantages, and cost tradeoffs with sintered and bonded magnets, as well as methods used to produce them.

Task 3. Vehicle System and Subsystem Interactions with Power Electronics
This task required analytical investigation of potential HEV power electronic and motor systems and the potential interactions between these systems and associated energy-conversion and related subsystems and components. Typical interaction subsystems/components include energy-storage subsystems, prime-mover engines, other vehicle electrical systems, thermal systems, and auxiliary power systems. The study required

- systems analysis to identify three potential vehicle system configurations, including approximate design configurations and operating regimes
- potential system and subsystem interactions that could influence the design and operation of advanced power electronics and motors.

Task 4. Feasibility and Reliability of High-Temperature Power/Control Electronics for HEVs

The purpose of this task was to perform a comprehensive study to determine how high-temperature–tolerant control and power circuits would affect the design and operation of HEVs. Future HEVs may have fuel cells that operate at high temperatures and use power semiconductor devices that can tolerate these high temperatures. However, the gate drives, sensors, and control circuits associated with power electronics currently cannot tolerate these temperatures.

Reliability of power converters has been and still is a big concern in automotive applications. Some issues are related to the electrical connection and mechanical attachment of silicon dies in power semiconductor modules. Wire bonding and die soldering technologies, widely used in commercially available power semiconductor modules, are failure-prone in harsh thermal environments. New packaging techniques need to be developed to eliminate the bond wire and solder joints. These new technologies need to be evaluated in automotive environments. In addition, long-term reliability of power converters and high-temperature electronics needs to be addressed at a system level.

The investigators were asked to identify the state of the art in high-temperature circuits and packaging/assembly techniques in the aerospace and other industries that may have applications in future HEVs. The investigators also made recommendations for steps needed to extend these high-temperature electronics technologies into passenger cars. Reliability and low cost were two of the main factors weighed during the study.

Conclusions and Summaries

Task 1. Reducing the Size of Passive Components of Inverters

Clarkson University—Pillay

Methods are shown for reducing the dc-link capacitor and ultracapacitors as well as highlighting the implications on the power electronics. The dc-link capacitors can be reduced by implementing technologies such as active filters, current and power balancing, pulse width modulation interleaving, and machine design. The current ultracapacitor technology suffices for energy storage needs, but its size and mass can be reduced by improving power electronics technology and optimizing the ratings of ultracapacitor cells.

Penn State University—Lanagan

Dielectric materials are divided into three broad classes: polymer, oxide, and glass ceramic. Polymer-film capacitors are presently used for power electronics applications, and high-temperature polymers will enable the use of high-ripple current capacitors with better reliability in HEVs. Oxide films have the highest energy density and thus the greatest potential volumetric efficiency of any of the dielectrics materials. High-dielectric-constant oxide films are presently

being explored by Motorola and electronic manufacturers for large-scale insertion into printed circuit boards. Glass ceramic materials will operate at 140ºC, and more research on graceful failure mechanisms is needed.

Global R&D topics encompass all research on and aspects of dielectric materials. Dielectric breakdown strength is important for component reliability and the ultimate voltage rating of a capacitor. The intrinsic dielectric breakdown strength must be known, as well as the effect of process defects on diminishing breakdown strength. Permittivity (dielectric constant) is a function of temperature, frequency, and breakdown strength, which will decrease the capacitance rating. Graceful failure mechanisms and capacitor reliability are strongly influenced by electrode/dielectric interfaces, which need further research. Capacitor reliability is a key parameter for HEV applications. Generally, highly accelerated life tests are used to predict long-term component life.

Task 2. Reducing PM Manufacturing Costs

Motorsoft—Hendershot

- One of the major costs is in the PMs. It is suggested that the minimum-cost rotor design will incorporate cubed magnets in order to eliminate costly grinding, which results in an increase of up to 20% in magnet cost.
- Embedded magnet rotor designs also are compatible with field weakening, which achieves the goal of a wide constant power output over a wide speed range.
- Stator designs should maximize slot fill. Designs cited in this report allow winding the coils in a manner that maximizes the slot fill; therefore, motor output power is maximized and winding temperature minimized.
- Taking advantage of low labor rates in the Far East and final assembly in the United States could reduce motor costs. The trend in manufacturing appears to be away from vertical integration and toward outsourcing parts and subassemblies from the Far East with final assembly retained in the United States.
- The motor's stator and rotor should be integrated into existing drive train components.
- Sensorless commutation should be pursued for reliability improvement and cost reduction.

Yeadon Energy Systems—Yeadon

- Any of the motors described in this report could provide acceptable performance and life if the disadvantages could be overcome.
- The PM dc motor would provide the lowest overall system cost because of the lower-cost drive.
- The SRM would be the next-lowest–cost system cost because it has no PMs.
- The ORNL BLDC motor is more costly than the IR version because of the higher magnet weight. (Further study of this motor is not recommended).
- The simplest from of the IR BLDC can meet the cost target of less than $7 per peak kW.

Task 3. Vehicle System and Subsystem Interactions with Power Electronics

University of Wisconsin—Jahns

This report presented a variety of concepts that, in the eyes of the author, hold the highest promise for reducing the cost of future PM machines. A key theme that permeates this discussion is the observation that the PM machine configuration and design play major roles in determining the machine's final production cost. Minimizing the amount and strength of the magnet material required to build a particular PM machine design can have a major impact on the production cost. This savings may exceed the savings that could be realized by reducing the per-kilogram cost of the magnets themselves.

Promising opportunities for PM machine cost reductions include the adoption of IMPM rotor configurations that reduce both the amount and strength of the required rotor magnets and the use of concentrated stator windings with segmented stators applied to surface PM machines. This could possibility be applied to future IMPM machines. Also, SMC materials offer possibilities for radically changing the way that electric machines are manufactured today by eliminating the need for laminated steel stator and rotor cores.

Barriers to the wide adoption of PM machines in electric propulsion systems include the need to deliver wide ranges of constant-power operation and the vulnerability of PM machines to high winding fault currents. Significant reductions in PM machine manufacturing cost probably can be achieved during the coming years. However, the technology barriers and gaps must be addressed

Lai

The technology assessment can be summarized as follows:

1. Single-stage versus double-stage power conversions: The low-voltage energy source and H.V. inverter-motor drive requires a substantial voltage boost, which can be achieved with the single-stage or double-stage power conversion that has been used in Toyota and Lexus HEVs. The question is whether some single-stage boost inverters can be used to save cost and to increase the system efficiency.

2. High-voltage versus low-voltage power electronics: High-voltage motor drives used in Toyota and Lexus HEVs have shown some improvement in power density and perhaps in motor efficiency. The question is whether H.V. power electronics using H.V. devices, typically rated at 1200 V, can take advantage of lower costs and improving efficiency.

3. System integration issues: There are two aspects of system integration. One is to integrate the motor and inverter, and the other one is to integrate all H.V. power electronics. The issues involved in these two aspects are

- Motor-inverter integration: determine the size, power level, and application for this level of integration.
- High-voltage power electronics integration: determine the impact of interference between inverters and overall EMI.

4. EMI issues: EMI can be improved with (1) better layout and packaging, (2) better filter design, (3) a novel inverter modulation scheme, and (4) novel gating control or soft switching. These can all become important research topics.

5. Efficiency issues: Power conversion efficiency remains a major issue as long as there are power conversion losses. Efficiency can be improved with (1) a better device, (2) better modulation, and (3) better gating or soft switching. Like EMI improvement methods, these efficiency improvement methods can be incorporated in overall better system solutions.

6. Energy storage and energy management issues: With advancements in energy storage components such as ultracapacitors, the opportunity to improve associated energy management systems is largely increased. The power electronics R&D topics in this area can be found in novel soft-switching converters that allow highly efficient operation while minimizing the passive component sizes.

7. dc bus capacitor issues: The major issues with the dc bus capacitor are related to capability to handle HF ripple currents under high-temperature conditions while maintaining a compact size and weight.

8. Advanced inverter topologies: Several new advanced circuit topologies are relatively immature and need some time and development effort to see if they can be the major contender for motor drive applications. The independent phase-leg resonant snubber inverter and the inductor-coupled zero-voltage transition inverter are two promising soft-switching inverter candidates for further R&D effort to see their efficiency impact. The Z-source inverter is a new type of inverter that needs further investigation of its voltage boost ratio and cost-effectiveness to compare with multiple-stage power conversions.

9. Motor technologies: The PM machine is a clear winner for traction motor drives. Whether the constant power is enhanced by the reluctance torque or by a higher voltage boosted by an intermediate-stage converter, the PM machine has been adopted by major Japanese auto manufacturers in their hybrid and fuel cell vehicles. Although further improvement of constant power range extension is needed, most R&D needs in this area are in refined engineering and manufacturing processes for power density improvement and cost reduction.

Texas A&M—Enjeti

Power electronics has a major role in HEV and fuel-cell–powered vehicles. Also, the integration of actuators with power electronics reduces the overall systems cost. In addition to the power electronics, the technology of the electric motor plays a major role in the dynamics of the vehicles and the type of the power converter required for controlling the vehicle operating characteristics.

The power semiconductor devices, converters/inverters, control and switching strategies, packaging of individual units, and system integration play a major role in bringing hybrid and fuel cell vehicles to market with reliability and affordability, The power electronics system should be efficient to improve the range and performance of the electric vehicles and fuel economy in hybrid vehicles.

In addition to the power devices and controllers, other components such as capacitors, inductors, bus bars, and the thermal system form a major portion of the power electronics. The packaging of all these units as one system has significant challenges. To meet the challenges of the automotive environment, several technical challenges need to be overcome, and new developments are needed from the device level to the system level.

University of Illinois—Krein
Power electronics technology is a dominant factor in the development of hybrid and fuel cell vehicle systems. When three vehicle configurations presented here are compared, it is clear that the power electronics subsystems share many common elements. If the present practice of building a system around a fixed dc bus voltage is retained, it is possible to identify common traction inverters, self-contained ultracapacitor interfaces, specific energy storage requirements, and other near-standard power electronics elements. Progress is limited, however, by costly semiconductor packages, other materials issues, and even the challenges of establishing a standard fuel cell dc bus voltage.

One key area that has not been addressed in prior research is the design of the traction unit as an integrated subsystem. The physics of electric machines is such that a given type and mass provides a specific rated force. The power density can be increased as desired by operating at higher speeds. An electric traction motor can be designed in conjunction with a selectable gearbox to reduce mass without compromise in performance. Similar efforts are well known in aerospace and marine applications, in which higher operating frequencies and speeds yield small machines with high power capability.

Task 4. Feasibility and Reliability of High-Temperature Power/Control Electronics for HEVs

Kevin Kennedy and Associates—Miller
It is clear that circuits for high-temperature electronics remain physically large, and the service companies involved in developing components for high-temperature electronics have made virtually no progress in this field since about 1994. It was actually easier to source high-temperature electronic components in 1984 than in 1994, and certainly easier than in 2004.

One of the fundamental reasons for the decline in high-temperature and high-reliability circuits expertise has been the shift away from MIL STD 883–qualified components toward replacement with commercial temperature- and reliability-rated components. This shift has removed the motivation in the industry to develop high-temperature electronics. Pockets of expertise remain in the military and aerospace sectors, where such products are needed to move engine control electronics out of the cockpit and onto the jet engines being controlled, thereby eliminating hundreds of pounds of wiring per aircraft. Oil exploration requires higher-temperature-rated and more robust electronics for downhole monitoring of drilling operations because wells are getting deeper and hotter. The geothermal industry is another that requires higher-temperature electronics for monitoring. But mainstream industries such as automotive, military land vehicles, naval surface ships, and submarines all benefit from higher-temperature and higher-reliability electronics.

Lopel Corporation—Shenai

Power electronics is in need of major breakthroughs in component and packaging technologies to make the next big leap at the system level. In addition to fuel cell vehicles, HEVs, and other automotive electronic applications, key drivers include power supplies, motor control, electronic ballasts, medical equipment, aerospace applications, and electric utilities. Major breakthroughs are expected within the next 5 years in power semiconductors, magnetic and passive components, and component and system packaging technologies.

Demands for energy efficiency have increased dramatically. In addition to cost savings, the consumer is demanding compact lightweight and battery-operated wireless devices in almost every application. Powering such functions has become a critical challenge in the information economy. A major thrust in addressing all these issues simultaneously has been to perform power conditioning functions at increased switching frequencies. High-frequency power switching, however, has led to rapidly diminishing returns in the field-reliability of critical power systems such as the computer and telecom power supplies. The primary reason has been an increase in power density and a lack of adequate thermal management technology. A new paradigm is needed in assessing and implementing advanced, reliable low-cost power/control technologies to successfully commercialize fuel cell vehicles and HEVs. A system-level approach, coupled with technology developments in strategic areas, needs to be pursued immediately in a collaborative environment.

The only solution to this problem is to develop breakthrough component and packaging technologies that result in dramatic improvements in power density and field reliability. Recent advances in SiC material technologies have shown great potential to achieve this goal within a reasonable period of time. With this objective in mind, a list of urgent tasks and developmental areas is shown in Fig. 2. Figure 3 is a 5-year roadmap that would complement existing governmental and private efforts and rapidly address mission-critical technologies for commercialization of fuel cell vehicles and HEVs. The funding requirements in various strategic technological areas are outlined in Fig. 4. The key building block to rapidly advance power electronic technology is the power semiconductor switch itself. Figure 5 illustrates important technology milestones and a schedule to successfully implement the roadmap shown in Fig. 3.

Two important factors that have critically hampered the widespread commercialization of SiC power switching technology are the cost and field-reliability. Recent advances in material technology promise nearly defect-free, 6-in.-diam. SiC wafers with various poly types within the next few years. With adequate funding and well-focused efforts, we believe that a successful materials program can be built to realize this vision. A materials program is outlined in Figs. 6 and 7.

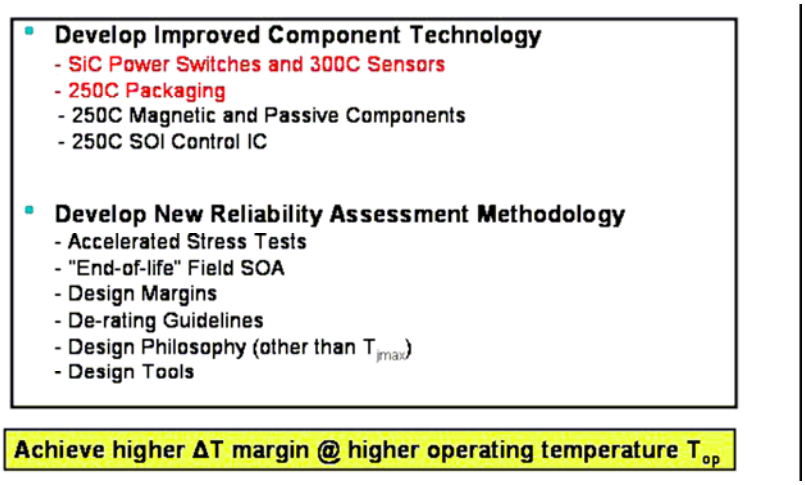

Fig. 2. Recommended key developmental areas in power/control electronics.

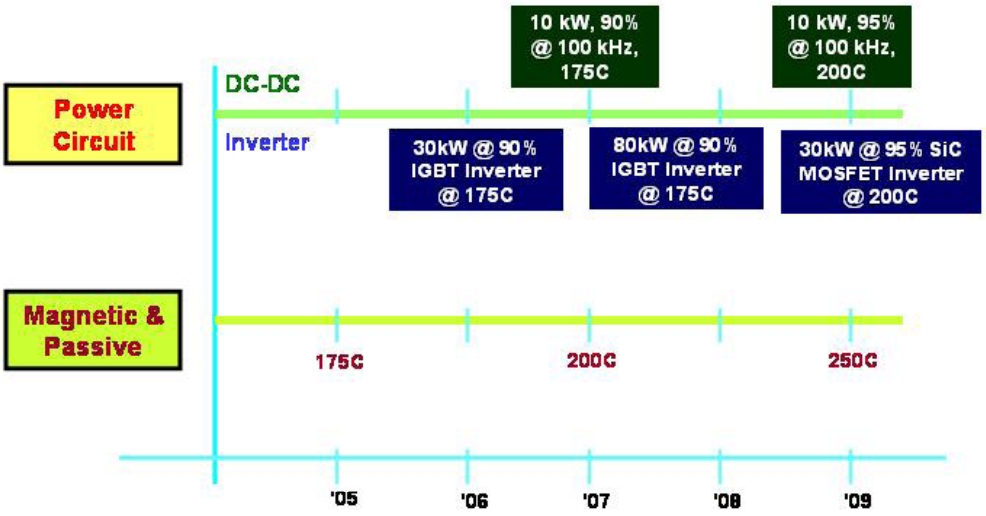

Fig. 3. A recommended five-year technology development roadmap.

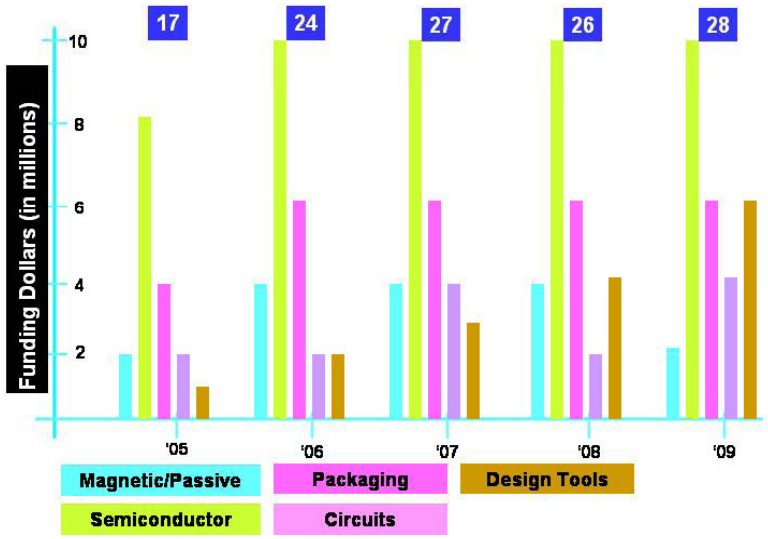

Fig. 4. Anticipated budgetary requirements to successfully implement the five-year technology roadmap.

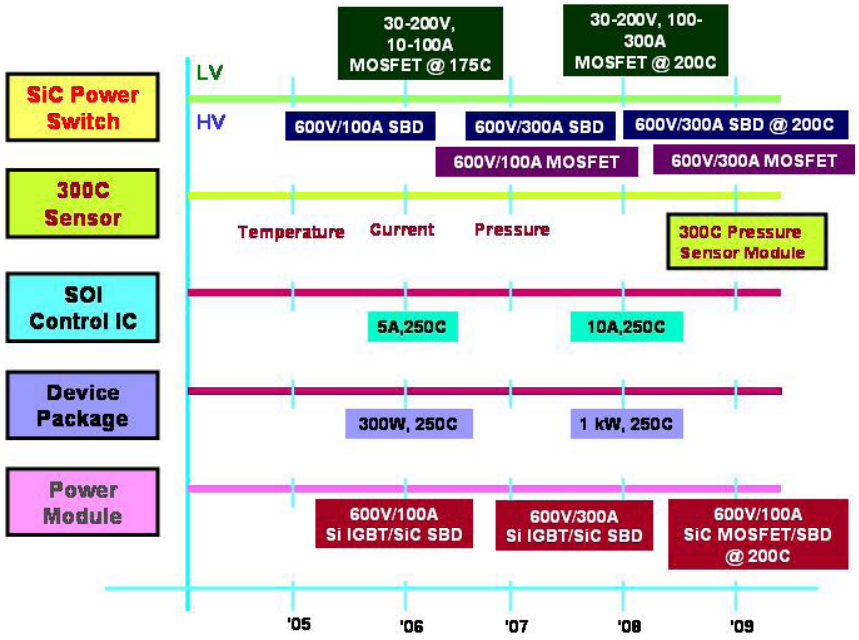

Fig. 5. A recommended roadmap for semiconductor device and packaging.

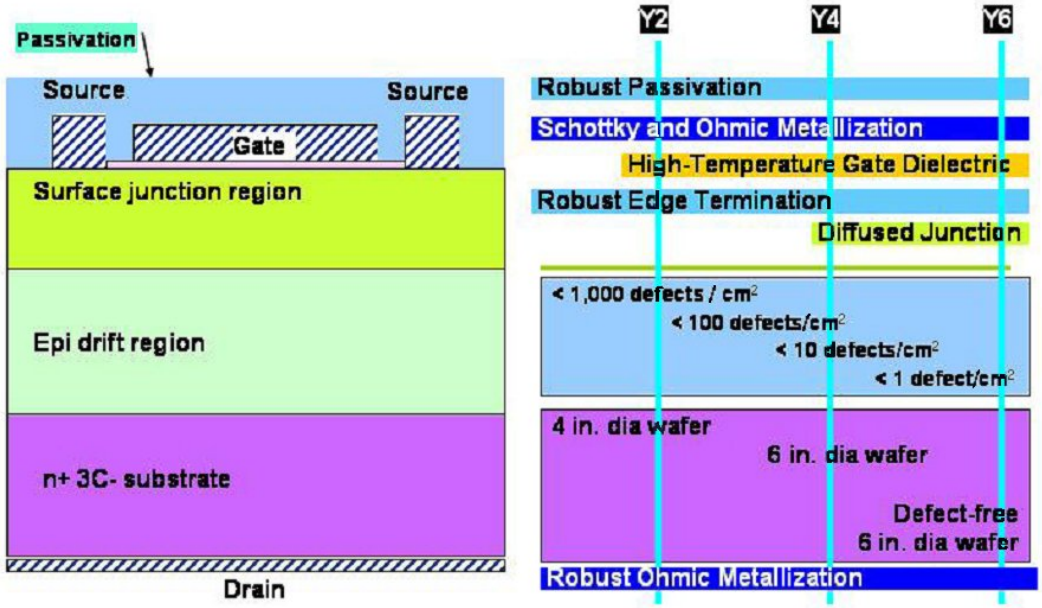

Fig. 6. Key material technology developmental areas in SiC.

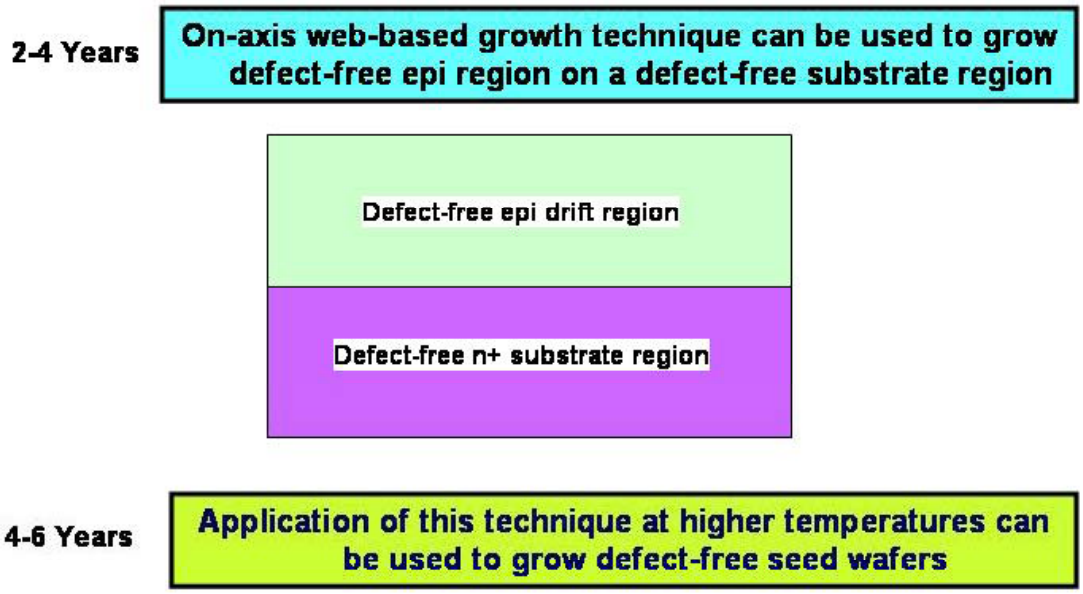

Fig. 7. Expected material development schedule in SiC.

Odendaal

Circuits for control and gate-drives are traditionally realized on double-sided and multilayer PCB for a convection-cooled environment. In automotive applications, the ambient temperatures in cavities where these circuits reside can rise to 150ºC, which is detrimental to performance and reliability. Again, better cooling and packaging strategies will have to be implemented (1) by adopting circuit assembly techniques that can be attached thermally to a heat sink and (2) by

adopting packaging, assembly and component technologies that will operate reliably at higher temperatures. Technologies for raising the temperature limit of small signal electronics for various applications, of which the majority were for sensing, have already been demonstrated with near-sufficient reliability. This is an indication that bridging the gap to include signal, control, and gate drive circuitry should be possible within a relatively short time span. Whether high-temperature solutions for the control and drive circuitries will be inexpensive enough to be adopted by the automotive industry within a reasonable amount of time is a harder question to answer. Gate-drive circuits for inverters of 50 kW and higher are power electronics circuits themselves, suffering some of the same cooling and reliability-related difficulties as the inverters as a result of large voltage isolation requirements and large capacitive and inductive components.

Capacitor technologies present one of the most critical barriers to realizing high-temperature electronics. A cost-effective, high-temperature substitute for electrolytic capacitors, which are key components in power electronics, would be required. Even the shelf lifetime of electrolytic capacitors is limited to a couple of years, thus constituting high maintenance cost in an automotive application. High-temperature capacitors with high energy densities, voltage ratings above 500 V, and lifetime expectancies of over 100,000 hours simply do not exist. High-density, H.V. capacitors are a critical enabling technology for future automotive applications.

Comparing all of the constituent technologies of power electronics technology, power semiconductor technology is by far in the lead, with magnetic components lagging the most. Still, wide-bandgap device technologies have not matured, and packaging of high-temperature power devices is still in the early stages. The first commercial discrete SiC MOSFETs can be expected in 3–4 years. High-temperature multichip modules for commercial use will not be available for another 5–10 years.

Other constituent technologies will lag by at least another 5 years before a complete high-temperature system can be realized. In a cost-sensitive application, the cost of such systems will prevent them from entering that market for at least another 5 years. Considering global industrialization and cost-competitiveness between electronics manufacturers on different continents, market penetration of high-volume, high-tech solutions is becoming increasingly difficult. Even if market downswings do not inhibit technology development within the next 10–20 years, the probability of having competitively priced high-temperature systems in automobiles on a mass scale within that period is unlikely.

High-temperature solutions must be found for each of the constituent technologies of power electronics if a complete high-temperature solution is sought inside an HEV. If this fails for one key constituent technology within the desired timeframe, then the entire system will suffer. A better strategy would be to invest in a research roadmap aiming at parallel technological advances that would each produce an incremental benefit but that are not dependent on one another for an improved systems solution.

There is no question that availability of cost-effective and reliable high-temperature electronics will have a tremendous impact on enhancements in weight, size, and performance of future automobiles. High-temperature power electronics technologies for 200°C junction temperatures in systems with 90–100°C coolant represent a long-term investment that may not pay off for

another 15–20 years in the automotive industry. A more conservative approach is proposed whereby benefits can be reaped within a term of 5–10 years by pursuing cross-cutting technologies that will advance silicon-based power electronics at normal and moderately raised junction temperatures. If chosen carefully, such technologies should also benefit high-temperature electronics once they become feasible.

University of Maryland—McCluskey

Power electronics devices and their packaging will play a major role in making the fuel cell HEV a reality. The total power controlled by electronics in a typical gasoline-powered hybrid exceeds 200 kW, and this will continue to grow as hybrid drives make their way into larger automobiles and trucks and as fuel cells take the place of internal combustion engines as a hybrid power source.[2] The electronic systems include power systems such as dc-dc converters, inverters, and motor controllers, along with small signal systems such as gate drivers and on-board engine, braking, and HEV computers. These systems use a range of active and passive devices and interconnection materials.

References

1. Philip G. Neudeck et al., "Characterization of 3C-SiC Films Grown on 4H- and 6H-SiC Substrate Mesas During Step-Free Surface Heteroepitaxy," pp. 213–216 in *Materials Science Forum*, **433–436**, 2003.

2.. *Fuel Cell Systems Explained*, John Wiley and Sons, New York, 2001.

DISBRIBUTION

1. D. J. Adams, Oak Ridge National Laboratory, National Transportation Research Center, 2360 Cherahala Boulevard, Knoxville, Tennessee 37932-6472
2. C. W. Ayers, Oak Ridge National Laboratory, National Transportation Research Center, 2360 Cherahala Boulevard, Knoxville, Tennessee 37932-6472
3. J. M. Bailey, Oak Ridge National Laboratory, National Transportation Research Center, 2360 Cherahala Boulevard, Knoxville, Tennessee 37932-6472
4. T. A. Burress, Oak Ridge Institute for Science and Education, Oak Ridge National Laboratory, National Transportation Research Center, 2360 Cherahala Boulevard, Knoxville, Tennessee 37932-6472
5. G. R. Callison, Oak Ridge Institute for Science and Education, Oak Ridge National Laboratory, National Transportation Research Center, 2360 Cherahala Boulevard, Knoxville, Tennessee 37932-6472
6. J. B. Campbell, Oak Ridge Institute for Science and Education, Oak Ridge National Laboratory, National Transportation Research Center, 2360 Cherahala Boulevard, Knoxville, Tennessee 37932-6472
7. S. L. Campbell, Oak Ridge Institute for Science and Education, Oak Ridge National Laboratory, National Transportation Research Center, 2360 Cherahala Boulevard, Knoxville, Tennessee 37932-6472
8. J. N. Chiasson, The University of Tennessee-Knoxville, Electrical and Computer Engineering, 314 Ferris Hall, 1508 Middle Drive, Knoxville, Tennessee 37996-2100
9. M. Chinthavali, Oak Ridge Institute for Science and Education, Oak Ridge National Laboratory, National Transportation Research Center, 2360 Cherahala Boulevard, Knoxville, Tennessee 37932-6472
10. C. L. Coomer, Oak Ridge National Laboratory, National Transportation Research Center, 2360 Cherahala Boulevard, Knoxville, Tennessee 37932-6472
11. J. K. Denton, Oak Ridge National Laboratory, National Transportation Research Center, 2360 Cherahala Boulevard, Knoxville, Tennessee 37932-6472
12. T. Q. Dam, Oak Ridge National Laboratory, National Transportation Research Center, 2360 Cherahala Boulevard, Knoxville, Tennessee 37932-6472
13. T. Q. Duong, EE-2G/Forrestal Building, U.S. Department of Energy, 1000 Independence Ave., SW, Washington, DC 20585
14. J. J. Eberhardt, EE-2G/Forrestal Building, U.S. Department of Energy, 1000 Independence Ave., SW, Washington, DC 20585
15. E. C. Fox, Oak Ridge National Laboratory, P. O. Box 2008, Building 5700, Oak Ridge, Tennessee 37831-6168
16. K. P. Gambrell, Oak Ridge National Laboratory, National Transportation Research Center, 2360 Cherahala Boulevard, Knoxville, Tennessee 37932-6472
17. E. T. Grostick, Oak Ridge National Laboratory, National Transportation Research Center, 2360 Cherahala Boulevard, Knoxville, Tennessee 37932-6472
18. G. L. Hagey, EE-33/Forrestal Building, U.S. Department of Energy, 1000 Independence Ave., SW, Washington, DC 20585
19. J. S. Hsu, Oak Ridge National Laboratory, National Transportation Research Center, 2360 Cherahala Boulevard, Knoxville, Tennessee 37932-6472

20. S. M. Jenkins, Oak Ridge National Laboratory, National Transportation Research Center, 2360 Cherahala Boulevard, Knoxville, Tennessee 37932-6472
21. J. S. Lawler, The University of Tennessee, Electrical and Computer Engineering, 402 Ferris Hall, 1508 Middle Drive, Knoxville, Tennessee 37996
22. K. T. Lowe, Oak Ridge Institute for Science and Education, Oak Ridge National Laboratory, National Transportation Research Center, 2360 Cherahala Boulevard, Knoxville, Tennessee 37932-6472
23. L. D. Marlino, Oak Ridge National Laboratory, National Transportation Research Center, 2360 Cherahala Boulevard, Knoxville, Tennessee 37932-6472
24. J. W. McKeever, Oak Ridge National Laboratory, National Transportation Research Center, 2360 Cherahala Boulevard, Knoxville, Tennessee 37932-6472
25. S. C. Nelson, Oak Ridge National Laboratory, National Transportation Research Center, 2360 Cherahala Boulevard, Knoxville, Tennessee 37932-6472
26. P. J. Olszewski, Oak Ridge National Laboratory, National Transportation Research Center, 2360 Cherahala Boulevard, Knoxville, Tennessee 37932-6472
27. P. J. Otaduy, Oak Ridge National Laboratory, National Transportation Research Center, 2360 Cherahala Boulevard, Knoxville, Tennessee 37932-6472
28. G. W. Ott, Jr., Oak Ridge National Laboratory, National Transportation Research Center, 2360 Cherahala Boulevard, Knoxville, Tennessee 37932-6472
29. B. Ozpineci, Oak Ridge National Laboratory, National Transportation Research Center, 2360 Cherahala Boulevard, Knoxville, Tennessee 37932-6472
30. S. A. Rogers, EE-2G/Forrestal Building, U.S. Department of Energy, 1000 Independence Ave., SW, Washington, DC 20585
31. M. B. Scudiere, Oak Ridge National Laboratory, National Transportation Research Center, 2360 Cherahala Boulevard, Knoxville, Tennessee 37932-6472
32. L. E. Seiber, Oak Ridge National Laboratory, National Transportation Research Center, 2360 Cherahala Boulevard, Knoxville, Tennessee 37932-6472
33. R. H. Staunton, Oak Ridge National Laboratory, National Transportation Research Center, 2360 Cherahala Boulevard, Knoxville, Tennessee 37932-6472
34. R. L. Smith, Oak Ridge National Laboratory, National Transportation Research Center, 2360 Cherahala Boulevard, Knoxville, Tennessee 37932-6472
35. D. P. Stinton, Oak Ridge National Laboratory, P. O. Box 2008, Building 4515, Oak Ridge Tennessee 37831-6068
36. R. B. Shelton, Oak Ridge National Laboratory, P. O. Box 2008, Building 5700, Oak Ridge Tennessee 37831-6168
37. G. J. Su, Oak Ridge National Laboratory, National Transportation Research Center, 2360 Cherahala Boulevard, Knoxville, Tennessee 37932-6472
38. R. A. Sutula, EE-2A/Forrestal Building, U.S. Department of Energy, 1000 Independence Avenue, Washington, DC 20585
39. L. M. Tolbert, Oak Ridge National Laboratory, National Transportation Research Center, 2360 Cherahala Boulevard, Knoxville, Tennessee 37932-6472
40. C. P. White, Oak Ridge National Laboratory, National Transportation Research Center, 2360 Cherahala Boulevard, Knoxville, Tennessee 37932-6472
41. R. H. Wiles, Oak Ridge National Laboratory, National Transportation Research Center, 2360 Cherahala Boulevard, Knoxville, Tennessee 37932-6472